ANALYSIS AND IMPLEMENTATION OF ALGORITHMS FOR EMBEDDED SELF-MIXING DISPLACEMENT SENSORS DESIGN

Antonio Luna Arriaga

▶ **To cite this version:**

Antonio Luna Arriaga. ANALYSIS AND IMPLEMENTATION OF ALGORITHMS FOR EMBEDDED SELF-MIXING DISPLACEMENT SENSORS DESIGN. Optics / Photonic. Institut National Polytechnique de Toulouse - INPT, 2014. English. NNT : . tel-04262513v1

HAL Id: tel-04262513

https://theses.hal.science/tel-04262513v1

Submitted on 12 Sep 2014 (v1), last revised 27 Oct 2023 (v2)

HAL is a multi-disciplinary open access archive for the deposit and dissemination of scientific research documents, whether they are published or not. The documents may come from teaching and research institutions in France or abroad, or from public or private research centers.

L'archive ouverte pluridisciplinaire **HAL**, est destinée au dépôt et à la diffusion de documents scientifiques de niveau recherche, publiés ou non, émanant des établissements d'enseignement et de recherche français ou étrangers, des laboratoires publics ou privés.

THÈSE

En vue de l'obtention du

DOCTORAT DE L'UNIVERSITÉ DE TOULOUSE

Délivré par :

Institut National Polytechnique de Toulouse (INP Toulouse)

Discipline ou spécialité :

Micro-ondes, Électromagnétisme et Optoélectronique

Présentée et soutenue par :

M. ANTONIO LUNA ARRIAGA

le jeudi 3 juillet 2014

Titre :

ANALYSIS AND IMPLEMENTATION OF ALGORITHMS FOR EMBEDDED SELF-MIXING DISPLACEMENT SENSORS DESIGN

Ecole doctorale :

Génie Electrique, Electronique, Télécommunications (GEET)

Unité de recherche :

Laboratoire d'Analyse et d'Architecture des Systèmes (L.A.A.S.)

Directeur(s) de Thèse :

M. THIERRY BOSCH

M. FRANCIS BONY

Rapporteurs :

M. GUY PLANTIER, EC SUP ELECTRONIQUE OUEST

M. WILFRIED UHRING, UNIVERSITE STRASBOURG 1

Membre(s) du jury :

M. JEAN-CHRISTOPHE VALIERE, UNIVERSITE DE POITIERS, Président

M. ERIC LACOT, UNIVERSITE JOSEPH FOURIER, Membre

M. FRANCIS BONY, INP TOULOUSE, Membre

M. THIERRY BOSCH, INP TOULOUSE, Membre

Acknowledgements

I would like to express my admiration and gratitude to my thesis advisor Prof. Thierry Bosch for giving me the opportunity of being part of the OSE research group. While his scientific skills and perpetual willingness to listen have made an enormous contribution to this work, is his humanity that allowed me to overcome the hard times comprised in this learning experience.

All my respect and compliments go to Dr. Francis Bony for co-advising my work. Always full of sureness, his insights and friendship increased the confidence on my background knowledge and empowered the joy of becoming proficient in the domain of embedded systems.

I'm indebted with Prof. Guy Plantier from ESEO and Prof. Wilfried Uhring from Strasbourg University for taking the time to assess my research work despite their many responsibilities and busy schedules. In the same manner, I'm also honored by the presence of Prof. Jean-Christophe Valière from Poitiers University and Prof. Eric Lacot from Joseph Fourier University, all who have kindly accepted to be part of the examination jury.

I'm grateful to all the researchers and staff of this group for their kindness and the positive work ambiance all these years, Marc Lescure, Michel Cattoen, Francoise Lizion, Olivier Bernal, Francis Jayat and more recently Adam Quotb. Clement and Emmanuelle Tronche for their help in a personal plane, as well as Julien Perchoux for his friendship and family time spent. During some period, I had the privilege to share teaching time with some of the members of this group, I would like to thank Danielle Andreu, Hélène Tap, Han-Cheng Seat, Emmanuelle Peuch and Gilles Lugan for their the trust and help in this enriching task.

I treasure the time spent with all my fellow PhD students, Emmanuel Moutaye, Lucie Campagnolo, Raphael Teysseyre, Florent Bouyjou, Bendy Tanios, Lucas Perbet, Blaise Mulliez, Jalal Al-roumy, Mohanad Yousef, Siegfried Chicot, Laura Le Barbier, Lavinia Ciotirca and Evelio R. Miquet. The concerts, jogging sessions, trips and talks that we had constitue a memorable part of my life.

My thoughts and appreciation for the many other great people who I had the pleasure to know and exchange opinions in this research center, Todor, Usman, Olivier, Chiara, Jean-Claude, Laurent, Luc Eric, Sabine, Wah, Florentin and Jose Luis. I'm also glad to account, Thibault, Lydie, Michel and Monique, and the many compatriots who shared with me and my family so many times of joy.

The work on this manuscript has been accomplished with the support and encouragement from the people who has been with me since the beginning, my family. My mother who has devoted her life to make me grow integrally as well as my brother and sisters. They who saw

me leave more than a decade, are always there to keep warm the brotherhood ties. Loneliness was finished with the arrival of my lovely family Renata and Kael, you have been shining my life all these years. There are no words to thank the precious time that you gave me, I dedicate this work to you.

Contents

Introduction

In the field of optical metrology, interferometry based instruments are widely used in science and industry for the measurement of different physical magnitudes like displacements, absolute distance, velocity and vibrations.

The usage of lasers as an intense source of coherent light, along with the digital processing of the data obtained from an interferometer, make this technology of enormous interest for extremely accurate measurements. Some practical applications involve the test of optical systems, studies of surface topography, measurement of refraction index of transparent mediums and thickness of materials.

In conventional interferometers (e.g. Michelson), the different arrangements of lenses, beam splitters, and mirrors aim to provide a reference and a measurement beam traveling different optical paths. By gathering the mixed wavefronts with a receptor, a measurement can then be performed based on the obtained interference fringes.

Optical feedback interferometry phenomenon, can be simply understood as the interaction between an emitted laser beam and a small portion of backscattered light from a pointed target that re-enters the laser's cavity. It is manifested as a different kind of interference fringes produced by the active modulation in amplitude and frequency of the standing beam, therefore its common name of self-mixing interferometry. By exploiting this phenomenon, similar measurements to those with conventional interferometers can be expected. The present manuscript focuses on self-mixing displacement measurement in order to reconstruct the movement of a remote target.

The so called self-mixing interferometers on its most common configuration are intended to use a laser diode as the light source, a built-in photodiode within the laser package, a focusing lens and the electronics circuitry suitable to exploit the interferometric signal recovered from the active cavity. Notable features of this sensing scheme are the reduced number of external optical components, the compactness, as well as its self-aligned and integrated nature.

As technology advances, nowadays the cumbersome arrangement of conventional interferometers can be avoided with expensive fabrication process involving the difficult alignment of optical components. Conversely, basic self-mixing configuration is a cost-effective solution for laser interferometry instrumentation.

Within the many publications in the field of displacement and vibration measurement by self-mixing, the technological tradeoff is simple to observe: in order to reach more spatial resolution, several external components are added to the basic configuration, increasing thus the overall cost of an instrument. Exploring the usage of this technology as an embedded sensor

makes sense if this premise is considered.

At the present time, a wide variety of methods and prototypes addressing specific issues while exploiting this phenomenon can be found on literature. Unfortunately, as have been recently signaled by one of the long-time researchers on this domain [1], "even minor changes of specifications usually require major changes and often a complete redesign of the instrument". For the sake of illustration, it can be found a self-mixing device measuring the displacement over human skin, while another completely different design is used over a metallic surface. Furthermore, a centimetric displacement measurement might be processed differently than a micrometric one.

In this context, this thesis aims to contribute into the approach of conceiving an embedded sensor for displacement measurement using the self-mixing interferometry configuration. This work has been carried withing the group of Optoelectronics for Embedded Systems (OSE) of the Laboratory for Analysis and Architecture of Systems (LAAS) with a part of financial support held by CONACYT. Within the group strategy, the adherence of conceiving a robust signal processing rather than using external components to assist the measurement has been followed. On the understanding that this implies a detriment of the spatial resolution obtained by specific prototypes on literature, this research paves the goal of achieving a flexibility on system requirements by using a modular approach prone to hardware-software partitioning of the proposed algorithms. As it can be advised, this contribution can still benefit of the accuracy gained by using more stable external configurations, with the added value of enlighten a development framework for industrialization purposes.

The manuscript has been structured as follows:

In **Chapter 1**, self-mixing phenomenon is introduced on its theoretical formulation. The different working regimes attained on the laser are explained at this point since their consideration is of major impact on this work. Concepts related to SM phenomena are further explained by introducing a behavioral model for a practical simulation of SM signals. The different domain applications of this instrumentation scheme are also described within the phenomenon presentation. Finally, a meta-analysis on the devices proved to work on real environment for displacement measurement helps to address the state-of-the art as well as to highlight the trends to undertake on embedded domain. This detailled examination makes part of the proceedings of an international conference made during this thesis.

Displacement measurement has been analyzed in two abstract functional blocks: The proper detection of interferometric fringes and the reconstruction of the target movement from those detected fringes. After an overview of reported methods on SM displacement reconstruction, **Chapter 2** first presents an analysis carried over a prior reconstruction algorithm from our research center, with the goal of a practical embedded implementation. It is

followed by our proposed flexible algorithm for displacement elaboration from previously detected fringes. It has been presented in an international conference as an original evolution of the analysed algorithm backed by filtering techniques, allowing aleatory displacement reconstruction from irregular samples. Such an algorithm allowed the development of a real-time basic demonstrator that helps to understand the efforts underlying self-mixing phenomenon, as well as the strategy chosen to approach the usage of systems with limited resources. This last makes also part of the proceedings of an international conference attesting the incursion of digital signal processors for embedded SM sensor implementation.

In **Chapter 3**, several reported methods for SM fringe detection are presented. Then, a prior detection algorithm from our research center is also evaluated considering an annoying phenomenon of SM signal degradation known as speckle. To further address the robustness of measurements face to signal changes at different feedback conditions, an spectral analysis of displacement SM signals is then provided. To stay with the premise of keeping the basic instrument setup, a new signal processing for improved fringe detection is presented and consolidated as a patent filed. It has demonstrated better performance against the previous proposal and stands as a pure algorithmic solution to handle fringe amplitude modulations due to speckle patterns.

Our algorithms from the two defined functional blocks are further validated in **Chapter 4**, for a set of conditions starring its pertinence. After this experimental assessment, some compatibility proposals with existing methods are described as a means to gain in reliability. Since the algorithms were conceived with the intention of being implemented as a System-on-Chip (SoC), we conclude this work with a roadmap for an embedded implementation advancing the field of codesign for architectural exploration. This might inspire further research endeavors and shall approach a SM sensor capable to be adapted at different requirements specifications.

Finally, a general conclusion is given summarizing the present work contribution on this still flourishing research community.

Chapter 1

Emerging self-mixing sensors

Contents

Few years after the invention of lasers, optical power variations inside a gas laser cavity due to the interaction of the emitted beam with the backscattered light from a pointed target, were first demonstrated for metrology purposes in 1963 by King & Stewart [2].

The optical feedback, more commonly known as self-mixing (SM) phenomenon, was considered as an undesirable effect modifying frequency and amplitude of the lasing field. At present time, optical feedback is still mitigated for certain applications, for example in telecommunications by using obliquely cleaved end faces on optical fibers or by means of optical isolators on DVD players [3, 4].

Nonetheless, as early as 1964 the usage of those induced modulations as an interferometer was depicted [5]. In 1968, Rudd [6] reported the first *auto-aligned* configuration using a *HeNe*

laser demonstrating the measurement of **velocity** by exploiting Doppler frequency. The interest to use SM as a reliable technique for *instrumentation* was then revealed.

Later on, a **range finder** using a CO_2 laser was presented by Honeycutt in 1972 [7]; followed by a SM interferometer in 1978 using a polarized *HeNe* laser and analog circuitry to measure target **displacements**. The *compactness* and self-aligned features of the scheme were highlighted [8].

Notably results in researches on injection-locking in laser sources were carried by Spencer & Lamb in 1972 [9]. While the first experiences of optical injection in semiconductor lasers were performed in 1980 by Lang & Kobayashi with an *AlGaAs* **Laser Diode** (LD) at 840 nm [10]. On the same year, Dandrige *et al.* [11] presented an acoustic LD sensor measuring sinusoidal displacements as small as 9×10^{-5} nm. Also with the usage of LDs, a velocity measurement was demonstrated by Shinohara in 1986 [12], accompanied of a range finding application by Beheim & Fritsch [13]. Further researches of feedback effect were actively carried by many other teams for more than a decade.

The introduction of LD's into SM interferometry can be seen as the boost element to spread this technique. This might be explained by the *low-cost* quality conferred to the instrument.

By 1995 a simple configuration to detect the direction of the displacements from SM signals was presented [14], followed by the first demonstration of a LD-SM interferometer for **vibration** measurement over non-prepared surfaces [15].

SM interferometry is nowadays considered a reliable technique to perform accurate measurements [16]. The first SM sensors exploiting Doppler frequency began to be commercialized by Philips® for applications like a computer mouse (Logitech V400), and as user interface devices for handheld portable equipment such as mobile phones and MP3 players [17].

Beyond the measurement of absolute distance, displacement, velocity, vibrations and correlated applications [18–21]; many other physical quantities have been reported like: thickness [22], refraction index [23] and roughness [24]. Even the determination of some properties of the LD itself, like: linewidth [25] and α-factor [26]. Medical domain presents also a great potential for SM deployment as attested by the many publications that can be found in this field [27–29].

In light of those achievements, it is appropriate to point out SM phenomenon as an active research domain with high potential to incursion on industry and embedded applications.

After the theoretical presentation of SM, this chapter outlines the procedure for displacement, absolute distance, and velocity measurement. Then, it is presented a critical analysis on the state-of-the-art of devices for displacement and vibration reconstruction.

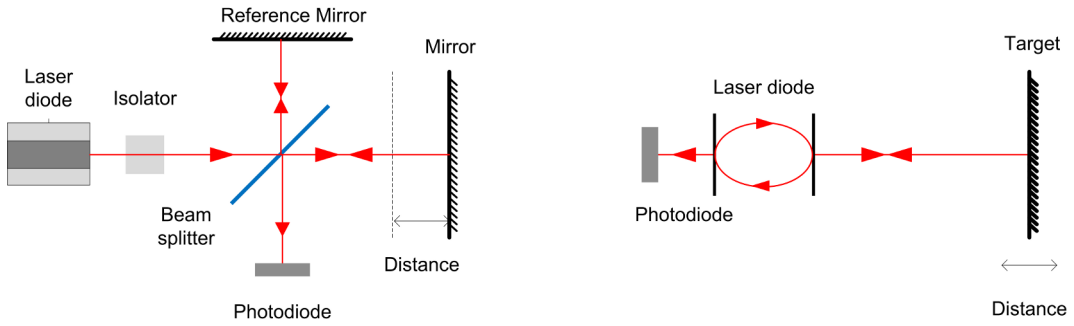

Figure 1.1 – Comparison between a conventional interferometry setup and the basic representation of a SM interferometer.

1.1 Theory of self-mixing phenomenon

So far it has been mentioned that SM happens when a small fraction of emitted beam is backscattered to the laser cavity. That is, when a coherent light beam is pointed on a target, an interferometry pattern can be recovered on the source as a result of the interaction (*mixing*) between the reflected light and the in-cavity unperturbed field of the source. In fact, the emitted power is then modulated if the target moves along the pointed axis, if the injection current on the LD is modulated, or even when the refractive index between the laser and the target is varying.

The basic representation of a SM interferometer is illustrated on the right of Fig.1.1, it comprises a LD and a photodiode (PD). On the left, it is compared to a conventional interferometer setup (e.g. Michelson). A collimating lens is usually needed in both configurations. This representation allows to observe the preconized SM features of simplicity, compactness, integration, self-alignment, and cost-effectiveness that can be achieved. The requirements are that the distance between the target and source be less than half the coherence length of the source. In order to obtain a clean SM interferometric waveform, the laser shall work in a single longitudinal mode, and be biased well above the threshold so as to have low side-mode content [30].

Many commercial LD's integrate a monitoring PD in their package for emission power control, by detecting frequency and amplitude variations induced by SM phenomenon. This PD is disposed with a certain inclination in order to avoid a reflection with the back facet of the casing (Fig.1.2).

SM interferences occur in the semiconductor **active medium**, whereas classical interferences are normally observed in passive medium like free space. This important difference confers a particular shape to the recovered SM signals as compared to the sinusoidal form observed from conventional interferometers. As it will be shown later in this chapter, in most practical cases of displacement measurement, when a LD is powered in continuous wave

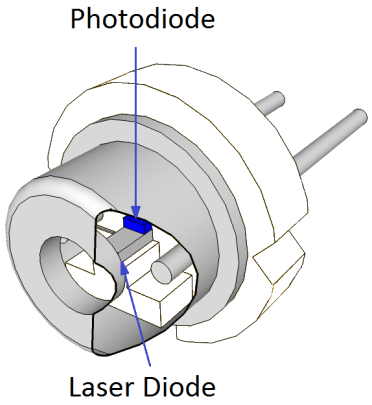

Figure 1.2 – Schematic diagram of a LD package with a built-in PD.

mode, SM shape varies from quasi-sinusoidal to saw-tooth form as a function of the backscattered light.

In some recent SM setups using Vertical-Cavity Surface-Emitting Lasers (VCSELs), the use of the PD has been eliminated by **directly** monitoring the variations of the LD **junction voltage** [31, 32]. Furthermore, the usage of a collimating lens can also be cut out for certain configurations like short-range measurement [33]. The core of a SM based device can thus be reduced to a LD that simultaneously acts as a light source, as a micro-interferometer, as well as a light detector, plus the circuitry needed to exploit the signal.

The following section aims to explain SM phenomenon by detailing the interaction happening in the active medium as a model of coupled cavities, with the target acting as an external optical cavity.

1.1.1 Fabry-Perot cavity model

1.1.1.1 Stand-alone LD

Considering first a stand-alone LD of length ℓ modeled as a Fabry-Perot cavity (Fig. 1.3), The reflection coefficients for the electric field amplitude are denoted as r_1' over the bounding interface I_1 and r_2 over the front face of the laser I_2.

Laser's oscillation condition imposes that the electrical field equals itself after a round trip in the cavity, therefore the emission happening in the active cavity for the stand-alone LD, can be described by:

$$r_1' r_2 e^{\left(-j\frac{4\pi\mu_{e_0}\nu_0}{c}\ell\right)+(g_{th_0}-\alpha_p)\ell} = 1 \tag{1.1}$$

where μ_{e_0} represents the effective refractive index of the active region, ν_0 is the LD emission frequency, c is the speed of light, g_{th_0} is the threshold gain of the active region and α_p is the

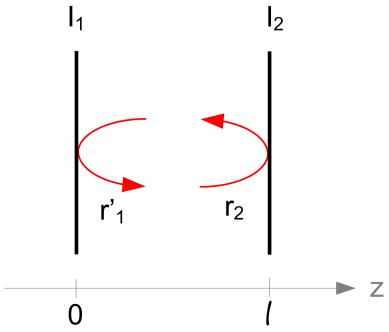

Figure 1.3 – Modeling of the active medium of a laser diode as an equivalent Fabry-Perot cavity.

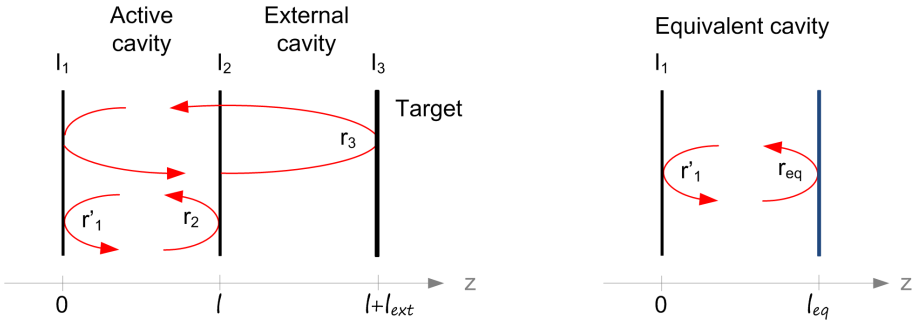

Figure 1.4 – Modeling of a laser diode in presence of a target by an equivalent Fabry-Perot cavity.

coefficient representing the losses mainly due to absorption by free carriers [34].

By solving for the modulus and argument of this equation it is possible to find the threshold gain and the allowed optical frequencies with q, the longitudinal mode for the LD emission without back-reflections,

$$g_{th_0} = \alpha_p - \frac{1}{\ell} \ln \left| r_1' r_2 \right| \tag{1.2}$$

$$\nu_0 = q \frac{c}{2\ell\mu_{e_0}} \quad q \in \mathbb{N} \tag{1.3}$$

1.1.1.2 LD in presence of a target

Now, considering the same LD in the presence of a target (interface I_3 and reflection r_3 of Fig.1.4) located at a distance ℓ_{ext}, the equivalent Fabry-Perot cavity model correspond to the association of the previously described cavity model and the external cavity created.

Again, the oscillation condition imposes that the electrical field equals itself after a round trip in the cavity, in this case there is a round trip inside the LD, and a second round trip for the reflection with the target. For the sake of simplicity on equations, the equivalent distance ℓ_{eq} is named again ℓ, while the equivalent reflection coefficient for the electric field amplitude

is denoted as r_{eq}. When the amplitude of the reflection coefficient of the target r_3 is small as compared to that of the LD front facet r_2, the multiple reflections in the external cavity can be neglected [35]. The amplitude of reflection coefficient for the equivalent cavity is thus written as:

$$r_{eq} = r_2 \left(1 + \zeta e^{-j2\pi\nu_F \tau_{ext}}\right) \tag{1.4}$$

where ν_F is the optical frequency of the LD in the presence of a target, τ_{ext} is the time of flight of the laser beam in the external cavity and ζ is a parameter denoting the coupling effect between the target and the laser cavity, with ϵ representing a mismatch between the reflected and the lasing modes (such as $0 < \zeta < 1$).

$$\tau_{ext} = \frac{2\ell_{ext}}{c} \tag{1.5}$$

$$\zeta = \epsilon \left(1 - r_2^2\right) \frac{r_3}{r_2} \tag{1.6}$$

It follows that the LD emission happening in the presence of coupling with a target can be described similarly to Eq.(1.1), whereas in Eq.(1.7) the subscript F denotes the condition of target reflection.

$$r_1' r_{eq} e^{\left(-j\frac{4\pi\mu_{e_F}\nu_F}{c}\ell\right)+\left(g_{th_F}-\alpha_p\right)\ell} = 1 \tag{1.7}$$

The argument Φ_{eq} and modulus $|r_{\text{eq}}|$ of (1.4) allow to approach the threshold gain and the allowed optical frequencies for the LD in the presence of a target.

$$\Phi_{eq} = \zeta \sin\left(2\pi\nu_F \tau_{ext}\right) \tag{1.8}$$

$$|r_{eq}| = r_2 \left(1 + \zeta \cos\left[2\pi\nu_F \tau_{ext}\right]\right) \tag{1.9}$$

By relating (1.1) with (1.7) i.e. both conditions of the LD emission:

$$\frac{r_{eq}}{r_2} e^{-j(\Phi_F - \Phi_0)} e^{(g_{th_F} - g_{th_0})\ell} = 1 \quad \text{where} \begin{cases} \Phi_{\text{F}} = \frac{4\pi\mu_{\text{e}_\text{F}}\nu_{\text{F}}}{c}\ell \\ \Phi_0 = \frac{4\pi\mu_{\text{e}_0}\nu_0}{c}\ell \end{cases} \tag{1.10}$$

Replacing r_{eq} for its exponential form $|r_{\text{eq}}|e^{j\Phi_{\text{eq}}}$ and grouping:

$$\left[\left|\frac{r_{eq}}{r_2}\right| e^{(g_{th_F} - g_{th_0})\ell}\right] e^{-j(\Phi_F - \Phi_0 - \Phi_{eq})} = 1. \tag{1.11}$$

By solving for the modulus and argument of Eq.(1.11) it follows that the relation between the threshold gain and the phase for the LD in the presence of a target and the stand-alone LD are:

$$g_{th_F} - g_{th_0} = -\frac{\zeta}{\ell}\cos\left(2\pi\nu_F\tau_{ext}\right) \tag{1.12}$$

$$\Phi_F - \Phi_0 = \frac{4\pi\ell}{c}\left(\mu_{e_F}\nu_F - \mu_{e_0}\nu_0\right) + \zeta\sin(2\pi\nu_F\tau_{ext}) \tag{1.13}$$

The effective refractive index μ_e depends on the density of electrons n and the emission frequency ν. Thus, for a small (supposed linear) variation in these parameters for the case of a diode with external coupling as compared to the stand-alone case, we obtain the expression for the variation in the effective refractive index.

$$\Delta\mu_e = \mu_{e_F} - \mu_{e_0} = \left(\frac{\partial\mu_e}{\partial n}\right)\Delta n + \left(\frac{\partial\mu_e}{\partial\nu}\right)\Delta\nu \tag{1.14}$$

Substituting this differential of the effective refractive indices in the phase equation (1.13), we then obtain:

$$\nu_0\left(\frac{\partial\mu_e}{\partial n}\right)\Delta n + \left[\left(\frac{\partial\mu_e}{\partial\nu}\right)\nu_0 + \mu_{e_0}\right]\Delta\nu + \zeta\frac{c}{4\pi\ell}\sin(2\pi\nu_F\tau_{ext}) = 0. \tag{1.15}$$

Now, considering the analytical form of the refractive index μ_e, the electric field E of the plane wave propagating along the z axis, with a wave vector k, can be written as:

$$E = E_0 e^{-jk\mu_e z} \quad \text{with} \begin{cases} \mu_e = \mu_e' - j\mu_e'' \\ k = \frac{2\pi}{\lambda} = 2\pi\frac{\nu_F}{c} \end{cases} \tag{1.16}$$

Furthermore, for a constant density of injection current higher than the threshold of laser emission, the electrons' densities are equal to that of the threshold. Thereby, for a small change in the gain and the electron density between the diode in the absence and presence of target, we can write the following relationship given by Petermann [34]:

$$\left(\frac{\partial\mu_e''}{\partial n}\right) = -\frac{c}{4\pi\nu_0}\left(\frac{\partial g}{\partial n}\right) = -\frac{c}{4\pi\nu_0}\left(\frac{g_{th_F} - g_{th_0}}{n_F - n_0}\right) \tag{1.17}$$

The relation between the emission frequencies of the laser diode (1.18) is then obtained by introducing the relation (1.17) into the relation (1.15). The parameter α is the LD's linewidth enhancement factor expressing the relationship between the gain on density of electrons and the refractive index [36]. It can be denoted by the partial derivative of the real part of the effective refractive index as compared to its imaginary part. The relationship between the refractive index

and the wave frequency leads to the definition of group index $\overline{\mu_{e_0}}$.

$$\overline{\mu_{e_0}} = \mu_{e_0} + \nu\frac{\partial\mu_e}{\partial\nu} \qquad \text{and} \qquad \alpha = -\left(\frac{\partial\,\mathrm{Re}(\mu_e)}{\partial\,\mathrm{Im}(\mu_e)}\right) = -\left(\frac{\partial\mu'_e}{\partial\mu''_e}\right)$$

$$\nu_F - \nu_o + \frac{c}{4\pi\ell\overline{\mu_{e_0}}}\zeta\sqrt{1+\alpha^2}\sin\left(2\pi\nu_F\tau_{ext} + \arctan(\alpha)\right) = 0. \tag{1.18}$$

By introducing the feedback coupling coefficient C [37] (defined hereafter), and τ_ℓ the time of flight inside the LD cavity, we finally obtain the expression for ν_F, the emission frequency of the laser subject to feedback

$$\tau_\ell = \overline{\mu_{e_0}}\frac{2\ell}{c} \tag{1.19}$$

$$\nu_F - \nu_0 + \frac{C}{2\pi\tau_{ext}}\sin\left(2\pi\nu_F\tau_{ext} + \arctan(\alpha)\right) = 0. \tag{1.20}$$

$$C = \zeta\frac{\tau_{ext}}{\tau_\ell}\sqrt{1+\alpha^2} \tag{1.21}$$

The adimensional parameter C is of great importance in SM metrology, it depends simultaneously on the time of flight through the external cavity τ_ext and therefore on the distance to the target. It relies also on the target to LD coupling parameter ζ, and therefore on the quantity of light retro-diffused by the target.

1.1.2 SM feedback regimes

In order to understand the adimensional parameter C of the feedback coupling, let us rewrite the relation (1.20) as an expression to solve the possible optical frequencies $\Delta\Phi_\mathrm{L} = 0$:

$$\Delta\Phi_\mathrm{L} = \nu_F - \nu_0 + \frac{C}{2\pi\tau_{ext}}\sin\left(2\pi\nu_F\tau_{ext} + \arctan(\alpha)\right). \tag{1.22}$$

This so-called phase equation, may be simulated with Matlab® software as a function of $\nu_\mathrm{F} - \nu_0$, for different values of C. The zero crossings of these curves correspond to solutions of the phase equation, thereby possible emission frequencies or modes of the laser.

The representative values of Fig.1.5 correspond to $C = 0.5$ (dashed line), and $C = 7.5$ (solid line). White circle denotes only one solution for $C < 1$, while black circles represent multiple solutions for $C > 1$ in Eq.(1.22). This means that a laser subject to feedback will have single or multiple lasing respectively.

Considering the case of 3 possible solutions for the phase equation, the maximum value of C that has been found numerically is $C \approx 4.7$ [38]. In this case, the laser is found to stay single-

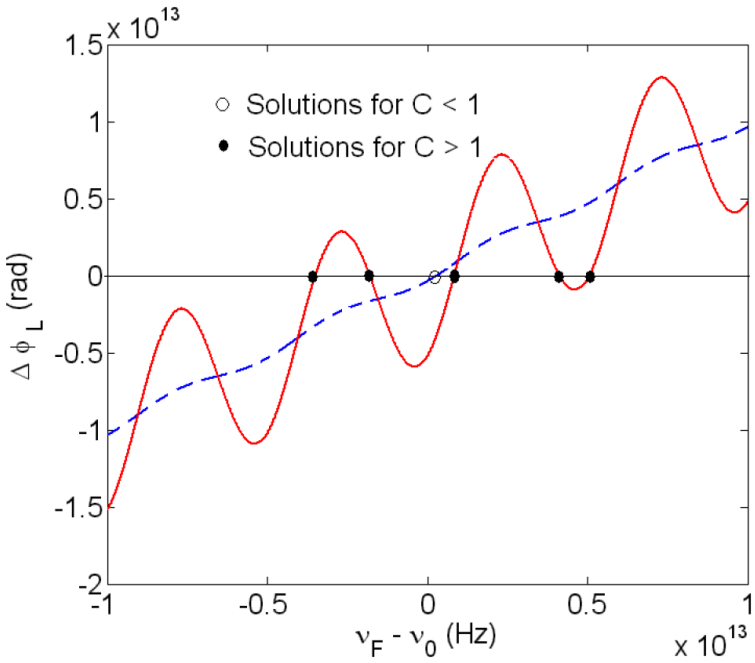

Figure 1.5 – Illustration of solutions that can be obtained from the phase equation as function of C.

mode because, among the three possible modes, only the mode having the narrowest spectral width will be chosen by the laser [39].

The functioning of lasers subject to feedback effect has been classified into a 5 zones diagram (Fig.1.6) by Tkach et Chraplyvy (T-C) [40]. Each zone or regime characterizes the spectral behavior of the laser as a function of the distance, and the reflected light ratio.

Regime I The feedback fraction of the amplitude is less than 0.01%. The linewidth of the laser oscillation is narrow for low feedback and becomes broad at increased amount. The interferometric SM signals can be exploited in this regime.

Regime II The feedback fraction of the amplitude is less than 0.1%. Mode hopping becomes present. However by performing good coupling of the signal, it will be shown in this manuscript that this is the prefered working mode if simple signal processing is to be used.

Regime III The feedback fraction of the amplitude is $\sim$ 0.1%. The laser is perfectly single-mode and the spectral width is very narrow. This condition is difficult to obtain experimentally because of the narrow feedback ratio.

Regime IV The feedback fraction of the amplitude is $\sim$ 1%. The laser loses all its coherence properties and the laser linewidth is broadened greatly. At this point SM as instrumentation

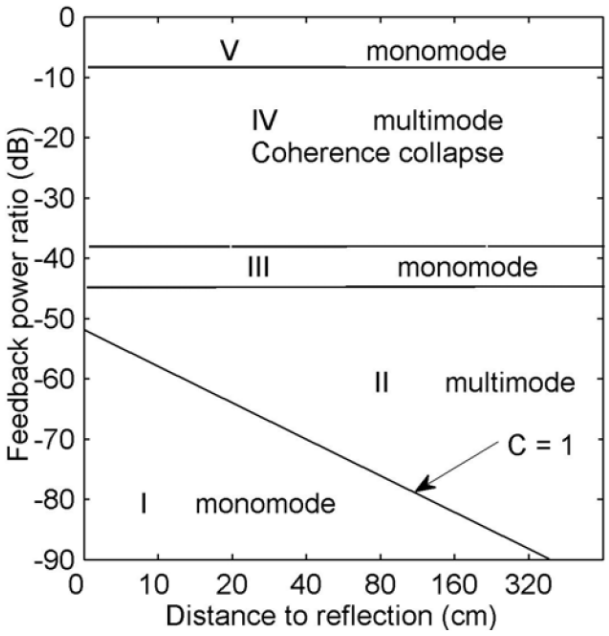

Figure 1.6 – The regimes of feedback effects at different power ratio, as a function of reflection distance.

might not be reliable.

Regime V The feedback fraction of the amplitude is more than 10%. The laser comes back to be single-mode with a very high rejection on the lateral modes of the laser cavity showing a very narrow linewidth. In this case, the laser accomplishes a sort of injection detection of the time of flight between the laser and the target [41]. However, in this condition the laser shows high instability and has been found to be more likely for chaos applications [42].

The diagram of Fig.1.6 was established in 1986 using a 1.5 μm distributed feedback (DFB) laser, however the authors mentioned that would be valid for Fabry-Perot cavities. In fact, Petermann [43] established a numerical approximation for LD's correlating the adimensional coupling factor C. It can be roughly stated that values $C < 1$, belong to region I and they are referred in literature as **weak** feedback, whereas values of $C > 1$ fall in region II and are referred as **moderate** feedback. This classification allows to refer the SM signals based on their feedback properties, as well as to identify working conditions for different applications, like the revisited version of the diagram in [44].

1.1.3 Monitored output power expression

With a photodiode usually built-in in the LD's package, the available information from SM phenomenon is the Optical Output Power (OOP). In order to formulate an expression for the

OOP for the LD in the presence of a target we must start from the equation of recombination of electrons in the laser cavity as a function of time, assuming that all carriers are injected into the active zone of the LD [45, 46]:

$$\frac{dn_0}{dt} = \frac{1}{e}\frac{dJ}{dx} - \upsilon_g N_0 g(n_0) - \frac{n_0}{\tau_n} \tag{1.23}$$

where n_0 is the density of electrons for the stand-alone laser, t is the time, e the elementary charge, J the current density, υ_g the group velocity, N_0 the density of photons for the stand-alone laser and τ_n the electron average lifetime.

Assuming that the LD is driven by a constant current density J and that its gain remains linear, we obtain the following set of equations for the LD in both cases, stand-alone and in presence of a target:

$$\begin{aligned}\frac{J}{ed} &= \upsilon_g N_0 \frac{\partial g_{\text{linear}}}{\partial x}(n_{th_0} - n_{\text{null}}) + \frac{n_{th_0}}{\tau_n} \\ \frac{J}{ed} &= \upsilon_g N_F \frac{\partial g_{\text{linear}}}{\partial x}(n_{th_F} - n_{\text{null}}) + \frac{n_{th_F}}{\tau_n}\end{aligned} \tag{1.24}$$

where d is the width of the laser cavity. The notation in subscript th represents a variable threshold, n_{null} is the density of electrons that results in attaining a null gain. By equalizing both expressions and assuming that $\Delta n_{\text{th}} = n_{\text{th}_F} - n_{\text{th}_0}$ is small, we can express the density of photons in the presence of a target as a function of the density of photons under free running conditions:

$$N_F = N_0 \left[1 - \Delta n_{th} \frac{\upsilon_g \left(\frac{\partial g_{\text{linear}}}{\partial n} \right) - \frac{1}{N_0 \tau_n}}{\upsilon_g \left(\frac{\partial g_{\text{linear}}}{\partial n} \right) (n_{th_0} - n_{\text{null}})} \right]$$

which can also be written as:

$$N_F = N_0 \left[1 - \frac{\Delta n_{th}}{n_{th_0} - n_{\text{null}}} \left(1 - \frac{1}{\upsilon_g \left(\frac{\partial g_{\text{linear}}}{\partial n} \right) N_0 \tau_n} \right) \right]. \tag{1.25}$$

Considering the linear gain with respect to the density of electrons [34], we have:

$$\frac{g_{\text{th}_F} - g_{\text{th}_0}}{g_{\text{th}_0}} = \frac{n_{\text{th}_F} - n_{\text{th}_0}}{n_{\text{th}_0} - n_{\text{null}}} \tag{1.26}$$

Recalling equation (1.12) giving the gain of the diode in presence of the target as a function of gain of the stand-alone diode, and approaching $n_{\text{th}_0} - n_{\text{null}} \approx n_{\text{th}_F} - n_{\text{null}}$, we can introduce the phase $2\pi\nu_F\tau_{\text{ext}}$ in the expression of the density of photons (1.25)

$$N_F = N_0\left[1 + m\cos\left(2\pi\nu_F\tau_{ext}\right)\right] \quad \text{with} \quad m = \frac{\zeta}{g_{th_0}\ell}\left[1 + \frac{1}{\upsilon_g N_0 \tau_n \left(\frac{\partial g_{\text{linear}}}{\partial n}\right)}\right] \tag{1.27}$$

where m is a parameter representing a modulation index for the LD. So, considering that the power of laser emission is proportional to the density of photons, then the emitted optical power from the laser subject to back-reflection can be expressed as [45]:

$$P(t) = P_0\left[1 + m\cos\left(2\pi\nu_F\tau_{ext}\right)\right]. \tag{1.28}$$

where the emitted optical power from the laser without back-reflection is P_0.

It can be noticed that OOP from (1.28) and the optical frequency from (1.20) in the presence of a target are dependent on the phase, thereby involving the distance to the target by means of τ_{ext}. As mentioned in the introduction of section 1.1, the emission of the LD will be modified either if the injection current is modulated (ν_{F} is modulated) or if the target is in motion (τ_{ext} is modulated) or both. This relationship is of major interest in SM instrumentation since it links the OOP that we have access, to the parameters from phase equation (1.20) that we want to estimate.

1.2 Measurement of physical parameters by SM

Exploiting SM phenomenon for metrology applications is thus reliable, here we briefly explain the major physical parameters measured, namely: displacement, vibration, velocity and absolute distance. Each of them open well defined research subdomains as usually encountered on SM literature. The number of published papers on SM instrumentation has been rapidly increasing for the last two decades, therefore many other representative applications achieved by using SM phenomenon have been left referenced on the Chapter's introduction.

1.2.1 Displacement

Considering the basic SM setup of Fig.1.7(a), when a target is moving on the optical axis of the falling beam, the length of the external cavity is varying and thus a SM signal can be recovered. A proper exploitation of the signal shall lead to retrieve the target's displacement.

The information on the direction of the target movement is implicit on each of the interferometric fringes. For the sake of illustration, Fig.1.7(b) plots an experimental signal, obtained with a target performing a sinusoidal movement of 300 Hz and amplitude of ≈ 4 μm. Considering a LD on the near infrared (IR) with wavelength λ_0=0.785 μm, the 10 fringes

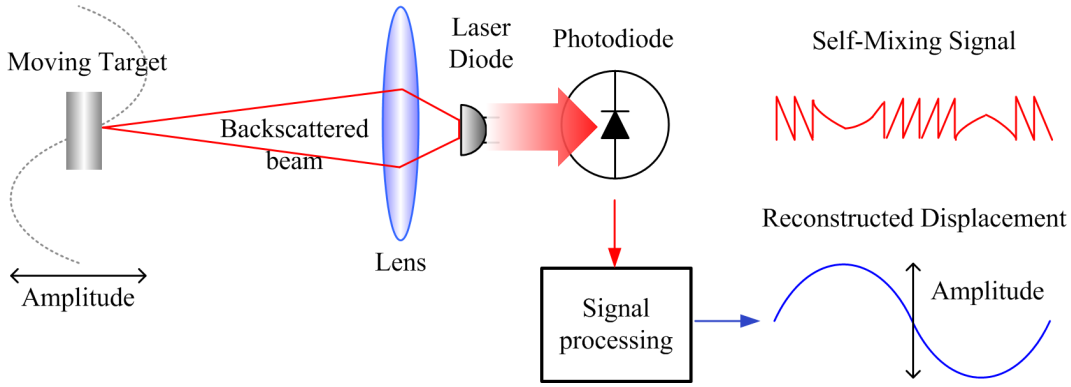

(a) Basic representation of displacement measurement setup by SM.

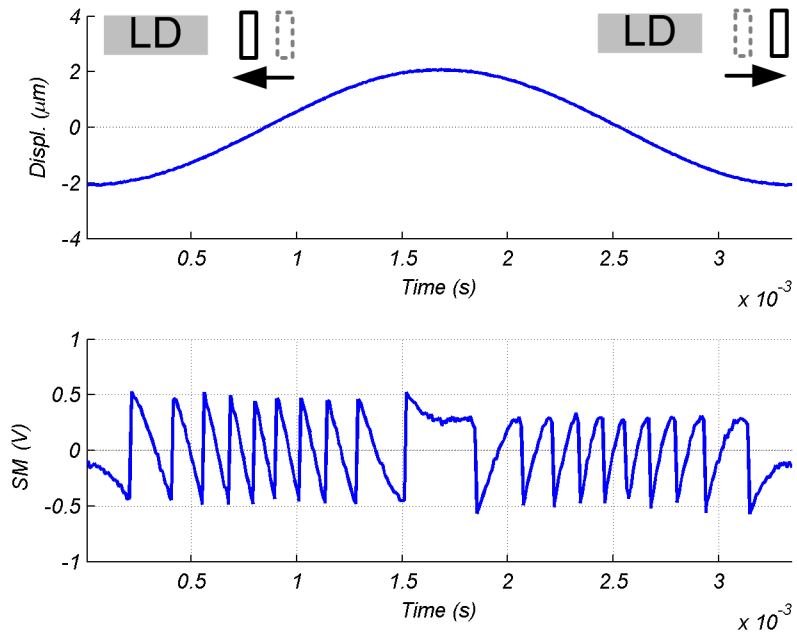

(b) Experimental SM signal with characteristic sawtooth-like fluctuations.

Figure 1.7 – A SM signal can be obtained from a LD when a target moves on the optical axis of its falling beam. By processing this signal, displacement information can be retrieved.

counted on each of the halves represented, correspond to the amount of displacement traveled by the target moving towards or away the LD. From this sawtooth-like signal it can be noticed that the slope change can be used to identify opposite directions of target's motion.

In informal way, it can be stated that the amount of interferometric fringes recovered by the photodiode seems proportional to the displacement of the target. The simplest way to approach the displacement $D(t)$ from the interferometric signal with a resolution of half-wavelength, is by counting the number of fringes N and adding them with their proper direction sign, i.e:

$$D(t) = N\frac{\lambda_0}{2} \tag{1.29}$$

An example of such a method has been used in a 3 degrees-of-freedom SM motion sensor, for simultaneous measurement of the linear displacement and two rotation angles (yaw and pitch) of a moving object over a range of 1 m, using a laser head comporting 3 LD's and a signal processing board interfaced to a computer [47].

1.2.2 Velocity

The working principle of this technique is by exploiting the Doppler-Fizeau effect. Let us refer to the common example of Doppler phenomenon when an acoustic wave from a vehicle siren (source), is perceived at higher frequency as it approaches to the listener. The analogy to an optical wave can be applied, but considering the LD (source) as static and the scattering target performing the relative movement.

The relation between source frequency and received frequency is expressed by the Doppler frequency F_{D}. For the case of SM signals it corresponds to the interferometric fringes' frequency [48]. Yet, developing the Doppler effect equation for the case of a moving target at velocity V_F can be written [49]:

$$F_D = \frac{2V_{\mathrm{F}}}{\lambda} \tag{1.30}$$

Exploitation of Doppler effect can also be applied to the velocity measurement of a translating/rotating target [Fig.1.8(a)]. The introduction of the inclination angle respect to the target normal θ, gives:

$$V_{\mathrm{F}} = \frac{\lambda F_{\mathrm{D}}}{2\cos(\theta)} \tag{1.31}$$

Such a setup from [50] has been used to demonstrate the feasibility of a laser Doppler velocimeter in a multimode VCSEL of λ=850 nm, at various distances from the target, and with cooperative and non-cooperative surfaces. Fig.1.8(b) depicts an example of the electrical

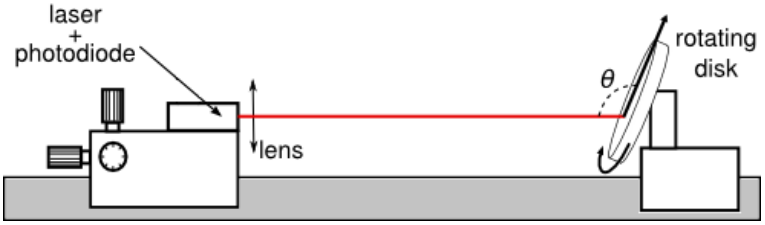

(a) Basic representation of velocity measurement setup by SM.

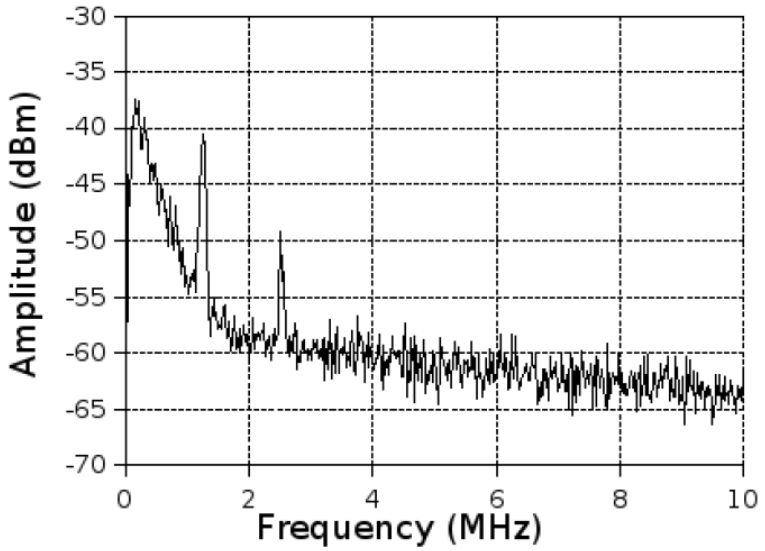

(b) Example of electrical spectrum of Doppler velocimetry signal.

Figure 1.8 – Laser Doppler velocimetry demonstration with a VCSEL sensor from [50].

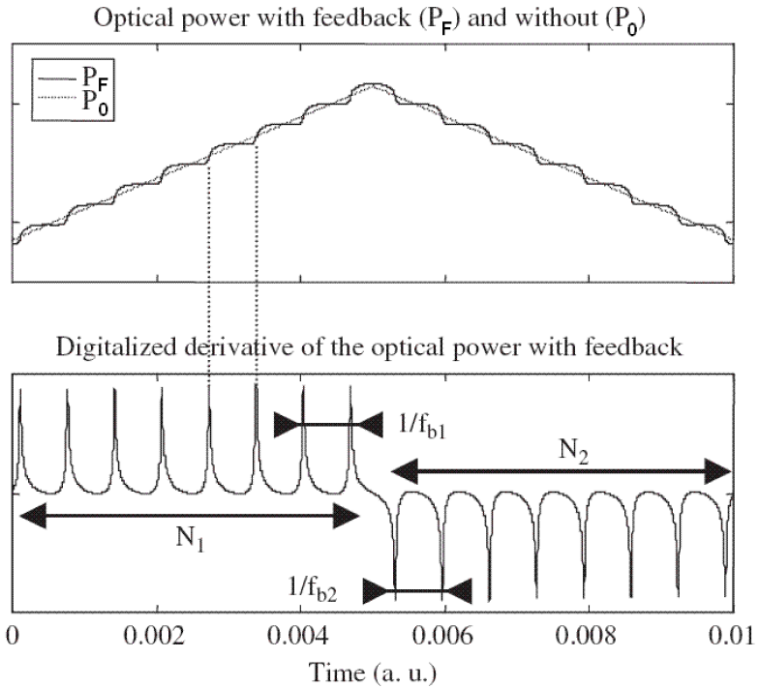

Figure 1.9 – Optical power variations and their corresponding beat frequencies for a triangular injection current.

spectrum of the velocimetry signal obtained for this device.

As mentioned in the introduction of this chapter, velocity was the first instrumentation usage for SM interferometry, being also the first technique implemented into a recently commercialized sensor. As an example of active research in this field, other than the use of VCSELs, it can be mentioned the measurement of fluids for biomedical applications, instead of solid surfaces.

1.2.3 Absolute distance

This configuration requires a modulated injection current on the LD, instead of using a continuous wave mode. With this condition, the equivalent Fabry-Perot cavity's length will be modified because of variations in the active cavity caused by the current modulation, enabling the external cavity length to be constant.

The modulation current corresponds to a properly shaped triangular form, inducing a variation $\Delta\lambda$ of the emitted optical wavelength, corresponding to a wave number variation $(-2\pi\Delta\lambda/\lambda^2)$. Variations of the optical power P_F due to the SM signal will therefore be superimposed on the triangular carrier corresponding to P_0, the optical power without feedback (Fig.1.9). By performing a derivative of this SM signal, it is possible to retrieve characteristic spikes for further processing.

Considering $N = N_1 + N_2$ the number of spikes generated by a complete period T of the modulating triangular form, the distance D can then be expressed by the approximate relationship (1.32) [51]. With $\Delta\nu$ the optical frequency shift.

$$D \approx \frac{\lambda^2}{2\Delta\lambda}N \quad \simeq \frac{c}{2\Delta\nu}N \tag{1.32}$$

Accuracy improvement can be obtained by using the *beat frequencies* f_b between the pulses of the upward and downward triangular signal. This exact relationship is [52]:

$$D = \frac{c}{4(d\nu/dt)}(f_{b1} + f_{b2}) \quad \text{or possibly} \quad D \simeq \frac{cT}{8\Delta\nu}(f_{b1} + f_{b2}) \tag{1.33}$$

As it will be presented later in this chapter, the current modulation is used in some SM devices as a pre-calibration tool, or also as a means to distinguish the direction of the target. However, as pointed out in [16], beat frequency of the produced spikes f_b, suffers of distortion due to thermal effects when the injection current is modulated at a frequency lower than 10 MHz. This requires an optical or electronic reshape in order to achieve a true lineal optical frequency sweep $\Delta\nu$ if FFT based method have to be used.

Range measurements are limited to the half coherence length as conventional interferometry. The minimum coherence length of a laser subject to feedback has been calculated to be [53]:

$$L_{c\mathrm{min}} = \frac{c}{\pi\delta\nu_{\mathrm{max}}} \tag{1.34}$$

where the maximum value of spectral linewidth $\delta\nu$ of the semiconductor laser without back-reflection is:

$$\delta\nu_{\mathrm{max}} = \frac{\delta\nu}{[1 - Ce^{-\pi\delta\nu\tau_D}]^2} \quad \approx \frac{\delta\nu}{[1 - C]^2} \qquad \text{for short distance.} \tag{1.35}$$

An example of a recent range finder is able to perform measurements up to 2 m with a resolution of 100 μm with a real time processing [54]. While the first reported device performed a resolution of 15 mm over a distance of 1.5 m [13].

1.3 SM signals for displacement measurement

This section introduces some of the complexity encountered while dealing with SM signals for measurement purposes. Since the present work focuses on displacement reconstruction, signal representations correspond to the typical monitoring of an harmonic movement from a target. However these concepts can be extended to the case of other kind of SM signal exploitation.

1.3.1 Behavior of SM signals

From the equation of the monitored optical output power of a laser subject to back-reflection [Eq.(1.28)] it can be inferred that SM signals obey a pseudo periodicity. It can be demonstrated [49] that this 2π pseudo periodicity approaches displacement to half-wavelength of the laser. Thus, just like in traditional interferometry, the basic fringe equivalence is denoted ($\lambda/2$).

By using Eq.(1.28), and iteratively approaching the modified phase as a function of the target movement from (1.20) it is possible to obtain the basic behavior of SM signals. Instead, a quite recently high-level behavioral model has been presented by Plantier *et al.* [55]. This allows to represent SM phenomenon by using basic block diagrams and to simplify the solution of nonlinear equations involved in this problem. In the present work we use systematically this behavioral algorithm for the simulated signals.

Prior to further explaining SM related phenomena, let us illustrate with a simulation, three characteristic shapes of SM fringes that can be obtained while monitoring a target performing a sinusoidal movement. Fig.1.10(a) shows a very weak feedback regime signal of $C = 0.2$, with its fringes of quasi-sinusoidal shape. Such a SM signal closely resembles the signals obtained with classical interferometers. Fig.1.10(b) presents the limit of week feedback regime ($C = 1$). The slightly asymmetric fringes in the form of sawtooth are characteristic of SM signals. Fig.1.10(c) represents a moderate feedback regime with $C = 4$. The sawtooth-like signal becomes sharper, but also an hysteresis phenomenon raises. It will be explained in detail on Chapter 3.

To complement the introduction to SM signals, it is convenient to observe in Fig.1.11 the working procedure of the algorithm used to synthesize SM signals that has been used.

Let $D(t)$ represent the instantaneous distance between the LD driven by a constant injection current and a remote surface which backscatters a small amount of signal into the LD cavity. At this point the laser wavelength λ_0 is no longer constant but slightly modified and becomes a function of time λ_F when $D(t)$ varies. Writing x_F and x_0 as two phase signals function of λ_F and λ_0, where the subscript F denotes feedback and 0 denotes no feedback, i.e. free running conditions.

$$x_F(t) = 2\pi \frac{D(t)}{\frac{\lambda_F(t)}{2}} = 2\pi\nu_F(t)\tau(t) \tag{1.36}$$

$$x_0(t) = 2\pi \frac{D(t)}{\frac{\lambda_0(t)}{2}} = 2\pi\nu_0(t)\tau(t) \tag{1.37}$$

Then, the phase equation (1.20) can be written as:

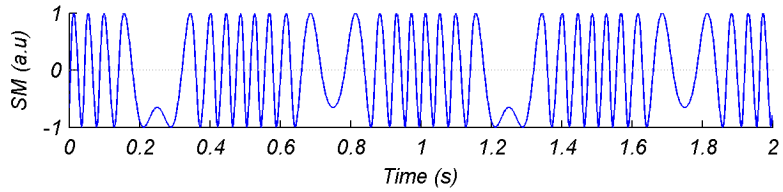

(a) Very weak feedback regime ($C = 0.2$).

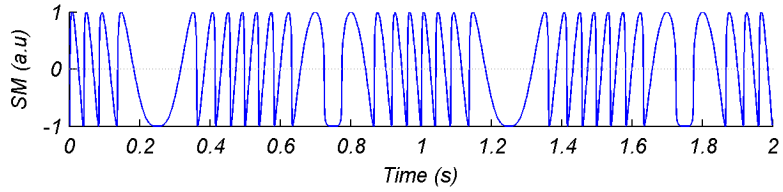

(b) Weak feedback regime ($C = 1$).

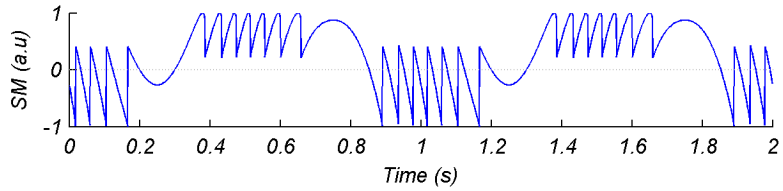

(c) Moderate feedback regime ($C = 4$).

Figure 1.10 – Shape in time variation of simulated SM signals for the same harmonic target displacement of 4λ.

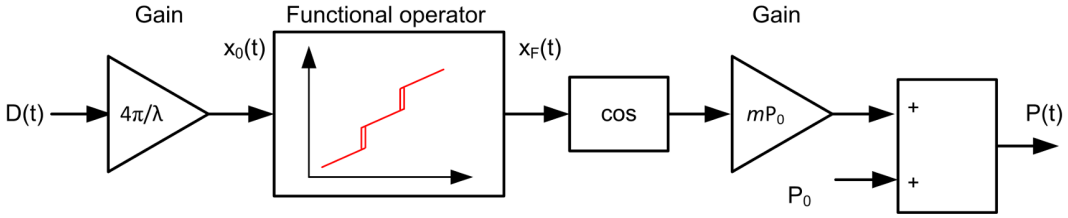

Figure 1.11 – Block diagram of the general behavioral model describing SM signals.

$$x_F(t) - x_0(t) + C \sin\left[x_F(t) + \arctan(\alpha)\right] = 0 \tag{1.38}$$

By writing G as the relation between x_F and x_0 [49], with F its inverse function, then:

$$x_0(t) = G\left[x_F(t); C; \alpha\right] \tag{1.39}$$

$$x_F(t) = G^{-1}\left[x_0(t); C; \alpha\right] = F\left[x_0(t); C; \alpha\right] \tag{1.40}$$

This relation has following property for any k integer:

$$x_F(t) = x_0(t) = k\pi - \arctan(\alpha), \quad \forall k \in \mathbb{N} \tag{1.41}$$

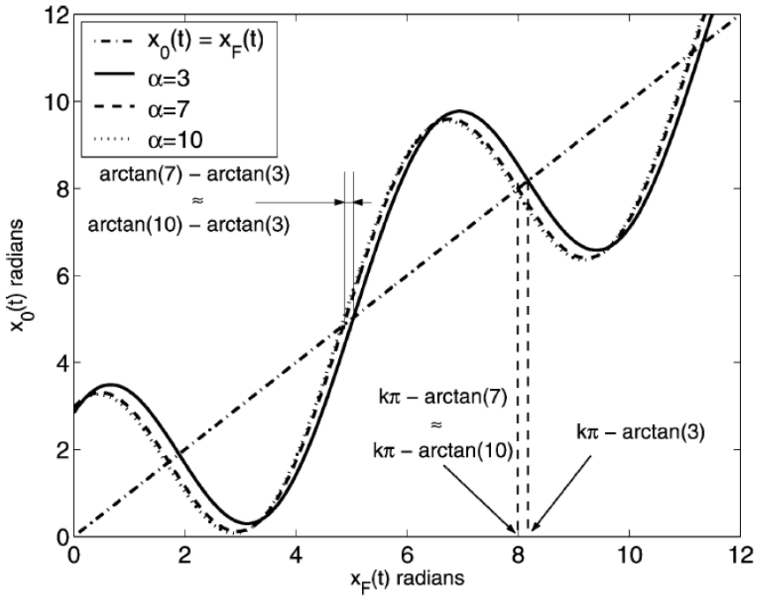

Figure 1.12 – Three different calculated plots of Eq.1.39 obtained with $\alpha = 3$, $\alpha = 7$, $\alpha = 10$ and $C = 3$. The dash-dot curve represents a linear relation between x_F and x_0 [55].

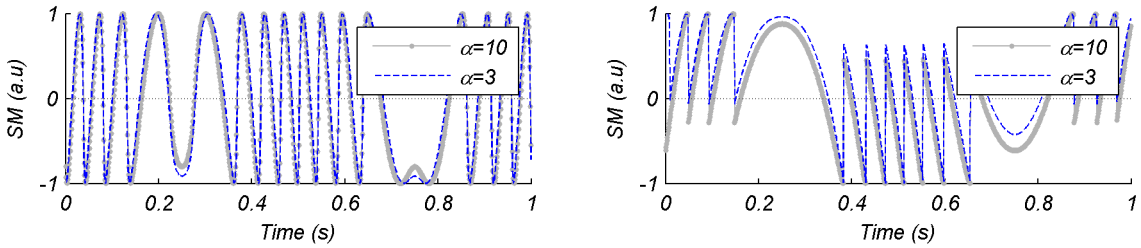

(a) Weak feedback regime ($C = 0.7$) $\alpha = 3$ and $\alpha = 10$. **(b)** Moderate feedback regime ($C = 3$), $\alpha = 3$ and $\alpha = 10$.

Figure 1.13 – Variations in α parameter for simulated SM signals for the same harmonic target displacement of 4λ.

The influence of α on the shape of the SM signal with feedback is said to be of second order as even a large variation can only cause a small drift as depicted in Fig.1.12.

Let us now represent the effect on the OOP signal of a variation in α for a constant C in the weak feedback regime and another in the moderate feedback in order to confirm prior observation (Fig.1.13).

The interferometric shape of SM signals depends mainly on the feedback coefficient C. As a matter of fact, variations of C are achieved experimentally just by translating the laser spot on the target for a given constant distance as it changes the mode mismatch [56, 57]. To illustrate this volatile behavior of SM signals face to certain surfaces, in Fig.1.14 two different SM signals have been acquired from a white paper surface target performing a peak-to-peak displacement amplitude of 4.13 μm. Considering the laser's wavelength of λ=0.785 μm, expected 10 fringes

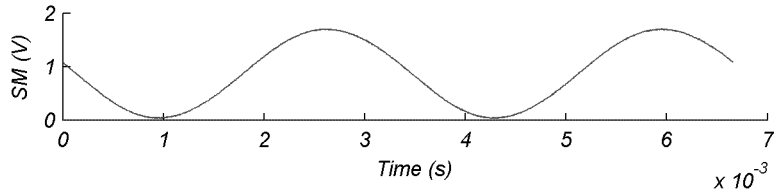

(a) Reference movement of a target pointed by a LD.

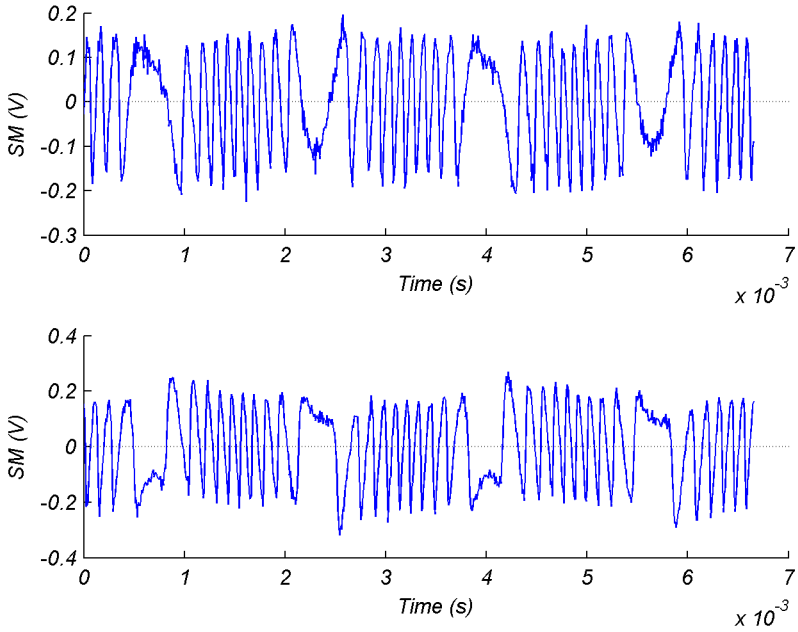

(b) Two data sets of acquired SM signals over the same target movement at slightly different spot position.

Figure 1.14 – Experimental signals from white paper surface depict the complexity on dealing with SM phenomenon when temporal domain shape is not constant.

are properly observed in one data set. However in the other one, only 9 fringes are obtained after a small spot position variation. This phenomenon of fringe-loss shall be detailed in Chapter 2.

1.3.2 Speckle effect, an overview

Another effect that must be accounted in the case of SM signals, are the speckle-pattern statistics. In general, when a rough target is pointed by a laser beam, the speckle is observed in the form of alternately dark and bright spots that are spread randomly in space [Fig.1.15(a)].

This granularity corresponds to a random phase superposition of the backscattered waveforms when the illuminated surface presents roughness relative to the fixed spot size. The exploitation of this phenomenon opens the way to well documented research domains, however in the case of SM signals, is merely considered as a parasitic noise since it introduces

(a) Spotted texture of a pointed laser beam.

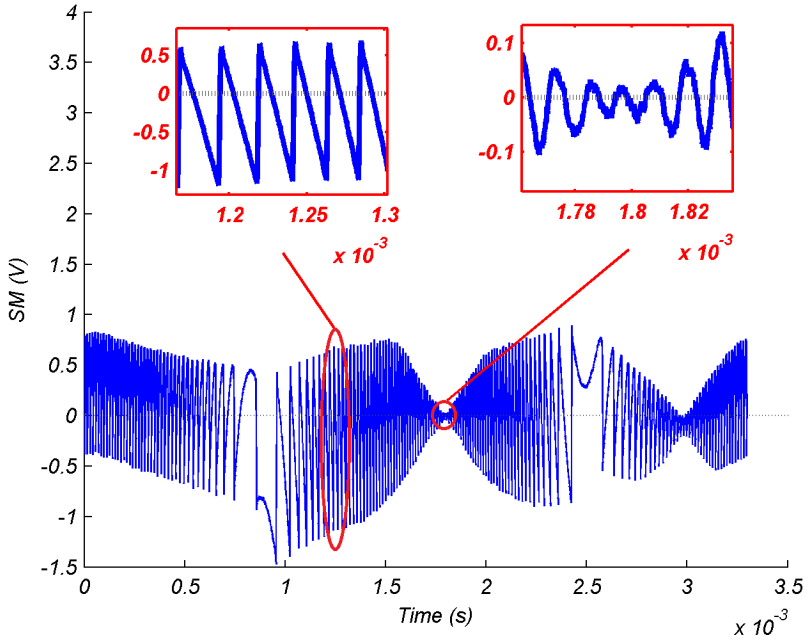

(b) SM signal with added envelope shape, zoom at two segments with different feedback.

Figure 1.15 – Experimental signal to illustrate random amplitude attenuation by speckle phenomenon.

random amplitude attenuations to the already non-linear frequency modulated signal [51].

To illustrate the added envelope shape in time domain produced by speckle, a real SM signal has been acquired under experimental conditions (detailed in Chapter 4). From Fig.1.15 it can be appreciated the difficulty of fringe handling by simple procedures like threshold detection based schemes. As it will be shown in different applications of SM interferometry presented in brief, this condition exposes SM systems to produce unreliable results as the signal might not be exploited properly. This statement shall be detailed in next chapters as it has been one of the subjects of interest during this thesis.

1.4 State-of-the-art on displacement measurement devices by SM

Since this thesis work aims to approach SM interferometry towards the development of an embedded sensor, we state that a non skilled in the art user, should be able to perform a measurement without deep comprehension of the subtleties of SM phenomenon. Likewise on the industrial side, the ease of development might allow to embrace this technology for common applications. Furthermore, the robustness of an instrument face to different use cases must be well established. Indeed, SM devices offer nowadays a limited flexibility in their range of applicability, because even **minor changes** of specifications **usually require** major changes and often a complete **redesign** of the instrument [1].

Focusing on the particular application of displacement measurement, there can be found on literature several methods to improve the accuracy of the measurements, the most representative of them will be presented to introduce Chapter 2 and Chapter 3. Instead, this section presents a **meta-analysis of the devices performing a displacement reconstruction by SM** meeting the criteria for *in-situ* measurement [58]. To narrow the pertinence of results, the information corresponds to the last ten years of published papers in the domain, disregarding the seminal reports of evolutive devices. It is presented in chronological order and entitled by a distinguishable characteristic of the sensor.

1.4.1 Speckle Tracking (ST)

By using piezoceramic actuators, this system tracks the brighter spots in the x-y plane to ensure a maximum amplitude of the measured signal. A phase-sensing loop and a liquid crystal attenuator help to control the feedback level to a suitable exploiting condition (Fig.1.16). To exploit the signal, the system uses an analog derivative filter as front-end to extract the interferometric fringes. Then two solutions can be used for the displacement measurement process. The analog version uses count-down buffers to measure the amplitude, while the digital version uses a field programable gate array (FPGA) and a computer (PC) for rendering information. The signal processing carried by the FPGA is based on an adaptive threshold and a fringe counter integrator. The program on the PC receives the counter information, multiplies by the corresponding $\lambda/2$ factor and graphically renders the displacement information. The reported [59], characteristics are:

- **Precision:** About 400 nm.
- **Displacement range:** Up to 500 000 μm.

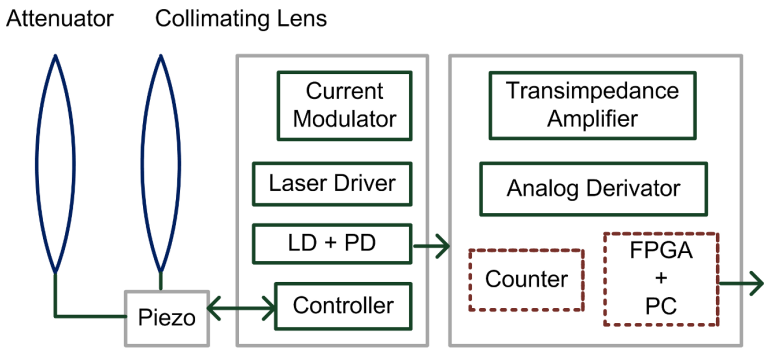

Figure 1.16 – Block diagram of the speckle tracking system.

- **Movement frequency:** Up to 1 KHz.
- **Robustness against speckle:** Attained by the transverse micro-displacements of the laser beam.
- **Validation environment:** Experimental in real-time, with ease of use.
- **Feedback level:** The used technique avoids obtaining weak feedback from several materials. The signal processing is well suited to treat moderate feedback.

1.4.2 Fringe Locking (FL)

This system uses an electronic feedback loop acting on the LD wavelength in order to keep constant the phase of the signal. In order to track the interferometric fringes, the operational amplifier (OP-AMP) is fed by the SM signal and the voltage level of half a fringe. The output of this amplifier in differential mode is converted to current and used to feed the LD (Fig.1.17). In order to calculate the proper magnitude, the distance between LD and target is measured as pre-requisite by the same system. To this end a range finding technique is used, it consists on driving the LD by a triangular current modulation over one cycle and calculate the displacement of the generated fringes. By means of a low-pass filter and the feedback loop, the target's displacement is reconstructed. The reported [60], characteristics are:

- **Precision:** 0.1% of actual output signal reading (e.g. 180 nm for max. displacement).
- **Displacement range:** Up to 180 μm.
- **Movement frequency:** From 0.1 Hz to 70 KHz.
- **Robustness against speckle:** The optical arrangement in this device helps to attain an efficient coupling for a variety of surfaces.

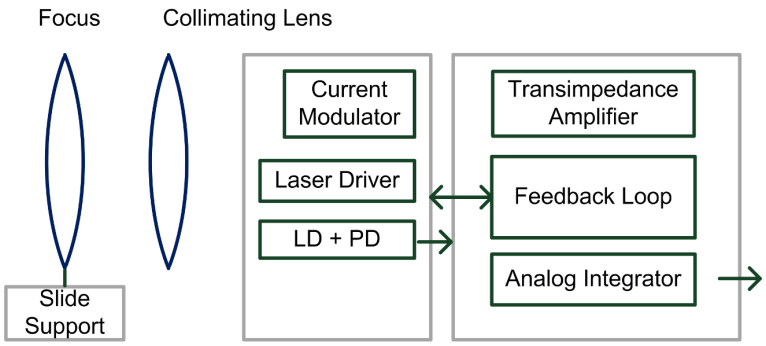

Figure 1.17 – Block diagram of the fringe locking system.

- **Validation environment:** *In-situ*, the laser spot must be adjusted to obtain a convenient signal amplitude before measuring.
- **Feedback level:** The preferred working condition is the moderate feedback.

1.4.3 Switching Algorithms (SA)

This system uses a mechanical pickup similar to the one included on CD players, to move the collimating lens along its longitudinal axis at power-on or at reset (Fig.1.18). It uses current modulation on the LD as the previously described fringe locking system. By means of this autofocus process, the maximum amplitude of the SM signal can be reached. After locking the best lens position, a peak finder algorithm decides between applying an algorithm suited for weak feedback or another algorithm for moderate feedback. The algorithm for $C < 1$ calculates the duty cycle (DC) of the interferometric fringe to affect its contribution on the reconstructed displacement towards or away the LD. The second algorithm performs an unwrap of the SM signal at the trigger points obtained by the peak finder algorithm. Finally the displacement is retrieved in analog form. The reported [61], characteristics are:

- **Precision:** About 400 nm for weak feedback and 50 nm for moderate feedback.
- **Displacement range:** Up to 10 000 μm, limited by the focus depth.
- **Movement frequency:** Inferred 7 Hz max. for a sampling rate of 1 MHz.
- **Robustness against speckle:** Performed by the autofocus system before a measurement and by DC algorithm for weak feedback.
- **Validation environment:** Experimental in real-time, with apparent ease of use.
- **Feedback level:** The signal processing is well suited to treat weak and moderate feedback.

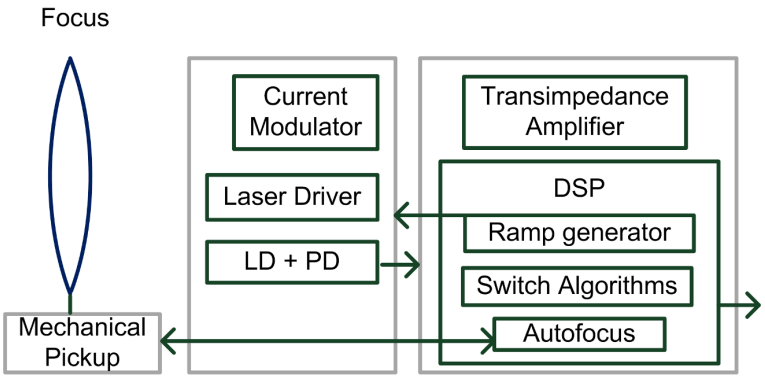

Figure 1.18 – Block diagram of the switching algorithms system.

1.4.4 Accelerometer Assisted (AA)

This system uses a solid state accelerometer (SSA) disposed next to the LD in order to subtract extraneous movements affecting the displacement reconstruction of the remote target. This particular setup opens the possibility for embedding this technology to non-stationary support (e.g. optical table or anti-vibration material). The SM signal is treated by a micro-converter device delivering a displacement signal containing the parasitic movements. On the other hand, the accelerometer displacement is retrieved by a double integration performed into standard operational amplifiers. Both displacement outputs are fed into a Digital Signal Processor (DSP) for proper subtraction (Fig.1.19). The DSP performs phase and gain adjustments to produce the final target displacement [62].

- **Precision:** About 96 nm, dependant on SSA noise characteristics.
- **Displacement range:** Tested for 20 μm.
- **Movement frequency:** From 40 Hz to 500 Hz.
- **Robustness against speckle:** Not directly reported.
- **Validation environment:** Experimental in real-time, with ease of use.
- **Feedback level:** From the reported method, it is inferred that SM signal processing is best suited to moderate feedback.

1.4.5 Critical analysis

Presented devices respond to the requirements for a robust usage, however the diversity of design approaches requires to establish further selection criteria.

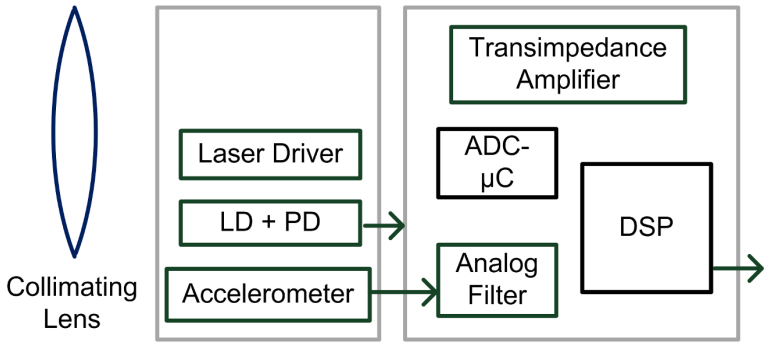

Figure 1.19 – Block diagram of the accelerometer assisted system.

Table 1.1 lists the observed system tradeoffs in order to support the deployment of reliable SM sensors. The usage of external components, the choice of signal processing, the precision and bandwidth are discussed.

1.4.5.1 External components

Perhaps the most noticeable characteristic from above devices is the usage of external components to the basic SM configuration. While this brings stability on the measured signal, it is important to consider the impact on the bulkiness and price of manufacturing process. Usually optical parts are more expensive face to electronic components, low-cost is one of the reasons of the popularity of SM interferometry face to the traditional interferometers.

The FL system, presents a fair agreement in terms of development price, in part by its simple **optical** arrangement. However the distance separating the collimating lens from the focusing lens prohibits its usage on **size-restricted** devices.

The **mechanical** solution in ST, suggests a controlled environment on the sensor head to allow the micro-displacement tracking to work properly. Therefore an indirect cost of deployment is to be considered.

Devices SA and AA seem to better satisfy the constraints of price and size, being privileged for **embedded** applications.

It is observed that devices ST and FL deal with the signal stability by using external components, allowing a simpler signal processing. On the other hand, devices SA and AA increase the complexity of the treatments at expenses of reducing the bulkiness of the components.

1.4.5.2 Signal processing

Displacement reconstruction in coarse resolution is the easiest signal processing to implement. While more precision is required a variety of solutions rise and the choice does not

seem evident. An aspect that might assist this task, is to consider the **maintainability** of the designs.

The ST system uses a simple method for its analog implementation and similar approach for the digital version thanks to the good signal quality obtained by external components.

The FL system presents an interesting analog electronic design. Thought simple in principle, it requires a careful design of each of the steps and the knowledge of the underlying equations for the displacement calculation.

Devices SA and AA use more complex algorithms, however they are implemented mostly on digital processors allowing more flexibility and **reproductivity** of the devices.

1.4.5.3 Precision and bandwidth

As observed on SA system, a modification of the target's movement condition may affect the precision of the system. Even if devices ST and FL are robust face to speckle phenomenon, they are less precise than the elaborations SA and AA using more complex signal processing. The fully analog system in FL is the one offering more bandwidth, thus suitable for more applications.

The good maintainability of digital implementations is then compromised by the sampling frequency of analog-to-digital converters and the proper handling of the acquired signal. However, the implementations in SA and AA offer more flexibility to be scaled for measuring bigger amplitude displacements. When precision and bandwidth are not strictly defined, a digital approach shall be privileged.

	Speckle Tracking	Fringe Locking	Switching Algorithm	Accelerometer Assisted
Measure	<50 cm	<180 μm	<1 cm	20 μm
Precision	400 nm	0.1% of displacement (e.g. 180 nm)	400 nm (weak) 50 nm (moderate)	96 nm
Movement frequency	<1 KHz	(0.1 Hz, 70 KHz)	7 Hz (inferred)	(40 Hz, 500 Hz)
External parts	Piezoceramic actuator, LD current modulator	Lenses arrangement, LD current modulator	Mechanical autofocus, LD current modulator	Accelerometer (MEMS)
Processing hardware	Analog filter, Count-down buffers or FPGA	High speed OP-AMP based design	EZDSP F28335	Analog® μ-converter, dsPIC33FJ128GP
Main feature	The biggest amplitude measurement	The best bandwidth	Performance for weak and moderate feedback	The less bulky and non-constrained to stationary support
Validation movement	Sinus, Manual disp. on a slit	Sinus, Triangular, Squared from speaker	Sinus from speaker	Sinus, Random mounted on a shaker

Table 1.1 – Comparison of analyzed systems in terms of design tradeoffs.

1.5 Conclusion

Emerging optical sensors exploiting self-mixing phenomenon incursion in metrology fields like displacement, vibration, absolute distance and velocity with the premise of being a low-cost, sensitive, integrated and self-aligned technology. Other than the application-representative references given in the chapter introduction, further research still occurs with other sources like terahertz lasers [63], in other target media like micro-fluidics [64], and communications like chaos cryptograpgy [1].

Although this technology is considered reliable from a research point of view, several hindrances related to the complexity of dealing with the different effects suffered by the interference pattern need to be addressed. By offering a versatile framework, further research areas are prone to embrace this approach in a more dynamic development environment. Previous critical analysis enlightens the several configurations that can be found in order to exploit SM signals, as well as the potential contribution of the present work as an approach to embed some of those proposed solutions.

This thesis work is backed by two fruitful research thesis held in our laboratory [49, 57]. From them it can be learned that the broad path to conceive displacement sensors based on SM interferometry can be understood in a more abstract form by identifying two main system's functional blocks:

- Proper **detection** of interferometric fringes from the incoming signal.
- Precise **reconstruction** of the target movement from detected fringes and its direction contribution.

The strategy followed in this thesis work is to avoid external components to keep low the parts cost, while increasing the efforts on robust real-time signal processing for *in-situ* system reliability. Within the aim to provide relaxed constraints in SM devices for a variety of requirements, the premise to ascertain particular operation conditions, notably in terms of feedback amount variations has been tried to be minimized.

It is worth to mention, that this approach is based on the believe of keeping the industrial interest on this kind of sensing scheme as compared to conventional interferometry devices.

Chapter 2

Target's displacement reconstruction

Contents

Approaching unified methods for SM signal exploitation has been the basis of the optimization path undertaken by the previously referenced manuscript of this research center [57]. Among the various published methods, those demonstrated for a variety of signal conditions and suitable for a real-time implementation observed by the determinism of their calculations, were retained for the present work. Thus, it was decided to explore the *Adaptive threshold algorithm* [65] for the fringe detection block, and the *Slopes Based Method* (SBM) [66] for the reconstruction block.

In continuity with processing steps provided by SBM, the work done for **displacement reconstruction** is presented in this chapter addressing the need for a straightforward implementation criteria suitable for an autonomous system with limited resources and reconfigurable/scalable capability.

First, many other original methods found in SM displacement reconstruction literature are introduced. Despite some incompatibilities with our premises of robustness and embeddedness, they might inspire new strategies that can be chosen in order to improve the

resolution of SM devices. Then, some of the algorithms derived from the referenced thesis works are sketched here as they provide the insights of one method developed during this research thesis, our generic algorithm for displacement reconstruction [67].

In order to introduce the contribution made at this point, **the interferometric fringes from an incoming SM signal are considered to be properly detected**. This simplification strategy for target movement reconstruction provides more confidence on SM exploitation process and serves to introduce another contribution made on SM fringe detection described on Chapter 3.

2.1 Solutions for SM displacement reconstruction

The increase of the spatial resolution beyond the basic half-wavelength is a common concern for SM instrumentation. By doing so, it could be expected to approach the development of applications similar to those of classic interferometry which uses well founded interpolation methods. The techniques and algorithms presented hereafter, correspond to the research carried over SM literature addressed to improve the resolution on the measured displacement.

2.1.1 Techniques to increase resolution

An interesting approach is to modulate the phase by means of an **electro-optical modulator** (EOM) composed for example of lithium niobate ($LiNbO_3$) crystal. Theoretically, W self-mixing signals can be used with phases spaced by $2\pi/W$. A sampling of these signals then results in a displacement with a resolution of $\lambda/2W$. Such an experimental device reported a resolution of $\lambda/10$ for 5 signal phase-shifts [68]. Also with the use of an EOM and novel processing techniques, resolutions of few nanometers for displacements of few μm in the case of weak feedback have been reported recently [69, 70]. The *restricted frequency operation* for the EOM and the sampling rate are a limiting factor on the measurement range of these solutions.

A different approach has been the use of **a pair of LD's** each with its own external cavity [71]. The first is used as a reference, whereas the other is perturbed by the target displacement. A spectrum analyzer and a counter are however needed to detect the beat frequency and visualize the spectrum. The reported reconstructed displacement has a resolution of 5 nm.

As a slight angle between the laser beam and the normal of the target favors **multiple reflections** of the beam before entering in the laser cavity, so in this case one can double or even triple the self-mixing fringes. Using a VCSEL of 850 nm, a resolution of $\lambda/6$ has been achieved for the case of a triple reflection for a target at 47 mm from the LD [72].

Such a multiplication of the self-mixing fringes has also been reported for **multi-mode** laser diodes. According to [73], depending on the amount of optical feedback, a subperiod appears in the amplitude modulation of the output power of laser under self-mixing. The experiments have shown that this subperiod appears independently of the length of the external cavity and is due to mode hopping between different longitudinal laser modes. A duplication or triplication of the fringes can then be used to increase the vibration measurement resolution.

Likewise, a change of the **wavelength source** leads to a variation in the number of fringes for a given displacement. An experiment using three different LD at 405 nm (blue), 650 nm (red), and 780 nm (IR), produced ≈3, ≈3.5 and ≈6 fringes, for a displacement of ≈ 1 μm. However, there where observed *important variations on the signal-to-noise ratio* (SNR), probably due to the high level of spontaneous emission in the case of the blue LD [74].

Quite recently, a **fully analog** SM laser vibrometer indicated a range measurement of 1 mm with 35 nm resolution. The design is based on the unwrapping of the signal, each time a jump of the sawtooth-like signal is detected [75, 76]. It has been signaled in [1], that an analog implementation should be privileged for analysis of periodic motions of *small amplitude* (≈ 100 μm) for an easy elaboration with nanometric resolution, while the digital processing provides by far a large dynamic range.

Notice that such solutions have not been used in the *in-situ* robust devices from Chapter 1 due some limitations related to the complexity added by the different techniques. i.e. setup of external components, or the difficulty to align and control the proposed scheme.

2.1.2 Algorithms to increase resolution

Usually in SM literature, it can be observed a marked distinction between the signal processing used for weak and moderate feedback. Actually feedback variations constitute one of the reasons behind the different solutions accounted nowadays.

A recent example addressing the need for a common processing is the one performing an algorithm switching (SA) analyzed in Chapter 1. Fig.2.1 depicts the *custom double-derivative* for a sampled SM signal from [61]. As described by the authors, the inner and outer ratios were experimentally established in terms of stability and computational requirements. By using this procedure, the system determines the location and slope of the fringes to trigger different algorithms for displacement reconstruction.

In the case of ***weak feedback***, the proposed displacement reconstruction for SA system presents a staircase waveform as result of a basic fringe counting integration, thus a resolution of $\lambda/2$.

Research in other elaborations for weak feedback, shows that an algorithm offered a

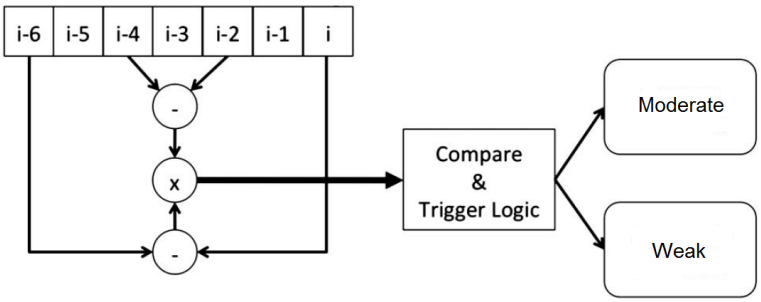

Figure 2.1 – Example of switching criteria for displacement reconstruction.

resolution of tens of nanometers for displacements of few μm [77]. However it requires a *time consuming estimation* of C and a preliminary experimental *calibration* to evaluate the linewidth enhancement factor α. Another solution in the same regime but considering noisy SM signals, proposed the use of extended **Kalman** filters as a position estimator of the target displacement. It has been evaluated in applications like structural analysis and damping evaluation [78]. Despite its robustness face to noise, this elaboration has a *convergence problem* if the starting point for the filter is not selected properly.

In the case of ***moderate feedback***, the slow semi-period of the fringe that is fairly linear, helps to reach sub-wavelength resolution by simple techniques. An early reported solution consist in **linearizing** the *normalized* optical power which has been approximated by an ideal sawtooth signal. This approach proved a resolution of $\lambda/12$ [79].

Referring back to SA prototype, an **unfolding** of the digitized SM signal each time a jump of the sawtooth-like signal is detected, has allowed improved functionality in this condition. Usefulness of this basic elaboration can be attested by the contemporary work in [80]. By combining a *scaled/normalized* SM signal with a staircase waveform from a fringe counting integration, the so called Consecutive-Samples based Unwrapping (CSU) demonstrated a convenient real-time displacement reconstruction.

Two other algorithms, namely the Phase Unwrapping Method (PUM) [81, 82] and the Slopes Based Method (SBM) [66] need to be detailed next as they have served to inspire the implementations presented along this manuscript. The former has found good acceptation due to its modularity to evolve into optimized/robust implementations avoiding calibration procedures by estimating C and α parameters. The later is the proposal retained in this manuscript for the displacement processing block, resulting of the optimization research carried by [57]. Notice that these approaches conform to the strategy of avoiding external components, conversely to the techniques previously presented.

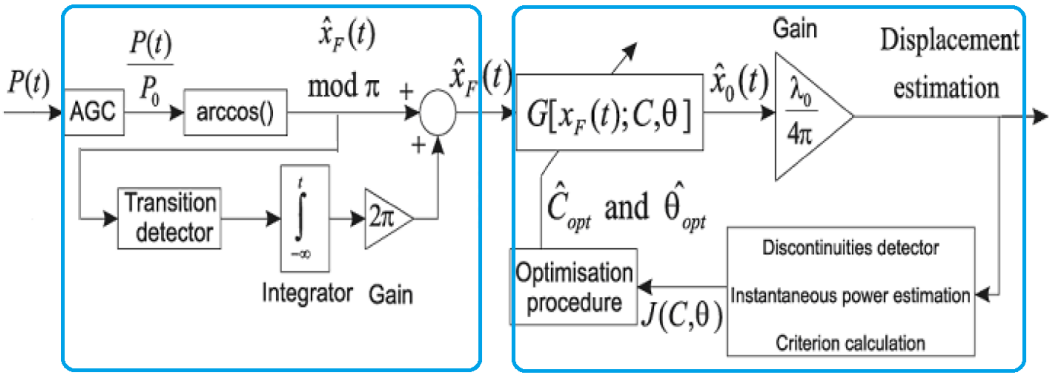

Figure 2.2 – Block diagram of the phase unwrapping method.

2.1.2.1 Phase Unwrapping Method (PUM)

Prior to the former description of PUM algorithm, let us outline the procedure for displacement reconstruction based on SM theory from Chapter 1.

Rewriting the free running phase equation (1.37), it is observed that displacement calculation can be obtained from:

$$D(t) = x_0(t)\frac{\lambda_0}{4\pi} \tag{2.1}$$

However, the only information available from the LD is the optical output power described by Eq.(1.28) involving the feedback affected phase x_F of Eq.(1.36), i.e.

$$P(t) = P_0\left[1 + m\cos\left(x_F\right)\right]. \tag{2.2}$$

By virtue of the phase equation (1.38) it is possible to envisage solutions to approach $x_0(t)$ and therefore to estimate the target displacement.

$$x_F(t) + C\sin\left[x_F(t) + \arctan\left(\alpha\right)\right] = x_0(t) \tag{2.3}$$

The principle of PUM is illustrated in Fig.2.2 and can be split up into two principal steps: 1) the rough estimation $\widehat{x_F}$ of the phase x_F, and 2) the joint estimation of C, α, and $D(t)$.

The **rough estimation** step begins by bringing the monitored OOP into a ± 1 interval, obtaining the normalized form $P`(t)$. The proposal states the use of an Automatic Gain Control (AGC) of P(t) to get $P(t)/P_0$. By doing so, it is expected to retrieve $\widehat{x_F}$ modulus π of the phase under feedback:

$$\widehat{x_F} = \arccos[P`(t)] \tag{2.4}$$

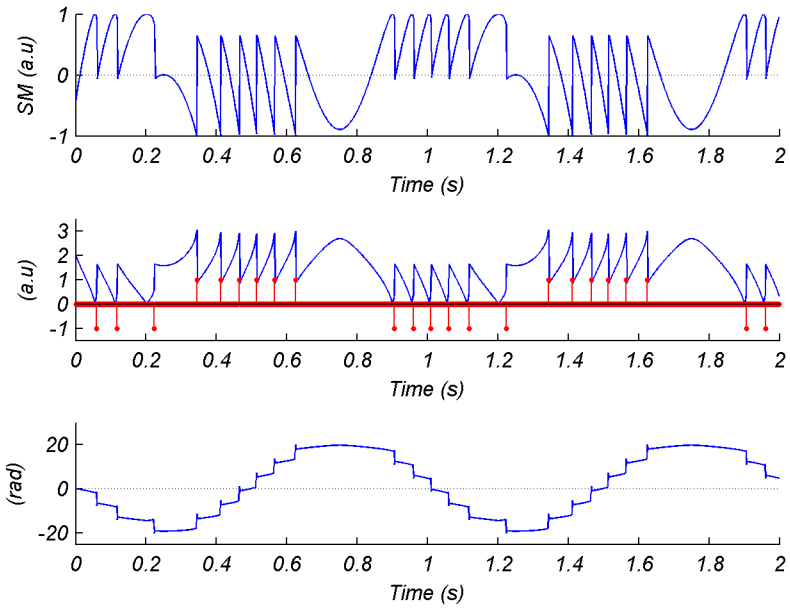

Figure 2.3 – First step of PUM algorithm, the unwrapping of the rough phase estimation.

Actually, it is shown in [26, 83] that the phase x_F exhibits many discontinuities with phase jumps equal to $\Delta x_F = 2\pi C/(1+C)$. For a practical implementation, the rough reconstruction adds or subtracts 2π at each of these phase shifts. This operation of unrolling the phase around each phase shift (or SM fringe) has led to the name of PUM.

The rough feedback phase reconstruction is thus elaborated like in Fig.2.3 for a normalized SM signal $P`(t)$. The corresponding $\widehat{x_F}$ mod π is represented alongside the assigned transitions from its thresholded derivative. Resulting unwrapped estimated phase $\widehat{x_F}(t)$ serves to trigger the optimization procedure.

The second step of PUM deals with the **joint estimation** of C, α, and $D(t)$. It is based on the idea that target displacement discontinuities are far less frequent than discontinuities of P(t) and x_F caused by the non linear behavior of SM signals. As $\Theta = x_F(0) + \arctan(\alpha)$ remains constant, so Eq.(2.3) becomes:

$$x_0(t) = x_F(t) + C\sin\left(x_F(t) + \Theta\right) \qquad \forall \quad t > 0 \tag{2.5}$$

By choosing an optimal set of parameters $\widehat{C_{opt}}$ and $\widehat{\Theta_{opt}}$, that would lead to a discontinuities minimization of the reconstructed phase $\widehat{x_0}$ by using Eq.(2.5). This procedure thus helps to correct the roughness inherent in the 2π phase unwrapping used in the first step of the method.

It has been brought forward that as long as $x_F(0)$ is unknown, α can only be approximated. However, the influence of α on the shape of the SM signal remains secondary and has no

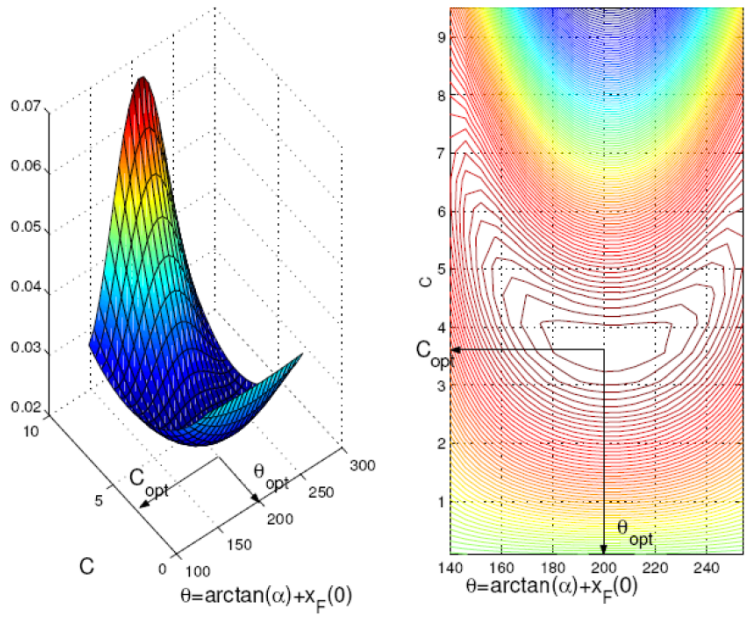

Figure 2.4 – Second step of PUM algorithm, the estimation of (C, Θ) from [49].

important consequence on the displacement measurement with PUM [57].

So, $\widehat{C_{opt}}$ and $\widehat{\Theta_{opt}}$ are given by the optimization of a criterion $J(C, \Theta)$, which is written as:

$$J(C, \Theta) = \sum_{k=0}^{K} \left[\widehat{x_0}(k) - \widehat{x_0}(k-1)\right]^2 . \tag{2.6}$$

where $\widehat{x_0}(k) \quad k \in \mathbb{N}$, is the discrete form of the phase $x_0(k)$. The criterion is evaluated over a temporal window containing K points of the time derivative of $\widehat{x_0}(k)$. Hence the optimal couple $\widehat{C_{opt}}$ and $\widehat{\Theta_{opt}}$ is the one which minimizes $J(C, \Theta)$, in order to allow the reconstruction of optimal displacement:

$$Argmin[J(C, \Theta)] = Argmin \sum_{k=0}^{K} \left[\widehat{x_0}(k) - \widehat{x_0}(k-1)\right]^2 . \tag{2.7}$$

An example of this calculation for an experimental signal of aleatory movement from [49] depicts this procedure (Fig.2.4): The minimum point found in the function space leads to the approximation of the couple (C, Θ). These values are then used in Eq.(2.5) to finally calculate $x_0(t)$ which leads to $D(t)$ by Eq.(2.1), without calibration and no external components.

2.1.2.2 Slopes Based Method (SBM) and fringe-loss compensation

Let us introduce this algorithm by first presenting an overview on the fringe-loss phenomenon suffered by SM signals, as it has also been conceived to handle this issue.

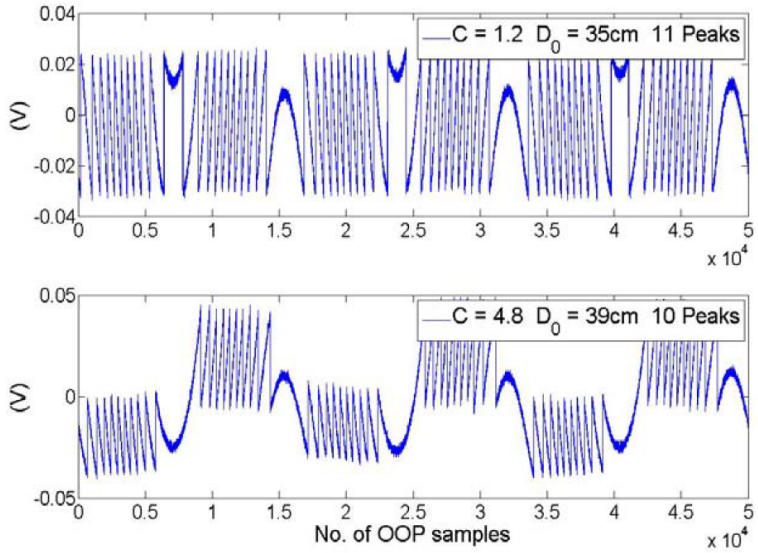

Figure 2.5 – Experimental SM signal showing fringe-loss phenomenon for increased C value from [57].

Fringe-loss in SM signals

Fringe disappearance frequently occurs for SM signals in presence of the multiple steady-state solutions ($C > 1$) of the phase equation (1.38), affecting the accuracy of the measurement. According to [84], the feedback phase is given by $\theta = \omega_0\tau_D + \arctan(\alpha)$, where ω_0 is the angular frequency of the solitary laser. The curve that separates the region of equal number of solutions of the phase equation can be expressed as:

$$\theta = (2k+1)\pi \pm \arccos(\frac{1}{C}) \mp C\sin\left[\arccos(\frac{1}{C})\right] \qquad k \in \mathbb{Z} \tag{2.8}$$

C parameter [Eq.(1.21)] plays an important role in fringe-loss accounting, due to its relationship with the feedback coupling efficiency. To illustrate this phenomenon, an experimental signal from [57] (Fig.2.5) depicts a variation of C by increasing the distance between a LD and the target of few centimeters. In fact, according to [84], a variation in C of 2π will cause a loss of 2 fringes for a fixed value of θ. Also, it has been observed that for a fixed value of C and constant target displacement amplitude, variations in θ will generally cause a loss of a single fringe [57].

In continuity with SM waveforms presented in Fig.1.10, a simulation for a harmonic target displacement of arbitrary amplitude ($4\lambda_0$), allows to further observe this phenomenon: starting with C equal to 1.2 [Fig.2.6(a)], each subsequent variation in C of 2π results in 2 lost fringes as seen in Fig.2.6(b-c). Therefore, for a LD subject to moderate feedback a diminution of the total number of fringes may be observed when C is increasing.

The accuracy of SM instrumentation relies on the **proper accounting of SM fringes**

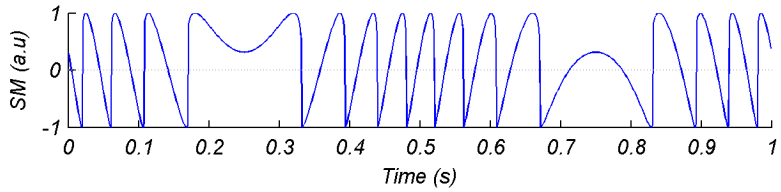

(a) Expected 8 fringes for $C = 1.2$.

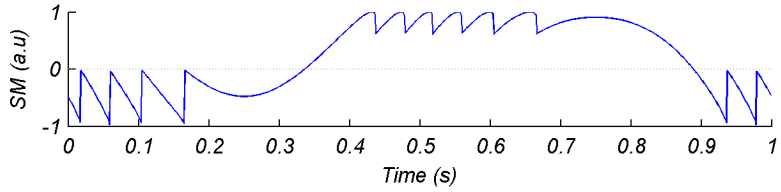

(b) Accounted 6 fringes for $C = 7.48$.

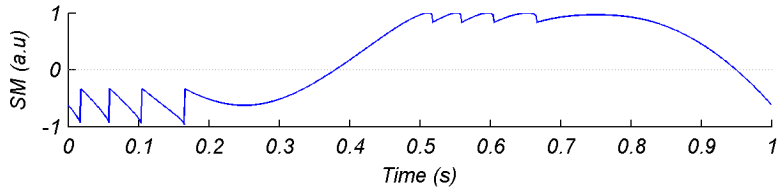

(c) Accounted 4 fringes for $C = 13.76$.

Figure 2.6 – Simulated SM signals for the same harmonic target displacement of $4\lambda_0$ showing fringe-loss.

during a measurement. As foreseen, in order to conceive accurate SM instrumentation, target displacement reconstruction needs to prevent the possible variations of feedback coupling.

Let us remind that C parameter can be affected depending on target's surface characteristics just by slightly translating the laser spot. Since hitting exactly the same point of the target surface is not realistic at all for most of *in-situ* applications, the interest for a means of satisfying this constraint becomes evident. To this end, a method compensating the transitions lost when C parameter increases by several orders has been proposed as part of the Slopes Based Method (SBM) exposed next.

SBM and fringe-loss compensation

The working principle of SBM consist in placing slopes of amplitude +/-2π at the points of fringe detection plus smaller segments at the maximum and minimum of phase reconstruction. To compensate the fringe-loss phenomenon due to possible variations of C, it conveniently adds the calculated missing transitions to maintain the same expected fringe amount. It can be seen as an improvement of the simple fringe counting method by means of:

$$D(t) = N\frac{\lambda_0}{2} + \varepsilon \tag{2.9}$$

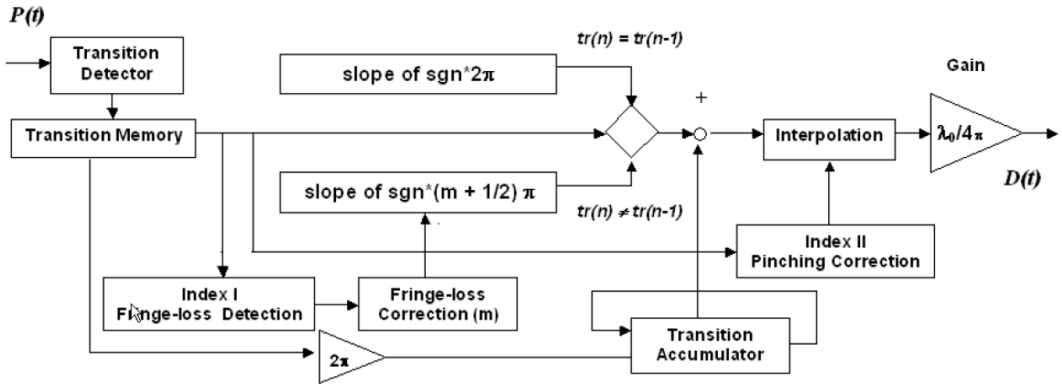

Figure 2.7 – Block diagram of the SBM and fringe-loss compensation.

where ε, is the excess fringe ($<\lambda_0/2$) corresponding to the point where the displacement changed direction [66]. Compared to PUM for a SM signal without fringe-loss, this can be analogue to its displacement estimation block achieved by the simultaneous extraction of C and α parameters.

The reconstruction algorithm depicted in Fig.2.7 is intended to happen between two detected fringes. This is done in order to provide an important reduction of calculation resources as compared to the iterative optimization of PUM.

The described algorithm steps are summarized as follows:

- From the incoming signal $P(t)$, the SM fringes characterized by the sharp edge of the sawtooth-like waveform in the case of moderate feedback, are assigned as $[tr(n)]$ where $n = 0, 1, 2, ...$, is the number of fringes **detected**.
- These so termed transitions are saved in the **Transition Memory** block along with their respective signs (sgn) and the number of samples, representing the time counted since the previous transition.
- Based on the sign of two previously detected transitions, the algorithm either selects a **slope** of $sgn \cdot 2\pi$ **block** or a slope of $sgn \cdot (m + 1/2)\pi$ block, where $m = 0, 1, 2, ...$, is the number of lost fringes and whose calculation procedure is linked to Index I parameter (addressed hereafter).
- The **Transition Accumulator** simply increments or decrements itself by 2π, at each new positive or negative transition.
- In the case of displacement waveform pinching, the **interpolation** block linked to Index II parameter, is used to correct this anomaly.
- Final displacement is found after the **Gain** block of $\lambda_0/4\pi$.

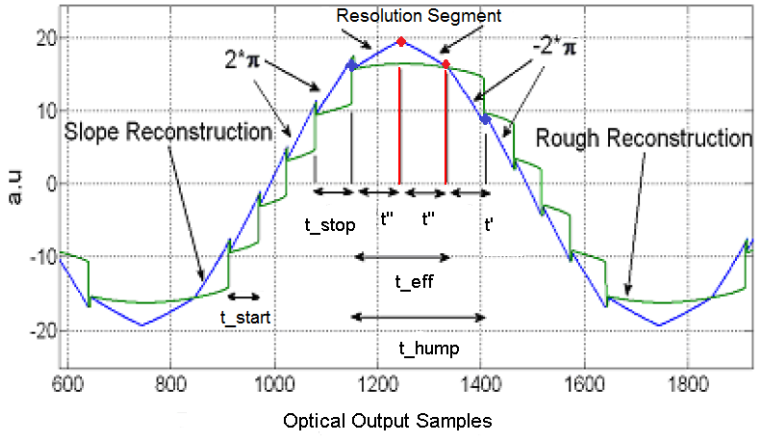

Figure 2.8 – Elaboration example of SBM and fringe-loss compensation.

An example of the fundamental working of this algorithm is shown in Fig.2.8. Same signed 2π segments create the phase waveform along the slope segments of $sgn \cdot (m + 1/2)\pi$. These last segments fulfil two roles: fringe-loss compensation and "ε" resolution improvement. The addition of $\pi/2$ at the maximum and at the minimum of phase reconstruction results in the maximum possible error of $\lambda_0/8$ at the vibration maxima and minima, i.e. when the direction of displacement of the target has changed.

The sign reversal of any two consecutive transitions $[tr(n) \neq tr(n-1)]$ triggers this compensated slope calculation function. It must be noticed that somewhere between these two transition instants the target displacement reaches its extreme point. Thus for an accurate displacement retrieval, in the case of signals with symmetric ascent and descent., the proposal defines specific segmentation points within the central transition-free zone defined as **hump**.

The procedure to define these segmentation points is as follows:

- The hump size is reduced by the number of samples of the transition pair prior to it (t_{stop}).
- The index value resulting from this reduction is marked as an intermediary point for slopes placement after the hump
- A second point is marked in the middle of the reduced hump size ($t_{\text{eff}} = 2t''$) and is assigned as the point for the maximum or minimum value for the reconstruction process.
- Once the intermediary points within a hump are established, the slopes for the direction reversal zone can be calculated.

To **compensate** the possible fringe-loss, a method for harmonic signals has been added to this algorithm: As m lost fringes correspond to a loss in phase amplitude of $m \cdot 2\pi$ so a direct addition of $m \cdot \pi$ at the maximum and $m \cdot \pi$ at the minimum of the reconstructed harmonic displacement, respectively compensates m lost fringes.

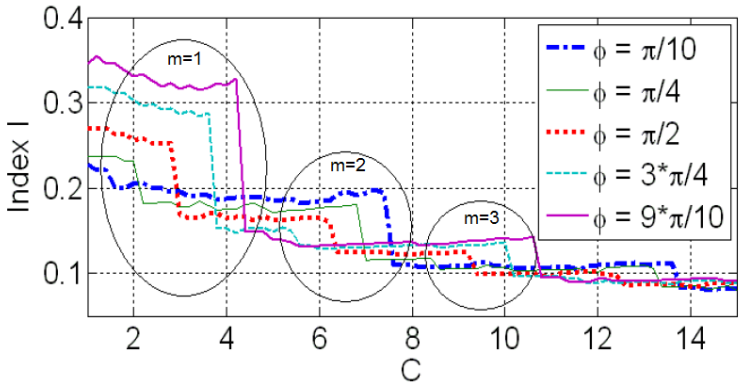

Figure 2.9 – Example of defined zones for Index I for a displacement of 6λ.

The proposed parameter **Index I** is used to define the value m, under the condition that C should remain constant for one period only. It is calculated as Index I = t_{start}/t_{hump}, where t_{start} is the time (or number of samples in a discrete implementation) between the first two consecutive same-signed transitions.

The behavior of Index I as a function of C and different values of θ helps to define specific zones for fringe-loss mapping. Fig.2.9 presents an example of the index evolution for 5 different phase variations ($\pi/10$ to $9\pi/10$) corresponding to a target displacement of 6λ. Each fringe loss results in a sharp fall in this value and this can be used to detect the fringe-loss. So, when there is no fringe loss a zero value is assigned to m. The first fringe loss gets $m = 1$, the second fringe loss $m = 2$, etc. Intersections between different curves start to appear after the third fringe-loss, therefore the method is valid for a variation of $C = 4\pi$.

The other useful ratio is Index II = t_{start}/t_{stop}, where t_{stop} is the time between the last two transitions before direction change. This second parameter helps to detect when the last fringe before direction reversal moves away from the rest of the fringes (corresponding to a decrease in Index II) until it merges into the central zone called *hump* (i.e. sudden increase in Index II corresponding to a fringe loss). Such a detached last fringe can cause a pinching of the reconstructed signal and is corrected using the Interpolation block of Fig.2.7.

2.2 Analysis of the Slopes Based Method (SBM)

Now that the algorithmic bases of previous works relative to displacement reconstruction have been presented. Let us present in this section, **the analysis performed to SBM for the purpose of embedded system implementation**. Indeed, within the goal of producing an embedded sensor exploiting the SM phenomenon. It makes sense to optimize proven systems and algorithms rather than reinventing the whole instrument architecture. Thus, a brief

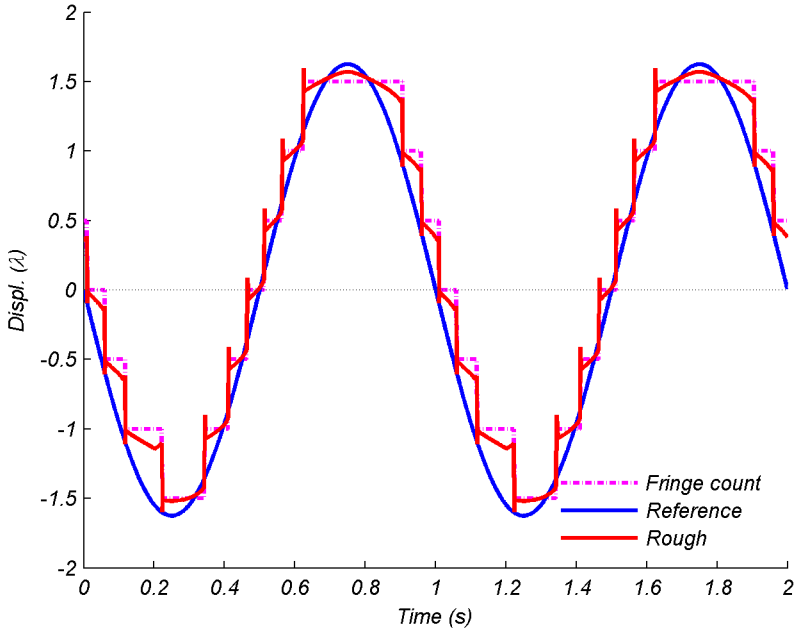

Figure 2.10 – Rough estimation and fringe counting of Fig.2.3 corresponding to a simulated target displacement of $3.25\lambda_0$.

summary on the research behind the slopes proposal is presented first followed by the assessment of its working internals. Finally the conclusions of this analysis serve to introduce the next section about our optimized proposal for generic SM displacement retrieval.

2.2.1 Framework

In the context of embedded systems, signal processing obeys to a hard real-time constraint, meaning that system behavior must always by satisfied in the imposed completion deadline. Feasibility and costs (e.g., in terms of system resources and silicium area) of hard real-time computing depend on how well known a priori are the relevant future behavioral characteristics of the tasks and execution environment [85].

The rough unwrapped phase from PUM provides a target displacement approximation which is improved by an iterative routine. On the other hand, it is known that a fringe counting unroll is the simplest solution to implement at expenses of lower resolution ($\lambda_0/2$). To illustrate this difference, Fig.2.10 shows a simulated target displacement of $3.25\lambda_0$ used to generate the SM signal of Fig.2.3 (thus $C = 3$). Notice that this value of amplitude produces 6 fringes leading the fringe counting method to a displacement measurement of $3\lambda_0$ peak-to-peak, whereas the rough unwrapped phase provides an estimation of $3.1\lambda_0$.

Since the goal is to provide a means for displacement reconstruction useful for a variety of

SM sensors, It can be observed that a reconstructed waveform describing a target's motion, can be approached from the rough phase estimation or from the fringe counting method.

From the analysis in [57], PUM has been found to be time consuming due to the minimization approach from a multivariable space and has been tried to be optimized for its useful implementation. It is reminded that the joint estimation step allows to approach a value for the reconstructed phase x_0, to finally produce the target's displacement by Eq.(2.1). The **Nelder-Mead** direct search method resulted in a promising candidate by means of a potentially parallel implementation [86]. It provides an optimized number of optical power samples necessary for joint estimation of C and α parameters. However, this implementation remained time consuming and a faster **hybrid** method considering the behavior of both parameters was also proposed [87]. Nevertheless it was mentioned that even with the important reduction in computing time for convergence of the function, the fundamental nature of the algorithm saving huge quantities of samples for a later processing remained of **non real-time nature**. This gave origin to the SBM with fringe-loss compensation under analysis.

As it will be described at the end of this manuscript, further research still exists in this path since evaluating parameters C and α allows to solve the phase equation used to retrieve target's displacement.

2.2.2 Assessment of SBM for embedded implementation

Let us remind that this thesis work aims to contribute to the final goal of producing a **sensor** exploiting SM phenomenon with the added feature of responding at different usage conditions for a wide variety of applications. The starting point has been the SBM proposal validated for **preprocessed** signals [66], as well as the pseudocode ALG.1 presented at the end of this section. To this end, the first concern has been to validate the determinism in the development of future system states and correctness of operations for increased use cases. In a second time, a reflection in terms of development effort and memory occupancy has served to refine this analysis. The efforts on internals inspection are condensed in the modeled blocks presented next.

2.2.2.1 Transition Detection

One important aspect to be noticed from this algorithm is the abstraction of SM fringe detection procedure from an incoming weak or moderate SM signal made by this block (Fig.2.11). Even if SBM has been *originally presented for the case of moderate feedback* where a preset threshold detection can be used, the displacement waveform elaboration can be applied to weak feedback signals by using a suitable detection procedure.

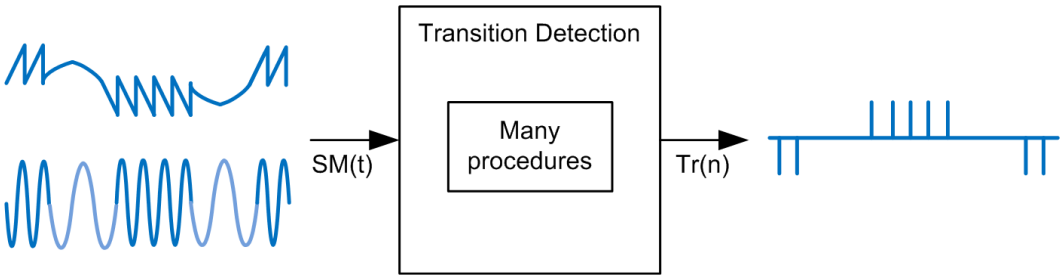

Figure 2.11 – Abstract transition detection block.

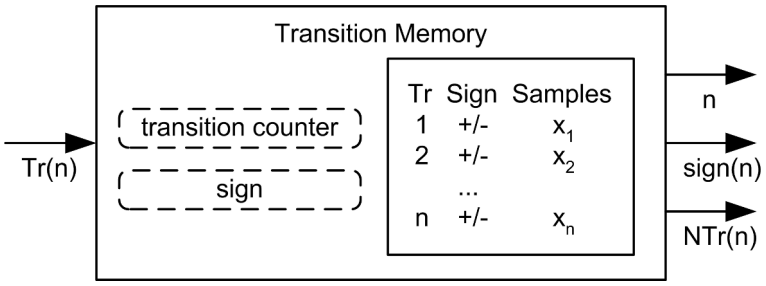

Figure 2.12 – Representation of the transition memory block.

The representation of this block as a general entity provides the requested feature of having unique processing for the reconstruction step. However it shall be explored in detail in following chapter as it constitutes a major source of robustness for the system.

2.2.2.2 Transition Memory

This function consists in a matrix buffer serving as pool of information for most of the other blocks. As represented in Fig.2.12 it mainly holds a vector of detected transitions from which displacement waveform is elaborated.

During a preparation step, it internally handles the sign calculation of the transitions and accounts the samples/time between them (NTr). Such a fundamental operations hardly require correctness evaluation, in consequence they have been left out of inspection. Once these signals are calculated, they are used for the subsequent processing step of slope calculation.

In terms of resources, the observed procedure for Index I & II calculation requires to identify transition direction reversal instants. Therefore memory utilization must be dimensioned to contain at least one maximum and minimum of the maximum displacement to be measured. The number of samples stored in memory is thus dependant on the sampling rate and maximum expected displacement for a given application.

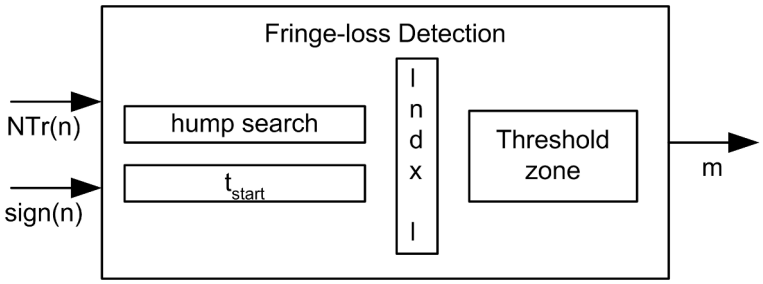

Figure 2.13 – Representation of the fringe-loss detection block.

2.2.2.3 Fringe-loss Detection

This function (Fig.2.13) requires the definition of Index I parameter which in turn relies on the calculation of t_{start} and t_{hump}.

It is reminded that t_{start} is set after t_{hump} which is defined as the central transition-free zone within a period of the harmonic movement. Since these two metrics are relative to the amount of displacement for a given period of time, it has been observed that the provided threshold approach to detect Index I variations requires a careful establishment to be useful. Fig.2.14, presents the calculated Index I parameter for three phase sets of four increasing amplitudes, generating simulated SM signals at different values of C. The dataset difference in phase illustrates the same broadening extrema depicted in Fig.2.9.

By placing curves obtained for increasing amplitude variations of target's displacement it can be observed that Index I presents a diminishing tendency. This implies that mapping threshold zones to define the corresponding m parameter for fringe-loss correction is an off-line procedure. i.e. a calculation done outside the processing chain of the instrumentation. Furthermore, it is observed that for increased amplitude a high precision of this value is mandatory for asserting expected fringe-loss zones.

Intersections between possible values of Index I reduce the zones that can be assigned for m. This implies that this coefficient might be interpreted wrong if evaluated over a signal with different amplitude from the original setting, or if phase variations are obtained. Fig.2.15 illustrates the transitions (scaled for visibility) corresponding to a simulated SM signal of amplitude 6λ and C=8 at two different phase instants $\phi = 9\pi/10$ and $\phi = pi/10$. From the 12 expected transitions, only 10 were accounted due to fringe-loss phenomenon. For $\phi = 9\pi/10$ it can be observed that the algorithm failed to properly compensate both transitions, whereas for $\phi = pi/10$ within the same conditions, the algorithm performed as expected. The pertinence of this use case is explained by the fact that in a real basic setup, there is no information about the incoming SM signal's phase.

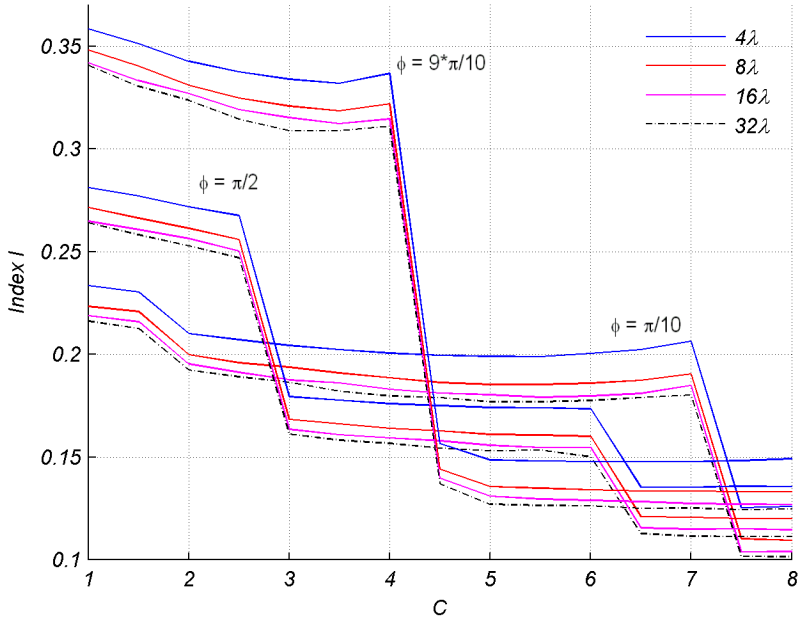

Figure 2.14 – Index I variations for different amounts of displacement at three possible phases.

2.2.2.4 Slope Calculation

The optimization step brought by SBM in terms of calculation relies on the usage of the basic straight line equation $y = ax + b$ to produce the reconstructed displacement waveform. The **Transition Accumulator** step from the slope block representation (Fig.2.16), behaves like a fringe counting method incrementing/decrementing itself according to the sign of a detected transition. The difference is the 2π scaling used to approach its output in terms of phase.

Mapping the different straight line equation coefficients, b corresponds to the staircase function obtained from the Transition Accumulator block, a is the gradient or slope of the current point x, producing the displacement output y.

Gradient evaluation can be represented by two major categories:

- The one for same signed transitions.
- The one for sign reversal providing the resolution at displacement maxima and minima.

The first case is a simple interpolation from the staircase signal, it requires a fixed vertical step of 2π and can be calculated by $a = sign \cdot 2\pi/NTr$.

The case of sign reversal needs more care for its evaluation as it defines different calculations for an accurate reconstruction. Previously described segmentation points within a hump serve to switch between six possible gradients whose general form is $a = sign \cdot m\pi/NTr_{adjusted}$. Where $NTr_{adjusted}$ is the segment size described by placed points within a hump.

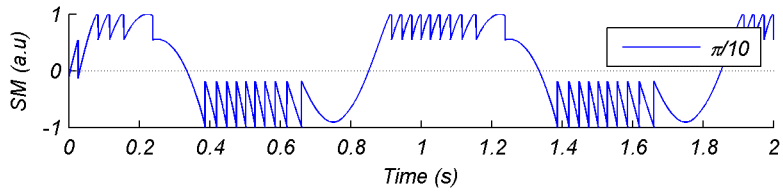

(a) Simulated SM signal for $C = 8$ and $\phi = pi/10$.

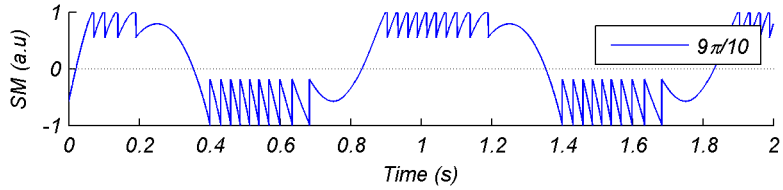

(b) Simulated SM signal for $C = 8$ and $\phi = 9\pi/10$.

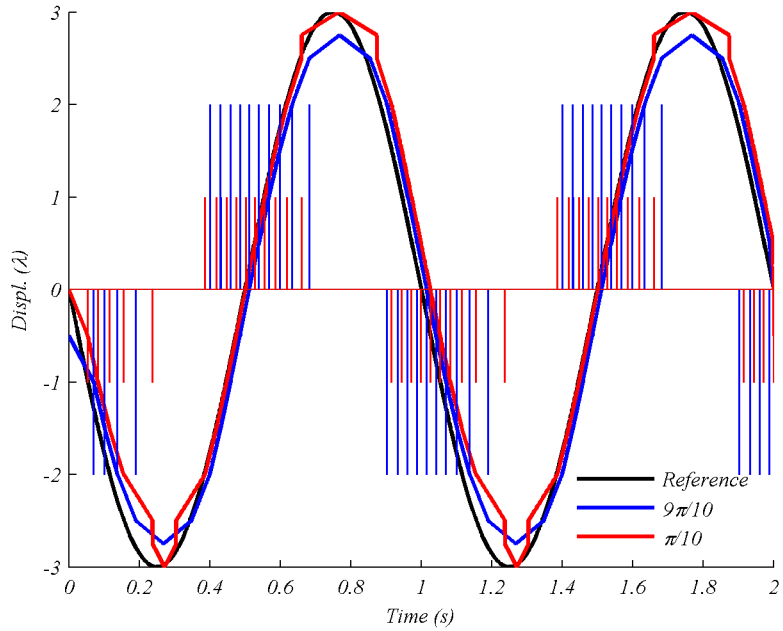

(c) Reconstruction from detected transitions at different phases.

Figure 2.15 – Index I interpretation for transitions from same SM signal at different phases for a displacement reference of 6λ.

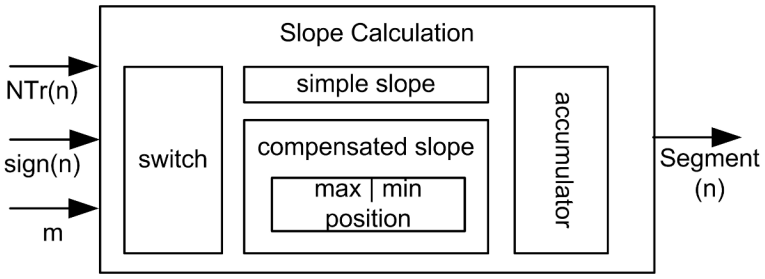

Figure 2.16 – Representation of the slope calculation block.

It is thus observed that the representative waveform equation $y = ax + b$ needs to evaluate its coefficients for each of the produced output points. In conjunction with proper vector indexing, this is a suitable operation for an autonomous implementation.

Hump search seems a trivial task from visual inspection, however its correct definition by the algorithm is a cornerstone for calculating precise Index I values and proper segmentation points. Two criteria to decide whether a transition space represents a hump were considered:

- Searching for maximum gaps within Transition Memory block.
- Defining as a hump, each space bounded by a change in sign of detected transitions.

To illustrate these hump setting criteria, Fig.2.17, depicts a displacement reconstruction obtained from a simulated SM signal of feedback $C = 1.1$ and amplitude 4λ for a harmonic movement. In this case, detected transitions around minima points (e.g. samples 131-225) present a bigger gap than the corresponding hump (e.g. samples 225-275). This implies that segmentation points within a hump are not properly located, producing the observed artifact over reconstructed signal.

Now, from ALG.1, full displacement vector is handled in memory, however a real-time implementation considering only the elaboration within this hump is not be possible since index values fall outside the boundaries. In case of software implementation this would lead to segmentation fault by pointer handling.

Regarding the first hump definition criterion, it can be seen that left most transition direction change is not considered for a correct Index I evaluation since the biggest gap is observed until next transition direction change (e.g. samples 637-861). For this particular case the assigned fringe-loss zone has not produced unexpected compensation assignment, however from previous example (Fig.2.15) it has been learned that slight variations in index I calculation might produce unreliable results.

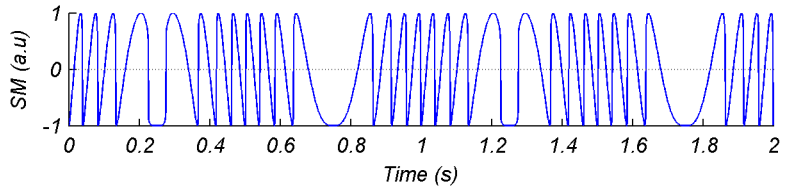

(a) Simulated SM signal for $C = 1.1$.

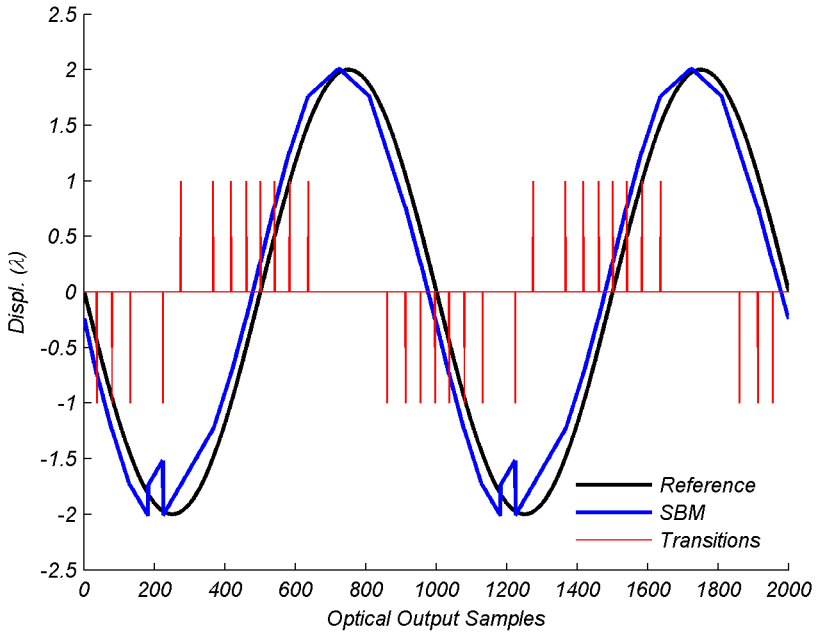

(b) Reconstruction from detected transitions with gap bigger than a hump.

Figure 2.17 – Indexing within hump definition for unconventional transitions.

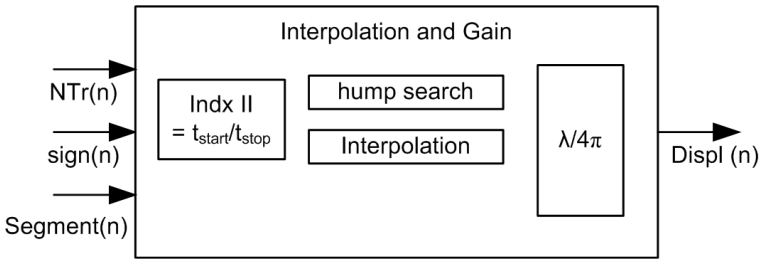

Figure 2.18 – Representation of last SBM steps.

2.2.2.5 Interpolation and Gain

Last steps described in SBM correspond to an occasional fix in waveform shape and the affectation by $\lambda/4\pi$ to obtain the equivalence in the amount of displacement retrieved for the target (Fig.2.18).

Interpolation block is triggered by Index II parameter. For it, same Index I analysis can be inferred as it is also based in relative fringe space and thus implies careful handling. Considering its proper setting for a particular case, the interpolation step acts over the signal segments in the hump zone producing a smooth effect on displacement maxima and minima when reconstruction pitching is observed. For useful real-time implementation, this elaboration requires to handle a displacement vector in memory, containing the relevant segment to interpolate. Furthermore the interpolation procedure (which has not been specified in [66]), might present an increased calculation effort to obtain desired smooth shapes in maxima and minima.

2.2.3 Assessment conclusion

SBM algorithm proposal whose validation was done for preprocessed signals, has been considered for implementation as a future SM sensor expected in the form of a System on Chip. In this context, fringe-loss detection feature results in a weak solution due to the relative value that can be obtained for Index I parameter and the complexity of asserting the zones accounting fringe-loss correction. It is not advised for practical implementation in a generic embedded system. However, it is indeed a useful abacus when information about C or the amount of displacement generating SM signals is available. It may be used for further exploration of SM signals.

Hump segmentation approach for slope placement, thought simple in principle, has been found to need a deep comprehension on indexing parameters. In consequence, identifying the behavior for unconventional fringe separation (i.e. other than clean sinus waveform), makes of this approach a complex implementation for versatile system requirements.

Interpolation procedure for occasional pinching, can be observed as a supplementary smoothing step triggered by Index II parameter. Since this value is also relative to target's displacement and its calculation needs to be detailed for a real-time evaluation, this block has been left out for further implementation.

In light of the exposed optimization opportunities for a characterizable real-time implementation, following section presents a simplified reconstruction proposal. It is advised that the essence of the algorithm has been maintained as its elaboration confers architectural flexibility as compared to PUM.

```
Input: Detected transitions vector
Output: Displacement reconstruction vector
begin Prepare segmentation points
    forall the input elements do
        Identify transitions sign and count samples between them
        Create a vector containing these values
        Identify transition direction reversal points
        Hump maximum point
        Next symmetric point
        Establish Index I and II
    end
end
begin Slopes reconstruction
    foreach input element do
        Create cumulated transitions staircase vector
        switch waveform segment do
            case From left to maximum hump
                Compensated slope calculation
                out(i)=Slope(i)+cumulated 2π
            endsw
            case From maximum hump to next symmetric point
                Compensated slope calculation
                out(i)=Slope(i)+cumulated 2π
            endsw
            case From next symmetric point to end positive hump
                Segment size
                Slope calculation
                out(i)=Slope(i)+cumulated 2π
            endsw
            /* Repeat previous 3 cases for negative hump segments    */
            otherwise Same direction segment
                Slope calculation
                out(i)=Slope(i)+cumulated 2π
            endsw
        endsw
    end
    if Interpolation then
        Smooth hump segments in out vector;
    end
end
```

Algorithm 1: Pseudocode for Slopes Based Method

2.3 Digital-to-Analog Conversion (DAC) based method

From previous section it has been observed that sub-wavelength resolution can be approached by improving the simple fringe counting method, thus avoiding expensive iterative calculations. After a feeling on SM signals behavior, it is foreseen that a *major demand of resources will come from the detection* of interferometric fringes rather than from displacement reconstruction step.

With this in mind, it has been intended to provide a simplified but consistent reconstruction algorithm derived from SBM, in such a way that it may be coupled with other signal processing blocks dealing with the characteristic feedback sensitivity of SM phenomena. More precisely, this method aims to work as a black box with specific exploitation artifacts for SM signals namely: robust detection, increase of resolution and fringe-loss compensation. The added values for a design are: an efficient real-time implementation, a high degree of maintainability and the ease to be synthesized for different processor architectures, software or hardware. Prior to proper algorithm description, it is presented next, the strategy followed for its elaboration.

2.3.1 Digital signal processing approach to displacement reconstruction

By doing an analogy with data unroll of fringe counting and phase unwrapping methods (Fig.2.10), it can be conceivable to achieve displacement reconstruction from SM signals in a similar fashion than Digital-to-Analog (D/A) workings.

From signal processing theory, a D/A converter model relates equally spaced input samples *x(n)* with time domain output signal $x_a(t)$ by:

$$x_a(t) = \sum_{n=-\infty}^{\infty} x(n) g_a(t - nT) \quad \text{with} \quad g_a(t) = \frac{\sin(\pi t/T)}{\pi t/T}, \tag{2.10}$$

Convolution kernel g_a which is also known as normalized cardinal sine (*sinc*), presents a rectangular shape transfer function thus denoting an ideal low-pass filter [88].

As illustrated on Fig.2.19, smooth reconstruction of $x_a(t)$ involves a weighted sum of interpolation function $g_a(t)$ and its time-shifted versions over an infinite interval. While a discrete windowed version can be used to approach this ideal solution, in practice, DAC circuits basically combine a sample-and-hold (S/H) process with a low-pass filter to achieve waveform elaboration.

A S/H circuit maintains the value of one sample until the next one is received producing a staircase output of period T, its impulse response is:

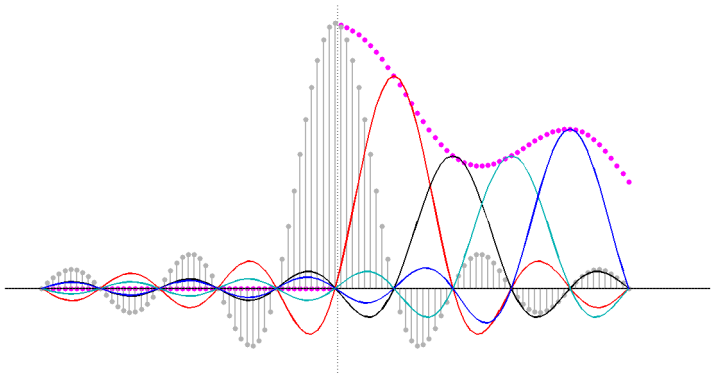

Figure 2.19 – Illustration of the ideal interpolator.

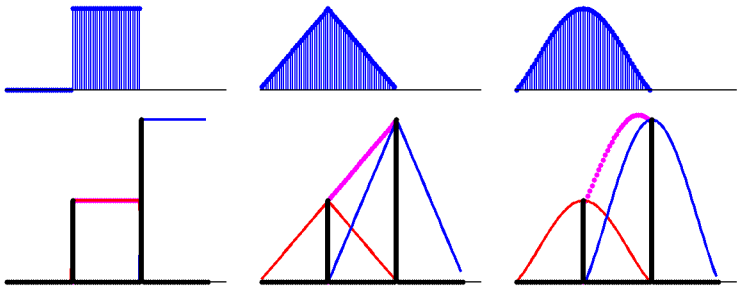

Figure 2.20 – Impulse response variations from ideal interpolator.

$$g_a(t) = \begin{cases} 1, & 0 \leq t \leq T \\ 0, & otherwise. \end{cases} \tag{2.11}$$

Replacing Eq.(2.11) in Eq.(2.10), the simplest interpolation model is obtained known as Zero-Order-Hold (ZOH). Linear interpolation connecting successive samples with straight-line segments corresponds to a delayed First-Order-Hold (FOH) model whose impulse response is:

$$g_a(t) = \begin{cases} t/T, & 0 \leq t < T \\ 2 - t/T, & T \leq t < 2T \\ 0, & otherwise. \end{cases} \tag{2.12}$$

Increased smoothness can be achieved by using more sophisticated higher-order techniques (e.g. cubic splines). In frequency domain, transfer functions for ZOH and FOH correspond to *sinc* and $sinc^2$ respectively [89]. These shapes are far from the rectangular function describing a low-pass filter in the ideal reconstruction process and thus explain observed variations in reconstruction models (Fig.2.20).

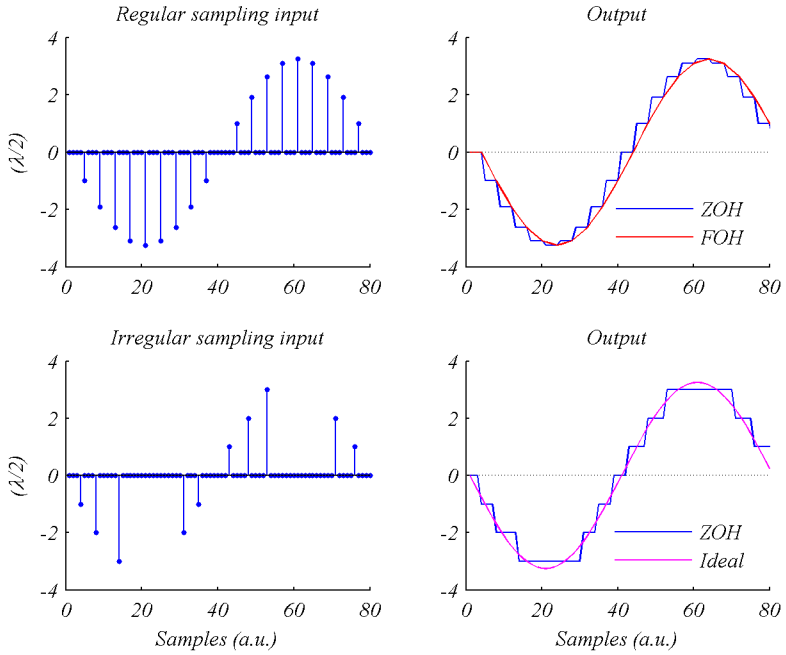

Figure 2.21 – SM displacement seen as an irregular sampling reconstruction.

Notice that linear interpolation with a FOH model, can be used to connect detected transitions from a SM signal similar to slopes placement of previous section. However, the need for defining intermediary points within humps from SBM, seems to be best satisfied by directly using a higher order interpolator in this zone.

Signal reconstruction from equally spaced samples can be achieved by conventional circuitry implementing previously described interpolation schemes. However, as illustrated on Fig.2.21 SM fringe transitions appear irregularly spaced since they are relative to the amount of displacement and target's movement frequency. Therefore, if conventional circuitry is used for SM displacement reconstruction, smooth waveform at signal maxima and minima is not possible and only a resolution of $\lambda/2$ can be obtained.

From a recent paper [90] proposing a set of reconstruction methods from nonuniform samples, it can be seen that many of the referenced literature is based on Lagrange interpolation. In fact, the already presented DAC model can be seen as a reduction of Lagrange's equation (presented hereafter) for the case of uniform sampling. For nonuniform samples, same authors state the difficulty of exact reconstruction as partly due to interpolation **function variations** between samples and the need to have **all sampling instants** for the calculation.

Reconstruction from irregular sampling is an active research domain surpassing the scope of present thesis which makes continuity of previous research paths towards an embedded

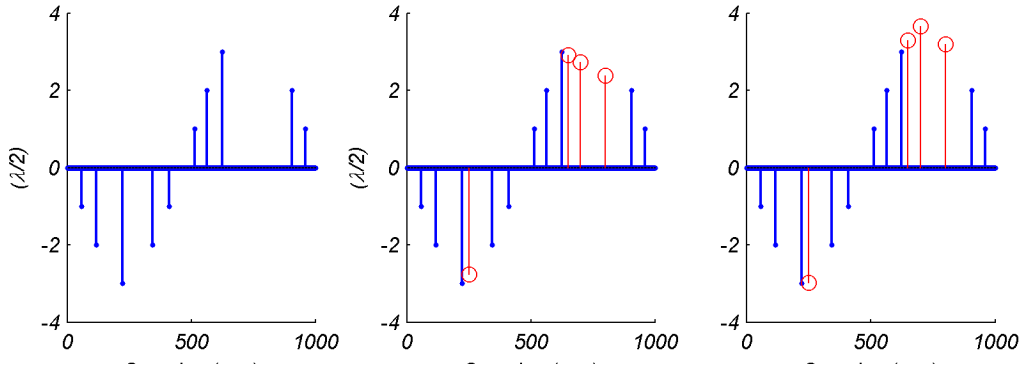

Figure 2.22 – Linear and quadratic Lagrange interpolation for SM displacement reconstruction.

implementation. However, let us briefly analyze the classical Lagrange interpolation for the case of SM signals. Lagrange interpolation is a method used to find a polynomial function f of order n that passes through $n+1$ data points in the form $(x, f(x))$ and is described by [91]:

$$f_n(x) = \sum_{i=0}^{n} L_i(x) f(x_i) \quad \text{with} \quad L_i(x) = \prod_{j=0, j\neq i}^{n} \frac{x - x_j}{x_i - x_j} \tag{2.13}$$

where $L_i(x)$ is a weighting function that includes a product of $n-1$ terms with terms of $j = i$ omitted.

Evaluating Eq.(2.13) as linear interpolation for the case of displacement reconstruction from irregularly spaced SM fringes gives:

$$D(x) = \frac{x - x_1}{x_0 - x_1} f(x_0) + \frac{x - x_0}{x_1 - x_0} f(x_1) \tag{2.14}$$

where $f(x_0)$ and $f(x_1)$ correspond to the cumulated value of a fringe counting method.

Also, evaluating Eq.(2.13) as quadratic interpolation gives:

$$D(x) = \frac{x - x_1}{x_0 - x_1} \cdot \frac{x - x_2}{x_0 - x_2} f(x_0) + \frac{x - x_0}{x_1 - x_0} \cdot \frac{x - x_2}{x_1 - x_2} f(x_1) + \frac{x - x_0}{x_2 - x_0} \cdot \frac{x - x_1}{x_2 - x_1} f(x_2) \tag{2.15}$$

Using Eq.(2.14) and Eq.(2.15) in previous example of irregularly spaced SM transitions. Fig.2.22 compares the results obtained for a linear and quadratic interpolation of three points selected within a hump zone in order to depict the differences obtained between both calculations. The former clearly corresponds to a FOH interpolation as derived from Eq.(2.10) and already discussed. The later seems to better suit the need for smoothness, however notice that this calculation required $x_0, x_1 and x_2$ points, i.e. two transitions previous to hump zone, and one transition after.

Interpolation via lagrange polynomial seems a promising elaboration to approach precision

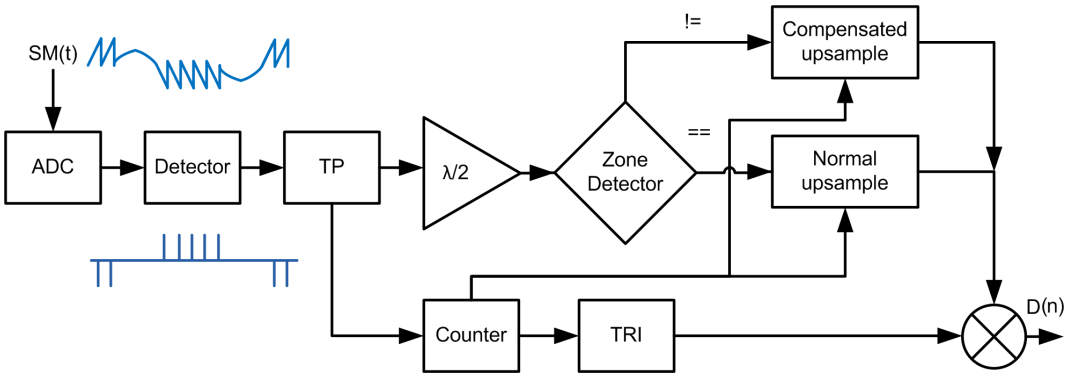

Figure 2.23 – Block diagram of DAC method.

in SM displacement reconstruction, however high order polynomial interpolators result in expensive calculations which might not be suitable for systems with restricted resources. Also, this calculation requires a whole data vector. In case of SM signals this implies to use a transition memory block like in SBM which was found to be dependant on the sampling rate and amount of displacement to be measured.

Since the intention is to provide a generic procedure, the nature of incoming SM signal is assumed unknown. In agreement with optimization brought by SBM over PUM, waveform elaboration has been tried to be simplified by using only two transitions for the calculations. With this background let us now present our algorithm for SM displacement reconstruction.

2.3.2 Algorithm proposal

Reconstruction process as depicted on Fig.2.23 starts by acquiring a SM signal which is fed into a (so far abstract) **fringe detector** block, whose purpose is to provide a train of peaks corresponding to a temporal detection of SM phase transitions (detailed in Chapter 3). Instead of allocating a transition memory pool like in SBM, the constraint for real-time elaboration is imposed at the arrival of any two transitions.

Transition Pair (TP) block parses detected fringes looking for a positive or negative value. From literature it is known that each SM fringe corresponds to a target displacement of $\lambda_0/2$, this scalar value has no incidence on algorithm's behavior and can be multiplied at the end of reconstructed waveform. Here it is immediately multiplied by TP block's output for empathy with 2π step from SBM.

Parallel to TP, Counter block simply keeps track of the number of samples (NTr) between two detected transitions. This value helps to generate a normalized triangular window (TRI) and defines the segment size for any of both upsampling blocks. Depending on the sign of TP values, Zone Detector module either selects a *normal* upsample procedure for same-signed

transitions, or a *compensated* upsample procedure for unequal signs.

Finally, each upsampled pair is convolved with a vector from TRI and thus, an interpolated segment corresponding to the target movement is generated.

Let us now describe the details of this procedure in order to expose its relation with DAC workings, however some particularities must be highlighted: 1) it works for irregular input samples, 2) its output is still in numeric form for further processing, 3) humps zones are interpolated in similar way to SBM.

2.3.2.1 Interpolation process

Referring to Eq.(2.10) it can be seen that filtering approach to reconstruction process can also be applied to the case of irregular samples, resulting in the implementation of an adaptive filter driven by the size of samples separating each transition pair T.

Reminding the fringe counting method, where a staircase shape is increased for positive fringes and decreased for negatives ones. TP vector $[tr(N-1) \quad tr(N)]$ is composed by previous and present detected transitions respectively, with $N = 0, 1, 2, ...$ being the number of accumulated fringes.

Signal $x(n)$ to convolve, results from upsampling TP by T. Two different elaborations are presented depending on the kind of segment to interpolate.

Fringes zone From TP module, if transitions share the same sign (positive or negative), then they are assigned to a *fringes* zone where simple linear interpolation is carried. The procedure to obtain an upsampled vector is described by:

$$x(n) = \begin{cases} TP(n/T), & n = 0, T \\ 0, & otherwise. \end{cases} \tag{2.16}$$

Lobes zone When a monitored target changes its direction, TP contains a positive value and a negative value or vice-versa. In this case a *lobe* zone is assigned requiring a particular interpolation in order to produce convenient shape to reconstructed waveform. Notice that this corresponds to SBM elaboration within humps. The procedure to obtain an upsampled vector in this condition is:

$$x(n) = \begin{cases} TP_{\text{sign}}(n/T)/2, & n = 0, T \\ TP_{\text{sign}}(0) + \varepsilon, & n = T/2 \\ 0, & otherwise. \end{cases} \tag{2.17}$$

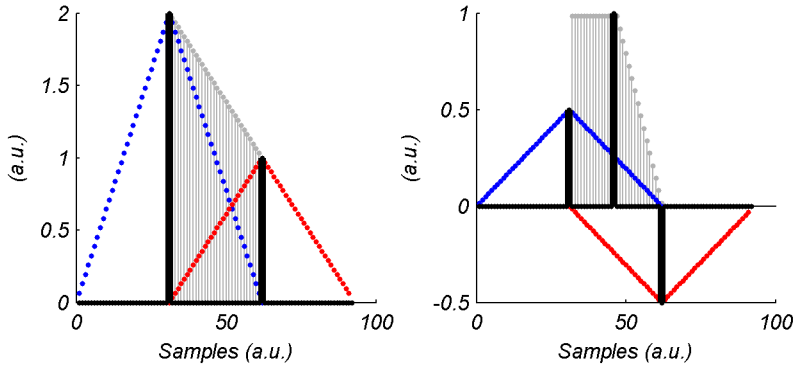

Figure 2.24 – Comparison of a normal interpolation in the fringes zone and a compensated one for the lobes zone.

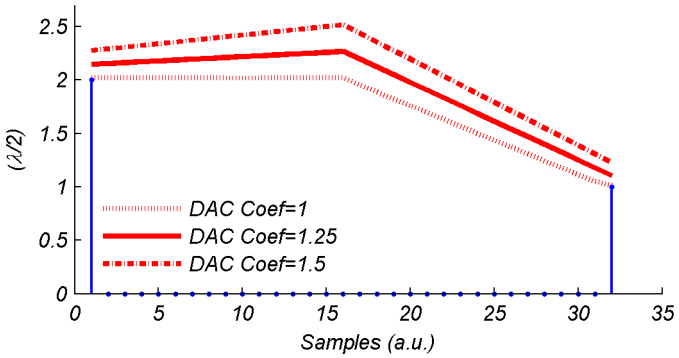

Figure 2.25 – Resolution modification by affecting one coefficient in compensated transition pair.

Let us illustrate these concepts by referring to Fig.2.24. On the left, a pair of transitions [2 1] has been upsampled using Eq.(2.16). Expected interpolation segment within these points shall result from convolution process with a delayed FOH impulse response [Eq.(2.11)] as depicted. On the right, same transition pair has been upsampled using Eq.(2.17). Notice that this equation exploits sign reversal between transitions in order to contribute to the up-down shape required for this zone.

This elaboration combined with a coefficient in the range [1 1.5] placed in the middle of the upsampled vector, allows to variate resolution in waveform elaboration as depicted in Fig.2.25. By using a coefficient equal to 1, excess fringe coefficient ε is set to zero leading to a resolution similar to a fringe counting method. A value of 1.25, provides a behavior equivalent to SBM proposal which adds $\pi/2$ on its elaboration, thus $\varepsilon = \lambda/8$. Finally a value of 1.5, leads $\varepsilon = \lambda/4$ to compensate up to half of a fringe in waveform elaboration.

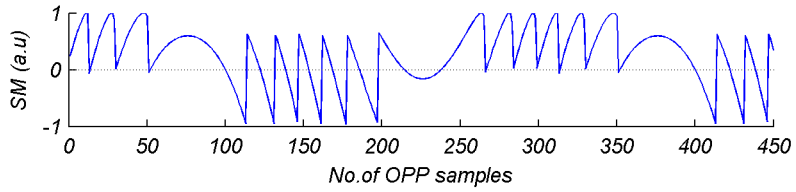

(a) SM signal for $C = 3$ and amplitude of $3.25\lambda_0$.

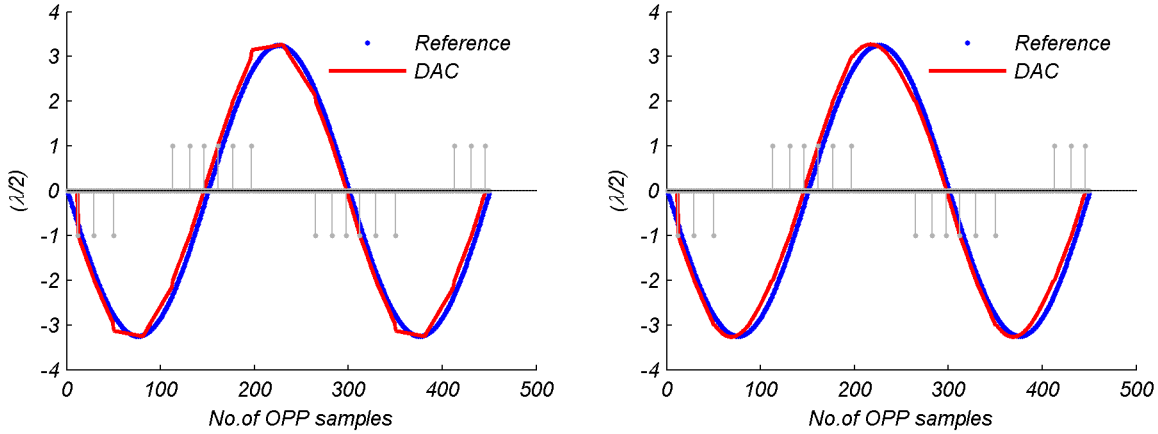

(b) Reconstruction using triangular convolution kernel vector.

(c) Reconstruction using rounded convolution kernel vector.

Figure 2.26 – DAC displacement reconstruction examples using different convolution kernel vectors for a same SM signal.

2.3.2.2 Displacement reconstruction

A discrete implementation of Eq.(2.10) to calculate a linear interpolated segment (x_{FOH}) can be described by:

$$x_{FOH}(n) = \sum_{k=0}^{T} x(k)h(n-k). \tag{2.18}$$

where x(k) is an upsampled vector from Eq.(2.16) or Eq.(2.17) and $h(n)$, the generated triangular impulse response. Mapping Eq.(2.18) to fringe counting equation with sub-wavelength resolution Eq.(2.9) the output of DAC algorithm is established as:

$$D(n) = x_{FOH}(n)\frac{\lambda_0}{2}. \tag{2.19}$$

Detected transitions corresponding to a simulated SM signal in moderate feedback regime with $C = 3$ and amplitude of 3.25λ [Fig.2.26(a)] (like the one used in Fig.2.3), were used to illustrate two different waveform elaborations.

First, the retained triangular kernel vector approach with lobe compensation set to $\varepsilon = \lambda/8$ is represented in Fig.2.26(b). For this small amount of displacement, a glitch in lobe section

reconstruction can be observed due to imperfect matching of the interpolated segment. One solution to this drawback can be done by dimensioning a smoothing filter when providing the analog signal at output stage.

Another solution is to modify the triangular impulse response by a rounded shape in order to approach a higher order interpolation as presented in Fig.2.26(c). This smoother reconstruction can be used instead of previous proposal, however this elaboration results in increased calculations that might not be necessary for certain applications.

Since this thesis work aims to provide general algorithms as a basis to develop versatile SM instrumentation for well defined requirements specification. It is convenient to highlight this algorithm's feature of being easily adapted, for example by affecting its vector coefficients it is suitable to meet a particular requirement like the smoothness of its output waveform.

2.3.3 Simulated measurement results

DAC algorithm as described in previous section has been used through the rest of this manuscript for waveform elaboration. A comparison against SBM for unfavorable conditions where transitions are not spaced as expected is presented here to further distinguish both algorithms.

The same SM signal used to observe the **issue of placement points within a hump** from SBM (Fig.2.17 with $C = 1.1$ and amplitude of 4λ), is analyzed in Fig.2.27. Displacement reconstruction using DAC method is presented along SBM reconstruction. Lobe compensation has been set to $\varepsilon = 0$ to illustrate resolution variation capability of this coefficient.

From both waveform elaborations it can be observed a direct dependence on the position of a detected transition within a fringe. In the case of DAC algorithm, it results in a pinching effect affecting the reconstructed target's movement shape. Notice however that calculations are still deterministic between two transitions, i.e. waveform elaboration is not corrupted because of indexing issue found in SBM. Therefore a real-time implementation of DAC method shall produce the same elaboration like the represented here.

A second comparison is presented in Fig.2.28. This time a SM signal with $C = 3$ for **a damped displacement** has been simulated and the transitions detected by thresholding. Variations in the number of fringes and its frequency, serve to stress the complexity of handling the irregular gaps between transitions.

From the first cycle of reconstructed signal, a slight resolution variation can be observed between SBM and DAC method due to a difference on their ε compensating parameter. For the second cycle, SBM elaboration produces spikes at signal maxima and minima explained by the placement of sectioning points within a hump. As previously mentioned, these positions

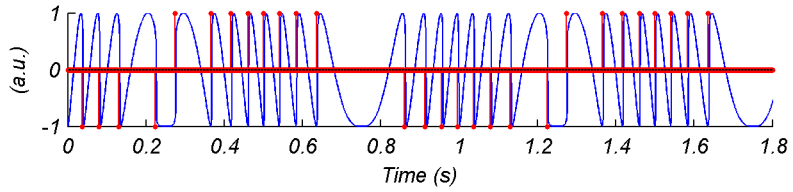

(a) SM signal for $C = 1.1$ and amplitude of 4λ.

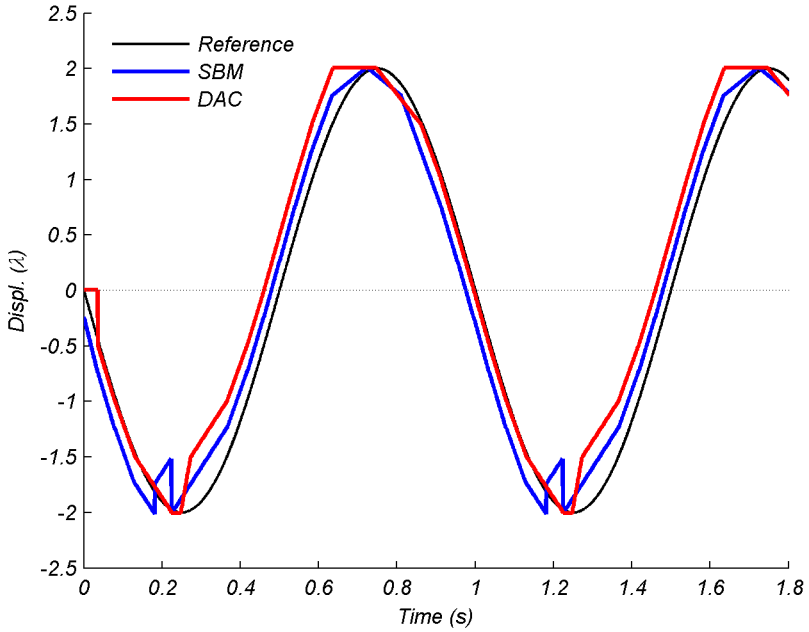

(b) Displacement reconstruction by proposed method and previously analysed SBM.

Figure 2.27 – Comparison between SBM and DAC for unconventional transitions.

depend on the gap between previous transitions exposing the system to unexpected behavior. On the other hand, DAC algorithm keeps coherent with the signal elaboration even if obtained smoothness is not fully satisfactory. Finally, the matching difference between reference displacement and both algorithms can be observed as a direct dependence of the detected transitions and not merely as a failure of SBM or DAC.

2.3.4 Experimental measurement results

After observing a coherent behavior of DAC algorithm. It was decided to implement it as part of an embedded system in order to observe its viability for real-time signal elaboration. As a matter of fact, by the time this work was accomplished, two of the referenced embedded implementations from Chapter 1 were published. Looking back to their waveform elaboration, it can be observed that both of them basically rely in the unwrap of its input SM signal. Thus,

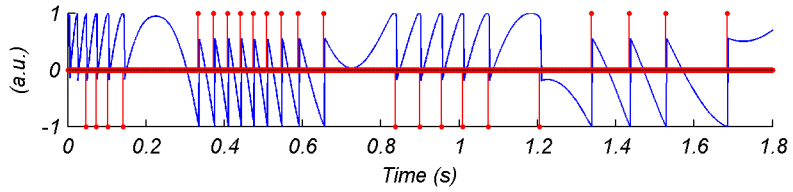

(a) SM signal for $C = 3$ and a simulated damped displacement.

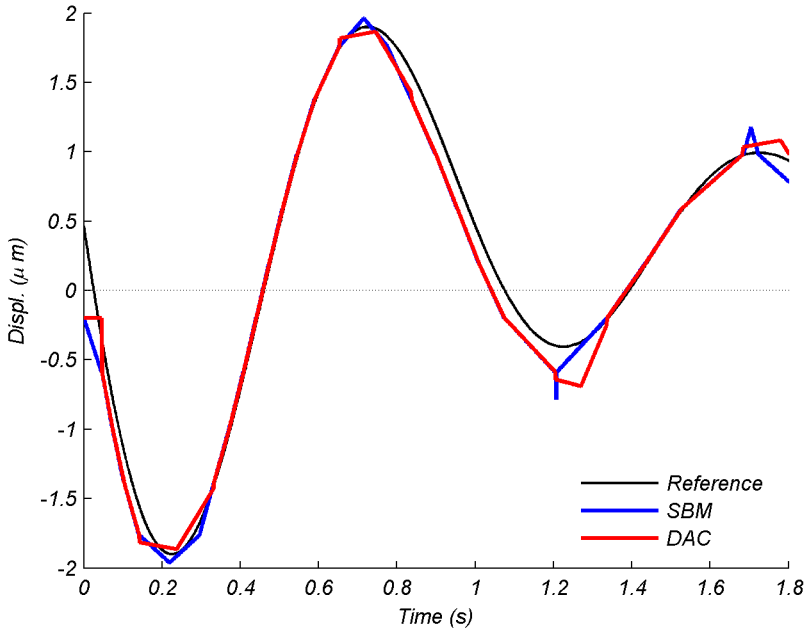

(b) Damped displacement reconstruction by proposed method and previously analysed SBM.

Figure 2.28 – Comparison between SBM and DAC for transitions from a damped movement.

confirming the interest for another solution in this context.

2.3.4.1 Real SM signal

By using a Hitachi LD (HL7851G) of λ_0 =785 nm driven in continuous wave, an experimental signal was acquired with an oscilloscope for postprocessing. The setup used for gathering a SM signal (Fig.2.29) consist in the basic displacement measurement scheme where a lens focuses an emitted beam and the backscattered light is monitored by the laser's built-in photodiode and converted to voltage by a transimpedance amplifier.

The moving target was a piezoelectric transducer (PZT) with nanometric resolution from Physik Instrumente (P753.2CD) [92], configured to produce a harmonic displacement of 4.5 μm i.e. $\approx 6\lambda$ for its symmetrical forward-backward trajectory. For simplicity, information about target frequency has been avoided. However it shall be presented next in the context of

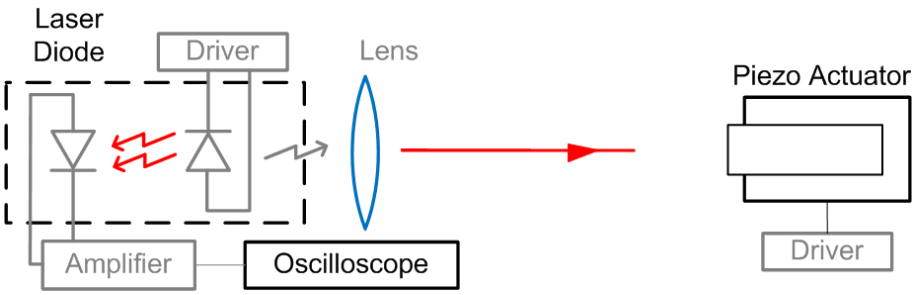

Figure 2.29 – Experimental setup for SM signal acquisition.

embedded implementation.

Sawtooth like shape of acquired signal from the metallic surface denotes moderate feedback [Fig.2.30(a)], therefore transition detection has been achieved by thresholding its derivative. Due to signal noise, manual removal of spurious fringes has been necessary to provide a clean train of detected transitions. For this peak-to-peak displacement amount, 11 fringes were accounted as expected (i.e. no fringe-loss).

Displacement reconstruction by SBM against proposed DAC algorithm is compared in Fig.2.30(b). By leaving a default maxima/minima placement equal to π, the amplitude provided by SBM algorithm resulted in 4.71 μm [$(11 fringes \cdot 2\pi) + \pi + \pi \cdot {}^{\lambda}/_{4\pi}$].

Now, by setting DAC coefficient to 1.25 ($\varepsilon = \lambda/8$). The amplitude provided by DAC algorithm resulted in 4.52 μm [$(11 fringes \cdot {}^{\lambda}/_{2}) + \lambda/8 + \lambda/8$], thus being more precise than SBM for this particular example.

2.3.4.2 Implementation for real-time operation

In order to satisfy the usage as an embedded device, DAC algorithm has been implemented with focus on memory consumption and calculation time. Sequence diagram of coded algorithm (Fig.2.31) [93], begins by the active process of **transition detection**. In this case it corresponds to a simple derivative of the signal and a precalculated threshold comparison.

Zone detector stage launches the **counter of samples** when a transition is signaled by an interruption signal. When the counter reaches two transitions it is restarted to zero and gives an acknowledge message to the **zone detector** which will then distinguish two different zones of SM signal based on transition's pair sign. It will affect to *fringes zone* if the signs of transitions are equal, otherwise it will consider them as belonging to a *lobe zone*, which corresponds to "ε" (positive or negative) of SM signal.

Kernel convolution module can be asynchronously driven by zone detector unit, corresponding to the triangular impulse response. **Upsampled signal** generation can be asynchronous as well, and relies on the values of accumulated present and previous transitions.

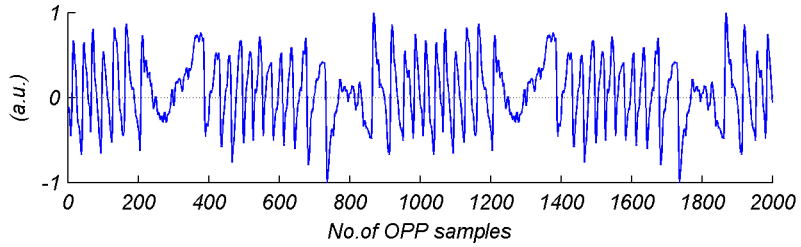

(a) SM signal monitoring a piezoelectric in movement.

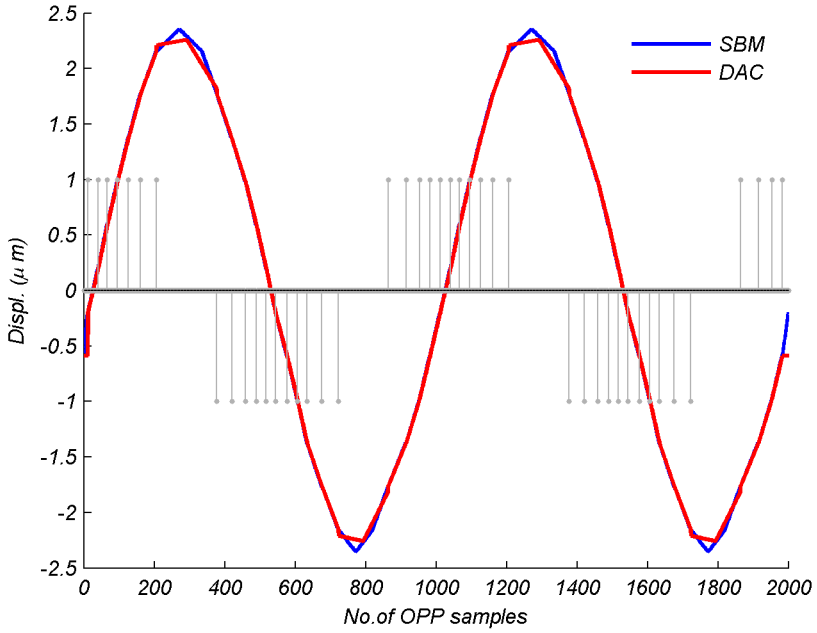

(b) Reconstructed displacement from detected transitions.

Figure 2.30 – Comparison between SBM and DAC method for experimental signal.

These two tasks can be implemented in parallel for performance increase. However both vectors must be synchronized when calling **filter** module in order to keep coherent the calculated segments.

Once a convolved segment has been calculated, it is affected sample by sample by the gain factor $\lambda_0/2$, and can be sent out to a D/A converter to recover the analog reconstructed displacement.

2.3.4.3 Proof of concept

In order to provide a basic validation for further exploring constraints related to embedded system development. Previously described sequence diagram has been implemented into an off-the-shelf development board comporting a Digital Signal Processor (DSP), TMS320C6416 from Texas Instruments. Despite the 16-bit fixed-point architecture which is more suitable for

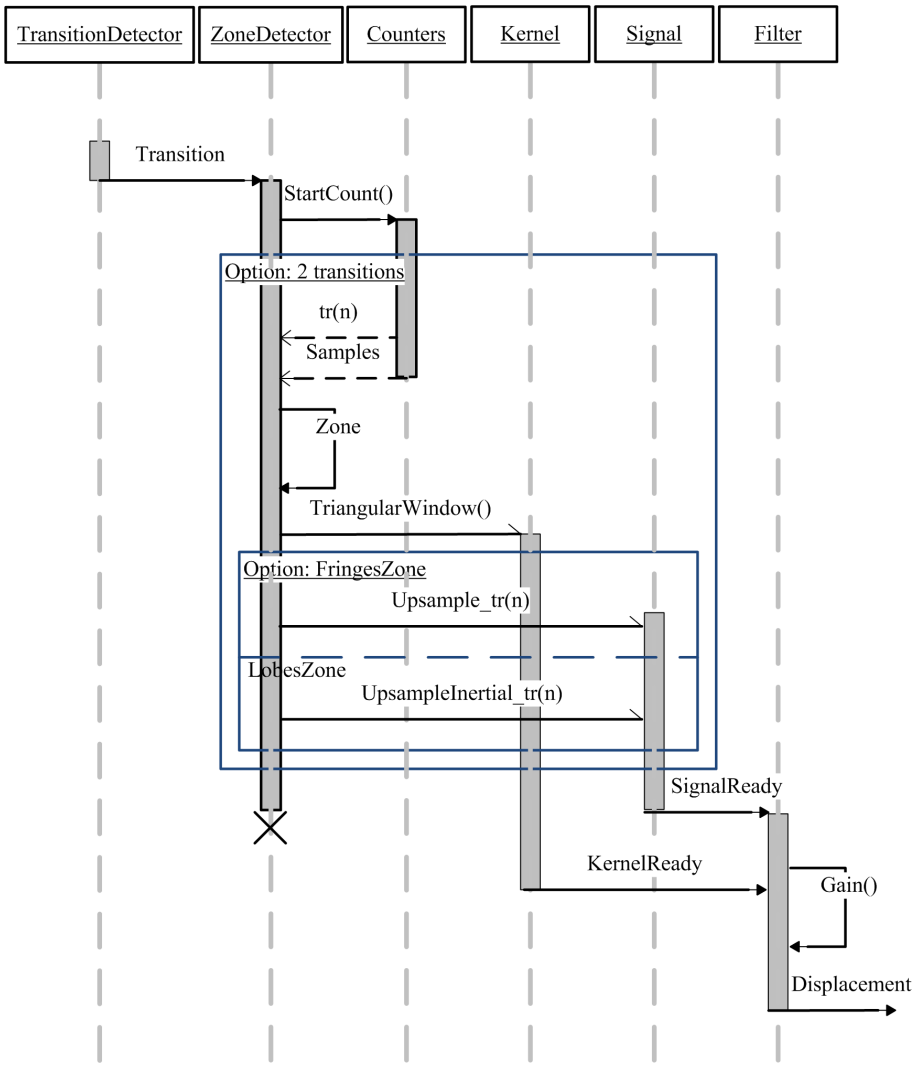

Figure 2.31 – Sequence diagram of implemented DAC algorithm.

optimized algorithms rather than prototyping, this is a low cost powerful processor offering a performance from 4800 up to 8000 million instructions per second (MIPS) at clock rates between 600 MHz and 1 GHz respectively [94]. An analog interface circuit, TLV320AIC23 16-bit stereo codec, is provided to handle input and output of signals. It uses a 12 MHz system clock allowing sampling rates of 8, 16, 24, 32, 44.1, 48 and 96 KHz, thus comprising the range of audio signals [95]. This board also offers 16 MB of synchronous dynamic RAM (SDRAM) and 512 kB of external flash memory.

Since a robust detection of SM interferometric fringes was not considered for the development of this algorithm, a test with a real SM setup even in optical table with controlled ambient temperature was not possible with the weak derivative based detection scheme used for this prototype. Instead, a Tektronix AFG3022 function generator preloaded with a modeled SM signal of same characteristics as the experimentally acquired SM signal of section 2.3.4.1

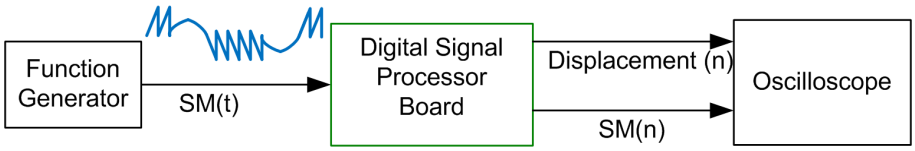

Figure 2.32 – Illustration of the validation setup for real-time embedded implementation.

(a displacement of $6\lambda_0$ and $C = 3$), has been used to validate coherence in the results and evaluate performance of the algorithms.

Setup diagram of Fig.2.32 depicts the analog SM signal fed to the board's A/D converter via its LINE IN socket. For reference, the acquired SM signal is sent out of the board along the reconstructed displacement via HEADPHONE and LINE OUT connectors and monitored by an oscilloscope.

Let us now refer to Fig.2.33(a) where an estimation of the fringes' frequency in the simulated SM signal for $6\lambda_0$ displacement is presented. By observing different frequencies for the moving target it is possible to calculate frequencies suitable to be used with the selected board. Since the shape of SM fringes is quite complex, it has been proposed to use a sampling rate at least 10 times greater than the estimated frequency of a single fringe. For example a target frequency of 8 Hz gives an estimated fringe frequency of 275 Hz, therefore a sampling rate proposal of at least 2.75 KHz.

Considering the lowest sampling frequency of 8 KHz available for this board, a chosen fringe frequency of 275 Hz contains 29 points [Fig.2.33(b)], thus satisfying the practical constraint of having at least 10 points to describe a SM fringe.

The interest of drawing this kind of abacus to design suitable use cases in terms of memory and sampling rate can be observed by considering a second example with a fringe frequency of 3.4 HKz. Notice that this value might be obtained just by increasing the target frequency to 100 Hz while keeping the observed 11 fringes. In this case, leaving the lowest sampling frequency of 8 KHz would give only 2 samples to describe a fringe. While this is coherent with Nyquist sampling theorem, it provides a weak description of SM signals. Thus, according to Fig.2.33(b) a sampling rate bigger than 32 KHz should be used for this second example.

Since the real-time constraint has been imposed to the arrival of 2 fringes. The example chosen imposes $1/275$ Hz=3.63 ms as the maximum time allowed to DAC algorithm to perform its calculations. With the profiler tool provided by the DSP development suite, the average execution time required to calculate a displacement segment from two transitions in the fringe zone resulted in $\approx 20\,\mu$s while in the lobe zone it took around $260\,\mu$s. Thereby, for this particular SM signal the treatments are largely respecting the real-time requirement.

From Fig.2.34 it can be seen that signal reconstruction of 8 Hz has been achieved properly. The measured contribution of each of the detected transitions into the DAC is close to 14 mV,

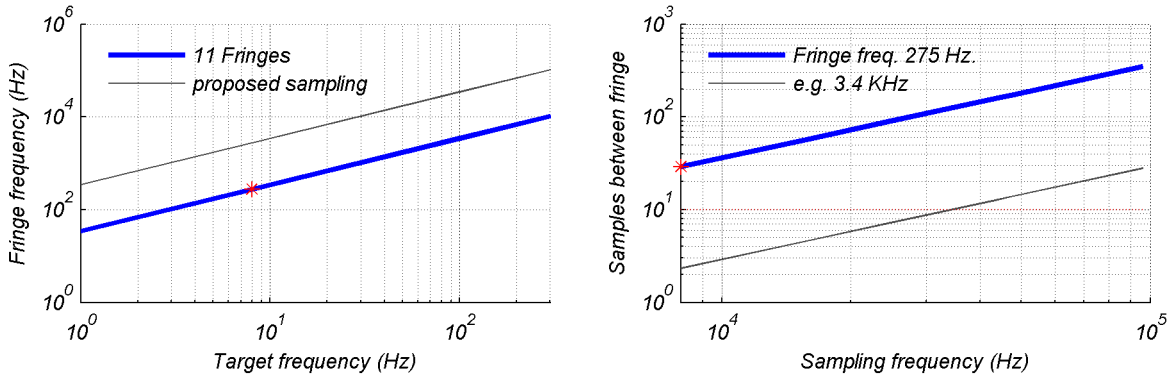

(a) Estimated frequency of a fringe for a varying target movement.

(b) Estimated amount of points per fringe at different sampling frequencies.

Figure 2.33 – Abacus used to propose suitable use cases for selected DSP board.

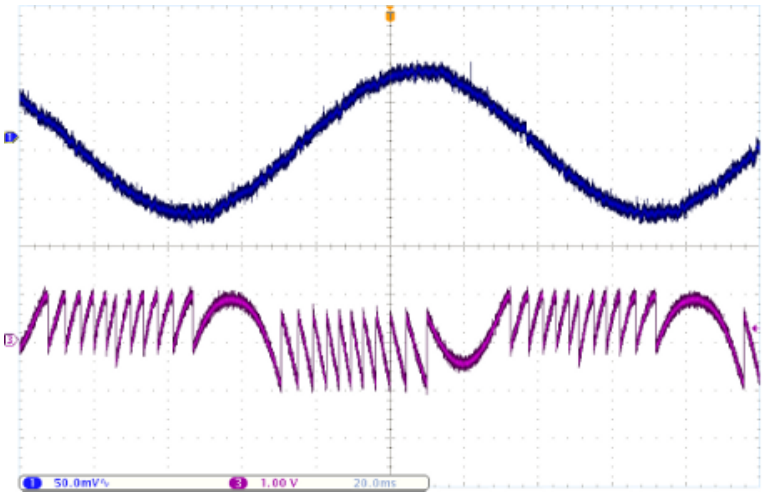

Figure 2.34 – Real-time reconstruction on top of simulated SM signal.

providing a peak to peak amplitude 160 mV. Since the calculated step size of the TLV320AIC23 is of 0.043 mV for an analog output of 2.83 V, a slightly bigger amplitude value was expected ($\approx$ 189 mV). However sensitivity characterization has not been considered for this prototype, as the focus was merely on a proof of concept of algorithm's behavior.

2.3.4.4 Assessment conclusion

Proposed DAC algorithm has been conceived as a simplified implementation of SBM for real-time displacement reconstruction in embedded systems. The relevance of its operation has been inspired by the signal elaboration of D/A converters and validated by simulation. The implementation approach states the problem of SM displacement reconstruction as the efficient usage of an adaptive filter, driven by the number of samples separating two transitions. This

simplicity allows a straightforward estimation of the resources needed to synthesize a given application, as well as a maintainability by classical system design techniques.

A basic prototype has been roughly evaluated as it was observed the urge for a reliable transition detection scheme. Based on the coherent behavior observed and relative simplicity, we consider DAC method as a contribution to get a step closer in the creation of a robust autonomous sensor based on SM technology for displacement measurement.

2.3.5 Critical analysis

Let us finish the presentation of our proposed DAC algorithm for displacement reconstruction by comparing it against the major features of SBM as summarized in Table 2.1. Such analysis in the context of embedded implementation and system versatility is discussed next.

Feature	Slopes Based Method (SBM)	DAC method
Real-time working	Time boundaries difficult to establish due to processing over complete data buffers prior to waveform elaboration every 2 transitions	Time constraint defined for 2 transitions along all the calculations
Implementation	Complex handling of points within humps and fringe compensation	Standard comprehension through convolution operator
Displacement versatility	Requires redimensioning several vectors within the implementation. For an embedded system, memory consumption might penalize many practical applications at increased displacements or frequencies	Adaptability only requires to dimension memory according to the average number of samples in a fringe
Resolution	Excess fringe compensation of $\lambda/8$	Comparable at equal conditions
Fringe-loss	Current implementation not suitable for autonomous usage	Not used, but accessible via compensation coefficient
Validation	off-line via PC, from recorded signal	in-line via DSP, from signal generator

Table 2.1 – Comparison between SBM and DAC method.

2.3.5.1 Embedded implementation

The initial goal for either SBM or DAC algorithm has been to be implemented as part of an embedded sensor exploiting SM phenomenon. As presented in the analysis of SBM section,

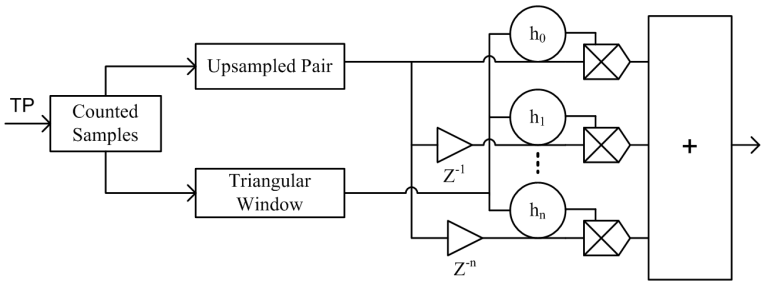

Figure 2.35 – Convolution mechanism summarizing the proposed displacement reconstruction.

the simplification in terms of calculations brought by SBM over the iterative process of PUM allowed to approach a real-time implementation. This statement is not merely related to the usual misconception that fast calculations lead to real-time. In fact, SBM has been privileged because it showed a determinism for signal elaboration allowing to impose completion deadlines.

However, the evaluation of SBM for unfavorable scenarios where indexing points used for waveform calculation were overlapped, demonstrated that this approach needs to be modified in order to prevent memory corruption for an embedded implementation working with only 2 transitions as proposed. Also, the fact that some of the tasks (e.g. transition memory, hump search) were designed to process a complete data buffer prior to waveform elaboration, penalizes the definition of time boundaries associated to the detection of 2 fringes. To alleviate this, DAC algorithm truly works every 2 transitions along its different procedures. In particular the kernel generation and convolution product itself can be observed as the most critical process to define.

Thinking in the worst case scenario where contiguous transitions might be detected each instant of the sampling rate, simple solutions exist, for example copying the input samples over a staircase signal resulting from a fringe counting unwrap, or the usage of integrators and low-pass filters. Such a situation imposing this hard real-time constraint may happen for a noisy SM signal if a weak detection scheme is used. To fulfill this requirement, the programming strategy of working with a frame buffer of data can be used in both algorithms to bypass this constraint on the full system implementation. However another solution can be explored for DAC algorithm: to implement parallelism on the convolution stage.

Since the basis of displacement reconstruction by DAC is the well known convolution algorithm, it is expected that optimized implementations can be analyzed in straightforward manner according to particular needs. For example, referring to the abstract representation in Fig.2.35 a rough implementation could be designed in a high level simulator and then be refined up to a fully hardware implementation without further knowledge on SM phenomenon, but supported by well founded signal processing concepts.

2.3.5.2 System versatility

Memory usage is also a concern in embedded sensor design since this resource is usually of limited size. As demonstrated with previous estimation abacus, if sampling rate is increased to allow greater target's frequencies for a given displacement amount or bigger displacements for a given frequency, then there will be more samples between each transition pair. To provide a versatile instrument exploiting a same reconstruction algorithm at different displacement conditions, such algorithms must be dimensioned according to a given requirement specification. SBM requires to modify several of its tasks to this end, in particular the Transition Memory block might require a considerable size to allow the hump search routine for fringe-loss detection to operate properly. The validation of SBM for preprocessed signals made unnoticeable this constraint which became evident while considering its implementation into an embedded platform. Conversely, DAC design has considered this requirement again by keeping the 2 transitions approach along the calculations allowing a convenient resources estimation as well as a straightforward adaptability for different requirements.

In terms of resolution, it has been shown that both algorithms improve the basic resolution from a simple fringe counting method, producing comparable waveforms by defining a suitable excess fringe compensation parameter. However if fringe-loss feature of SBM is considered, it shall result in improved calculations for particular cases suffering of this phenomenon. DAC algorithm offers the capability to incorporate a fringe-loss correction by affecting the same coefficient used for excess fringe compensation. However due to the weakness encountered in current proposal to cure this phenomenon for a real-time usage, this implementation has been left out in the context of general algorithm.

The off-line validation of SBM allows to further explore fringe-loss issue and possible solutions for real-time implementation. On the other hand, the simplified design of DAC algorithm allows an in-line displacement reconstruction introducing more confidentiality to exploit SM phenomenon for embedded instrumentation. It can be roughly stated that SBM's simplification backed with a signal processing approach has allowed to design DAC, a versatile algorithm for embedded implementation. Even if any of both algorithms follow a perfectly smooth displacement due to the linearity of segmentation approach, it is highlighted that waveform elaboration remains in digital form, thus traditional smoothing solutions can be added prior to final displacement exploitation.

2.4 Conclusion

Different solutions to retrieve the motion of a remote target have been presented in this chapter. With a focus on algorithm proposals, Slopes Based Method (SBM) has been carefully analyzed due to its simplified approach over the well referenced Phase Unwrapping Method (PUM). With the intention of having a practical embedded implementation of SBM for a variety of SM signal conditions, some incompatibilities were detected along with several optimization opportunities. In particular, fringe-loss issue seems more pertinent to be analyzed off-line with *a priori* knowledge of the signals, rather than trying to correct it by a generic real-time processing scheme. Furthermore, if typical conditions of SM signals are expected (e.g. $0.2 < C < 4$), loosing one fringe or two can be considered as a secondary concern for displacements over the tenth of μm as this error could be comprised within the measurement tolerance.

The experience while working with SM signals showed that without laboratory conditions, dealing with the detection of SM fringes is a major issue that needs to be addressed in detail, whereas the reconstruction process can be simplified at expenses of a loose in resolution. In this context a new algorithm was proposed.

The so called DAC based method resulted in a generic algorithm for displacement reconstruction, offering an efficient implementation, a high degree of maintainability and the capability to be synthesized for different processor architectures, software (SW) or hardware (HW). It has been implemented over an off-the-shelf digital signal processing board to demonstrate its feasibility and the ability to be coupled with other algorithms aiming to provide increased performance for a SM sensor within the same frame. To this end, the up to now abstract scheme of SM fringe detection shall be explored in next chapter.

Chapter 3

Robust detection of SM fringes

Contents

From the two abstract blocks proposing the description of a SM displacement measurement system of Chapter 1, our contribution on displacement reconstruction has already been exposed. This leads us now to present the efforts made to properly detect incoming SM signals.

This chapter begins by presenting some original methods found in literature addressing the need for robust detection of SM fringes. Then, the analysis of the *adaptive threshold algorithm* [65] in the context of non-cooperative signals, shall serve to introduce the spectral analysis carried on SM signals as an alternative to deal with their complex shape in time. Finally, our proposal for SM **fringe detection algorithm** aiming to avoid restrictions over the feedback value and suitable for real-time implementation shall be presented.

3.1 Solutions for SM fringe detection

Increased sub-wavelength resolution exposed in previous chapter requires SM fringes to be properly detected. Each undetected fringe shall result in an added error of half-wavelength of the final displacement measurement, thus making an instrument unreliable.

Even though peak detection on its general form seems a trivial task for visual inspection, it is an active research topic in many fields involved with signal analysis. Following section reports observed methods and algorithms from SM literature addressing the issue of SM fringe detection.

3.1.1 Techniques to stabilize a working mode

Overall processing of SM signals can be simplified if we are able to restrict their behavior for a set of use cases. This strategy can be observed since the first reported low-cost SM vibrometer [15] were the LD was **mounted on a piezoelectric transducer** (PZT) to compensate changes in the laser operating frequency and an opto-electronic arrangement was used to keep the system working on weak feedback.

The Fringe Locking (FL) system resulting from a combination of an optical arrangement and an electronic feedback control shown in Chapter 1, is another good example of this kind of solution. A variant of this configuration using **two servo stabilized LD's** working in differential mode resulted in a speckle insensitive proposal allowing to provide a large dynamic range of amplitude measurement [96]. In a recent study from the same research group [97], it is informed that frequency compensation of the wavelength-modulation in a pump **current controlled LD** shall lead to an optimized analog control loop and thus an increase of performance. As a side note, the commercial SM sensor from Philips mentioned in Chapter's 1 introduction, operates the LD with a triangular current modulation to reveal the direction of target surface motion by comparison of the measured Doppler shift on the rising and falling slopes in the waveform [17].

A different elaboration consist in **acting on the focus** of the system by means of a liquid lens (LL) as proposed in [98]. The idea is to maintain the SM phenomenon in moderate feedback regime with no hysteresis in a dynamic way thanks to the adaptive optical element. The setup was mentioned to also increase the dynamic range of the distance between the target and LD. Such a system reported a good performance over a distance range of 6.5 cm to 265 cm for a target vibration signal reconstitution.

As a matter of fact, the practical introduction of variable focal lens controlled by an external voltage has demonstrated a great potential for embedded applications in last years. With response times around 30 ms and dissipated power of a few mW [99], the usage of LL seems a promising option in our context as its electronic control can lead to an automation of

the complete setup.

While these solutions allow to simplify signal processing of interferometric fringes, the usage of certain external components might not be fully compatible with the premise of conceiving a versatile embedded SM sensor. Also, as already seen in Chapter 1 this diversity still penalizes the embracement of a consolidated solution for industrial development.

3.1.2 Algorithms for SM fringe detection

While designing a SM based instrument, the choice for a detection scheme will be influenced by the required operational environments. Simple solutions like a fixed threshold comparison require constrained environments as can be appreciated from previously exposed literature. This is usually employed in laboratory conditions when the research goal is not related to the robustness of a SM instrument.

Since SM signal exhibits two major distinguishable shapes in time domain depending on the feedback coupling: weak ($C < 1$) and moderate ($C \geq 1$), the natural approach is to deal with each of them separately by means of different signal processing solutions as observed with the Switching Algorithm (SA) system of Chapter 1.

An example of improved processing, corresponds to the usage of **wavelets** to locally extract the frequency behavior and detect discontinuities characterizing the SM fringes. By properly choosing the wavelet to use in case of moderate feedback regime, [100] demonstrated to effectively extract the position of noisy phase transitions due to hostile industrial environment. A further step in robustness face to noisy signals was proposed in [101]. This method avoids false transition detection in moderate feedback regime by using an **evolutionary** algorithm, however this solution involves very long computations.

Not long ago, a method for accurate displacement reconstruction from SM signals at low signal-to-noise ratios and in presence of disturbances has been proposed [102]. The idea is to extract a single **beat frequency** over a segment containing at least a few fringes in order to calculate the instantaneous velocity of the target and integrate it over the time to reproduce the movement of a monitored target. A sinusoidal regression is needed to provide the phase and then the sign of the averaged velocity found. This method reported to rectify the problems of speckle, electromagnetic interference and mechanically induced parasitic fluctuations from an ultrasound solder vibrating at 20 KHz with an amplitude of 40 μm.

The usage of SM sensors like conventional laser Doppler velocimeter has also been discussed in [103] with the measurement of a rotating disc at constant velocity. Certainly, **velocity integration** allows to average single spikes or signal losses for displacement elaboration. However an autonomous implementation shall require a definition of the

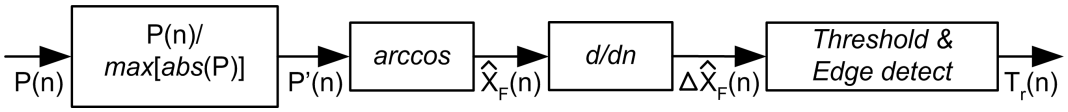

Figure 3.1 – Block diagram of signal detection performed in PUM.

frequency range to cover, in order to keep accurate results over the time.

Two other solutions in time domain working at different feedback levels by a unique algorithm are presented next. The referred *duty cycle algorithm* and the *adaptive threshold algorithm* seem to be compatible with the versatility desired in our research. They are introduced by further explaining the basic functionality of fixed threshold fringe detection.

3.1.2.1 Fixed threshold

Looking back into PUM proposal (Fig.2.2), a practical fringe detection implementation is depicted in Fig.3.1. First, a representative set of fringes is required in order to correctly normalize the signal for its usage with *arccosine* function. Then, the derivative of resulting modulus π signal, serves to establish a threshold comparison and a subsequent edge detection to designate positive or negative transitions according to the moving target's direction. This manually adjusted threshold value is introduced to ascertain variations in a differentiated signal, corresponding to a real shift in phase and discriminating those corresponding to noise.

A fixed threshold value, however, cannot be reliable in case of feedback change as the peak-to-peak fringe amplitude of the signal decreases when the feedback level C increases (Fig.3.2). If a small threshold value is selected for a moderate feedback regime to compensate its small signal amplitude, then it results in false detections for the case of a weak feedback signal having major peak-to-peak fringe amplitude. Likewise, a higher threshold value chosen for a weak feedback signal would miss the transitions in case of a moderate SM signal. Furthermore, a derivative based threshold might produce the opposite behavior since the sharp transitions of a sawtooth like signal produce bigger differentiated values than those obtained for weak feedback.

For above reason a fair tradeoff between simplicity of elaboration and system reliability, consists in working with sharped sawtooth signals allowing to perform only the derivative stage plus a pre-calculated threshold comparison, saving thus the calculation relative to *arccosine* function. In our context, this implementation cannot be retained due to the lack of robustness face to variations on the SM signal amplitude considering a general non constrained environment.

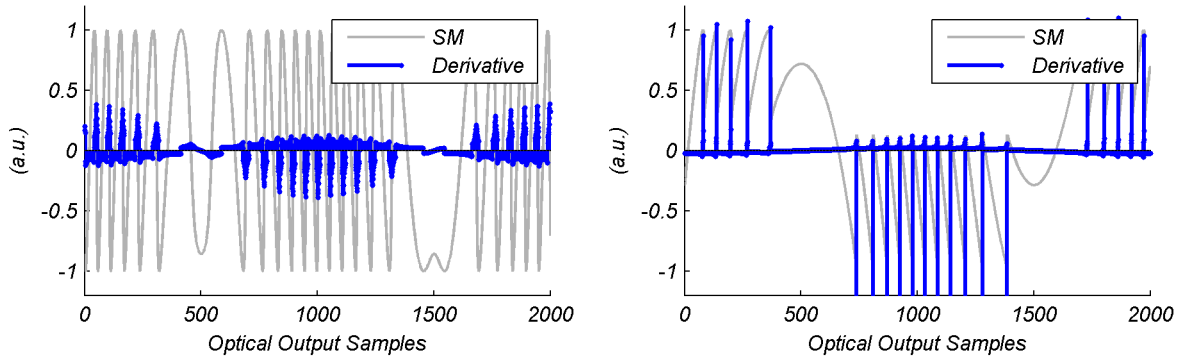

Figure 3.2 – The difficulty of settling a derivative based threshold when SM feedback changes for a given application.

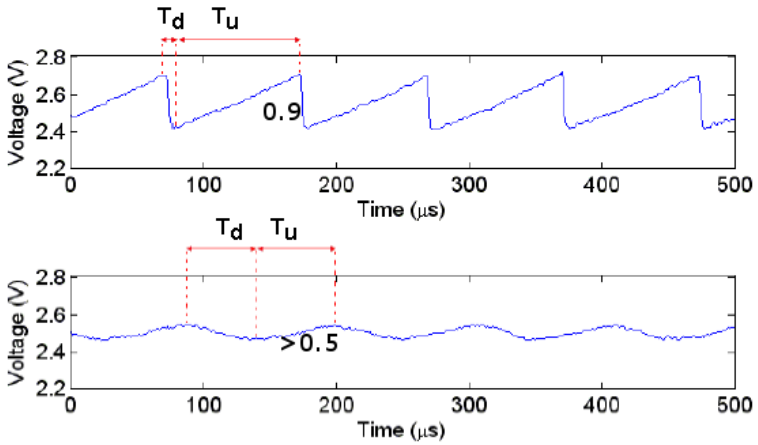

Figure 3.3 – Duty cycle calculation example for moderate (top) and weak (bottom) feedback experimental signals from [105].

3.1.2.2 Duty cycle algorithm

A proposed technique for real-time signal processing, consists in calculating the duty-cycle (DC) of the interferometric fringes in order to properly distinguish the target direction even for weak feedback condition [104, 105].

The underlying working principle can be observed from Fig.3.3 where two different segments of an acquired SM signal are presented, corresponding to a target moving at constant speed. T_u is defined as the time between a maximum and the next minimum inter-fringe point. Conversely T_d is the time between a minimum and the next maximum. The DC value δ is calculated by $\delta = T_u/(T_u + T_d)$. For this particular example, a value of $\delta = 0.9$ is reported for the sawtooth-like signal corresponding to a moderate feedback, and a value slightly superior to $\delta = 0.5$ for the almost sinusoidal signal for weak feedback. Since both conditions meet the criteria $\delta > 0.5$, then a positive transition is assigned for those fringes.

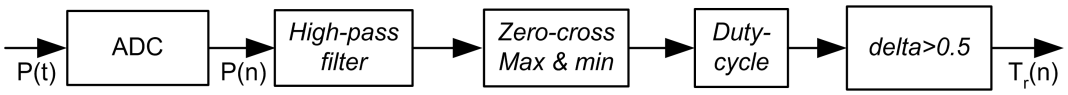

Figure 3.4 – Block diagram of the DC transition detection.

In order to dissect the fringes from a signal, a high-pass filter is applied at the input stage avoiding signal offset due to hysteresis phenomenon. Then, the algorithm localizes zero-crossings and identifies temporal positions of the signal maxima and minima within a window between two consecutive zeros. Once mapped the positions of a set of maxima and minima, three subsequent positions are analyzed in order to calculate the DC of a single fringe as described above.

The block diagram summarizing this process is illustrated in Fig.3.4. Notice that spurious noise can affect the zero-crossing search method and certainly falsifies the assignation of maxima and minima necessary for a correct interpretation of the δ value. However, by combining this method with suitable electronics and with a well focused beam, a real-time implementation can be achieved as demonstrated in SA device from Chapter 1.

3.1.2.3 Adaptive threshold algorithm

This proposal aims to cover the range of feedback regimes by a fully automated algorithm that converges to the optimum threshold level needed to correctly detect the SM signal fringes [65]. As remarked from its self-descriptive name, the central idea is to replace the static fringe detection approach used in PUM by a series of decisions undertaken from an iterative threshold calculation. Fig.3.5 presents the block diagram of relevant steps for each SM regime.

Following the same procedure for a fixed threshold calculation, the starting point is set to 5% of the peak amplitude of the differentiated phase $\Delta\widehat{x}_{\mathrm{F}}$. The initial low threshold provides a twofold solution: it ensures a detection even for high values of C, and if ever no transitions are detected then the SM signal is classified as a **strong** regime signal and no further processing is done. Since this low threshold possibly detects many false transitions for those signals that shall have higher peak amplitudes (lower C), the following steps consist to identify the remaining feedback regimes, namely: moderate, weak and very weak (when the SM signal is almost a sinusoidal).

The *iterative process* is based on the idea of dividing the acquired signals in two segments: The positive peaks from the derivative (P>0) and the negative (P<0). The transitions obtained for a given threshold value are saved along with the sign of the OOP signal corresponding to the instant of the fringe transition detection. Then, the algorithm tests only those transitions which were obtained for P >0 (assigned as negative ones). If ever *alternating positive and negative*

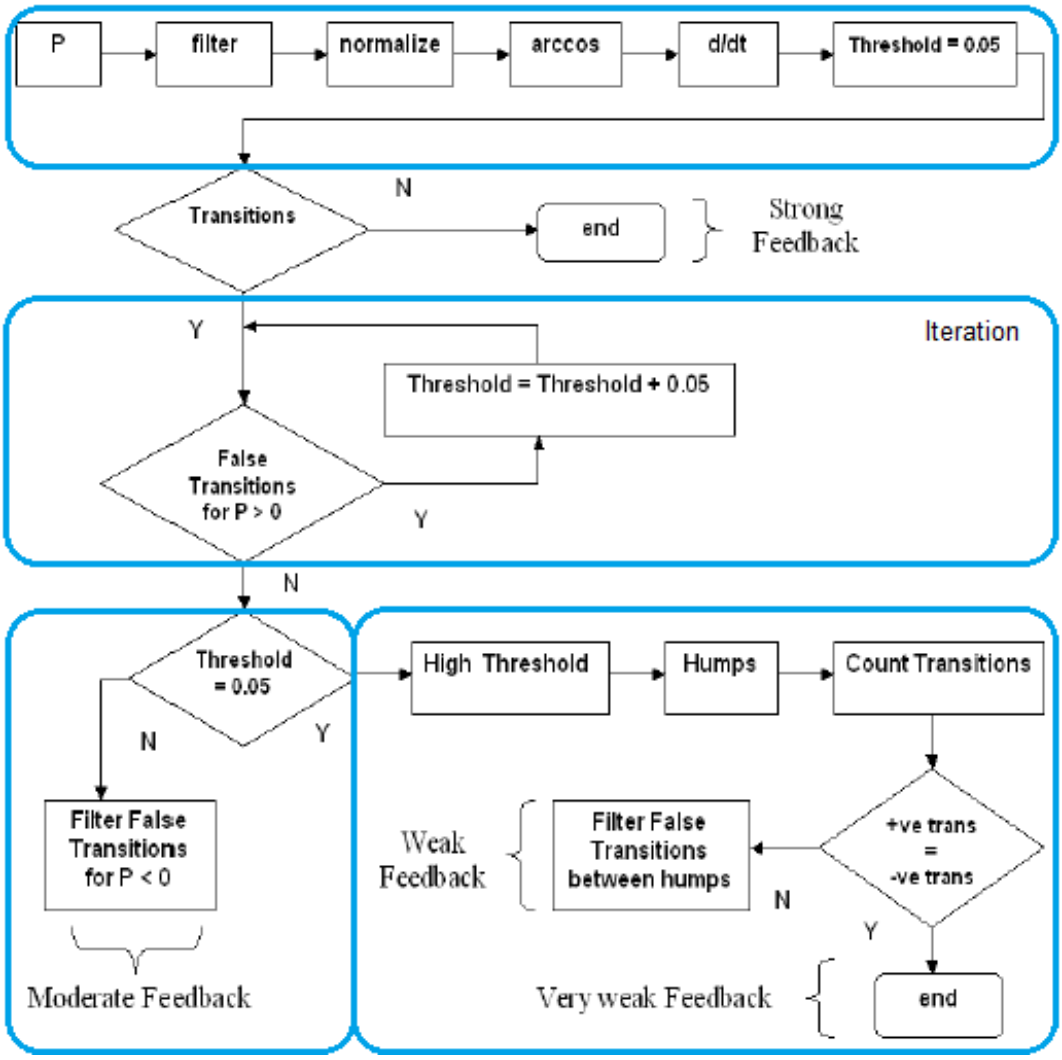

Figure 3.5 – Block steps of the adaptive threshold algorithm.

transitions are obtained for P>0, it signifies that the threshold is too low and it is incremented by 5%. This loop continues until the threshold value becomes large enough to rule out the possibility of a false transition detection for P>0 as illustrated in Fig.3.6(a-b) for a simulated signal with $C = 4$.

Once the iterative threshold has converged, if it resulted different to the initial value of 5%, then the signal is classified as **moderate** feedback. To provide the final output, it detects the corresponding transitions on the P<0 segment and simply removes all those false transitions of opposite sign [Fig.3.6(c)].

Since the normalized fringe amplitude lies on the [1 -1] range in the case of **weak** (and very weak) feedback regimes, the lack of hysteresis makes impossible to separate the OOP fringes into two halves. As a consequence, the test of presence for alternating false transitions in P>0 fails (i.e. only negative transitions are accounted by this test). This condition is denoted by the

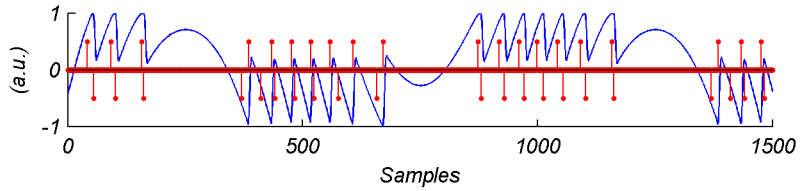

(a) Threshold=0.1.

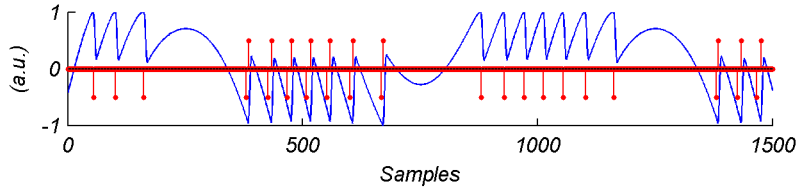

(b) Threshold=0.15.

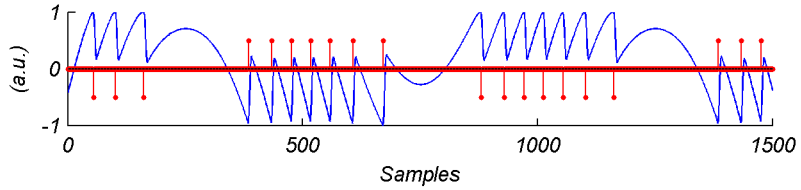

(c) Filtering for P<0.

Figure 3.6 – (a) and (b) show alternating transitions for P>0 segments, while (c) shows the removal of false transitions for P<0 segment.

decision block *Threshold=0.05* and helps to trigger a different procedure to deal with this kind of signals.

The first step for this algorithm's section is represented by the *High Threshold* block. It consists in repeating the transition detection procedure with a high threshold value which alone clears all the false transitions for the weak SM signals with C close to 1, but still insufficient to remove many false transitions of smaller values of C.

Further processing consists in detecting the central zone of the OOP where the target changes its movement direction. Reminding the proposal in SBM of previous section, this *central zone or hump*, is defined as the maximum number of samples between two transitions. In addition, a next step designates all those transition-free regions into a hump array that are comparable to the maximum hump.

Once the humps have been identified, the algorithm starts the task of eliminating the existing false transitions by *counting the number of positive and negative transitions* between humps. As illustrated in Fig.3.7, the more the value of C decreases, the sawtooth aspect of SM fringes tends to be sinusoidal. In this case the algorithm detects and removes these false transitions within a given inter-hump zone as compared to the correct transitions.

Finally, an equal number of positive and negative transitions within a region which is supposed to contain only one type of transitions, defines a **very weak** signal (Fig.3.8). In this

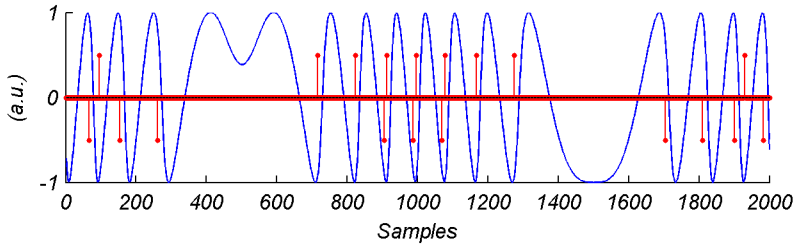

Figure 3.7 – Effect of some sinusoidal fringes which lead to imperfect detection for $C = 0.5$ and threshold = 0.45.

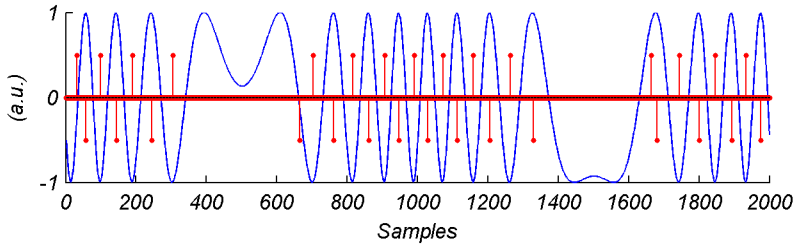

Figure 3.8 – All sinusoidal fringes which lead to equal number of positive and negative transitions for $C = 0.05$.

case the same issue of directional ambiguity seen in classical interferometers is enforced and only displacement information can be recovered.

3.2 Analysis of the adaptive threshold algorithm

As already mentioned, the *adaptive threshold algorithm* makes part of an important prior research work held in our laboratory [57]. Since it conforms to the strategy of having single processing for different SM regimes aiming to be implemented as a real-time System-in-Package (SiP), it has been decided to further analyze its determinism and correctness of calculations in this context.

Now that the adaptive threshold algorithm has been introduced. **This section presents the work carried to evaluate its robustness for detecting SM fringes.** To this end, let us first expose the considered approach for its usage face to signal changes at different target conditions.

3.2.1 Non-cooperative SM signals

Other than parasite noise from measurement environment or the LD itself, when roughness of the surface under measurement is such that a slight misalignment with the normal of target's movement affects considerably the exploitation of interferometric SM fringes, a condition of non-cooperative signal may be argued.

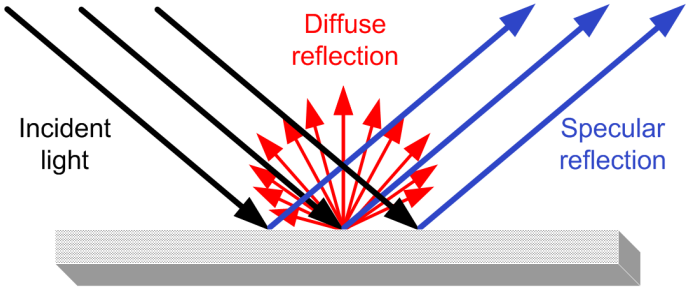

Figure 3.9 – Emission diagram of a regular surface.

In Chapter 1, this vulnerability of SM signals was introduced with the overview of **speckle** phenomenon (Fig.1.15). In our context, this source of disturbance can be further described by referring to Fig.3.9. Specular reflection happens when a beam from a single incoming direction is reflected into a single outgoing direction, like in a mirror or highly polished metal. Conversely, Lambertian or diffusing reflection corresponds to a uniform distribution of light energy in space. So, spatial-coherence destruction of the interferences is caused by interaction of the beam with the diffusive surface at two levels [106]. Many common materials present different levels of roughness, therefore they exhibit a combination of both reflections.

A rough surface illuminated by a laser beam can be seen as an infinite set of points emitting coherent light [107]. Due to interference phenomenon, the light intensity at any point in space depends on the optical path difference between the beams emanating from the emitting points of the illuminated surface. That is the reason behind the fact that speckle appears all the more important as surface roughness approaches the light beam wavelength.

Now, when a laser beam points continuously the target or when the target moves transversally, the spot scrolling results in a strong amplitude modulation or fading of the SM signal in small periods of time. Although SM effect has been used typically to measure micrometric displacements, the same principle can be extended to measure displacements of the order of several centimeters or even decimeters. However one must be aware of the increased probability of falling into speckle affected areas. The linear and transverse displacement measuring system proposed in [108] is a good example of centimetric displacement (up to 40 cm) reached without speckle by using a plane mirror target.

Recently three approaches have been presented *to overcome speckle* issue in the case of large displacements. First, in [109] an analysis of speckle effects related to the surface roughness and the laser beam spot size is presented. Fig.2 on that publication depicts a speckle affected SM signal from which different sections were parsed through a phase unwrapping method to calculate the corresponding C values. The large C value found in fading regions suggested a fringe loss condition, while in larger amplitude zones it resulted in smaller values.

One solution to overcome this issue consists to dynamically adjust the spot size of the

pointed laser beam. By using an ARTIC 416SL LL from Varioptic® with 80 ms of response time, their system proved autonomy by modifying the **position of the focal point** of the lens as a function of the SM signal amplitude. This can be seen as a non-mechanical variant of the Speckle Tracking (ST) system presented in Chapter 1.

The second solution also published in [109], consist in using a **sensor diversity technique** for a faster signal elaboration. Two LDs with different wavelength and spot size pointed to the same target resulting in different speckle pattern effects. By using a SNR calculation over the signals, the developed algorithm alternates the processing of the signals when fading or small amplitude occurs in one channel. The displacement reconstruction is done with a fringe counting algorithm.

In a pure algorithmic implementation (thus avoiding additional optical/electro-mechanical components), the proposal in [110] relies on **tracking the signal envelope** added by the speckle phenomenon. In Fig.3.10 the first part of the detailed algorithm up to the fringe detection step is depicted, for the sake of simplicity, the second part dealing with displacement reconstruction is presented as an abstract block. After a denoising low pass filter, a derivative of the SM signal is calculated. Then a search sliding window of a pre-calculated size n is used in order to account the local maximum and establish the upper and lower envelopes. By comparing the envelope amplitudes and retaining the greater values, a combined envelope is defined. This envelope is used to estimate local fluctuations in the SM signal not corresponding to a SM fringe. A second search sliding window is passed over the combined envelope in order to identify the deeply modulated SM fringes and then establish dynamic cut-off levels. Only those samples of the combined envelope with amplitude greater than this cut-off level are retained in the cut envelope and the rest of the samples is not considered for fringe detection. Finally, the fringe detection is defined by matching the first SM derivative points with the cut envelope values.

A drawback for an autonomous implementation of previous method is related to the correct definition of the window size. As indicated in the document proposal, an increase in either n or the rate of displacement can lead to omission of speckle modulated SM fringes.

3.2.2 Assessment of the adaptive threshold algorithm

The starting point for this study has been the *adaptive transition algorithm* proposal [65] validated for **preprocessed** signals in following scenarios comprising various lasers operating at different wavelengths:

- Simulated signal for different feedback values.
- Experimental signals from moderate to strong feedback.

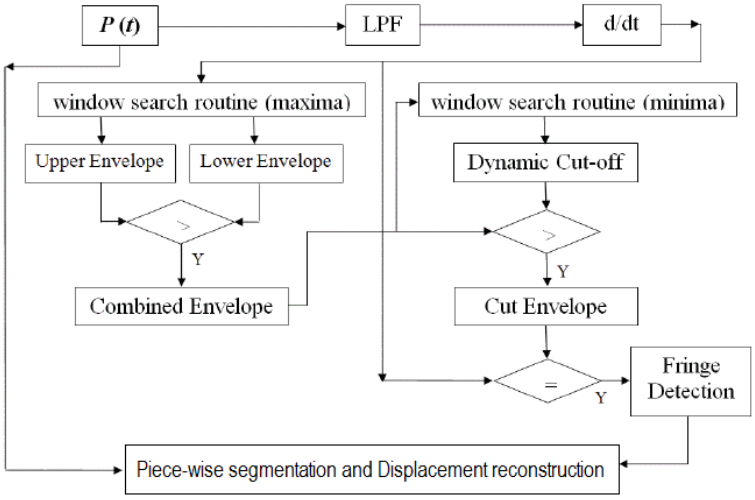

Figure 3.10 – Detail of the envelope extraction proposal.

- Experimental signal in weak feedback
- Defocused signal with different Signal-to-Noise Ratio.
- Random SM signal from a shock concrete pillar.
- Experimental transition-free signal from strong feedback.
- Experimental mixed moderate-strong feedback from a shock concrete pillar.
- Weak feedback in free space and within an optical plate.

From that work, the versatility to handle different levels of feedback based on autonomous decisions has been proved. Now, within the goal of validating its usage for a wide variety of applications, the concept of non-cooperative signals has been introduced. Notice that working with this kind of signals implies to deal with a dynamic change of C factor and, generally speaking, a random amplitude modulation. Therefore, the efforts on internals inspection presented next are focused in this use case without loosing the scope for an embedded implementation.

3.2.2.1 Iterative threshold

This procedure corresponds to pseudocode ALG.2, receiving a denoised and normalized SM signal. From it, the iteration criterion warranties this step to converge and thus making it suitable for autonomous implementation. Notice however that input data buffer is fully processed for each threshold step increase of 0.05, making difficult to fit time boundaries for a real-time embedded system.

```
Input: Denoised and normalized SM signal
Output: Phase transitions for SM>0
begin Calculate arcos and its derivative
    while False transitions do
        Transitions for varying threshold
        forall the input elements do
            if SM >0 then
                Check consecutive +/− transitions;
            end
        end
        if False transitions then
            Increase threshold by 0.05;
        else
            End loop;
        end
    end
end
```

Algorithm 2: Pseudocode for iterative threshold

Looking for robustness in case of non-cooperative signals, a use case has been proposed: A simulated SM signal for $C = 2$ and amplitude $6\lambda_0$ has been affected in amplitude with a sinusoidal wave as an attempt to illustrate degradations by speckle pattern found in real measurement environments. As depicted in Fig. 3.11(a), an initial low threshold serves to detect all the fringes in the signal even with amplitude variations. As already described, this low threshold needs to be incremented in order to avoid the obtained false transitions represented along the simulated signal.

Now, since original proposal increases the threshold for a set of acquired fringes. The problem of detecting different fringe amplitudes by a same threshold value rises again. This can be observed in Fig. 3.11(b), where the adaptive threshold algorithm failed to properly detect all SM fringes after converging in few iterations. This is explained because iteration condition only avoids false transitions, but it does so by settling a threshold which is not convenient for all the fringe amplitudes in the signal.

3.2.2.2 Moderate regime decision

Continuing with the proposed flow path, another particular example in moderate feedback regime has been proposed: the case when less than one period of expected target displacement is fed into the algorithm. In fact by sectioning the acquired SM fringes, it could be expected that previous case which fails to detect variable fringe amplitudes could be corrected. However, this algorithm requires a positive and negative part of a SM signal to work properly as demonstrated

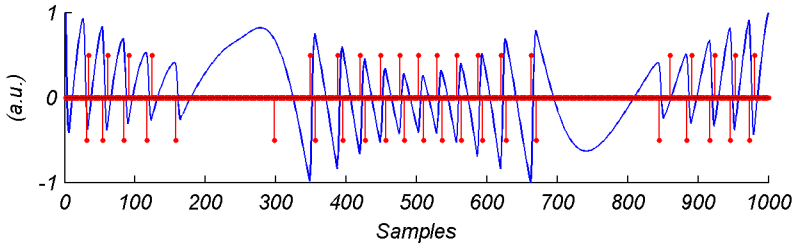

(a) Simulated SM signal corresponding to $6\lambda_0$ displacement and $C = 2$, threshold = 0.05.

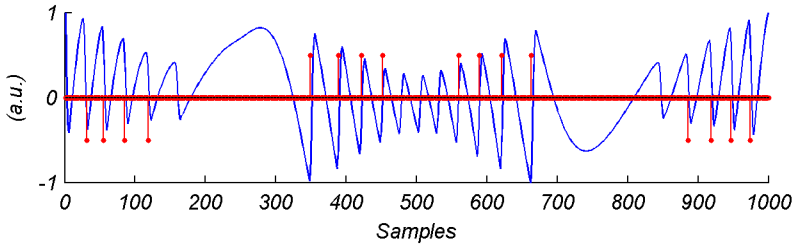

(b) Failure to detect transitions when signal amplitude is not constant.

Figure 3.11 – Simulated amplitude modulation over one period of SM signal.

next.

First, a simulated SM signal corresponding to $6\lambda_0$ and $C = 3$ has been properly processed in Fig.3.12(a). Initial low threshold of 5% first produced false transitions in P>0 segment, thus triggering a threshold increase of 5%. After 5 iterations (Threshold = 0.25) no more false transitions were observed in SM>0 section, thus transitions for SM<0 were removed. Prior to producing final transitions train, a cleaning procedure has been required to avoid spurious detections for samples surpassing this threshold.

A second test with same SM signal characteristics was carried. This time only one part of the SM signal was fed into the algorithm, the particularity of this segment is that it does not trigger the threshold increase for P>0 segment, i.e. the algorithm does not find false transitions for P>0. As a consequence, this segment in moderate feedback has been treated by the procedure defined for weak feedback, assigning wrong transitions as illustrated on Fig.3.12(c). Notice that this would be the acquired signal if the frequency of the moving target decreases relative to previous example.

3.2.2.3 Weak regime decision

Let us now present the path for processing signals in weak and very weak from the block diagram in Fig.3.5. The Humps based filter corresponding to ALG.3, relies in proper indexing of hump segments where the target changes its movement direction.

As feedback amount decreases, alternated positive and negative transitions are detected in

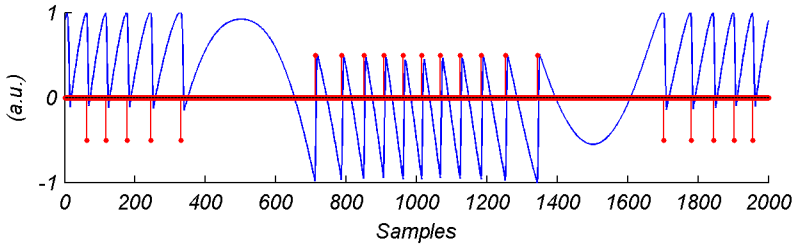

(a) Simulated SM signal corresponding to $6\lambda_0$ displacement and $C = 3$ along properly detected transitions.

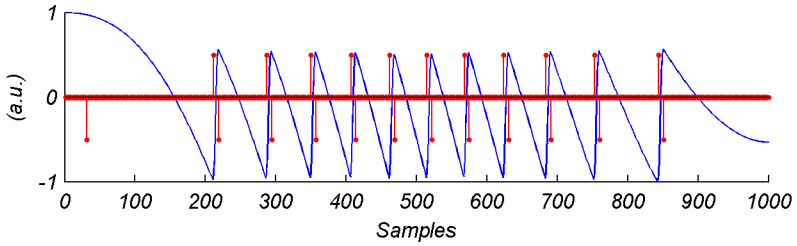

(b) A segment of previous SM signal with transitions for an initial threshold = 0.05.

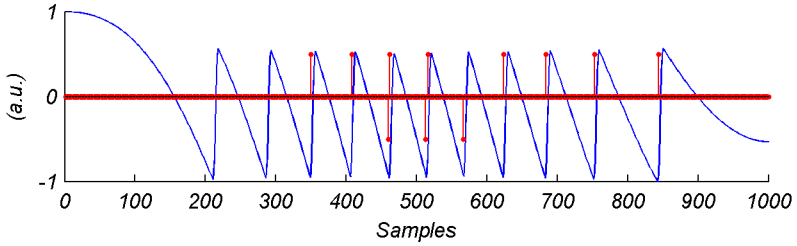

(c) A segment of previous SM signal with transitions assigned improperly.

Figure 3.12 – Use case where a moderate feedback is treated by the procedure defined for weak feedback.

```
Input: Denoised and normalized SM signal
Output: Corresponding phase transitions
begin Transitions for threshold = 0.45
    Clean spurious detections
    Isolate single humps and index them
    foreach detected transition do
        Count +/− before hump
        Count +/− after hump
        if Positive after > Negative after then
            Remove negatives in output vector for this region;
        end
        Repeat for negative
        if Positive after = Negative after then
            Observe sign of mid point in hump
            Remove corresponding sign in output vector
        end
        if Positive before = Negative before then
            Remove opposite remembered sign in output vector
        end
        Repeat if conditions for before region
    end
end
```

Algorithm 3: Pseudocode for humps based filter

major quantity. Conversely to duty cycle algorithm which measures a set of fringes to assign its corresponding direction, the adaptive algorithm makes use of symmetry property as criterion. In this way, segments divided by humps get assigned transitions for opposite direction. Notice however that this approach requires to clearly distinguish free fringe zones due to a direction change. Also the initial direction for a set of fringes must be asserted.

3.2.3 Assessment conclusion

This algorithm has been analyzed in order to be implemented as part of an embedded system. SM signals with fringes at different amplitudes has been considering to approach conditions usually observed in non-constrained environments.

The analysis carried by two simulated signals shows that at least one segment with P>0 and another with P<0 of the expected target displacement are needed for a correct processing. During this period, the signal shall not suffer amplitude variations to be properly processed. In case of weak feedback, hump segmentation to symmetrically filter out transitions implies that no spurious detections must be done prior to this step.

It is stressed the fact that such an algorithm has passed successfully extensive validations

with preprocessed signals. Despite its iterative nature, this algorithm can be part of an embedded system on the knowledge that memory and time constraint must meet at least one period of expected target displacement to measure. The observed dependence to prevent spurious transitions implies a considerable design effort to denoise and normalize SM signals from a real measurement. Based on these observations, it has been considered that adaptive threshold algorithm is more suitable for off-line signal inspection.

In the present manuscript we explore the path of avoiding external components to provide a development framework meeting requirement specifications in a straightforward manner and respecting real-time constraints. From the explored algorithmic solutions for robustness, frequency domain analysis seems the most effective way to exploit SM interferences without relying on the fringe shape. On the other hand, the usefulness of certain time-domain processing steps observed from previous analyzed algorithms suggests that a tradeoff can be reached between different domain solutions. To this end, an analysis on spectral characteristics of SM signals is presented next.

3.3 Spectral analysis of SM signals

In this section we aim to provide a practical interpretation of SM signals in terms of frequency characteristics rather than establishing a rigorous theoretical formulation. By further understanding the influence of feedback variations over different conditions of SM signals, it is envisaged to propose a signal processing allowing to deal with a variety of SM signals in a robust context.

3.3.1 Variations on feedback amount

In time domain, it is relatively easy to observe a difference between SM signals in moderate feedback regime characterized by a sawtooth shape, and signals in weak feedback describing a quasi-sinusoidal shape. To explore these differences in frequency domain, first the case of weak feedback has been observed by means of a simulated SM signal. Fig.3.13(a), corresponds to an acquired signal with sampling rate of 1 KHz from a target performing a constant forward-backward triangular movement at 1 Hz with peak-to-peak amplitude of 4λ. For simplicity only the first half of the signal is presented, i.e. a single direction with constant fringe frequency. The range of C was changed from 0.01 to 0.3 to observe its spectral evolution while keeping its characteristic quasi-sinusoidal shape.

The calculated periodogram [Fig.3.13(b)] of the power spectrum density (PSD) indicates the band-limited nature of weak feedback signals and its increased bandwidth with the increase

in C, also observed in [111]. For the given example, the detected frequency of SM fringes at 16 Hz and the subsequent even and odd harmonics distinguish thus the variation of pure sinusoidal to quasi-sinusoidal shape when the phase equation has one solution.

In a second analysis comprising the transition from weak to moderate feedback [$C = 0.7 \rightarrow 1.3$ in Fig.3.14(a)], the amplitude was increased to 6λ to obtain a major number of fringes within the period of the triangular target movement. The sampling frequency was also affected to 10 KHz obtaining an average of ≈ 416 points per fringe ($^{sampling}/_{fringe\,frequency}$). The estimated PSD was calculated using the *pwelch* Matlab® software function with a 50% overlap and a Hamming window of size 2^{10}.

The first observations from Fig.3.14(b) are the fringe frequency of 24 Hz, along the expected harmonics. Then, for C values going from 0.7 to 1.3 an increase of dB on the high frequency harmonics confirms its major impact over the shape of SM signal. This observation is in accordance with basic Fourier series theory which defines a sawtooth-like shape as an infinite sum of even and odd amplitude scaled sinusoids [112].

Finally, considering a moderate feedback with hysteresis phenomenon in Fig.3.15 for $C = 4$ along the previous simulated signal with $C = 1.3$. The calculated PSD decreased as the magnitude of the observed signal became reduced, while fringe discontinuities proper to a sawtooth shape became more evident. Notice however, that this apparent power reduction corresponds to the observed signal and not to a reduced amount of power. This will be detailed next with the presentation of hysteresis phenomenon.

From these signal analysis, a criteria to distinguish between weak and moderate feedback regimes could be based on observing the relative number of harmonics of the fundamental frequency from a small segment of SM signal. Such a classification shall help the decision of a particular signal processing as discussed in previous section or to trigger a stabilization procedure to keep stable a signal spectrum. This solution can meet a real-time constraint due to its simplicity of calculation, however the autonomy of such a solution will rely on a strict characterization of the possible spectral scenarios for the variations of a received SM signal.

3.3.2 Sawtooth signals and hysteresis

From the previous experience, the impact of hysteresis phenomenon on spectral behavior required further explanation. Let us remind that optical frequency of a LD might present multiple lasing modes as a function of feedback variations. This corresponds to the case $C > 1$ when phase equation presents multiple solutions. In practice, this can be observed by injecting a beam into a wavelength meter and observing an increase of peaks around the constructor's wavelength of a given LD. Among the multiple wavelengths, only one exits the optical cavity

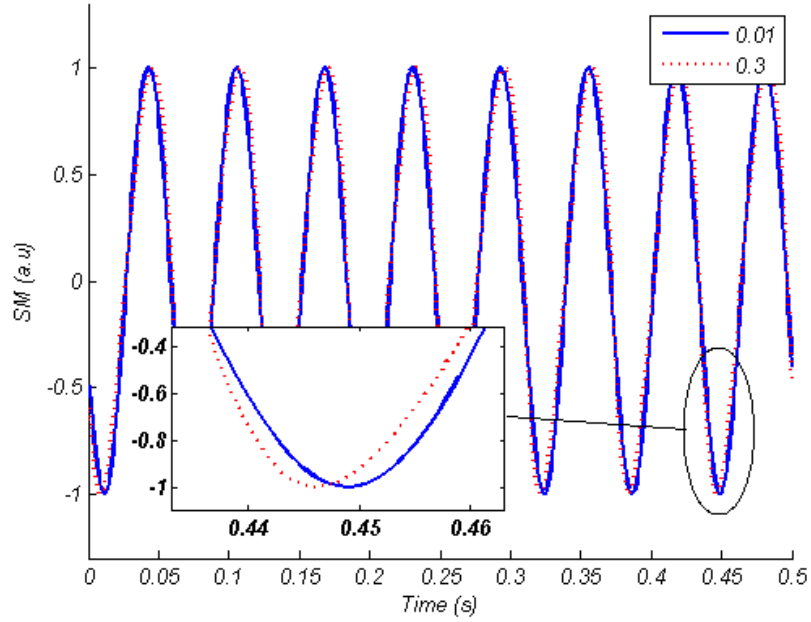

(a) Simulated SM with C=0.01 and 0.3 from a target at constant velocity.

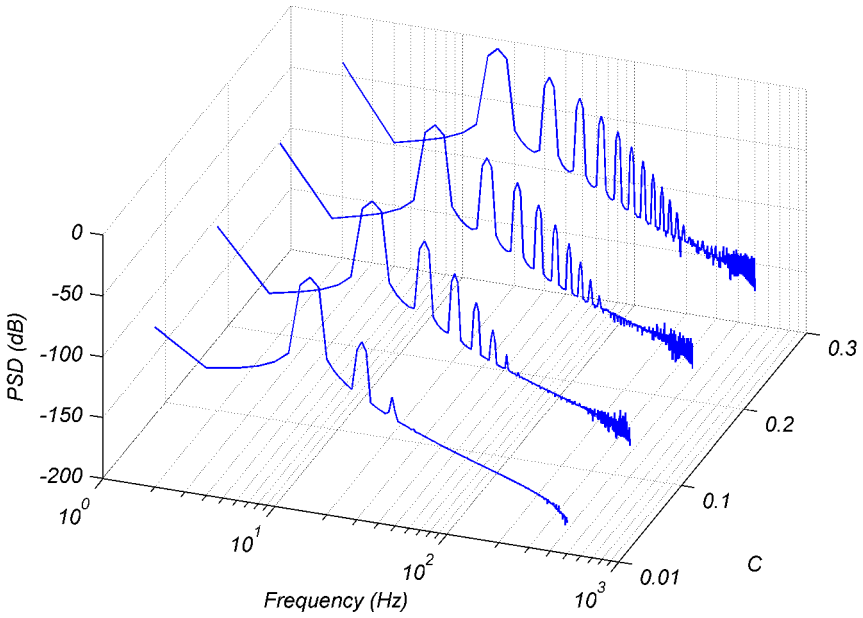

(b) Power spectral density for variations in C.

Figure 3.13 – Harmonics increase in weak feedback regime for constant velocity.

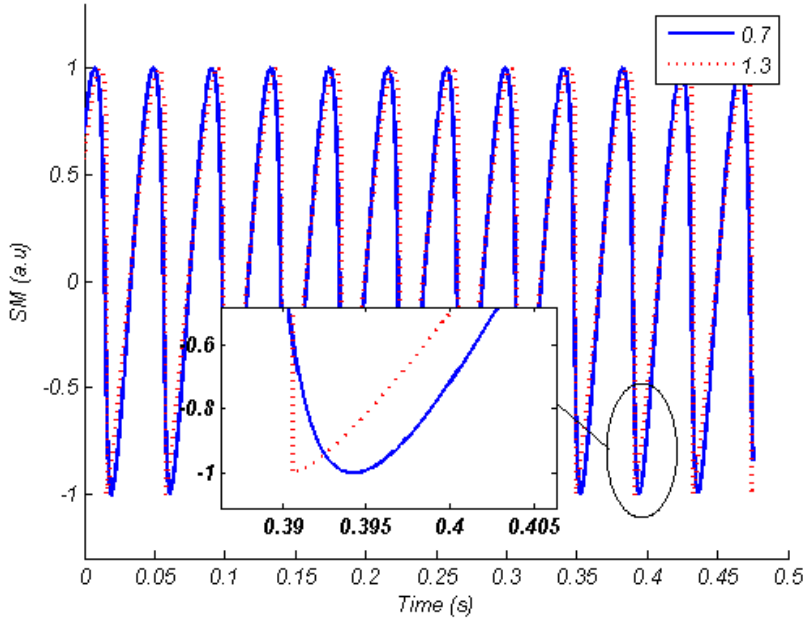

(a) Simulated SM with C = 0.7 and 1.3 from a target at constant velocity.

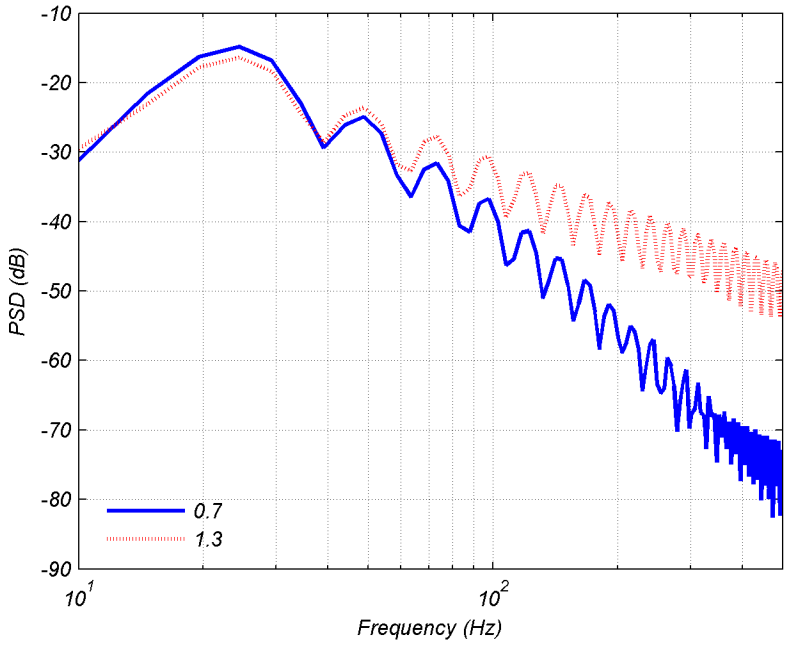

(b) Power spectral density for a variation in C.

Figure 3.14 – Harmonics increase from weak to moderate feedback regime for constant velocity.

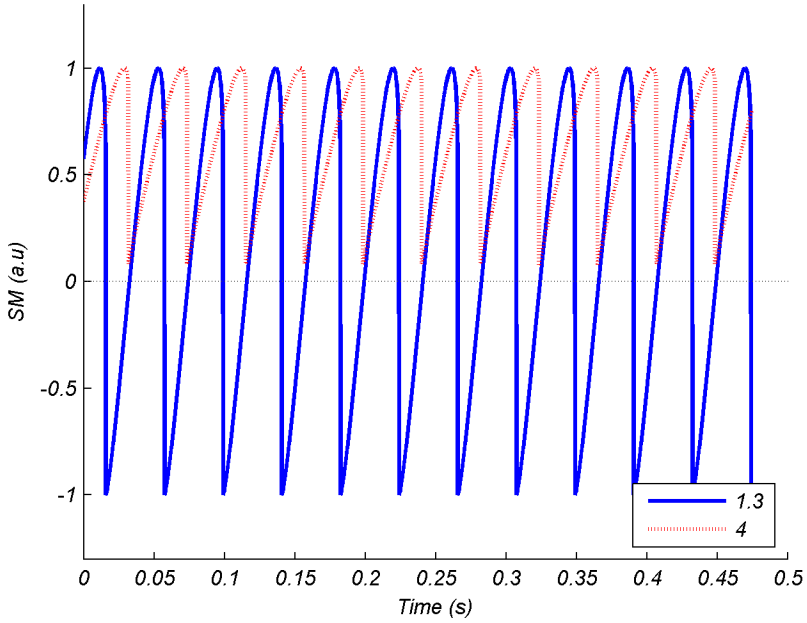

(a) Simulated SM with C = 1.3 and 4 from a target at constant velocity.

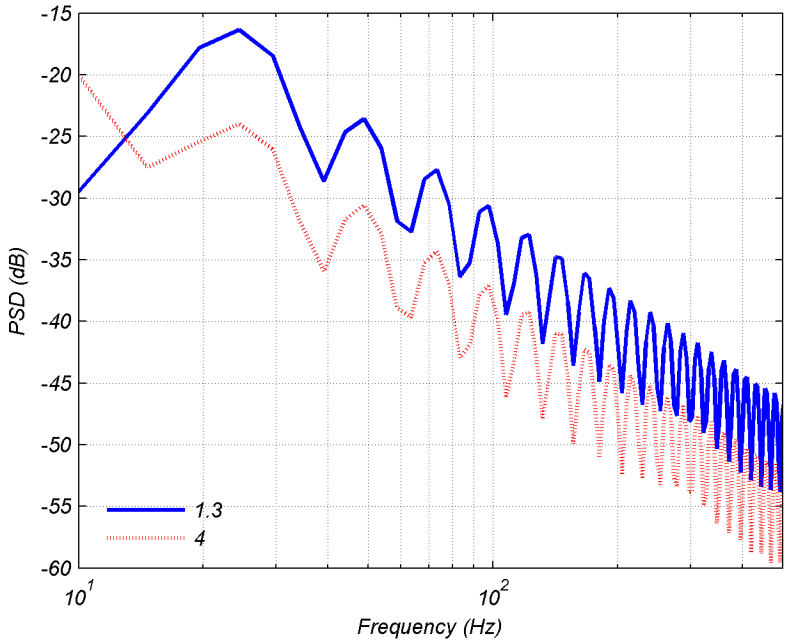

(b) Power spectral density for a variation in C.

Figure 3.15 – PSD decrease at moderate feedback due to hysteresis phenomenon for constant velocity.

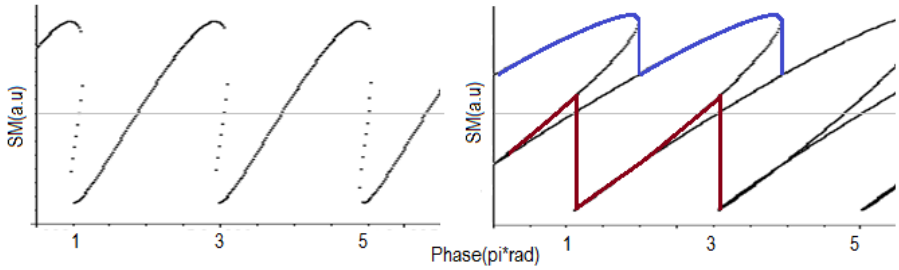

Figure 3.16 – Transition from a sawtooth-like signal to hysteresis affected signal.

at a time meaning that the obtained SM signal presents physical discontinuities on its elaboration.

This phenomenon is depicted in Fig.3.16, on the left a SM signal without hysteresis is increased in the amount of optical feedback by increasing the reflectivity of the pointed target. On the right, the SM signal is elaborated by the sharp switching between periods producing the hysteresis phenomenon. Notice that depending on the increase or decrease of the laser-to-target distance, jumps happen in the upper or lower section of the signal and the amplitude of SM fringes varies. This behavior also explains the rounded and sharpened peaks observed while acquiring a full period of a harmonic movement of a target.

Recently, [113] performed a detailed analysis on the discontinuities obtained from the steady-state equations used to describe the behavior of SM signals. By carefully controlling the round-trip time, reflectivity and bandwidth of the acquired signal, their experiment showed high-frequency damped oscillations where the steady-state model predicts points of discontinuity. Furthermore, by considering a dynamical model of the feedback LD equations, a numerical solution allowed them to draw an abacus giving the oscillations period and decay time for these oscillations versus round-trip time and reflectivity of the setup. Two relevant observations can be taken from this study: it means that target distance and reflectivity can also be estimated from the same SM signal typically used to retrieve the target movement, it also confirms the physical behavior of a sawtooth-like SM signal elaboration.

3.3.3 Time-frequency analysis of SM signals

Conversely to conventional velocity measurement where constant Doppler frequency intervals are assumed, usually in harmonic displacement retrieval each fringe has a slightly different frequency. Therefore, methods based on the integration of a beat frequency present an inaccuracy relative to the window size used to perform the spectral analysis. The discrete Fourier transform (DFT) used for the spectrum analysis requires thus a localized temporal resolution in order to provide a qualitative observation. We have used instead, a short time

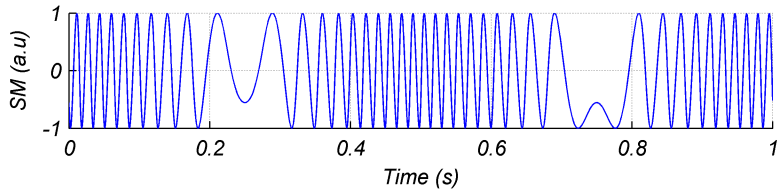

(a) Simulated SM with $C = 0.2$ from a target performing sinusoidal movement.

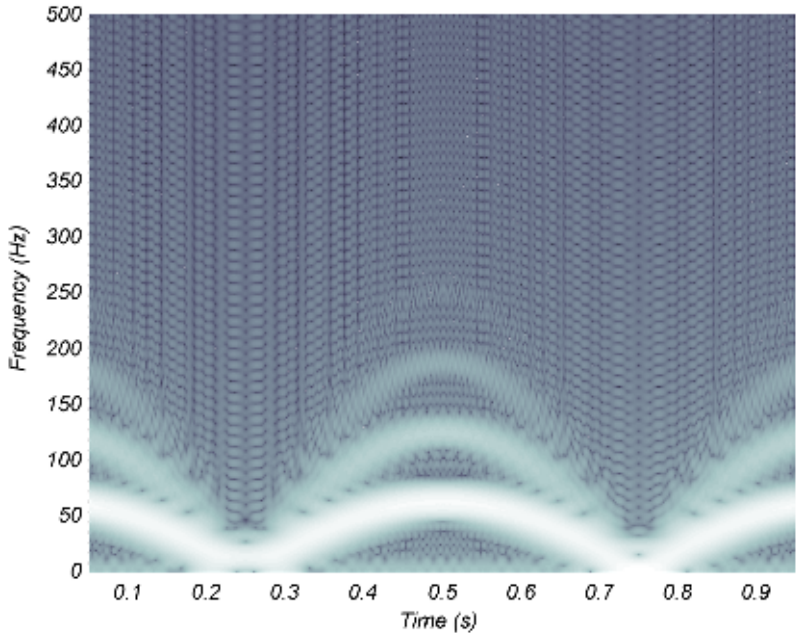

(b) Spectrogram for a sinusoidal movement and weak C.

Figure 3.17 – The varying fringe frequency relative to target movement can be identified in weak feedback regime.

Fourier transform (STFT) to perform the analysis of weak and moderate feedback signals for variable velocity taking care of the well known compromise between time and frequency resolution depending on the window size.

In Fig.3.17(a), a simulated SM signal with $C = 0.2$ corresponding to a sampling rate of 10 KHz from a target performing a sinusoidal movement with peak-to-peak amplitude of 10λ and a period of 1 second is considered for this analysis. For an average of 250 points per fringe, the spectrogram using STFT and a relative small window is calculated in Fig.3.17(b). The humps corresponding to a direction change are observed at 250 and 750 ms respectively. Notice that the maximum frequency of 60 Hz at 500 ms corresponds to the highest tone from the input signal and at least two of its harmonics can be clearly observed at 120 Hz and 180 Hz respectively. The harmonics for the side frequencies present a more important vanishing as a result of multiple interferences on the spectrum.

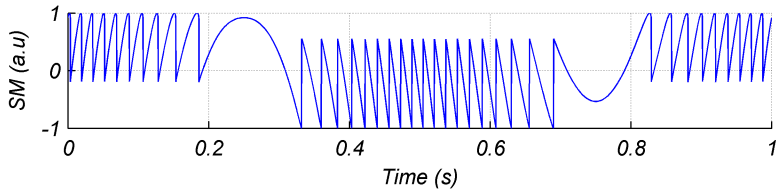

(a) Simulated SM with $C = 3$ from a target performing sinusoidal movement.

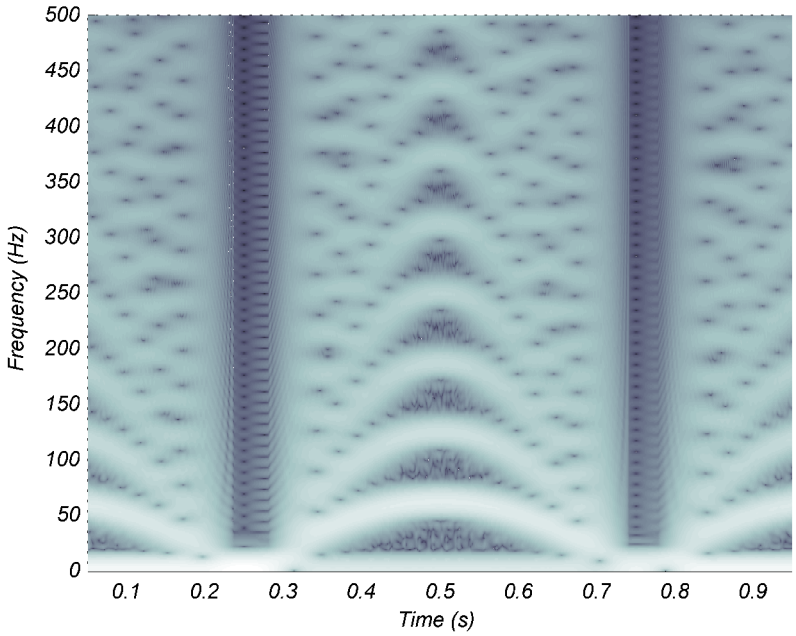

(b) Spectrogram for a sinusoidal movement and moderate C.

Figure 3.18 – Harmonics increase in moderate feedback regime plus the varying fringe frequency relative to target movement.

Consider now, Fig.3.18(a) where a simulated SM signal with $C = 3$ corresponding to a sampling rate of 10 KHz from a target performing a sinusoidal movement with peak-to-peak amplitude of 10λ and a period of 1 second is considered for this analysis. For the same previous parameters except feedback value, the spectrogram is calculated in Fig.3.18(b). Again, the humps corresponding to a direction change are observed at 250 and 750 ms respectively. However, even if the maximum frequency of 60 Hz at 500 ms can be easily observed, the harmonics above the presented range were meaningless due to the important vanishing as a result of multiple interferences on the spectrum.

Chirp SM signals obtained from a variable target movement require careful analysis due to the broad spectrum obtained from the influence of harmonics at each frequency instant. While sawtooth-like signals from moderate feedback are the preferred time-domain processing due to its simplicity of detection, in frequency-domain they are undesirable if a simple filtering

approach is wanted to extract its features.

3.3.4 Generalities on instantaneous frequency

To introduce the motivation of this subsection, it is worth to quote Boashash [114] from his work on instantaneous frequency: "Nonstationary signals in particular do not lend themselves well to decomposition into sinusoidal components. For such signals, the notion of frequency loses its effectiveness, and one needs to use a parameter which accounts for the time-varying nature of the process. This need has given rise to the idea of instantaneous frequency (IF)". For the previous analyzed case of chirp SM signals affected by harmonics resulting of a high feedback value, further concepts like instantaneous phase and amplitude aim to account the nature of this signal.

It must be stressed that instantaneous frequency concept has not been fully embraced since its early proposal by Carson and Fry in 1937 and formalized by Van der Pol in 1946, as the apparent inconsistency of associating the terms instantaneous and frequency [114]. Demonstrations on failing conditions over very specific signals can be found in literature (e.g. [115]). Conversely, there are many other recent researches that took advantage of the utility of this concept and its computation, proposing improved tools to perform time-frequency analysis over signals [116].

In general terms, IF is understood as the rate of change of phase angle at a given time. i.e.:

$$IF = \frac{1}{2\pi}\frac{d\phi(t)}{dt} \tag{3.1}$$

With the introduction of the concept of analytic signal from Gabor in 1946 (see [117] for historical background), a conventional approach is to calculate the Hilbert transform (HT), in order to generate a unique analytic representation in the complex plane of the data. Prior to a further definition of HT, let us introduce the concepts of envelope and instantaneous phase related to IF.

Considering a simple harmonic motion $s(t) = a \cdot \cos(2\pi f t + \theta)$, with $\phi(t) = 2\pi f t + \theta(t)$. Its analytical signal is $s(t) = s(t) + jy(t)$, with $y(t)$ called quadrature signal for being out of phase by $pi/2$ from $s(t)$ in the complex plane. The representation of the analytical form in polar coordinates is $z(t) = a(t)e^{j\phi(t)}$, where the instantaneous amplitude or envelope is defined by:

$$a(t) = \sqrt{s^2(t) + y^2(t)} \tag{3.2}$$

and the instantaneous phase:

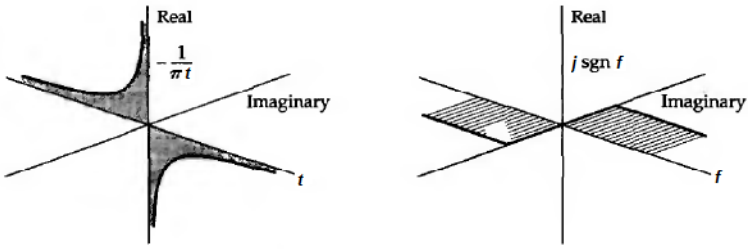

Figure 3.19 – Representation of Hilbert kernel in time and frequency domains.

$$\phi(t) = \arctan(\frac{y(t)}{s(t)}) \tag{3.3}$$

On its simplest concept, Hilbert transform $\mathcal{H}$ can be represented as a filtering process between the kernel $(-\pi t)^{-1}$ and the signal $s(t)$ of interest i.e. [118]:

$$\mathcal{H}[s(t)] = \frac{-1}{\pi t} * s(t) \tag{3.4}$$

Expressed in frequency domain via Fourier transform $\mathcal{F}$:

$$\mathcal{F}\{\mathcal{H}[s(t)]\} = j \cdot \text{sgn}(f)\mathcal{F}\{s(t)\} \tag{3.5}$$

where $sgn(f)$, the *signum* function is defined as 1 for positive frequencies, -1 for negative frequencies and null at zero as depicted in (Fig.3.19). Therefore, it can be presented as a mathematical tool allowing to represent a signal on its analytical form by performing a 90° phase shift of the original signal over the orthogonal plane without modifying its amplitude.

3.3.5 Instantaneous phase calculation of SM signals

Based on the potential observed from instantaneous frequency theory and its intrinsic relationship with phase calculation, it was decided to test the impact over SM analysis in the quest for robust signal processing.

The well accepted PUM described in Chapter 2 relies on the rough phase calculation $\widehat{x_F}$ via an *arccosine* function over a normalized SM signal $[P`(t)]$ of Eq.(2.4). It is reminded that PUM was originally proposed to work for moderate feedback due to the simplicity of peak detection and the unambiguity of fringe direction retrieval. Also, accounting the precision error observed by [119] as well as the previously described possibility to increase its usage for weak feedback [65]. It can be guessed that further improvement on SM exploitation might come from estimating its phase differently. Even if the usage of *arccosine* function (which returns the angle whose cosine is the given SM sample) is mathematically correct for a rough phase calculation,

it makes more sense in the case of weak feedback when the fringe shape is quasi-sinusoidal, rather than for sawtooth-like SM signals.

Figure 3.20 presents a comparison of instantaneous phase calculation against conventional calculation proposed in PUM for the representative simulated signals in weak and moderate feedback used in previous section [Fig.3.17(a) for $C = 0.2$ and Fig.3.18(a) $C = 3$ respectively]. By virtue of Eq.(3.3) it has been possible to calculate the instantaneous phase in modulo 2π within the range $(-\pi,\pi]$ via the four-quadrant *arctan* function (arctan2), which is a variant of the trigonometric function *arctan* allowing to distinguish diametrically opposite directions from the input vectors for unambiguous results.

Comparing the calculated phase via *arccos*, SM maxima points [-1 1] agree [π 0] respectively. In the case of weak feedback [Fig.3.20(a) for $C = 0.2$] a *triangular* shape is obtained, while for moderate feedback [Fig.3.20(b) for $C = 3$ and beyond] a marked discontinuity can be identified as result of the proximity of maxima points in the sawtooth-like shape. This explains better why PUM algorithm is intended to work mainly on moderate feedback using a thresholded derivative for positive and negative peak detection. Considering the calculation made by the arctan2 function, it can be observed a major simplicity to interpret fringe phases in the case of weak feedback by using a single fixed threshold. In case of moderate feedback, the need for further detection processing is evident as the calculated phase is not constant in amplitude. However it can be observed a wrap pattern associated with hysteresis phenomenon.

To look further into phase calculation over the 2π interval provided by *arctan2* function, in Fig.3.21(a) a simulated SM signal with C=7 and same characteristics as previous two examples has been used for evaluation (10 λ displacement). From this example, it can be noticed that *arccos* calculation produced a mirrored phase mapped version of the input signal for moderate feedback. By using *arctan2* function, hysteresis phenomenon confirms an increasing offset causing a wraparound of instantaneous phase values [Fig.3.21(b)]. However, it has been observed that by calculating the **absolute value of this instantaneous phase**, same discontinuity points can be observed with both procedures [Fig.3.21(c)]. This means that *arccos* and *abs(arctan2)* may lead to similar results for transition detection from a rough phase estimation. Notice that input SM signal needs to be normalized prior to the former procedure, while the analytical calculation is required for the later procedure.

Since both phase calculations can produce comparable results at different feedback values, further analysis has been required to evaluate their behavior face to signal amplitude variations to approach a real scenario. In this condition, acquired signals are not initially normalized and are prone to externally induced variations. To this end, a simulated SM signal also for a 10λ displacement but with $C = 1$ was used. It has been combined with a sinusoidal signal of unitary

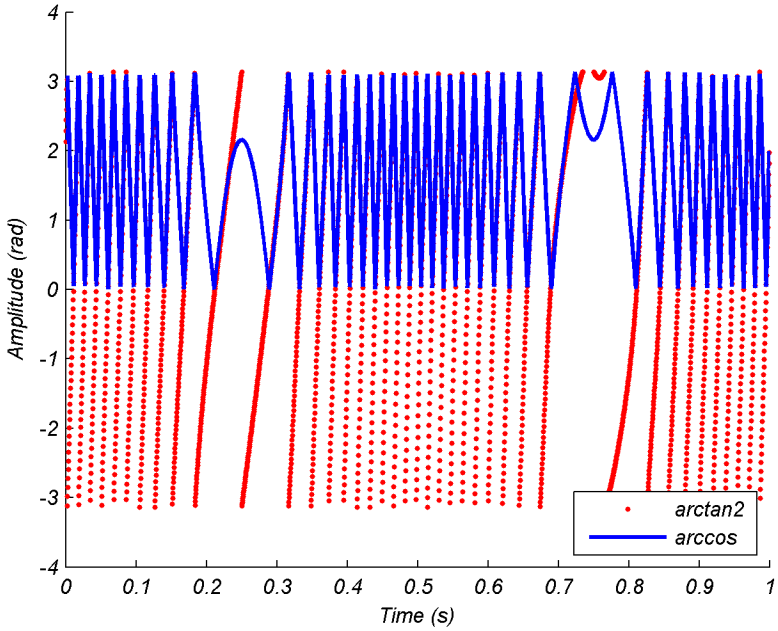

(a) Comparison of phase calculation for the SM signal in Fig.3.17(a) for $C = 0.2$.

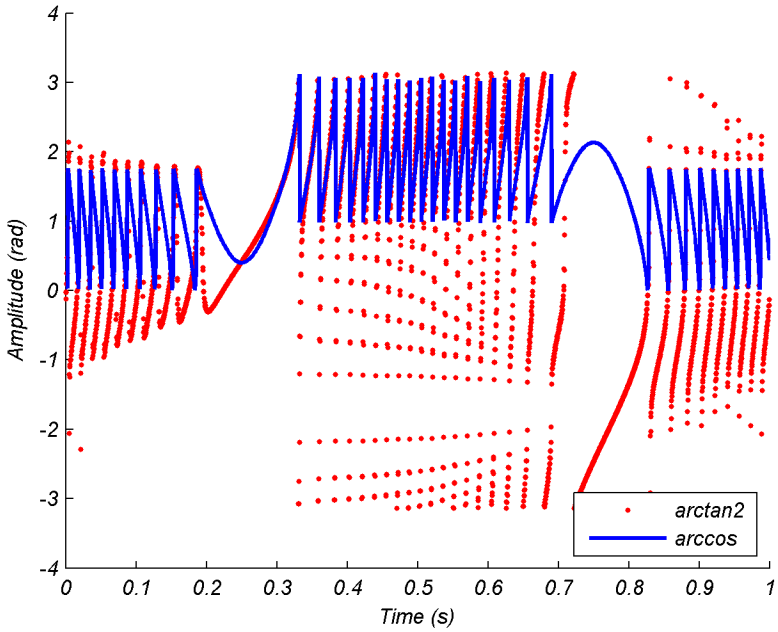

(b) Comparison of phase calculation for the SM signal in Fig.3.18(a) for $C = 3$.

Figure 3.20 – PUM method provides one fringe discontinuity in moderate feedback, while arctan2 shows a simplicity to interpret fringe phases in weak feedback.

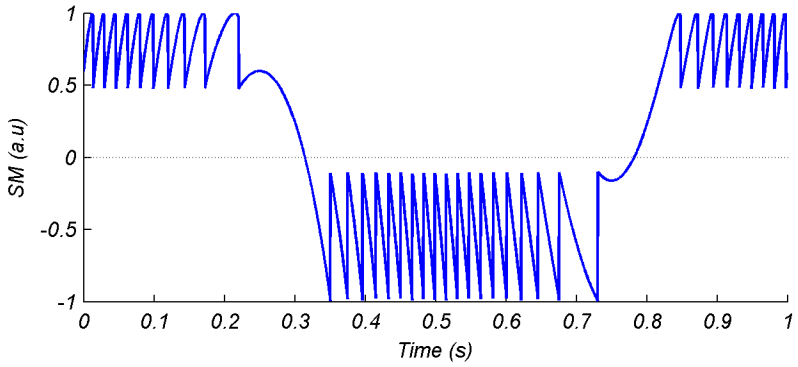

(a) Simulated SM signal with $C = 7$ and 10λ displacement.

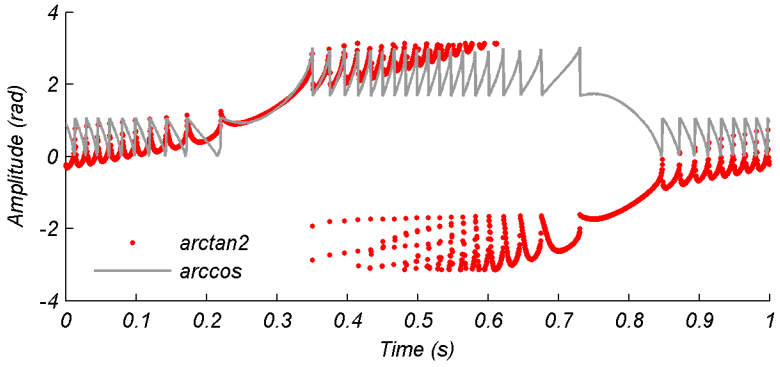

(b) Comparison between phase calculation by arctan2 and *arccos* function.

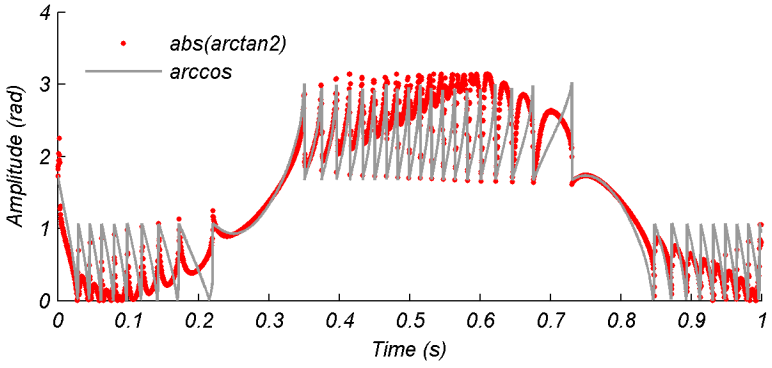

(c) Comparison between absolute phase calculation by arctan2 and *arccos* function.

Figure 3.21 – Using the absolute value of a calculated instantaneous phase provides similar results to conventional phase calculation.

amplitude and 0.25 Hz of frequency, providing amplitude modulation to the SM chirp signal [Fig.3.22(a)].

Again, using the conventional calculation by *arccosine* function shows a mirrored phase mapped version of the input signal [Fig.3.22(b)]. Therefore, a thresholded derivative might require a very low value to properly detect the SM fringes. Conversely, absolute phase calculation by proposed arctan2 function is not affected by amplitude variations as depicted in Fig.3.22(c). Notice that this simulated signal illustrates just a segment of fringe amplitude variations, however this condition might happen with speckle phenomenon at any time. This interesting result, allows to observe that using the analytic SM signal for instantaneous phase calculation results in improved calculations face to *arccos* procedure typically used for thresholding detection.

3.3.6 Discussion on spectral analysis

The spectral analysis carried in this section provides increased confidence on SM signals behavior notably in terms of processing complexity. A qualitative criteria to discriminate between weak or moderate feedback signals is related to the relative number of harmonics and its strength observed for a single fringe frequency. Therefore if such classification is required to develop convenient signal processing, time-based analysis can be complemented by observations in frequency domain.

Creating the analytical form of SM signals via Hilbert transform may lead to further formalism, in this manuscript it has been covered as a practical implementation to track frequency variations over the time. This results in a different approach from the conventional analysis based on sliding short time Fourier transforms which has also been presented here.

Using absolute values of instantaneous phase calculation provides equivalent results than PUM for both feedback levels, with the added value of removing the normalization step required for *arccos* calculation. Improved performance is observed face to amplitude variations over SM signals as it works with orthogonal signals.

In the case of speckle affected signals where feedback coupling variations affect the shape in time of the fringes, a fixed threshold could be used for a fringe detection algorithm in the range of very weak feedback up to $C \approx 1$. Furthermore, a convenient projection over the range $(-\pi,\pi]$ can be exploited to avoid ambiguous fringe detection happening with *arccos* for non sawtooth-like signals.

In the case of hysteresis affected signals, the extended projection results in a wraparound that needs to be corrected for a proper phase interpretation. Indeed by fixing this issue, it can be expected to increase the feedback range covered by a fringe detection algorithm with fixed

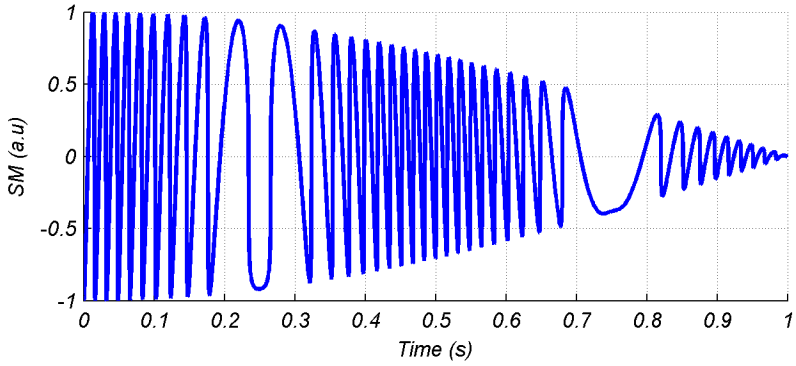

(a) Simulated SM signal for $C = 1$ with amplitude modulation.

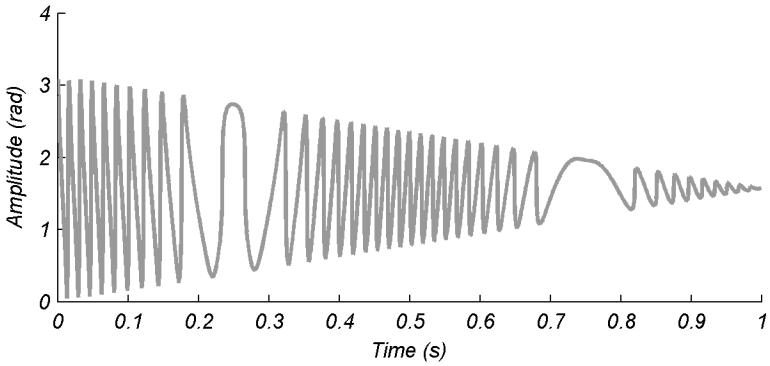

(b) Phase calculation using *arccos* function confirms mirrored phase mapped version of the input signal.

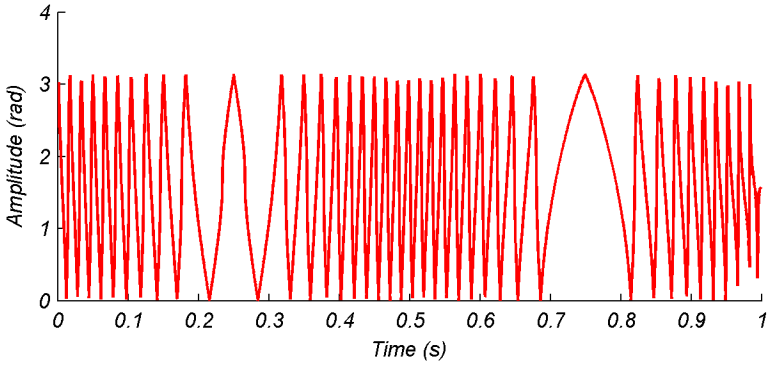

(c) Absolute phase calculation using *arctan2* function is not affected by amplitude variations of the input signal.

Figure 3.22 – Comparison between instantaneous phase calculation and typical phase estimation by *arccos*.

threshold simplifying thus this task. After many attempts, the algorithmic effort to correct this wrap around resulted worthless. However a promising strategy consist in locally removing hysteresis offset. This is detailed in next section as a consolidated generic fringe detection algorithm.

3.4 Real-time generic detection of SM fringes

Just like in the case of displacement reconstruction, the idea of having a generic fringe detection algorithm seems an attractive solution to increase the scope of SM applications. Based on the different analysis of SM exploitation methods presented in this manuscript and the signal processing robustness exposed in previous section, a relatively straightforward algorithm is proposed to find SM fringes of a wide variety of feedback levels. The proposal relies on time-domain peak detection from a frequency-domain calculation of the instantaneous phase of a SM signal. It is intended to produce a train of detected phase transitions with proper target direction information, suitable to meet time boundaries and deterministic behavior for a real-time implementation.

In order to reproduce the motion of a pointed target, in this work it shall be finally coupled with previously proposed DAC based method (2.3) in next chapter. In this section, the algorithm internals are presented followed by a validation and comparative against the previously analyzed adaptive threshold algorithm.

3.4.1 Algorithm proposal

An overview of this algorithm is presented with the block diagram of Fig.3.23. After an analog-to-digital conversion, a denoise procedure is proposed in order to provide SM fringes with reduced influence of high frequency noise. It is followed by an offset removal step which allows to compensate hysteresis phenomenon by locally approaching a zero-mean of the acquired signal. Notice that such a procedure has impact over hysteresis affected signals and has no influence over the rest of situations were the feedback value is lower. This allows to keep the generic approach by having a zero-mean signal $P_z(n)$ for subsequent steps.

The analytic elaboration is the procedure allowing to calculate the instantaneous phase of a SM signal by providing a representation in quadrature of the fringes $P_a(n)$. According to

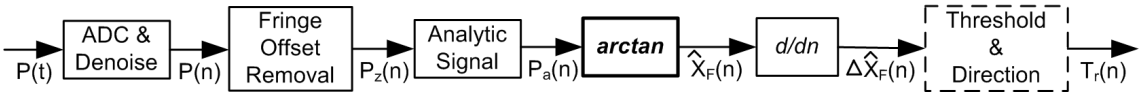

Figure 3.23 – Proposed algorithm for SM fringe detection.

previous discussion on spectral analysis, *arctan2* calculation results in a more robust phase observation as compared to conventional *arccos* function. Then, performing the derivative of this signal allows to observe peak frequencies for fringe discontinuities.

The thresholded detection scheme along direction assignation, produce a train of positive and negative transitions $T_r(n)$ serving as the required input of DAC algorithm for displacement reconstruction. It is stressed the fact that individual algorithm blocks are prone to implementation modifications for meeting specific performances, while the global algorithm structure remains valid for broad SM signal conditions.

3.4.1.1 Analog-to-digital conversion and Denoise

In order to keep the generality of current algorithm, specific requirements for an analog-to-digital conversion have been left out of scope of this research proposal. However this requirement, common to many instrumentation dealing with analog signals, will be discussed in the section of design considerations of next chapter.

Starting with an input SM signal in digital form, a denoise block has been used over raw experimental signals. (i.e. observed fringes without a particular acquisition filtering process). This block consists in performing a simple moving average filter over an acquired signal segment $SM_{in}(n)$ as follows:

$$SM(n) = \frac{1}{span} \sum_{j=0}^{span-1} SM_{in}(n+j) \tag{3.6}$$

The size span has been established as a small percentage of the estimated average fringe size within a processing window (e.g. 10%). This experimental setting is based on the idea of removing spurious derivative peaks of high frequency spikes in the signal, without strongly affecting the fringes' shape. To illustrate this procedure, an experimental signal has been acquired from a target rotating at constant speed (to be detailed later). As depicted in Fig.3.24 spurious peaks can be found over the fringes in uncontrolled conditions as SM signals are highly sensitive. The described denoise procedure has allowed to keep a generic validation approach of the proposed fringe detection algorithm. Even if such a calculation is feasible for real-time implementation, it is not properly considered as part of this algorithm since it can be removed for a well defined application as discussed.

3.4.1.2 Fringe offset removal block

It has been already shown that analytic SM signals allow to use a unique phase calculation over different feedback conditions, from weak to moderate, including amplitude variations

[Figs. 3.20(a) and 3.22 respectively]. However, feedback range became limited by hysteresis phenomenon as it affects the zero-mean of signals under analysis. In this context, eliminating hysteresis offset becomes an evident need.

As a first thought, zero-cross detection seems a reasonable solution to distinguish hysteresis affected signals and perform a convenient processing. However, strong speckle phenomenon also affects zero-crossing of fringes (as shown experimentally in Chapter 1, Fig.1.15 of this manuscript), thus leading to potential feedback misinterpretations. With the intention to keep a unique processing, our proposal relies into a local fringe's bias offset subtraction.

A common approach to reject this bias offset, is to estimate a bandpass filter preventing low signal fluctuations as well as high frequency noise components. To increase the researched versatility, a self-adapting nature is more convenient. The implementation that has been retained for handiness, consist in a running average filter whose kernel generation is triggered by pseudo-fringes boundaries. The detection of these pseudo-fringes obeys an auto-calculated threshold as explained hereafter.

Let us utilize two simulated signals side by side denoting same processing conditions. The representative feedback values are $C = 0.5$ [Fig.3.25(a)] and $C = 3$ [Fig.3.25(b)], for a SM signal from a sinusoidal target displacement of amplitude 5λ and 1 Hz of frequency.

As already presented along this manuscript, a common technique for raw fringe discontinuities observation, consists in performing a derivative of incoming SM samples. The resulting signal presents peaks of different magnitudes as can be observed in Fig.3.25(c)(d). Since the intention so far is to define **trigger points** for fringe detrending, a threshold point is settled between the root-mean-square (RMS) value and the maximum sample value in the acquired window.

The points outside the established threshold are referred as pseudo-fringes, since they do not make the whole researched transition train. These identified peaks help to reset the calculation of the running average filter aiming to approach a zero-mean SM segment. From Fig.3.25(e)(f) it can be observed the usefulness of performing this operation even for a set of fringes that have not been covered by the threshold.

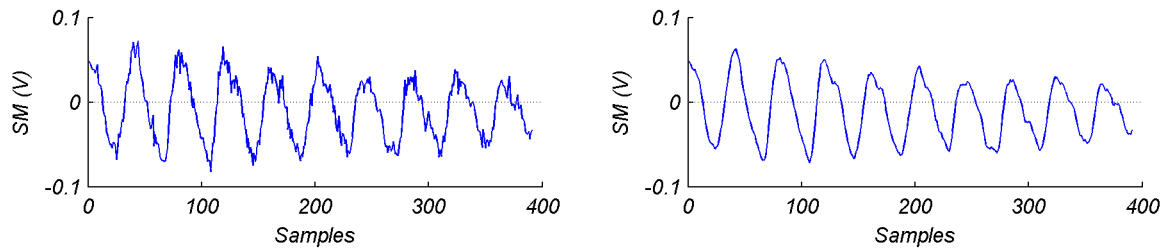

Figure 3.24 – Illustration of denoise procedure used over raw experimental signals.

Finally, by subtracting the running average to the original SM signal only biased fringes are expected to be adjusted. This minimizes the impact over non-biased fringes and avoids the need to distinguish hysteresis affected signals as depicted in Fig.3.25(g)(h). It is important to highlight the importance of pseudo-fringe points, since zero-mean fringes could be produced improperly and thus affecting the overall performance of the algorithm.

3.4.1.3 Analytic SM signal elaboration

When the shape of SM fringes does not present a sawtooth-like shape, direction exploitation of SM signals becomes more difficult. The lack of a reference arm in a basic SM configuration becomes evident as compared to classical interferometers. In literature there can be found proposals to exploit SM with increased robustness by using an orthogonal laser beam emission. For example, [120] used an off-the-shelf two-mode frequency stabilized HeNe laser to observe SM interferences. The horizontally polarized beam was used as reference, while the vertical beam was pointed to a moving target to finally recover the signal by an external photodiode. Also, using a Zeeman-birefringence dual-frequency laser, [121] reported a $\pi/2$ phase delay obtained when two orthogonal emitted beams are fed back into the laser cavity. By using this phenomenon, a displacement sensor has been proposed with an ease of direction discrimination from a mirror target.

Creating the analytic form of a SM signal can be seen as a means to provide further information aimed to simplify its exploitation. Referring to section 3.3.4, the formulation to obtain a SM signal in analytic form P_a can be stated as:

$$P_a(n) = P(n) + \mathrm{Im}\{\mathcal{H}[P(n)]\} \tag{3.7}$$

where $\mathcal{H}$ is the Hilbert transform of the SM signal placed in the orthogonal plane. According to Eq.(3.5) and in order to keep the system's real-time adaptability, the implemented frequency-domain technique to calculate the discrete analytic form of a SM segment with length N is [122]:

$$P_a(n) = IFFT \begin{cases} 2.FFT(P(n)), & n = (0, N/2 - 1) \\ 0, & n = (N/2, N - 1). \end{cases} \tag{3.8}$$

To illustrate different calculations of analytic SM signals. In Fig. 3.26 and 3.27 a sinusoidal displacement of amplitude 4λ has been used to simulate SM signals at increasing feedback levels. Fig.3.26(a) corresponds to the calculation of half period of displacement for weak feedback with $C = 0.2$. The bottom projection corresponds to the real axis of SM fringes describing the almost sinusoidal shape proper to this regime. Then, Fig.3.26(b) presents a waveform also in weak feedback, but for $C = 0.9$. While its projection does not show a

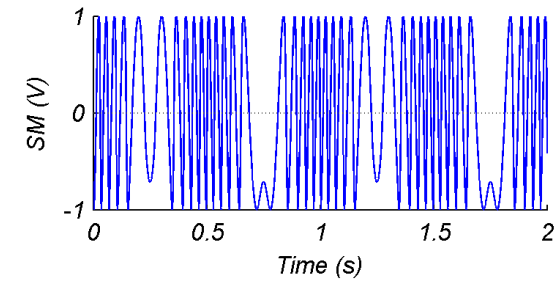

(a) Simulated SM signal with $C = 0.5$.

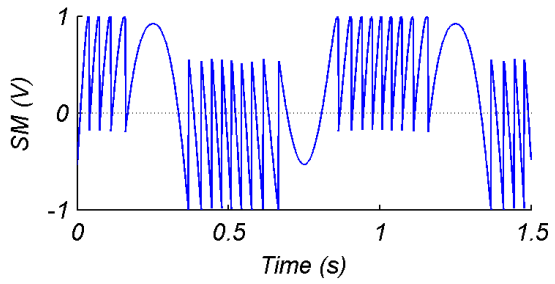

(b) Simulated SM signal with $C = 3$.

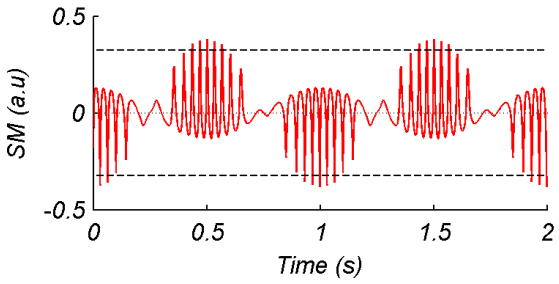

(c) Fluctuation threshold for $C = 0.5$.

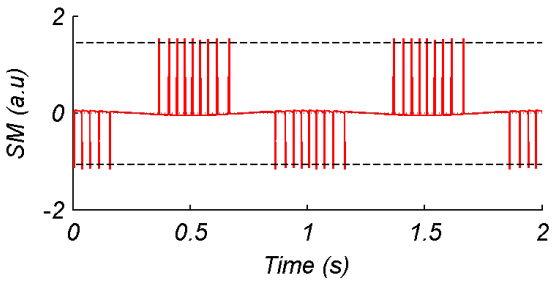

(d) Fluctuation threshold for $C = 3$.

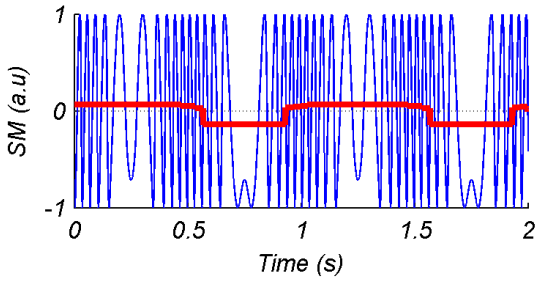

(e) Running average for $C = 0.5$.

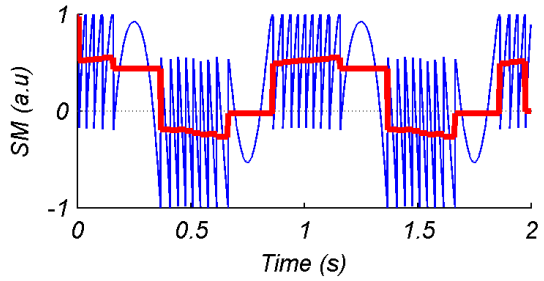

(f) Running average for $C = 3$.

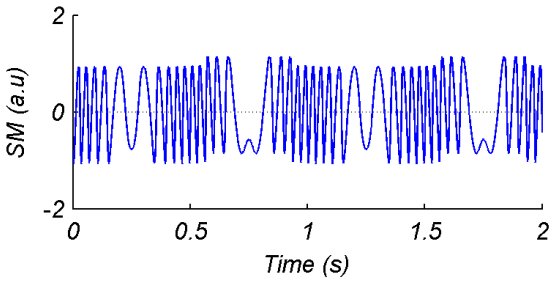

(g) Zero-centered SM signal for $C = 0.5$.

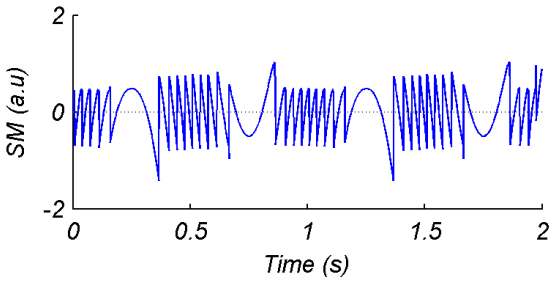

(h) Zero-centered SM signal for $C = 3$.

Figure 3.25 – Proposed fringe offset removal block.

perceptible modification against previous value of $C = 0.2$, an elliptical shape can be appreciated from the analytical SM signal.

Continuing to increase feedback values, in Fig.3.27(a) it can be observed that $C = 1.2$ (thus in moderate regime), produces a discontinuity on the analytical signal. This allows to confirm the change of regime even if the real SM signal (on bottom) does not show a perceptible difference as compared with previous value of $C = 0.9$. Finally, a simulation for $C = 3.6$ reveals not only a moderate regime by the discontinuity in the waveform. It also reflects hysteresis phenomenon as a more accentuated reduction in size of the observed analytical signal.

From these representations, it can be observed that calculated analytical form of the SM signal keeps coherent with the fringe's characteristics observed in real axis along the different feedback variations. This same behavior can be expected even at different amplitudes of the input SM signal. The utility of such an elaboration shall be observed in the next section related to the phase extraction.

3.4.1.4 Phase calculation

From the analytic version $P_a(n)$ and according to Eq.(3.3), the instantaneous phase of an analytic SM signal can be calculated by:

$$\phi(n) = \arctan\left[\frac{\mathrm{Im}(P_a(n))}{\mathrm{Re}(P_a(n))}\right] \tag{3.9}$$

It is known that *arctangent* function provides a phase in the range $(^{-pi}/_2\ ^{pi}/_2)$ hiding direction information on diametrically opposite points. To alleviate this, arctan2 function considers the signs of input vectors providing a four-quadrant calculation as follows:

$$\arctan 2(y,x) = \begin{cases} \arctan\left|\frac{y}{x}\right| \cdot sgn(y), & x > 0, y \neq 0 \\ \frac{\pi}{2} \cdot sgn(y), & x = 0, y \neq 0 \\ (\pi - \arctan\left|\frac{y}{x}\right|) \cdot sgn(y), & x < 0, y \neq 0 \end{cases} \quad \begin{cases} 0, & x > 0, y = 0 \\ undefined, & x = 0, y = 0 \\ \pi, & x < 0, y = 0 \end{cases} \tag{3.10}$$

Reminding that Eq.(3.10) has allowed to observe a constant phase unwrap of each fringe for different conditions suffered by SM fringes. Fig.3.28 presents on the left, a plane view of a small segment with few fringes of the previous analytical calculations for feedback values of $C = 0.2, 0.9, 1.2, 3.6$ from top to down respectively. On the right, from each obtained phase fringe unwrap, it can be appreciated how a derivative threshold can be used to detect discontinuities. In particular, from the bottom case for $C = 3.6$ hysteresis removal shall be an useful calculation to produce a zero-mean centered signal on the real axis, allowing a phase calculation similar to

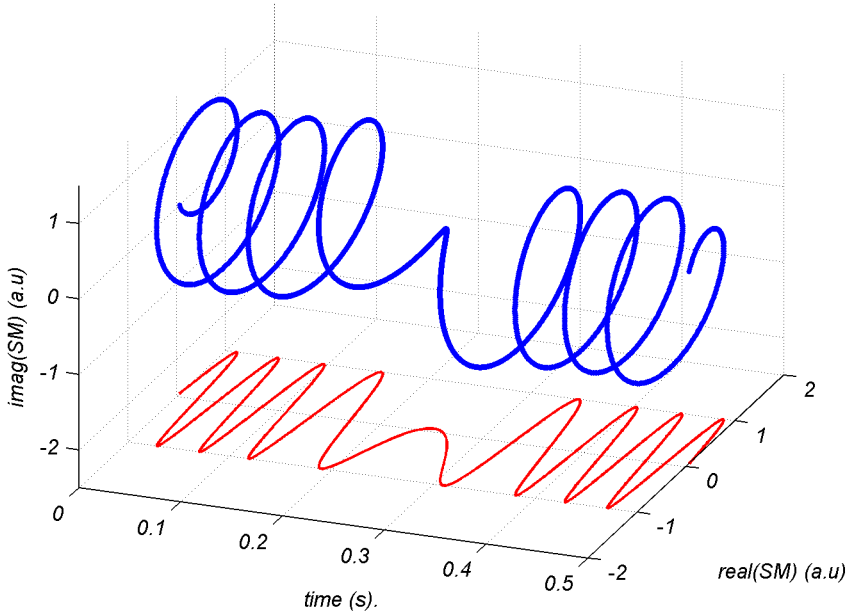

(a) Analytic SM signal with $C = 0.2$.

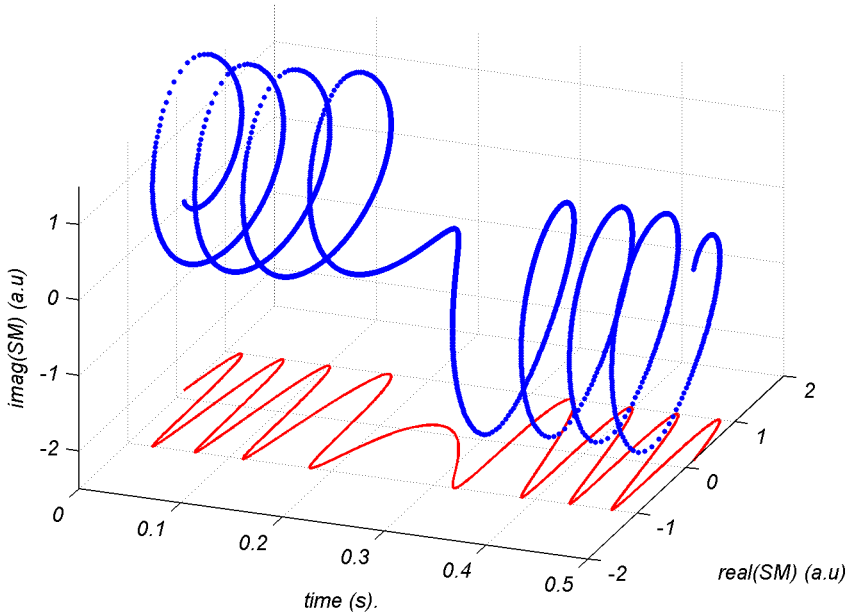

(b) Analytic SM signal with $C = 0.9$.

Figure 3.26 – Illustration of analytic SM signals in weak feedback for a sinusoidal displacement of amplitude 4λ.

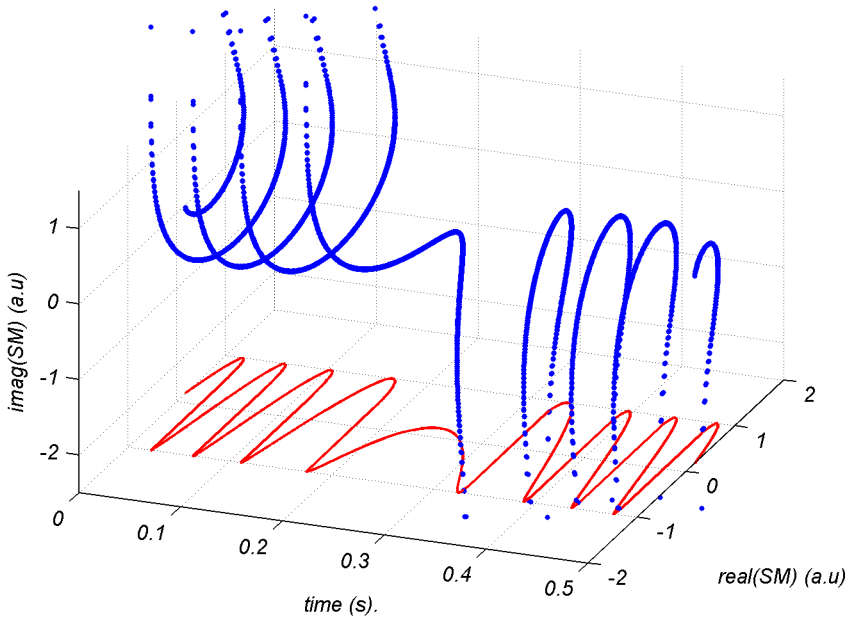

(a) Analytic SM signal with $C = 1.2$.

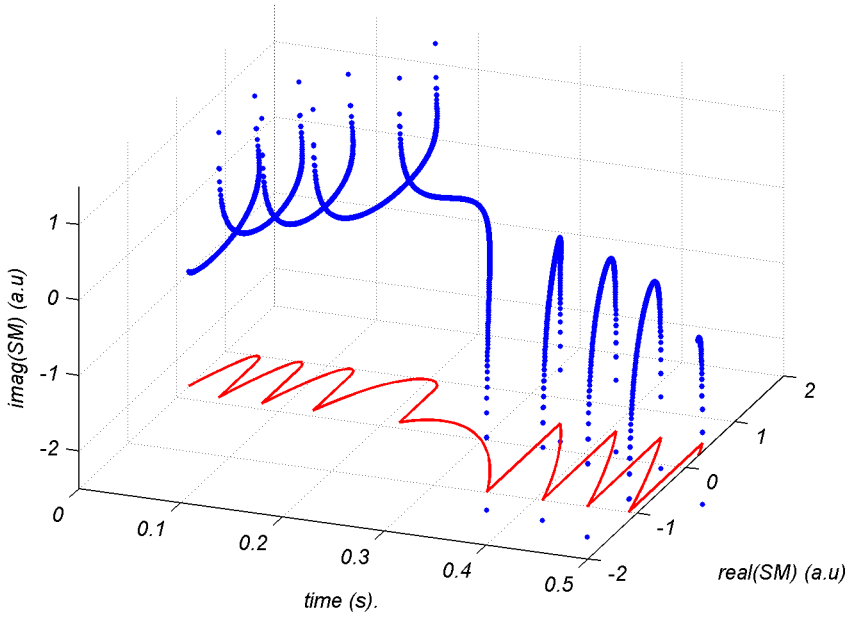

(b) Analytic SM signal with $C = 3.6$.

Figure 3.27 – Illustration of analytic SM signals in moderate feedback for a sinusoidal displacement of amplitude 4λ.

the other lower feedback conditions depicted.

By doing so, the iterative procedure of previously analyzed *adaptive threshold algorithm* can be avoided. However the most important feature of this procedure is the fact that it stays unaffected by amplitude variations over the signal allowing an increased coverage of signal conditions.

3.4.1.5 Derivative, Threshold and Direction assignation blocks

Now that the usefulness of instantaneous phase calculation to provide an homogeneous representation has been discussed. Let us present how to use this information for the case of displacement reconstruction via detected transitions. Fig.3.29 presents the phase derivative (i.e. instantaneous frequency) of previous signals ($C = 0.5$ and $C = 3$, for a sinusoidal displacement of amplitude 5λ), representative of weak and moderate feedback respectively. A variation of small frequency peaks can be observed (zoomed window) between both feedback regimes. Such differences can be confirmed by the spectral analysis previously shown. By settling a threshold to select the major peaks corresponding to the fundamental fringe frequencies of a chirp SM signal, increased robustness for fringe detection can be achieved disregarding their shape in time.

From the same figure, it can be noticed that some frequency peaks appear in opposite direction to the rest of the frequencies found, producing a supplementary contiguous peak to be detected. Indeed, these kind of spurious peaks were also observed in the adaptive transition algorithm due to thresholding. As discussed, that algorithm performs customized filtering for surrounding detected transitions. i.e. once a transition has been detected, the adaptive algorithm makes sure that no other peaks can be considered for a given number of samples (or time interval). This solution is acceptable for specific system requirements where an average arrival time between fringes can be estimated. However, to surpass this constraint and provide a generic implementation, the detection of a peak in opposite direction has been used to denote the removal of one subsequent detected transition. While the appearance of this peak in opposite direction seems to be related with direction changes of the moving target and needs to be further analyzed, its usage for the proposed solution has shown satisfactory results throughout the different validations done.

Finally, each fringe's direction must be determined to produce the transitions train which shall serve as input to the reconstruction algorithm (DAC) proposed in previous chapter. As a matter of fact, in SM literature there can be found several useful methods to reveal the direction of a moving target. In this manuscript we have already referenced: 1) a derivative based approach (with and without *arccosine* function), 2) the duty cycle calculation and 3) the assignation based in a comparison of positive and negative counted transitions of the adaptive

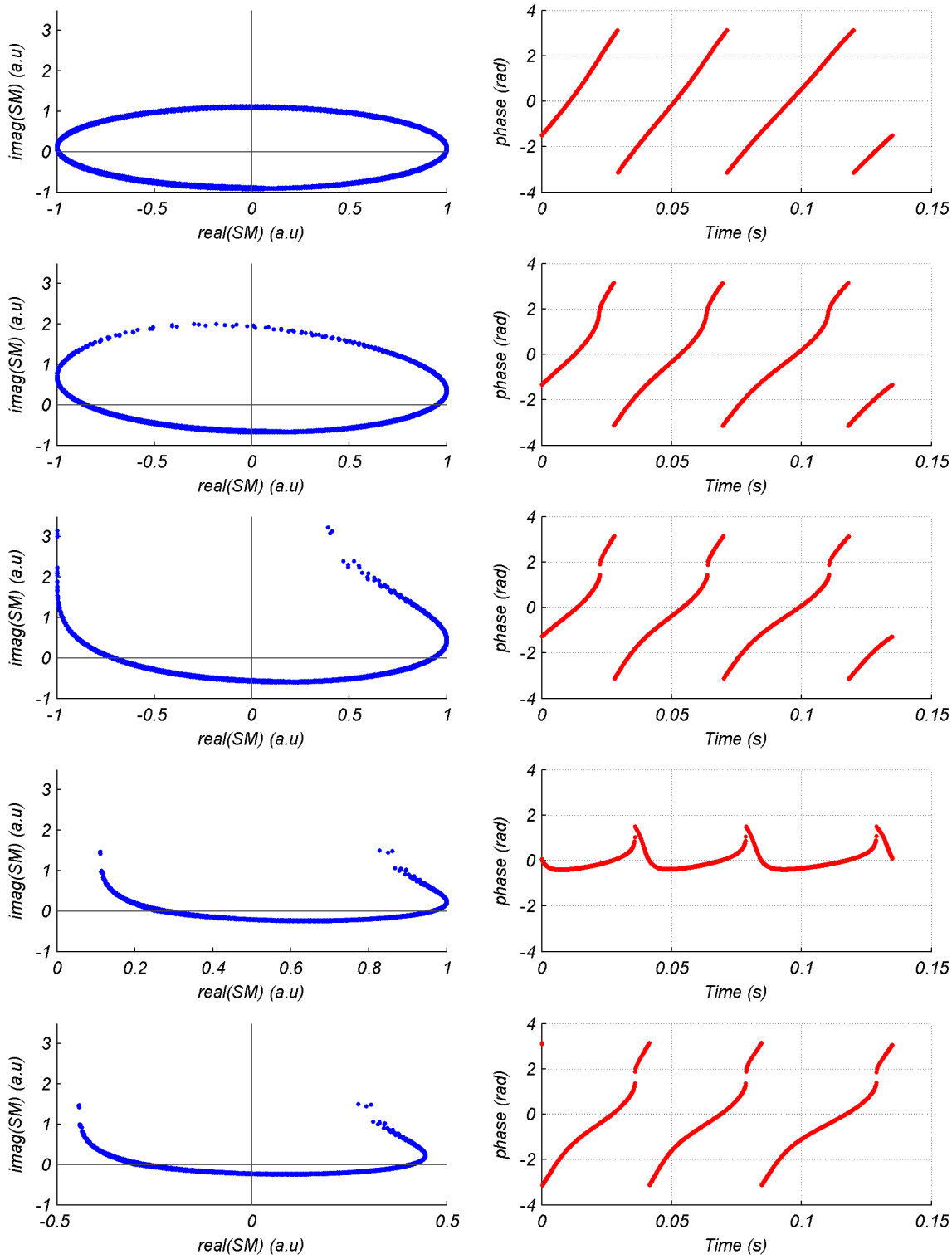

Figure 3.28 – (on the left) Plane view of few fringes from previous analytical calculations (figures 3.26 and 3.27) and (on the right) resulting phases for feedback values of C = 0.2, 0.9, 1.2, 3.6 and C=3.6 with offset removal, from top to down respectively.

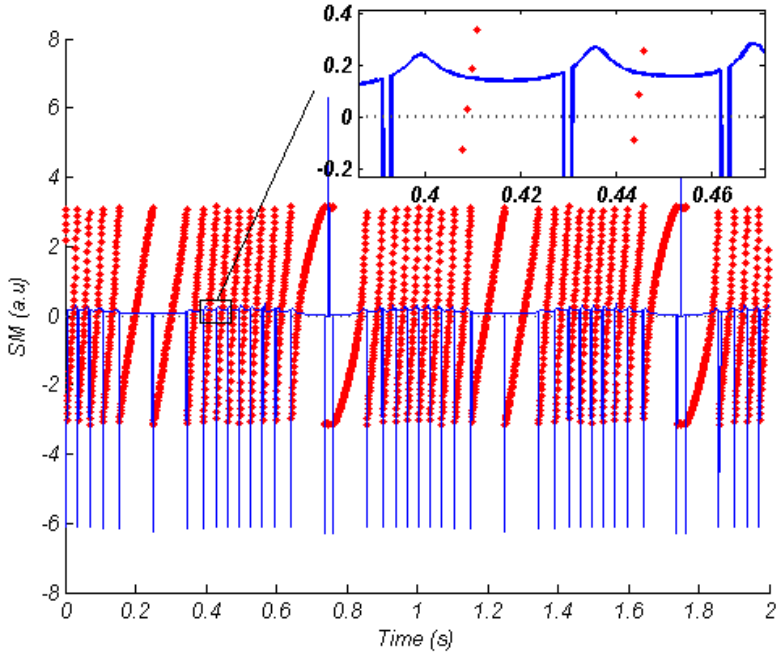

(a) Instantaneous frequency for SM signal with $C = 0.5$.

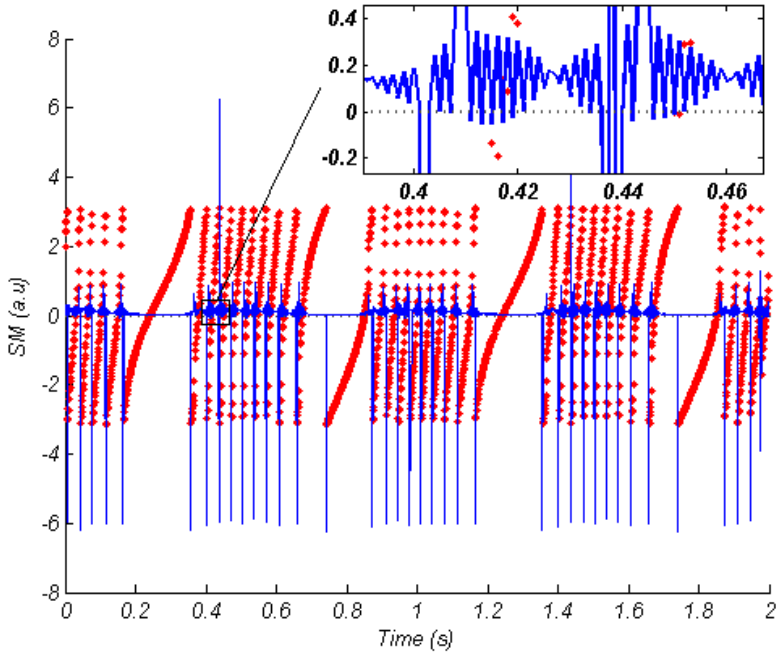

(b) Instantaneous frequency for SM signal with $C = 3$.

Figure 3.29 – Robustness is provided by segmentation via fundamental instantaneous frequencies.

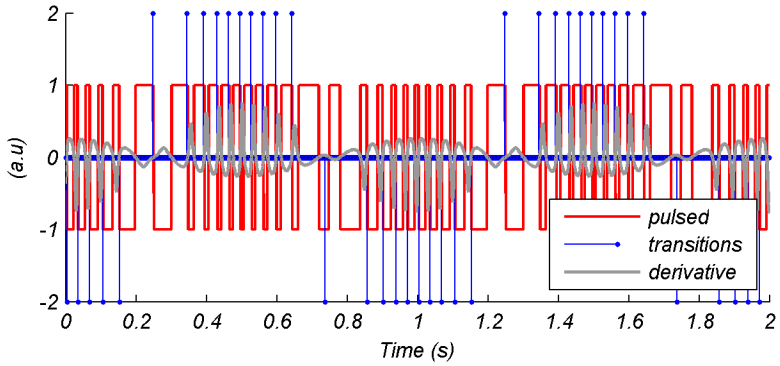

(a) Squared fluctuations for SM signal with $C = 0.5$.

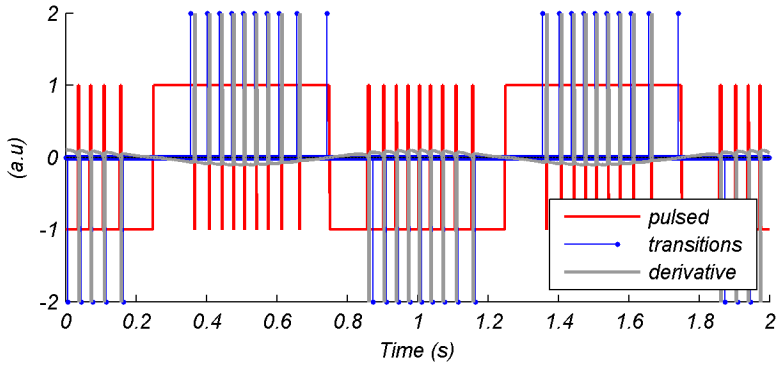

(b) Squared fluctuations for SM signal with $C = 3$.

Figure 3.30 – Fast direction assignation by multiplying frequency peaks with a pulsed derivative of the input SM signal.

threshold algorithm. It is worth to mention here a recently presented frequency-domain technique by [123] in the field of velocimetry. It consists in observing the spectrum of a signal acquired from a rotating target. Then by modulating the driving current of the measuring LD, they analyze a forward-backward shift of the spectrum frequency peak. As reported, it is possible to discriminate without ambiguity the direction of a moving target with this method.

In our current implementation, a simple procedure involving the signal calculations obtained from initial derivative step [Fig.3.25(c)(d)] has been used for fast elaboration. By transforming into positive and negative pulses these derivative fluctuations and multiplying them with the frequency peaks obtained by thresholding, transitions denoting the direction of the moving target can be obtained as depicted in Fig.3.30. Even if their placement varies from a feedback condition to another, it results in a suitably solution for a generic implementation.

In the case of noisy conditions from some experimental signals, the algorithm proposed by [105] relying on the duty cycle calculation provided improved results face to the pulsed derivative approach. A variant to this algorithm consist in integrating the instantaneous phase of each fringe, and assign a positive or negative direction depending on the resulting sign of

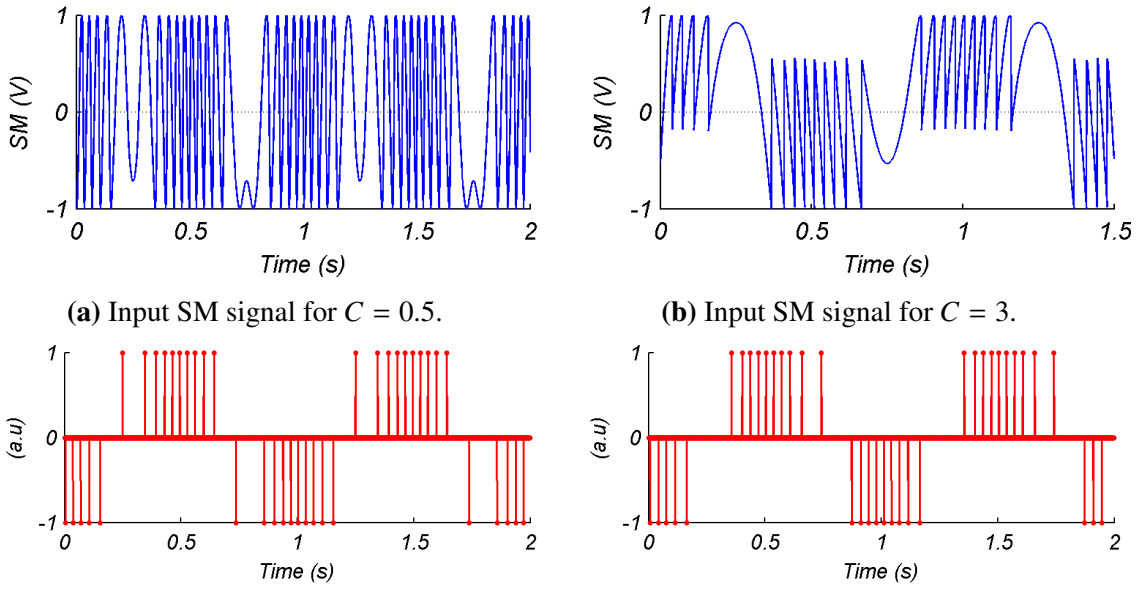

(a) Input SM signal for $C = 0.5$.

(b) Input SM signal for $C = 3$.

(c) Assigned transitions for $C = 0.5$.

(d) Assigned transitions for $C = 3$.

Figure 3.31 – Assigned transitions as the output of algorithm proposal for weak and moderate feedback.

the summation. Such improved solutions have been left of minor relevance as they increase the complexity of calculations and their added value can be appreciated only for a particular application.

To conclude this presentation, let us summarize with Fig.3.31, the equivalent outputs obtained from our proposed algorithm for two different feedback levels corresponding to the simulated signals used for demonstration of previous steps.

3.4.2 Simulated measurement results

In order to validate the contribution of our generic fringe detection algorithm, it has been compared against the unfavorable conditions tested for the adaptive threshold algorithm. Let us remind that this algorithm was analyzed with the intention of being implemented as part of an embedded sensor for a wide variety of usage conditions.

In Fig.3.32, the SM signal used to observe the issue of undetected fringes due to amplitude variations has been used as input to our algorithm ($C = 2$, amplitude of 6λ and amplitude modulation of Fig.3.11). For convenience, it has been denoted HT since it relies on a Hilbert transform calculation to obtain the analytic form of the SM signal (which is then used for improved phase calculation).

As depicted in Fig.3.32(b), HT algorithm has been able to successfully account all the fringes in the signal by exploiting its improved phase calculation scheme. Notice however that

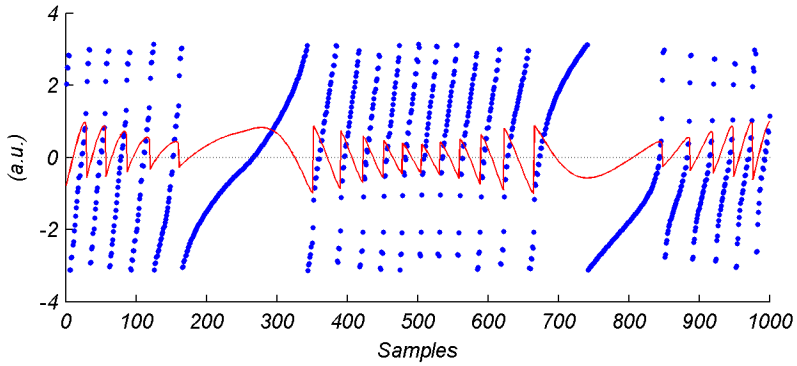

(a) SM signal with amplitude variations, along its calculated instantaneous phase.

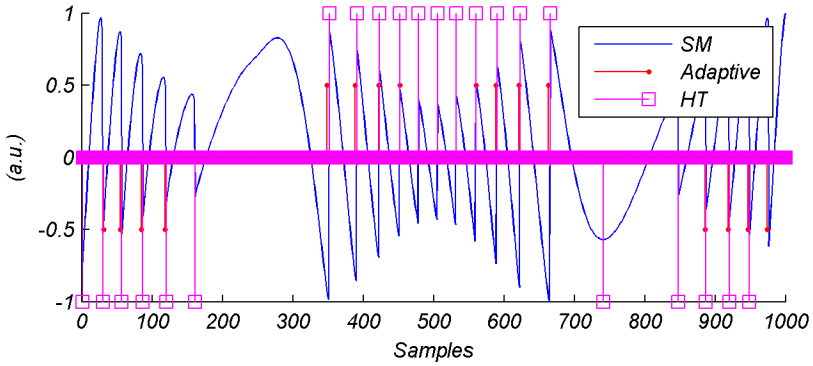

(b) SM signal with amplitude variations, along the assigned transitions.

Figure 3.32 – The issue of undetected fringes due to amplitude variations from Fig.3.11, alleviated by our proposed algorithm.

one extra peak has been detected for the second lobe corresponding to a target direction reversal. This happens because phase calculation itself does not distinguish this condition. As can be appreciated in the second lobe of Fig.3.32(a) a visual inspection allows to distinguish direction reversal as the maximum point within the hump. Therefore one solution to cancel this extra peak would be to search a maximum or minimum point between assigned transitions of opposite direction and remove the transition matching the index of the searched deflection point. This extra step, can be added within the fringe direction assignment procedure for a precise displacement reconstruction application. However, without specific requirements it is worthless to assign additional processing for this minor issue.

Other than the feature of working with different fringe amplitudes. It is important to highlight from this use case, that the iterative feature and the normalization step from the adaptive threshold algorithm have been conveniently simplified by the analytical SM signal elaboration, basically relying on a moving average filter, a Fourier transform and its inverse.

A second test is presented in Fig.3.33. This signal corresponding to an amplitude of 6λ and $C = 3$ was used in Fig.3.12 to show the need of the adaptive threshold algorithm to process

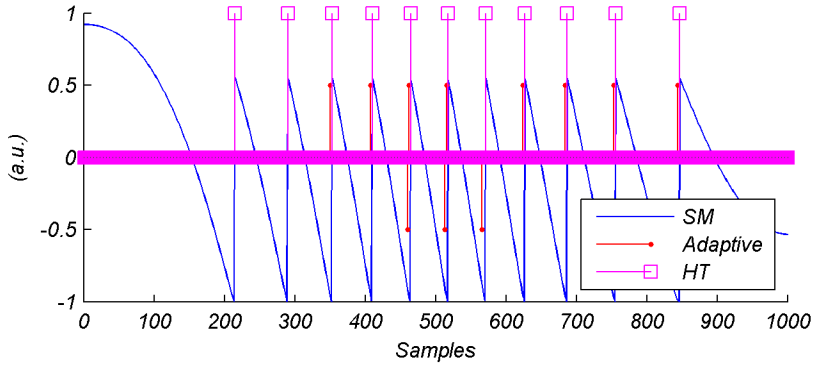

Figure 3.33 – The issue of processing a SM segment with only one direction on its fringes from Fig.3.12, alleviated by our proposed algorithm.

SM fringes for at least two segments of an expected target displacement (one positive and one negative). Also for this use case, HT algorithm has been able to successfully account all the fringes in the signal segment and assign its transitions in proper direction. This has been possible because all the processing blocks have been proposed considering a small set of fringes as input, in contrast with the approach followed by the compared algorithm. As a consequence, it can be expected for this proposal to measure different amounts of displacement without requiring to analyze particular conditions for its implementation.

3.4.3 Experimental measurement results

In order to observe the viability of our proposal for real usage, a test for peak detection has been proposed. The experimental signal in Fig.3.34(a) was acquired from a basic velocimetry setup (like the one depicted in Chapter 1 Fig.1.8): a distributed feedback (DFB) laser diode pointing the surface of a rotating disk at constant velocity in one direction.

From this signal it is clear to observe the speckle phenomenon as a random amplitude modulation strongly affecting SM fringes. For clarity, just a part of this signal has been fed into both compared algorithms [Fig.3.34(b)]. Looking closely to the fringes, it can be seen that those with bigger amplitude present a characteristic sawtooth-like shape allowing a simple target direction identification. On the other hand, those with smaller amplitude become more triangular and is almost impossible to observe a privileged sense (even if it is known that the target rotates only in one direction).

The obtained transitions from both compared algorithms are shown in Fig.3.34(c). Those corresponding to the adaptive algorithm (scaled down for clearness) present few gaps for undetected values after a threshold settlement. Concerning the gaps from current proposal, it can be seen an issue on fringe direction assignment. Keeping the fast derivative approach, one

solution resulted in denoising the input by a moving average as previously described, producing full detection of the fringes in the segment [Fig.3.34(d)].

3.4.4 Critical analysis

Let us finish the presentation of our proposed real-time generic fringe detection algorithm (HT based algorithm) by comparing it against the major features of the adaptive threshold algorithm as summarized in Table 3.1. Such analysis in the context of non-cooperative signals for embedded implementation is discussed next.

Feature	Adaptive Threshold Algorithm	HT Based Algorithm
Real-time working	Greater time boundaries to obtain positive and negative fringe segments. Iterative threshold needs to be evaluated in worst case scenario	Time constraint can be defined for small segments of fringes
Implementation	Requires normalization of input signal. Careful understanding of the several decisions undertaken, including its humps based filter	Analytical SM signal elaboration basically using a Fourier transform and its inverse does not require normalization
Detection versatility	Requires redimensioning several vectors within the implementation	Adaptability only requires to dimension memory to contain a small segment of fringes
Robustness	Works for different feedback conditions. Fails face to amplitude variations like in speckle	Works for different feedback conditions and also face to amplitude variations
Spurious detections	Specific filtering procedures aim to provide clean transitions	Also requires extra processing in some cases
Validation	off-line via PC, from recorded signal	off-line via PC, from recorded signal

Table 3.1 – Comparison between the adaptive threshold algorithm and Hilbert transform based proposal.

3.4.4.1 Embedded implementation

From the assessment conclusion about the analyzed adaptive algorithm, it has been mentioned that this algorithm can be implemented in real-time despite its iterative nature. However the fact that it requires two different segments of fringes to work properly implies that the critical time to process a signal must be defined according to this constraint which is

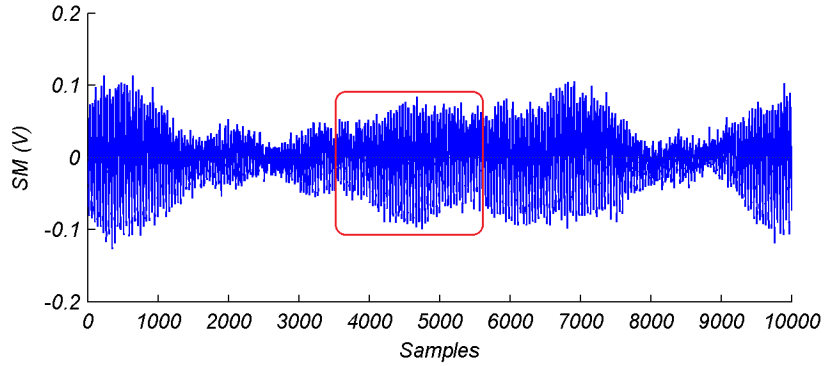

(a) Speckle affected SM signal at constant velocity.

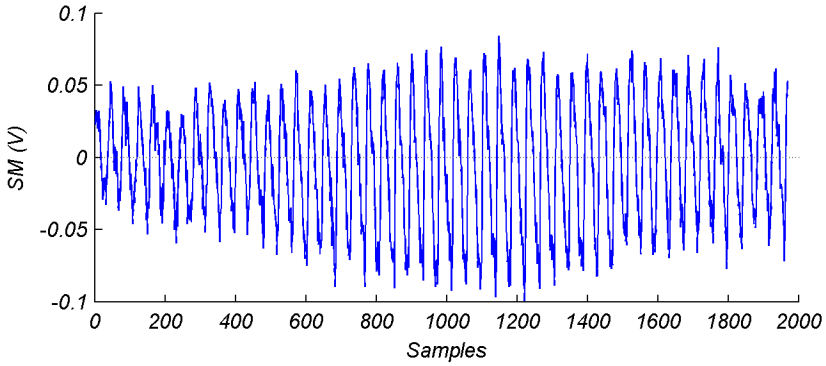

(b) A segment of SM signal for validation.

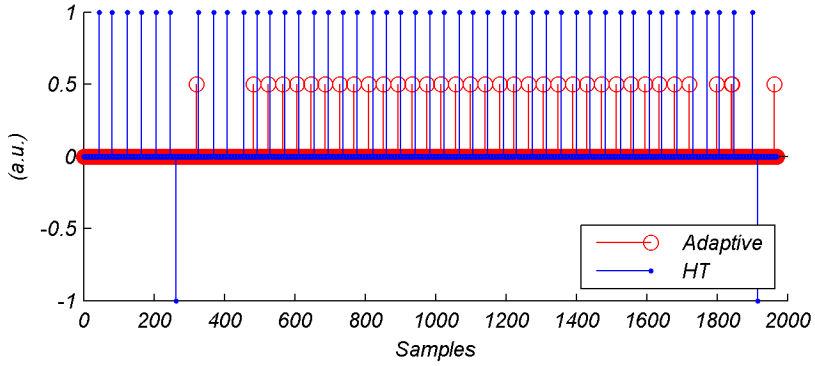

(c) Detected transitions by previous method and our proposal without denoise procedure.

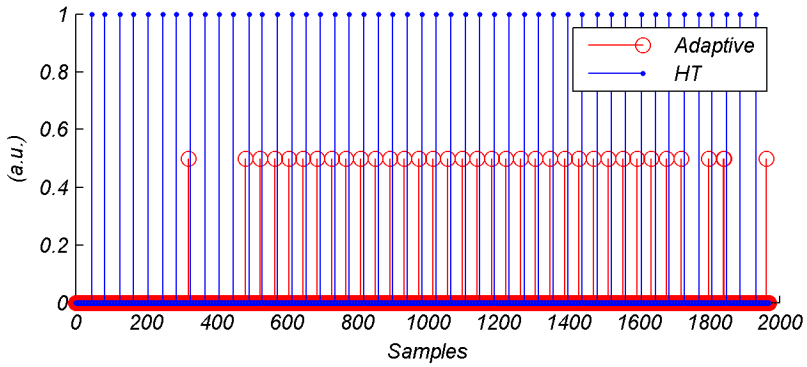

(d) Detected transitions by previous method and our proposal with denoise procedure.

Figure 3.34 – Experimental SM signal from a rotating disk used to obtain SM fringes with amplitude variations.

not straightforward to establish. Our proposed generic algorithm has been conceived since the beginning with the idea of working with a set of fringes, disregarding its size or direction information. As a result, a time constraint can be imposed according to a compromise between buffer size and calculation time simplifying the evaluation to meet deadlines.

While the implementation of the adaptive threshold algorithm requires a good understanding on the sequential decisions undertaken to process different feedback regimes and the working procedure of the humps based filter. The analytical SM signal elaboration proposed relies on concepts from signal processing like Fourier transform and its inverse. However the whole algorithm also requires to respect the sequence: 1) offset removal, 2) instantaneous phase calculation and 3) direction assignation.

If a working system is aimed to perform different requirements, the analyzed algorithm needs to be adapted in several blocks. In particular memory size needs to be well dimensioned to respect imposed constraints for an embedded usage. In contrast, the proposed algorithm only needs to observe its compromise against an imposed time constraint. Being more suitable for systems with low memory resources.

3.4.4.2 Non-cooperative signals

With the intention to approach the development of SM sensors for a wide variety of applications, non-cooperative SM signals were presented as those signals affected by random amplitude modulation and dynamic changes of C coefficient. This came in extent to the validation tests already covered in the published adaptive threshold algorithm, which produced satisfactory results handling different levels of feedback conditions.

In this context, the adaptive algorithm failed to detect some fringes since its iterative threshold works by blocks of fringes which in turn, need to share similar amplitudes. Let us highlight that techniques like speckle tracking [59] or focus variations [109] which avoid amplitude variations due to speckle could be coupled to this algorithm to overcome this issue. However our research goal to avoid external components, lead to an algorithmic solution able to be scaled for different requirements. The counterpart of avoiding the usage of supplemental elements, is that speckle affected fringes are more corrupted and are prone to ambiguous direction assignation. Face to this issue, the generic aspect of the proposed algorithm needs to be coupled with particular denoising procedures. This means that even if we have provided a generic approach for a reliable fringe detection, it should be considered as a framework which needs to be further refined to meet specific requirements.

Just like in the case of the adaptive threshold algorithm, the first validation step for our proposed algorithm has been achieved with preprocessed signals. However special attention has been taken to use different segments of signals covering the case when there is no *a-priori*

knowledge on the signals to process. With the intention to consolidate the process of SM signal exploitation for displacement measurement, it has been decided to perform further experimental validation by coupling the two proposed algorithms of this manuscript in the next chapter.

3.5 Conclusion

Exploiting SM signals at different feedback levels is a challenging task, even more when the target presents a non-cooperative surface. While passing from moderate to weak can be simply achieved by using optical attenuators, the contrary will require to explore LD coupling effect for a particular condition. Empiric solutions to improve feedback conditions consist in slightly increasing the LD's current, adjusting the focused beam, increasing the laser-to-target distance in some centimeters, or even using reflective paints on the target.

In this chapter more details related to the complexity of dealing with SM signals have been exposed along the various solutions from literature. One algorithm based on the duty cycle of the fringes was studied as a potential solution to handle different feedback levels, however it resulted a robust solution for direction discrimination and not properly for fringe detection.

Then, an important prior research work held in our laboratory was analyzed for extended usage conditions and embedded implementation. The required robustness for punctual situations like speckle phenomenon lead us to further research solutions by using signal processing techniques.

The introduction of instantaneous frequency concept largely used in other domains like geophysics, radar and speech processing seemed to satisfy the constraint of real-time implementation. Then, comparing the calculated instantaneous phase by this method against the calculation conventionally used in several algorithms, it was observed that the former is not a mirrored version of the SM signal. The instantaneous phase extended to the range $[-\pi\ \pi]$ results in a means to settle a constant threshold for fringe segmentation.

An algorithm for a generic fringe detection was then proposed based on this instantaneous phase calculation. In order to cover hysteresis affected signals, a means to remove the local offset of groups of fringes has been coupled to this algorithm. Based on this frequency-domain calculation, a time-domain fringe direction assignation for displacement reconstruction can thus be achieved. Compared against prior work it also covers different feedback regimes, with two identified advantages: 1) It works with amplitude modulated fringes with or without normalization, and 2) It can work with segments of fringes of different size and not necessarily with positive and negative segments of fringes.

The proposed algorithm for robust fringe detection is based on instantaneous phase calculation from an analytic SM signal. It is assisted by selective instantaneous frequency

extraction, allowing time-domain fringe direction identification for coupling with already exposed displacement waveform elaborations. Following chapter presents the validation made in this context, as well as possible variations to highlight its versatility.

Chapter 4

Reliable SM signal exploitation for embedded implementation

Contents

In order to introduce this chapter, let us recall some pertinent conclusions withdrawn from previous chapters. First, we presented a meta-analysis on devices performing a displacement reconstruction by SM meeting the criteria for *in-situ* measurement. The tradeoff between more elaborated signal processing and the usage of external arrangements to stabilize the self-mixing signals was then exposed. Then, two functional blocks exploiting SM signals for displacement reconstruction were approached by further analyzing prior work from our research laboratory. The case of displacement reconstruction was then studied and simplified by a new proposal providing waveform elaboration from incoming detected fringes. Similarly, the case of fringe detection was studied. From it, the problem of speckle lead us to analyze spectral properties of SM signals in order to be able to provide a solution. The retained approach consist in observing the instantaneous phase from an analytical SM signal, thus avoiding the need to maintain a particular shape for incoming fringes. In continuity with the research goal to develop algorithmic solutions suitable for implementation as embedded

systems with versatile requirements, a generic detection of SM fringes suitable to meet real-time constraints was proposed.

Lastly, in this chapter we combine our proposed functional blocks for detection of SM fringes and displacement reconstruction providing a framework for SM sensors development. After some experimental validations, the limitations of this method will be discussed and followed by a brief proposal of compatibility with existing methods for further research. To finish, the perspectives for embedded implementation shall allow to embrace the concept of producing a System-on-Chip with this technology.

4.1 Complete algorithm for versatile SM displacement reconstruction

The Hilbert transform based method for SM fringe detection combined with the D/A conversion based reconstruction algorithm, compose our complete proposal (Fig.4.1) to exploit SM signals for displacement measurement suitable for real-time processing evaluation at different system requirements.

Let us remind that by simplifying the reconstruction step, it was expected to use a major demand of resources for the detection block. Among the different calculations performed, the most expensive ones in current implementation are: 1) the fringe offset removal (moving average), 2) the analytic signal elaboration (FFT and its inverse essentially) and 3) the convolution prior to output a displacement signal. Notice that no particular processing architecture has been imposed, therefore it is expected a seemly implementation across different processing hardware in order to optimize these tasks for a given application. Also, the modular approach has been kept homogeneous to define critical calculation times in terms of the arrival of two detected fringes. Therefore if future modifications are proposed, it shall be less complex to identify trends for a real-time implementation.

Since a comparative validation of these two functional blocks has already been presented on each corresponding chapter, here we present supplementary testing as a complete displacement measurement system to gain more confidence on its viability for different usage conditions. It is highlighted the fact that our validation procedure considers the algorithm as a black-box, i.e. none of its working internals are modified across the different experiences. Thereby, when a behavioral parameter needs to be adjusted to provide satisfactory results it shall be mentioned and discussed on the limitations section. Let us advance this complete displacement exploitation procedure by a simulation next.

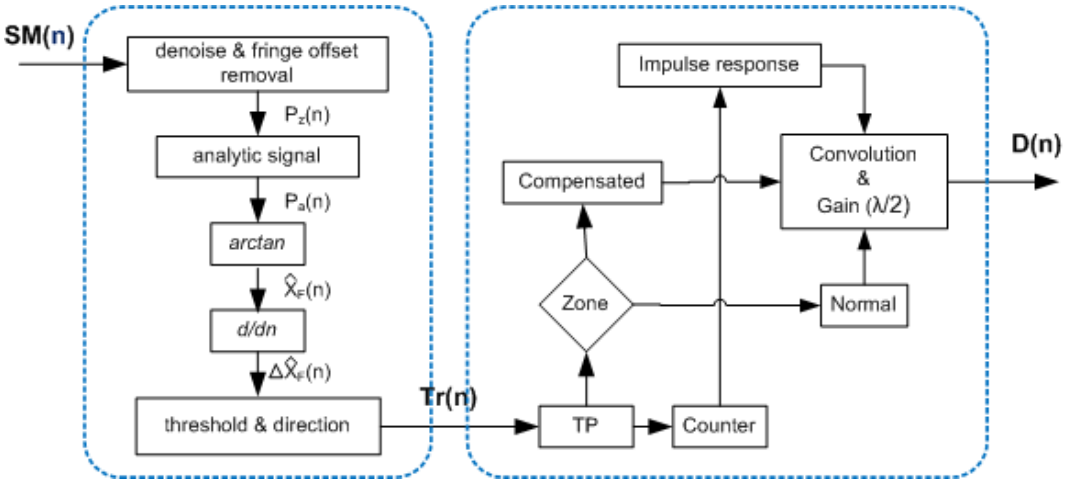

Figure 4.1 – Block diagram for the proposed versatile SM displacement reconstruction.

4.1.1 Simulated measurement results

To conclude with the processing steps of previous SM signals representative of weak and moderate feedback ($C = 0.5$ and $C = 3$ for a sinusoidal target displacement of amplitude 5λ), Fig.4.2 depicts these two signals along their assigned transitions and the obtained displacement reconstruction from them.

As it can observed, the waveform representing the target's movement does not describe a smooth sinus as expected, being more accentuated for the case of weak feedback. The unfavorable conditions for signal elaboration exposed in Chapter 2, confirm that the position of detected fringes has a direct influence for this behavior. In fact, [119] has signaled that the change of 180° on target's direction cannot be neglected in order to provide improved resolution from a phase unwrapped technique. It is convenient to highlight that the case of moderate feedback naturally reduces this ambiguity due to its characteristic fringe's shape, thus attesting its preferred usage among the many literature of SM displacement measurement.

As already mentioned, current implementation keeps a simplified technique for fringe's direction assignation in the context of framework, prone to be adapted for particular requirements. A procedure to obtain smoothness, consists in counting the number of samples between two transitions of different sign and compare against its previous and next counted samples between same signed transitions. Based on collected information, it is possible to decide wether or not to assign a transition to the reversal direction, to keep its contribution to ongoing direction, or to remove it if belongs to a spurious detection. This results indeed in a variant of Index II parameter from the analyzed slopes based method (also from Chapter 2) which was proposed to deal with observed pinching of the reconstructed waveform.

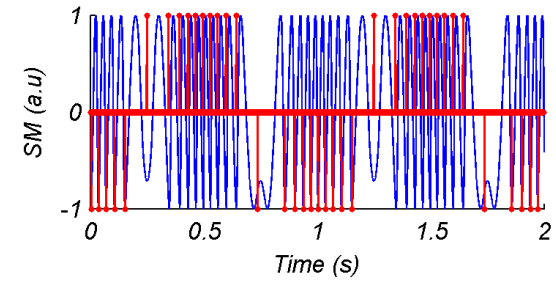

(a) Input SM signal for $C = 0.5$ along assigned transitions.

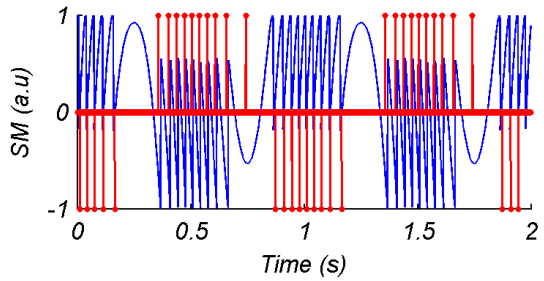

(b) Input SM signal for $C = 3$ along assigned transitions.

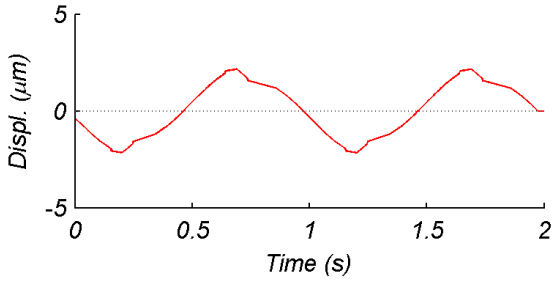

(c) Displacement reconstruction for $C = 0.5$.

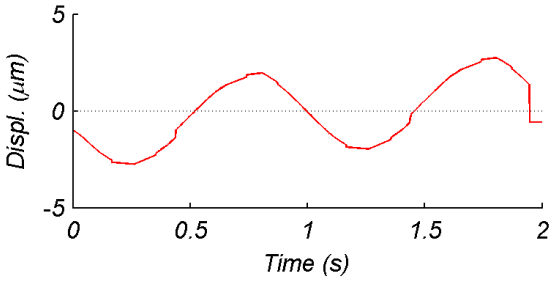

(d) Displacement reconstruction for $C = 3$.

Figure 4.2 – Overview of proposal for weak and moderate feedback.

4.1.2 Experimental validation: speckle

In order to validate the pertinence of our proposed algorithm, a smoke test was designed to obtain a forced speckle effect over micrometric displacement. Let us remind that dealing with this complex shape in time has demonstrated to be a major challenge in SM processing.

The experimental coarse setup (Fig.4.3) is intended to approach a real non-conditioned environment, on the believe that a better controlled arrangement shall lead to a detailed characterization of a designed SM sensor. A Hitachi LD with wavelength $\lambda = 785$ nm (HL7851G) was powered in continuous wave at 20 mW. The emitted beam was collimated through a lens with focal length of 5 mm and focalized to a random point over a commercial speaker with diameter of 80 mm. The distance from the LD to target was 45 cm. A sinusoidal wave of 300 Hz and 10 Vpp from a Tektronix AFG3022 function generator has been used to drive the speaker.

Two different materials were chosen to increase superposition probability of the emitted beam. In a first experience a surface area of the speaker has been coated with sandpaper of 425 μm average roughness (P40). Then, a slow-fading phosphor material active in the IR (VRC2 from Thorlabs) has been used to observe strong speckle degradations. By means of a transimpedance amplifier and an oscilloscope, SM signals from the LD's monitoring photodiode were recorded to apply our proposed algorithm.

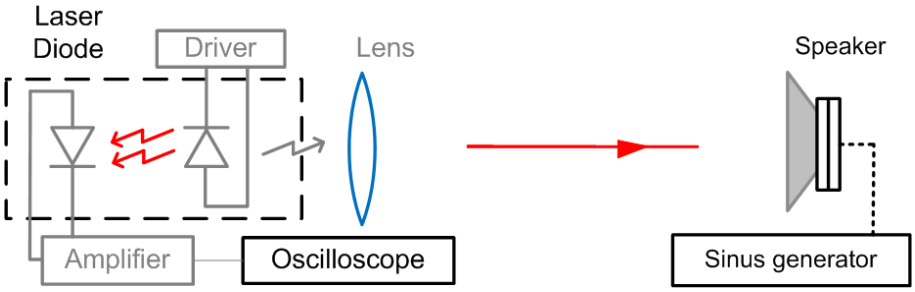

Figure 4.3 – Experimental setup to obtain a speckle affected SM signal.

4.1.2.1 Moderate speckle

Two acquired periods of a speckle affected SM signal obtained from the backreflected beam of the sandpaper-surface are represented in Fig.4.4(a).

The described algorithm steps are elaborated through Fig.4.4(b-d). From the fluctuation removal procedure, it can be appreciated a bigger amplitude over sharpened fringes in one direction of the target compared to the less sharpened fringes from the opposite direction. This, combined with the amplitude reduction due to speckle modulation highlights the impossibility to rely on temporal thresholding as already discussed. However this simple detection scheme grants the required zero-mean for subsequent generic calculations. For this signal without hysteresis, the non-intrusive nature of running average algorithm can be observed as the signal remains centered about zero. In this condition, the analytical SM form was created by using the Hilbert transform allowing the improved phase observation instead of *arccosine* function which would provide a mirrored amplitude modulated signal. Transition direction were assigned by the fast procedure of multiplying instantaneous frequency peaks with positive or negative squared pulses from the original SM derivative.

Finally, target displacement reconstruction at 300 Hz has been achieved properly as observed in Fig.4.4(e). At this point the interest has been to validate the pertinence of the fringe detection scheme and its coupling with our signal reconstruction algorithm. In particular, it can be seen that suitable waveforms are produced with the basic interpolation method implemented for the reconstruction algorithm (the triangular impulse response). It can be argued the lack of countermeasure for a comparative validation, notice however that the surface is a speaker cone. Indeed, this kind of electromechanical transducers can be characterized with theory in the field of acoustics, nevertheless this is out of the scope of the present work. A detailed inspection on the results shows a single calculated transition per fringe regardless momentary variations of C factor and amplitude. It is reminded that these two conditions are not often handled by many proposals in literature and correspond to a source of inaccuracy.

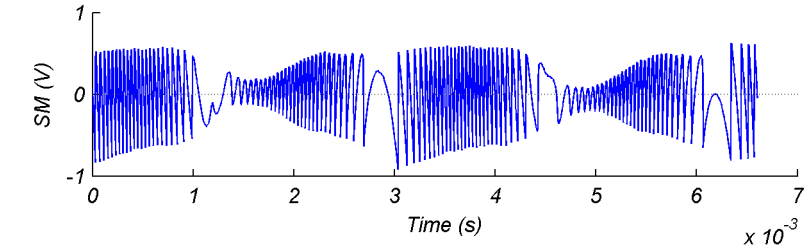

(a) Experimental speckle affected SM signal.

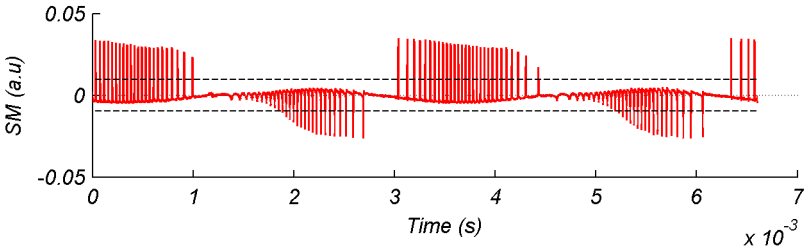

(b) Fluctuation threshold step.

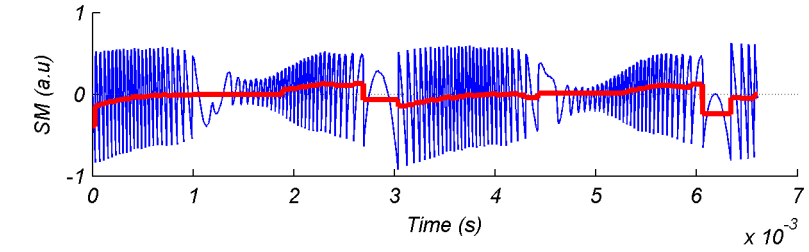

(c) Running average.

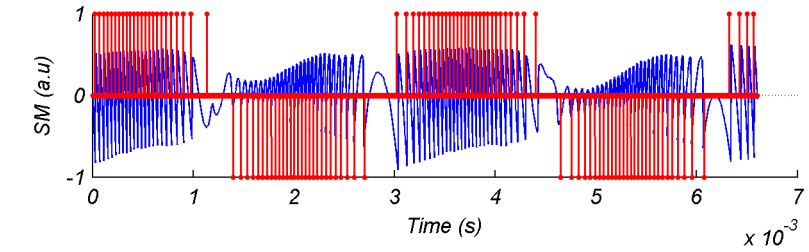

(d) Assigned transitions.

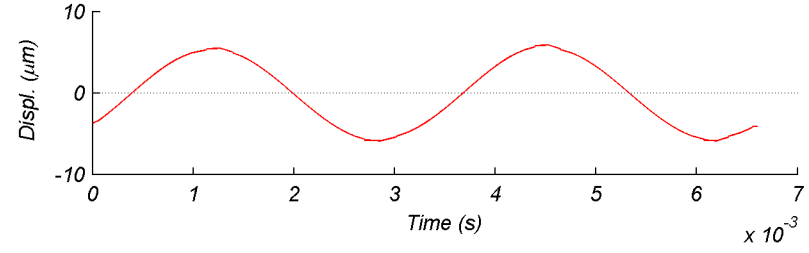

(e) Displacement reconstruction.

Figure 4.4 – Complete exploitation procedure applied over a real speckle-affected SM signal.

4.1.2.2 Strong speckle

Considering now the second experience when the backscattered beam comes from a phosphor material, stronger signal degradations can be observed over the monitored signal [Fig.4.5(a)].

In particular, amplitude fading can be observed at ≈1.7 ms and ≈3 ms for the first target period of 3.3 ms, as already depicted in Fig.1.15 of Chapter 1. Fluctuation removal step for this signal allows to clearly distinguish pseudo-fringes as a means to locally detrend biased fringes. The resulting zero-mean from running average algorithm [Fig.4.5(c)] is a convenient elaboration to bypass an envelope calculation which is more complicated when fringes are not equally spaced in time.

Once the average mean has been subtracted of the SM segment, its analytical version is calculated and instantaneous frequency peaks can be obtained. However Fig.4.6 depicts a weakness in the fast procedure of multiplying instantaneous frequency peaks with positive or negative squared pulses from the original SM derivative. It can be observed that transition direction has been assigned properly in the first fading zone (≈ 1.7 ms), but in the second fading zone (≈ 3 ms) the simple direction scheme failed. It assigned those transitions in opposite sense to the rest of surrounding fringes. A zoom in this area [Fig.4.6(b)] confirms that strong speckle, affected the feedback coupling factor and the zero-crossing of the fringes. By settling the pseudo-fringes level to a low level it could be possible to center also this small set of fringes to obtain improved results. However, ambiguity condition can be argued from the momentary quasi-sinusoidal shape of the fringes in this zone. This is then translated into a glitch over reconstructed displacement propagating along the waveform.

As mentioned before, duty cycle algorithm can be used to solve this ambiguity issue for not purely sinusoidal fringes. Instead of adapting that solution to our working algorithm, another procedure has been proposed to denote development versatility and perhaps to add robustness face to purely sinusoidal fringes. It consists in a statistical direction fixing of concerned transitions based on average fringe separation and number of surrounding blocks criteria in a similar fashion as a visual inspection. Fig.4.7 presents the reconstructed displacement for the second test were target periodicity of 300 Hz is confirmed, the increased amplitude is explained by the fact of hitting a different arbitrary point over the speaker.

It is important to insist in the modularity of such optional processing. In case of target displacement of several tens of μm, this ambiguity could be tolerated or even fixed by inexpensive analogue electronics, saving on processing complexity, while a precise elaboration certainly could add more processing.

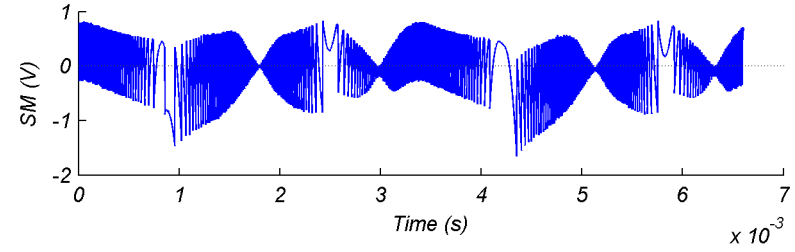

(a) Strong speckle affected SM signal.

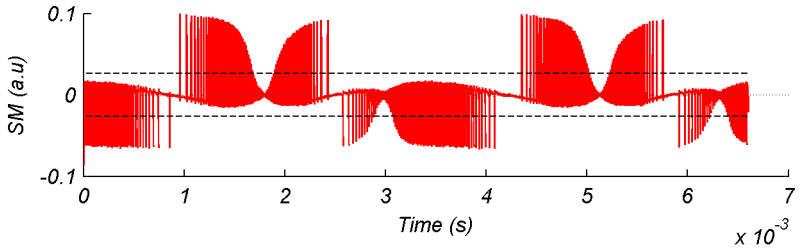

(b) Fluctuation threshold step.

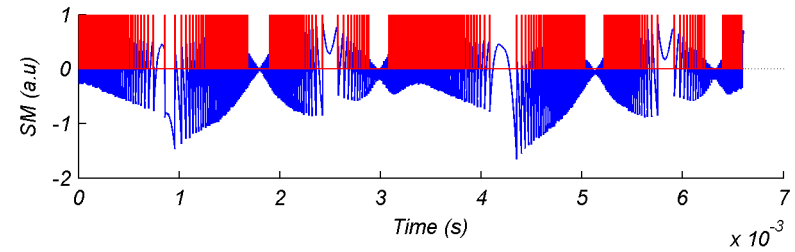

(c) Trigger points denoted by pseudo-fringes.

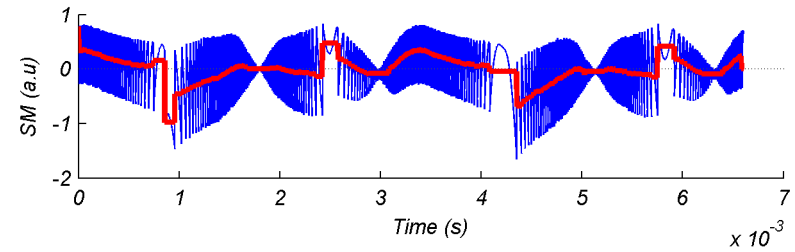

(d) Running average.

Figure 4.5 – Fringe offset removal steps for strong speckle affected SM signal.

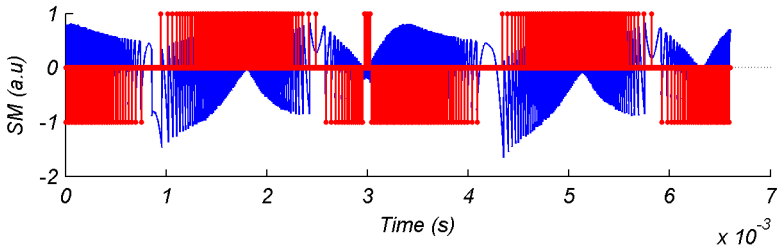

(a) Assigned transitions with ambiguous segment.

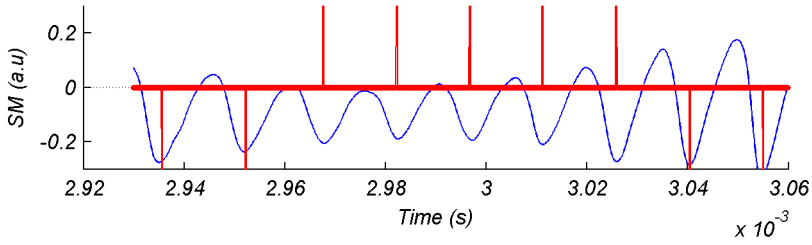

(b) zoom into ambiguous direction segment.

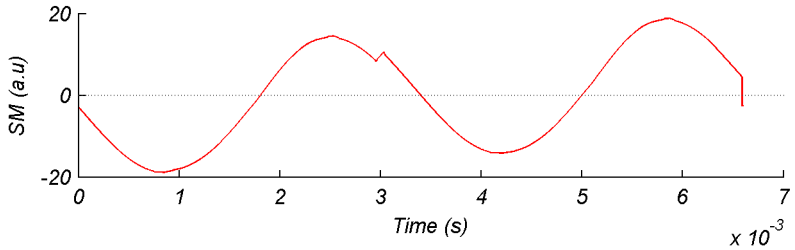

(c) Displacement reconstruction with glitch.

Figure 4.6 – Displacement waveform elaboration from improper direction assignment.

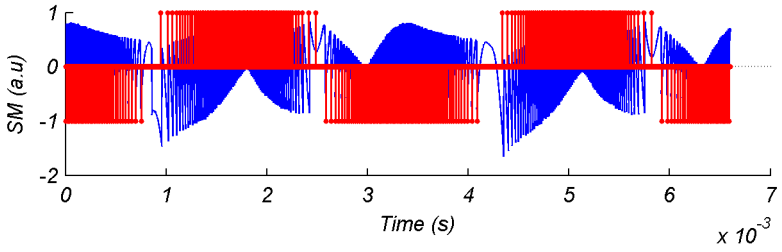

(a) Assigned transitions after statistical correction.

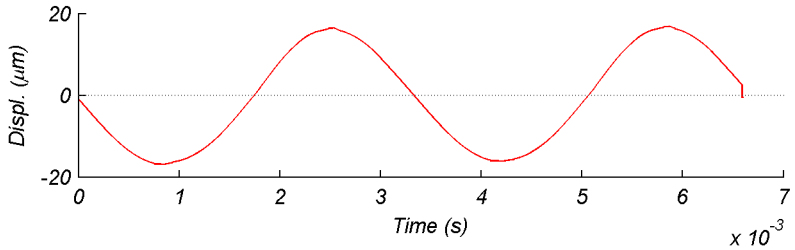

(b) Displacement reconstruction.

Figure 4.7 – Last processing steps for strong speckle affected SM signal.

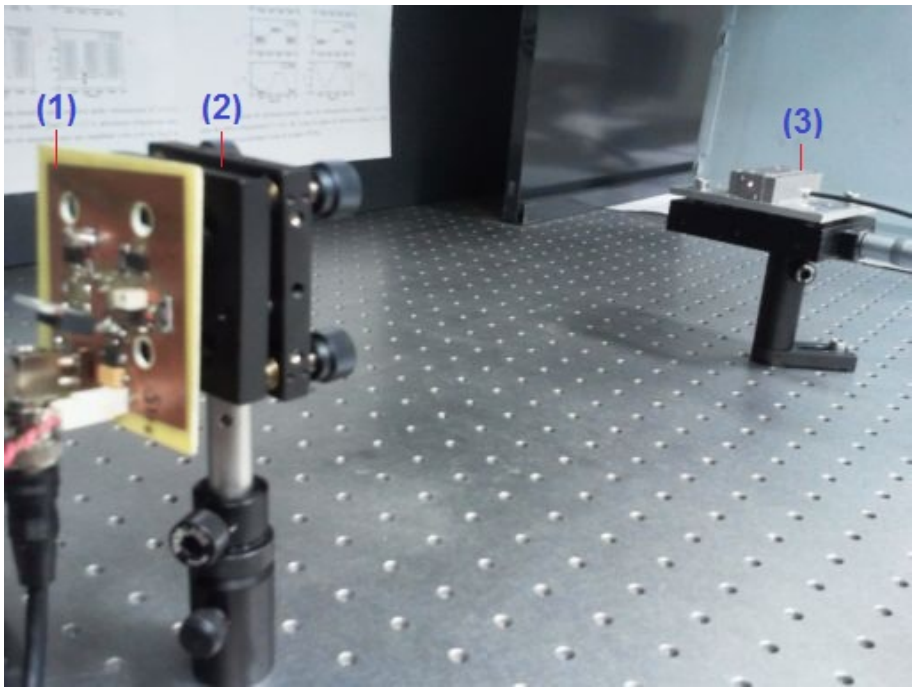

Figure 4.8 – Experimental setup to acquire displacement signals over different surfaces: (1) is the sensor card containing the LD, (2) the collimating lens which directs the beam towards the target, and (3) the PZT with the pointed beam.

4.1.3 Experimental comparative over different surfaces

With intention to observe the robustness of the algorithm over variations on SM signal quality, different materials were chosen and interchangeably placed on the surface of the commercial piezoelectric transducer (PZT) also used in Chapter 2. This PZT is equipped with a capacitive feedback sensor for direct-motion metrology with a resolution of 2 nm, and has served to provide us a reference counter-measurement for the analyzed reconstruction algorithms. The laser is the same HL7851G with wavelength $\lambda = 785$ nm, and the distance separating it from the target is about 40 cm (Fig.4.8). The targets were classified in 2 groups according to the obtained results: cooperative and non-cooperative.

4.1.3.1 Cooperative surface: metal

This is the case of the PZT without any other material on it. A sinusoidal signal of ≈2 Vpp at 300 Hz was used to drive the motion of this target. The feedback variations obtained from this metallic surface [Fig.4.9(a)] were observed to fall in moderate regime as attested by the sharpened peaks in one direction of the target, and more rounded in the opposite. By visual inspection, a total of 20 peaks per period can be accounted for this SM signal, meaning a forward-backward displacement of ≈4 μm. This is thus the expected behavior for the analyzed

adaptive threshold algorithm and our proposal based on the Hilbert transform.

Disregarding the first set of detected transitions due to algorithmic initialization differences, it can be observed [Fig.4.9(b)] that both of them detect 9 transitions in one direction and 10 transitions for the opposite. Let us insist on the fact that our goal is to validate a generic behavior of the algorithms and not to characterize an instrument. i.e. the signals under test have not been acquired in favorable conditions like a proper focusing or a well dimensioned denoise filter. Also, manual tuning of the algorithms has been limited in order to truly explore the robustness of the proposals for situations where these inattentions cannot be fully controlled. Notice however that adequate conditions shall lead to improved results for a particular design.

Using the detected transitions for both cases into our proposed reconstruction algorithm, the displacement of the PZT can be approached for both algorithms. The up-down trending observed in the waveform as a result of non-symmetric accounts, denotes the need for a detrending filter prior to provide the reconstructed displacement as an exploitable output. However both waveforms are equivalent in amplitude, providing $\approx$4 μm of the reference signal.

4.1.3.2 Cooperative surface: white paper

A standard printer paper was then placed on the surface of the PZT to observe a feedback variation while keeping the same characteristics on the experimental setup. The observed fringes resulted in ambiguous shapes, even for those segments previously offering sharpened peaks [Fig.4.10(a)], thus certainly denoting a weak feedback value. Again a (harder) visual inspection allows to account $\approx$20 peaks per period. Accounting the transitions for this test, our proposal offered 9 detections per swing while the adaptive algorithm gave 9 and 8 transitions per period.

In terms of direction assignment, out proposal required to replace the weak scheme based on the pulsed derivative by a similar approach like the duty cycle algorithms already described. The difference is that our implementation only observes the duty cycle of 1 fringe to affect its direction, rather than taking the measurement over 3 sets of maxima and minima points [105].

Keeping the humps based filter procedure of previous adaptive threshold proposal, an inversion on assigned transitions can be observed as a result of an unbalanced number of transitions detected by its early stage [Fig.4.10(b)]. The result is a displacement reconstruction out of phase against the reference signal [Fig.4.10(c)]. In terms of amplitude both algorithms provide similar results, but less than the $\approx$4 μm obtained for the metallic surface.

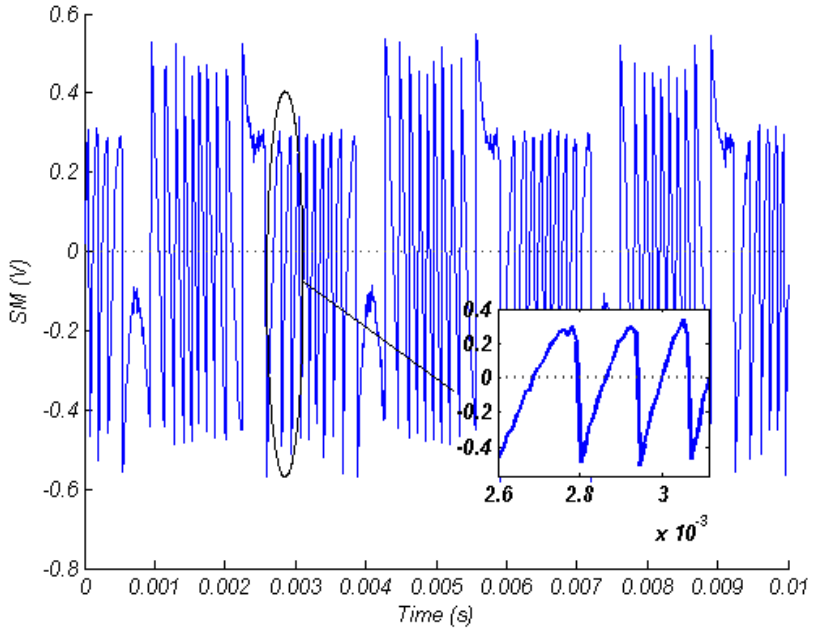

(a) Input SM signal, denoting moderate feedback.

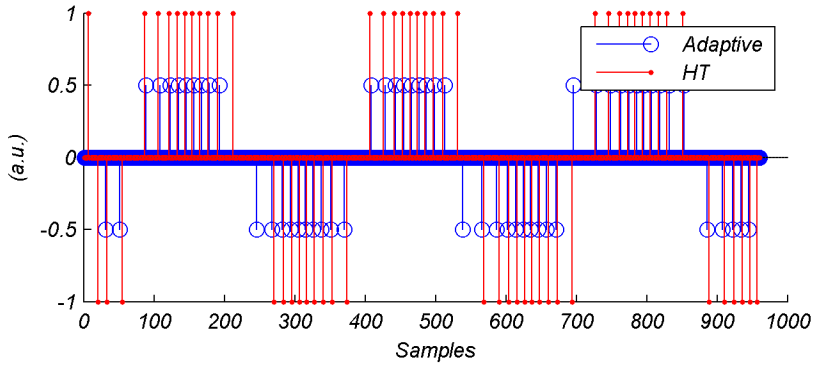

(b) Transitions found by previous method and current proposal.

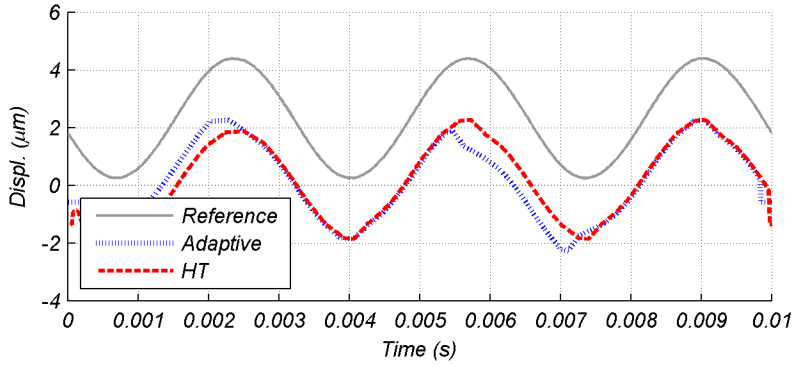

(c) Displacement reconstruction using proposed DAC algorithm.

Figure 4.9 – Experimental signal obtained from the PZT metallic surface.

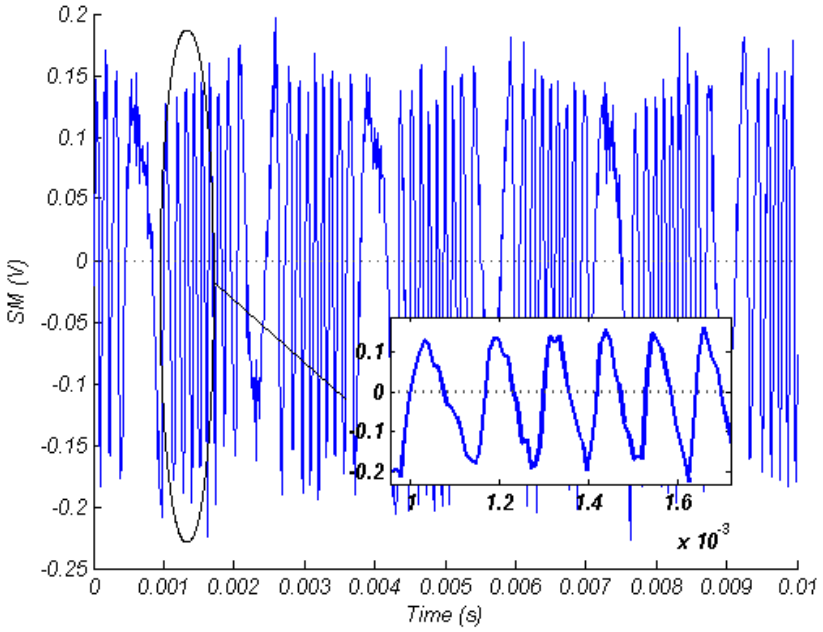

(a) Input SM signal, denoting weak feedback.

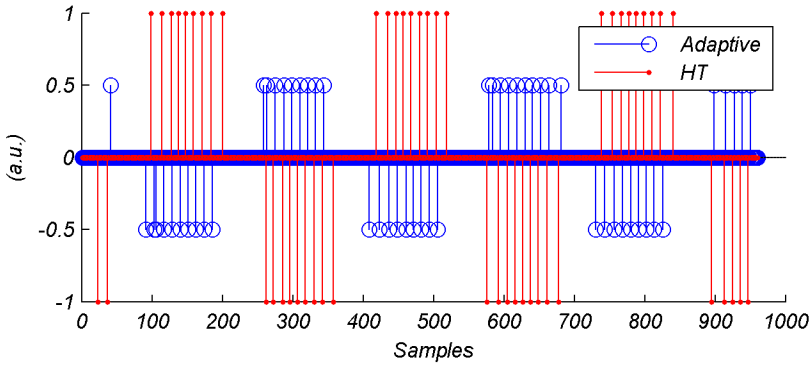

(b) Transitions found by previous method and current proposal.

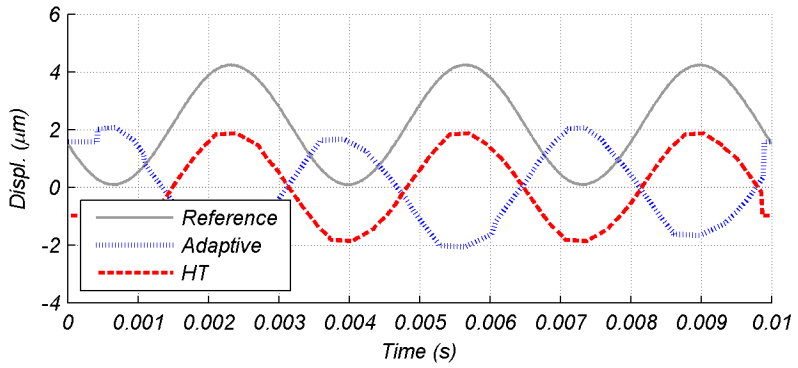

(c) Displacement reconstruction using proposed DAC algorithm.

Figure 4.10 – Experimental signal obtained from the PZT with a white paper on its surface.

4.1.3.3 Non-cooperative surface: wet white paper

The same standard printer paper was then wet with a drop of water to force a dynamic variation on the signal quality while keeping the same characteristics on the experimental setup. Two different kinds of signals were acquired in this condition [Fig.4.11(a-b)], notice however that the signal's amplitude for the second case became reduced and noisy because of the water. Visually inspecting the peaks on both signals, a total of 18 fringes per period can be accounted in this case. This might be explained by a potential variation in the pointed spot as exposed on Chapter 1.

In the first instant [Fig.4.11(c)], both algorithms detected all the transitions and assigned them properly. However in a second time [Fig.4.11(d)], the adaptive algorithm failed drastically to properly detect the transitions and as a consequence to properly assign their direction. After a careful analysis it has been observed that the issue belongs to a wrong decision taken by the adaptive threshold algorithm: after few iterations (threshold = 0.2) the search for false transitions in one side of the signal (P>0) became satisfied and then it attempted to remove false transition in the opposite side of the signal (P<0), however the amplitude variations of this segment were responsible of this threshold variation and the signal needed to be processed by the weak feedback procedure to avoid the transitions assigned in both sides for a same direction. On the other hand, our proposal only showed a minor issue by providing a swing of 10 transitions in the middle due to the noise condition. It is highlighted the fact that in both cases, the proposed algorithm was kept as a black-box with same denoise conditions.

Reconstructed displacement is then achieved constant for our proposal for these two examples demonstrating more robustness face to the previous algorithm, however it must be said that further testing sometimes produced one or two transitions assigned in wrong direction. This drawback shall be exposed within the next experiment.

4.1.3.4 Non-cooperative surface: slow fading material

The same slow-fading phosphor material active in the IR (VRC2 from Thorlabs) used for the first experimental validation was placed on the surface of the PZT in an attempt to obtain a micrometric speckle affected signal with countermeasure. The same characteristics on the experimental setup were kept except for the displacement amplitude which was slightly increased to provide ≈ 6 μm. As it can be observed, the resulting acquired signal is highly affected from one instant to another [Fig.4.12(a-b)]. This was not the case of previous experimental validation with this same material because the target (speaker cone) moved also transversally avoiding this level of signal degradation.

There can be accounted 28 fringes per period from both input signals. In the first instant

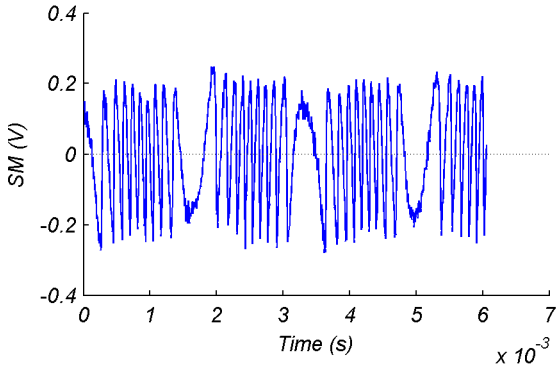

(a) Input SM signal at one instant of time.

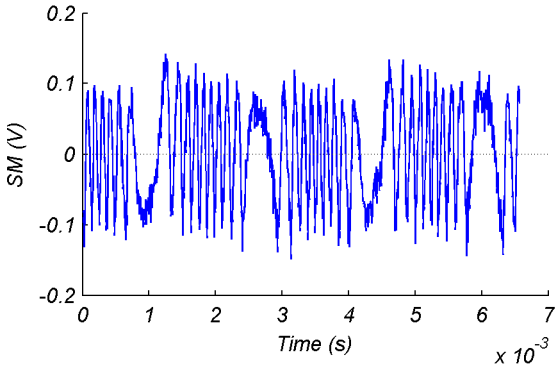

(b) Input SM signal in another instant of time.

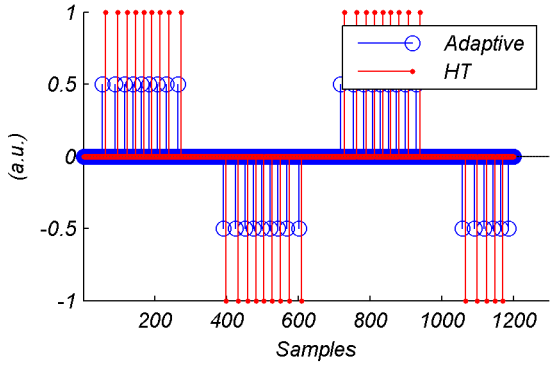

(c) Transitions found.

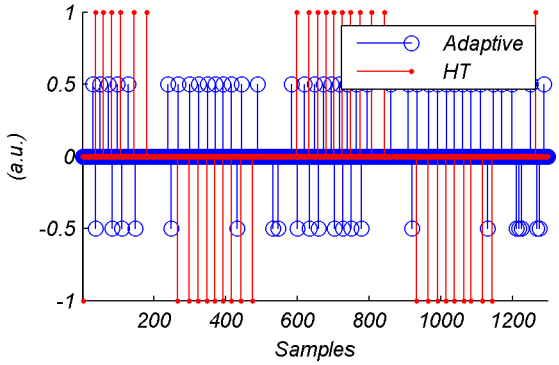

(d) Transitions found.

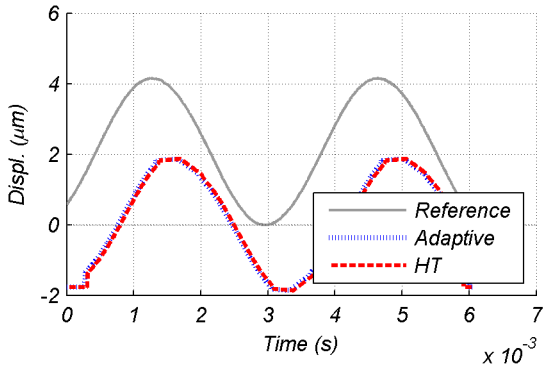

(e) Displacement reconstruction.

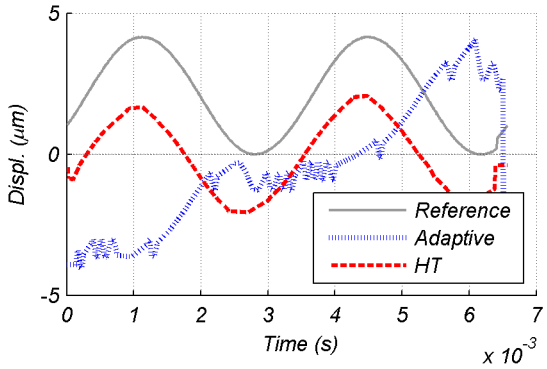

(f) Displacement reconstruction.

Figure 4.11 – Experimental signal obtained from the PZT with wet white paper on its surface.

[Fig.4.12(c)], both methods provided average results of 22 detected transitions in the beginning, but then a difference can be observed for the adaptive threshold algorithm which no longer discriminates the direction of its detected fringes. Our proposal also offers a degraded direction assignation, but still coherent with the targets direction. Again in a second time [Fig.4.12(d)], the adaptive algorithm failed drastically to properly detect the fringes due to the combination of noise and amplitude variations, falsifying the decisions taken for its filtering procedure. While keeping constant the segmentation stage made by the analytical phase calculation, our proposal required a direction assignation by improving our duty cycle implementation.

Comparing both instants of displacement reconstruction [Fig.4.12(e-f)] it can be appreciated the difficulty of the detection algorithms to handle this level of signal degradation. In the case of the adaptive algorithm it is impossible to provide a solution face to this condition. However, our current algorithm achieved better results just by improving the direction assignation block. Let us remind that in this context there are many proposals on literature as already exposed, so this limitation shall be alleviated either by improved algorithms or by hardware for a particular application.

4.1.4 Results and discussion

From the first experiment with the speaker cone, our proposal demonstrated to properly handle amplitude variations along the signal, disregarding its shape in time. This major research goal has been satisfied, allowing to perform measurements for an increased number of applications within the same framework. Then, a second experiment performing the same displacement over different surface conditions, provided an early observation of the scope of our solution. It has been further compared against the previously studied adaptive threshold scheme, to provide a reference of the requirements to produce robust instrumentation exploiting SM interferometry. The results are summarized in Table 4.1.

Let us remind that waveform reconstruction has been achieved by our D/A conversion based algorithm from Chapter 2 for both detection schemes, thus behavioral differences correspond to the fringe detection stage. The signal from the metallic surface provided fringes with a clear sawtooth-like shape with almost null hysteresis. Both algorithms detected and assigned properly these transitions. Indeed, this is the kind of surface mostly used in the reported assessment [65] of the analysed adaptive threshold algorithm.

Then, we have obtained a signal of weak feedback just by changing the surface under test (to paper) without affecting the LD's usage conditions. From it, both algorithms also detected these transitions, but previous proposal assigned them in opposite direction due to its fringe counting approach. Our proposal required an improved algorithm to assign the direction of

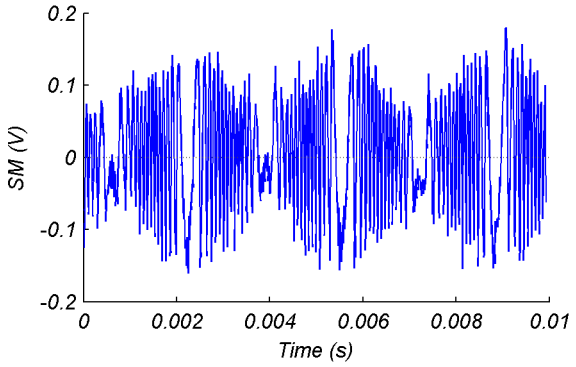

(a) Input SM signal at one instant of time.

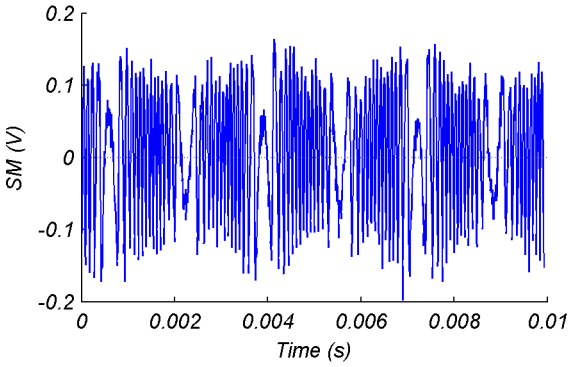

(b) Input SM signal in another instant of time.

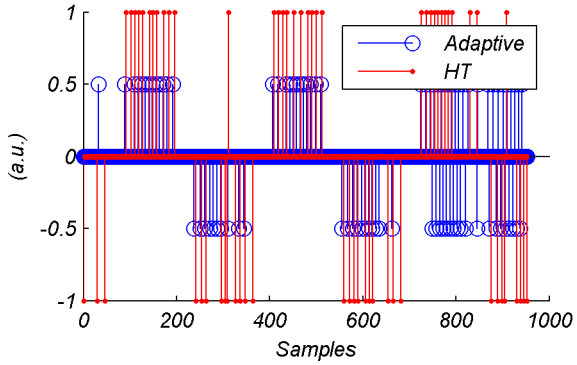

(c) Transitions found.

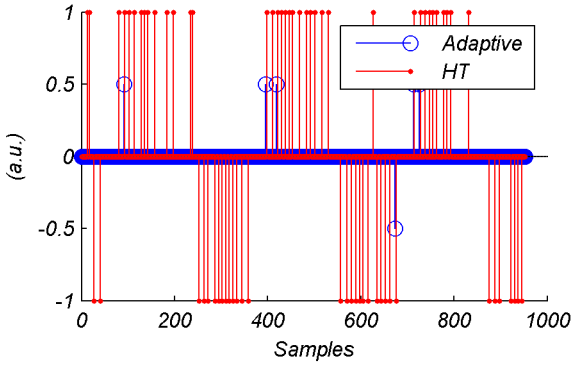

(d) Transitions found.

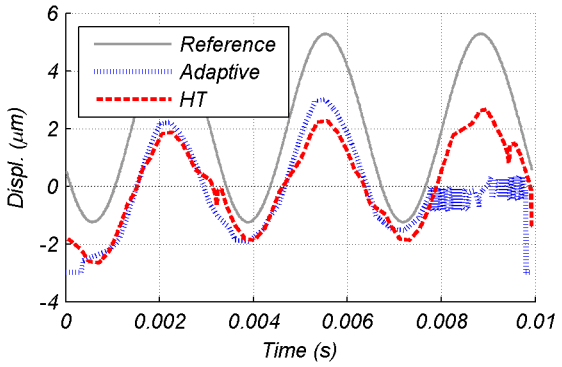

(e) Displacement reconstruction.

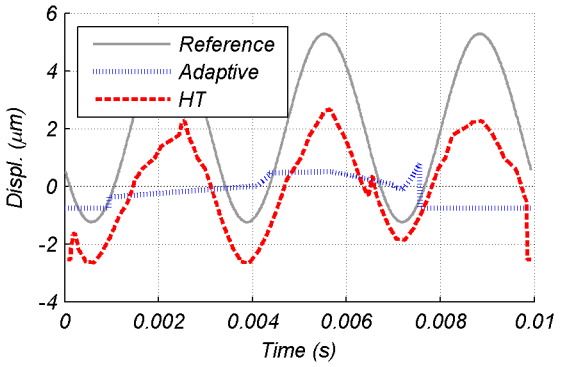

(f) Displacement reconstruction.

Figure 4.12 – Experimental signal obtained from the PZT with slow fading material on its surface.

Test	Observed signal	Adaptive Threshold Algorithm	HT based algorithm
Metallic surface	Clean moderate feedback	Correct	Correct
Printer paper	Clean weak feedback	Correct	Correct with improved direction assignment
Wet printer paper	Nosy moderate → weak feedback	Detection failed for some periods	Correct with improved direction assignment
Slow fading material	Noisy weak feedback	Detection failed for several cases	Better with improved direction assignment

Table 4.1 – Experimental results comparison between previous and current displacement reconstruction proposals.

detected fringes, but it did not affect the essence of its procedures. Direction ambiguity from SM signals of weak feedback is then an issue itself, which was considered of minor relevance in the beginning of this research work.

This became confirmed by observing the behavior face to non-cooperative surfaces. Conversely to the adaptive algorithm which completely failed to detect the fringes face to wet paper for some instants, our proposal just resulted in sporadic misassignments with our weak variant of the duty cycle algorithm implementation. This was also the case of signals severely affected in amplitude and feedback coupling from the slow fading material. Even with several attempts to improve our implementation of the duty cycle algorithm, it resulted in false assigned transitions. Face to this issue, the statistical based assignation discussed in the experimental validation is our available solution.

In a generic context, all the blocks from our proposal are suitable to be dimensioned for an embedded implementation due to their homogeneous behavior. However when the signals present a noisy weak feedback, it is necessary to modify the direction assignation procedure. The next section presents some possibilities to combine this work with recent proposals for improved results, notably in terms of precision. Despite these options, our proposed framework has demonstrated the versatility of processing signals from different conditions.

4.2 Compatibility proposal with existing methods

One of the issues addressed in this manuscript is the fact that even minor changes in the requirements from one application to another, usually imply major changes on a functional SM measurement system. In the context of algorithmic solutions suitable to be implemented

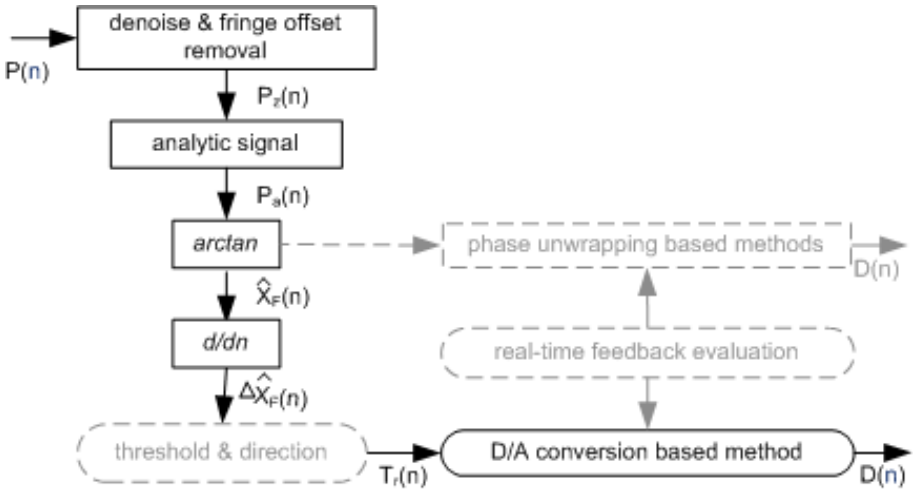

Figure 4.13 – Block diagram of identified opportunity areas for precision improvement.

in systems with low ressources, our proposals contribute by simplifying the implementation strategy in two ways: 1) by relying on standard signal processing concepts and 2) by adhering to the generic approach to handle a variety of signal conditions from different usage scenarios.

However, this modular framework still requires further improvement notably in terms of fringe direction assignation and precision characterization. Both parameters are intercorrelated and depend on the SM signal quality. In practice, it is very difficult to establish characterized values without specifying a minimum of usage conditions. Even so, in this section we highlight some identified solutions worth to explore to ease these tasks. Their compatibility with our base proposal is represented in Fig.4.13.

In particular, the non intrusive nature of the proposed phase calculation via the analytic SM signal calculation can lead to improved phase unwrapping methods. It is reminded that the benefit over a conventional *arccosine* function is the removal of a normalization step, as well as the robustness face to signal amplitude variations. Following such elaboration path would avoid the waveform elaboration through detected transitions approach (DAC algorithm), providing instead a displacement reconstruction via the phase equation (1.38) ($x_F(t) - x_0(t) + C \sin[x_F(t) + \arctan(\alpha)] = 0$). Notice, that this would require to advance the calculation of the feedback value C as described next.

4.2.1 Real-time feedback calculation

Trying to identify the feedback by a precise value of the adimensional parameter C is a cornerstone for accurate SM signal analysis. PUM provides a good estimation of the C value, however it resulted in a time consuming implementation even with the optimization procedures previously described in Chapter 2.

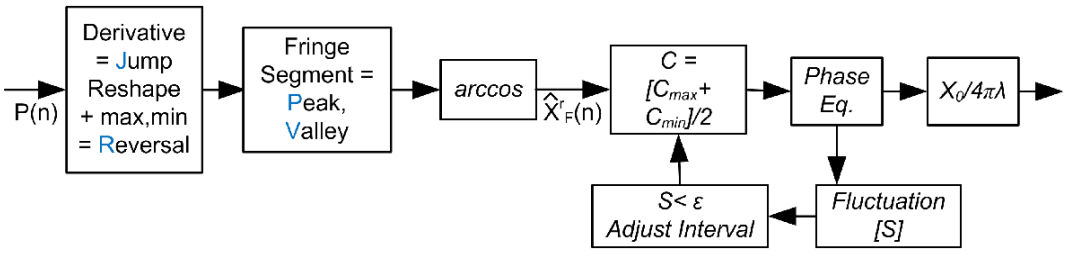

Figure 4.14 – Block diagram of the technique for real-time calculation of C.

An improved proposal to calculate the C value with less than 10 iterations and an accuracy of 98.77% [119], is represented in Fig.4.14. As stated by the authors, a correct segmentation of SM fringes allows an accurate rough phase reconstruction as described by its first three blocks. *Jump* points are found after a derivative of the SM signal, while *Reversal* points result from a search for maximum and minimum values between jumps. Then, by taking two segments of reverse points (one vibration cycle from the target) a search procedure for highest and lowest points identifies single fringes with their respective *Peak* and *Valley* points. With all the characteristic points located, the iterative calculation of C starts by defining preset values in the range [0.5, 9]. Based on the accurate rough reconstruction and the proposed value of C, the phase equation provides an approximation of the original phase. This approximation is then differentiated and integrated over the sampled window interval in order to define the fluctuation parameter (S). The interval of C values is updated in a divide and conquer strategy by the criteria of tolerance error ϵ.

In a contemporary publication from the same group [124], an approach for measuring the feedback parameter in the **frequency domain** is introduced to increase the range of calculated values up to about 10, with the advantage that it can be used for any optical feedback level. The proposed method begins by unwrapping the phase by an inverse cosine operation over a previously denoised and normalized SM signal. By defining $\theta_1(t) = \sin(\theta_F(t) + \arctan(\alpha))$, the two spectra $\Theta_F(f)$ and $\Theta_1(f)$ are calculated. Then, by defining suitable boundaries on the vanishing spectrum Ω_2, the C parameter is calculated by:

$$C = \frac{||\Theta_F(f)||}{||\Theta_1(f)||} \qquad f \subset \Omega_2 \tag{4.1}$$

To increase the accuracy of the estimate, a summation over all frequency components in Ω_2 has also been validated with this proposal. While the criteria for defining the boundary requires an off-line calculation, this method certainly enlightens the robustness that can be exploited from the frequency domain of SM signals.

As it can be observed, a means for target direction identification is always required to achieve improved results. To this end, let us briefly present a recent proposal next.

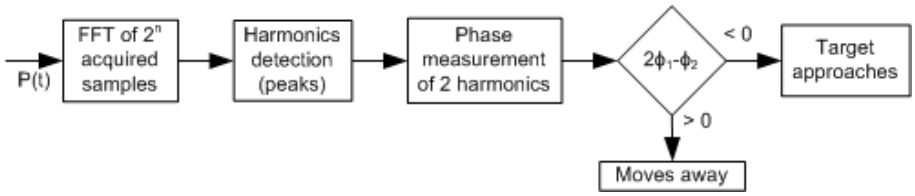

Figure 4.15 – Block diagram of phase based proposal for velocity sign retrieval.

4.2.2 Improved target direction identification

An algorithmic solution to measure speed and direction of a remote target in frequency domain [125], seems an interesting option to evaluate in our case of single fringe direction assignation. In fact, a quite recent implementation of this algorithm allowed a SM instrument to perform velocity measurement 10 meters away from the target [126].

The proposed elaboration (Fig.4.15) consists in detecting the harmonics of a set of fringes via a fast Fourier transform. From them, the first and second harmonics are taken to compute its phases ϕ_1 and ϕ_2. Finally by exploiting the property that a real and odd signal has a purely imaginary spectral representation, they are able to distinguish the sign of the movement by doing $\phi_{10} = 2\phi_1 - \phi_2$.

As mentioned by the authors, the prototype for long distances needed further processing to provide smoother position reconstructions (even from the approach of velocity integration) due to variations on the direction detection, in particular for poor optical conditions. Thus confirming the same difficulty faced by our current proposal.

4.2.3 External hardware assistance

As discussed in the beginning of this manuscript, industrial embracement of SM interferometry is penalized by the many options to provide reliable signal exploitation. The algorithms provided in this manuscript can be considered as a framework able to be combined with specific hardware, to meet critical requirements like precision and accuracy.

From the different devices observed along this work, three elements are foreseen suitable for improved embedded SM sensor design: 1) the usage of liquid lens for dynamic focusing, 2) laser current modulation for direction discrimination, and 3) the compensation of mechanical vibrations on the instrument via an accelerometer coupled to it. Let us remind that laser current modulation requires a particular reshape to achieve a true lineal optical frequency sweep. Also, the liquid lens might be limited in response time for certain applications.

It is worth to mention a potential benefit of our proposal with the promising solution coupled to an accelerometer, as it removes the need for an optical table support. The accelerometer's monitored signal on the optical axis is converted to displacement by applying

a double integration, it is then subtracted to the SM signal, providing a displacement reconstruction free of parasitic vibrations.

Regarding the noise obtained from acquired signals, a considerable effort needs to be addressed to provide clean signals to the different processing steps. Indeed, either time or frequency domain algorithms are prone to errors due to uncovered usage conditions. It is thus expected to observe more techniques of adaptive filtering from signal processing theory.

4.3 Perspectives for embedded implementation

Hilbert transform based **detection** and D/A conversion based **reconstruction** algorithms have been proposed in this manuscript with the idea of being implemented as part of embedded SM instrumentation.

Indeed, by miniaturizing a SM sensor it is possible to imagine parallel readouts. An example of this approach has been published in 2009 [127], where a monolithic VCSEL array served as a self-mixing imaging sensor. To finish this manuscript, let us briefly present in this section one expected path to undertake in our research of versatile systems by exposing the reconfigurability goal for our proposal.

4.3.1 Architectural exploration

The tradeoff of various types of architectures to implement DSP algorithms has been a topic of research since the initial development of its theory. Recently, the application of these DSP algorithms to systems that require low cost and the lowest possible energy consumption has placed a new emphasis on defining the most appropriate solutions. The fundamental challenge is how to map data processing algorithms onto the underlying hardware, while meeting application constraints for power, performance, and area [128].

Other than identifying potential applications for SM interferometry in embedded domain, the usage of a reconfigurable development platform shall allow new algorithm proposals to be aware of real-time processing trends as discussed on Chapter 2. Also, the ability to quickly explore many system realizations by selecting an architecture that best utilizes the intrinsic computational efficiency of silicon technology, shall result in a valuable contribution for industrial development.

Let us represent in Fig.4.16 the proposed base architecture in the form of a System-On-Chip (SoC) which might be used to assist this task. While some signal processing blocks are prone to be replaced by improved solutions, others might be just optimized via hardware (HW) or software (SW) implementations to meet specific constraints. For example,

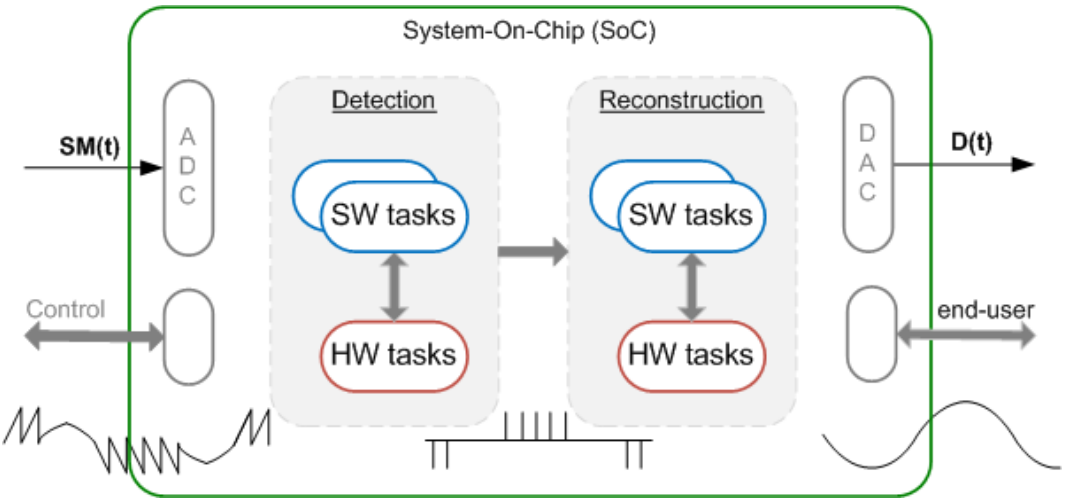

Figure 4.16 – Proposed reconfigurable architecture for our algorithms.

different amplitude measurements in same usage conditions might require to adapt a sequential computation in a processor, to a fast parallel calculation via logic circuits. More precisely, the detection stage of our proposal could calculate its Fourier transforms via a Field Programmable Gate Array (FPGA), and then assemble the analytic signal in a processor (software) for next steps. Similarly for our reconstruction algorithm, the creation of an impulse response and the summation of detected transitions could be handled in software, while the convolution stage could work continuously in a FPGA.

Such a level of dynamism requires to explore new paradigms on embedded system development and shall lead to further research in the field of reconfigurable systems. The expected approach to follow in our context, is the codesign strategy exposed next.

4.3.2 Hardware and software codesign

Traditionally, algorithms and architectures are developed by different engineering teams who also use different tools to describe their designs. This development cycle is prone to recurrent modifications in either software or hardware designs. However they are usually identified until an integration step (Fig.4.17), thus penalizing the cost and time of system's delivery. With the advent of complex systems, there is a pressing need for system architecture design to tightly couple into algorithmic and technology parameters in order to provide the most effective solution.

Codesign is a development strategy aiming to assist efficient system realizations. By providing new tools and common languages for HW and SW, a space of solutions can be explored considering parameters like: real-time constraints, performance, cost, power and reliability. Starting from specifications traceable along the development cycle, algorithmic

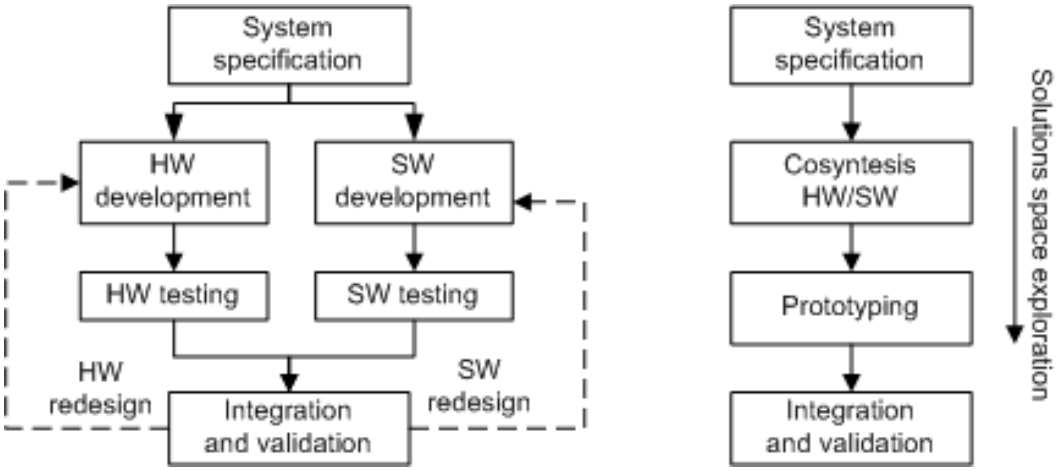

Figure 4.17 – Comparison between traditional system development codesign.

tasks are partitioned to be executed in HW or SW and then synthesized for evaluation within a common environment. This early interaction provides seamless integration of systems for final validation.

Among its different research domains, our first endeavors shall be in the context of HW/SW co-simulation of SM signal processing algorithms to estimate calculation time and memory usage in a variety of conditions. This shall lead to worthy contribution in embedded sensors exploiting the principle of SM interferometry.

4.4 Conclusion

In this chapter we have combined and further validated the two major contributions of this research work, the Hilbert transform based **detection** and D/A conversion based **reconstruction** algorithms. Since the later was demonstrated to be behaviorally equivalent with a simplified version of the slopes based approach from prior research, it was used for waveform elaboration along the different experiments.

Concerning our fringe detection approach, it was further compared against the analyzed prior research to stress its pertinence, but also to denote their limitations regarding fringe direction assignment. We have shown that low signal-to-noise ratios obtained for weak feedback coupling require further processing steps to provide satisfying results mainly for autonomous usage. Indeed, this is one of the recurrent issues addressed in SM literature as described in the section of compatibility proposals.

The signal processing design scheme and the coherence of its modular approach, bring forward the potential of this contribution to be considered as a framework for embedded SM instrumentation. Nowadays that hardware is relatively cheap and that algorithmic solutions

keep evolving, the challenges foreseen on the implementation of SM sensors shall meet the criteria of complex embedded system design, requiring advanced tools and methods. Therefore as part of this research work we have pointed out as first criteria for further development the computation and memory resources, however in the in the future is expected to consider power consumption and fabrication price.

General conclusion

This work has been presented in continuity of a path undertaken in this research center aiming to design versatile displacement measurement systems exploiting self-mixing phenomenon. Due to the reduced number of optical components, the compactness, self-aligned and integrated nature, the potential of this sensing scheme as a cost-effective solution lead us to further approach an embedded implementation suitable for industrialization purposes.

A research on reported devices suitable for real environment operation, allowed to confirm the variety of methods and prototypes addressing specific issues and applications. The complexity of dealing with the different effects suffered by the interference pattern takes an important role in this variety of published proposals. While this rich SM literature continually inspires improved solutions, it penalizes a dynamic development embracement face to the overwhelming task of evaluating feasible instrumentation.

Two abstract functional blocks were used to approach the exploitation of SM signals for displacement measurement: the detection of interferometric fringes and the waveform reconstruction from them. Prior published algorithms were considered as starting point for this thesis, the adaptive threshold algorithm and the slopes based method (SBM) respectively.

First SBM, was carefully analyzed for its usage into a system with limited resources like memory and calculation power, without disregarding the need for straightforward scalability. At this point, the interferometric fringes from an incoming SM signal were considered to be properly detected as an important challenge in this context was foreseen from the experience acquired while dealing with SM signals. The behavioral characteristics of SBM tasks and the viability to satisfy imposed completion deadlines were thus evaluated, in particular, the fringe-loss compensation feature was advised as non deterministic in a generic real-time context. Similarly, the segmentation of hump areas for slope placement was observed as a complex implementation prone to indexing errors. A simplified reconstruction algorithm was then proposed derived from interpolation theory as observed in digital-to-analog converters. This flexible elaboration allowed to implement a proof of concept for real-time displacement reconstruction on a digital signal processor (DSP) board.

Once this functional block was validated, the case of fringe detection via the adaptive threshold algorithm was studied. To observe more realistic usage conditions, non-cooperative signals from rough targets were also considered in the evaluation. In terms of real-time viability, it was observed its need for a considerable quantity of memory resources and calculation time due to the requirement to acquire SM fringes of a forward-backward movement to work properly. Despite its iterative nature, the feasibility to meet timing

constraints was confirmed but the implementation versatility requires a careful understanding of internal workings like the humps based filtering process. The weakness of this time-domain algorithm to handle amplitude variations at some instants over an acquired period became the motivation for a spectral analysis of SM displacement signals. From it, the analytical SM signal elaboration resulted in an interesting solution to observe the phase of SM fringes along the time. Conversely to a classical approach observed in previous reported methods, this instantaneous phase is insensitive to amplitude variations and works disregarding the shape in time of SM fringes. A new algorithm for fringe detection was then proposed with the intention to improve the real-time constraint definition, and compatible with our proposal for displacement reconstruction. It's strenght resides in a combination of hysteresis removal with an homogeneous phase observation from the SM fringes.

The simulations and experimental comparison showed its pertinence to be used as a generic approach suitable to handle punctual amplitude variations on SM signals. Further experiments over different surface conditions demonstrated a difficulty to properly assign the direction of each detected fringe when the feedback condition is weak and noisy. Some improvements to the current direction assignation procedure as well as variations in the denoise parameters, allowed better results as compared to the previous adaptive threshold approach. While analysing its compatibility features with existing methods, a contemporary publication confirmed the same difficulty faced by our current proposal. However we pointed out a path to follow in order to provide the most effective solutions to provide versatile SM sensors in this field.

Let us conclude this work by stating that the quest for an universal solution to process all the signals for any requirements specification is a complex task which can be better satisfied by having a consolidated framework like the algorithmic approach presented here. Complemented by a well understanding on the tradeoffs in terms of resolution, the usage of external components, stability of the signal and overall deployment effort, the appearance of SM sensors shall be taken to a dynamic stage of development.

Bibliography

[1] S. Donati, "Developing self-mixing interferometry for instrumentation and measurements," *Laser Photonics*, vol. 6, no. 3, pp. 393 – 417, 2012. (pp. vi, 23, 30 and 33.)

[2] P. King and G. Steward, "Metrology with an optical maser," *New Scientist*, vol. 17, pp. 180–182, 1963. (p. 1.)

[3] P. Hariharan, *Basics of Interferometry*. Academic Press, 1991, p. 45. (p. 1.)

[4] S. Imran and M. Yamada, "Numerical analysis of suppression effects on optical feedback noise by superposition of high frequency current in semiconductor lasers," *IEEE J. Quantum Electron.*, vol. 49, no. 2, pp. 196–204, 2013. (p. 1.)

[5] D. Clunie and H. Rock, "The laser feedback interferometer," *Journal of Scientific Instruments*, vol. 41, pp. 489–492, 1964. (p. 1.)

[6] M. Rudd, "A laser Doppler velocimeter employing the laser as a mixer-oscillator," *Journal of Scientific Instruments*, vol. 1, pp. 723–726, 1968. (p. 1.)

[7] T. Honneycutt and W. Otto, "A CO2 interferometer by reflected waves," *IEEE J. Quantum Electron.*, vol. 8, pp. 91–93, 1972. (p. 2.)

[8] S. Donati, "Laser interferometry by induced modulation of cavity field," *Journal of Applied Physics*, vol. 49, no. 2, p. 495, 1978. (p. 2.)

[9] M. Spencer and W. Lamb, "Laser with a transmitting window," *Physical Review A*, vol. 6, no. 2, pp. 884–892, feb 1972. (p. 2.)

[10] R. Lang and K. Kobayashi, "External optical feedback effects on semiconductor injection laser properties," *IEEE J. Quantum Electron.*, vol. 16, no. 3, pp. 347–355, mar 1980. (p. 2.)

[11] A. Dandridge, O. Miles, and G. Giallorenzi, "Diode laser sensor," *Electronics Letters*, vol. 16, no. 25, pp. 948–949, dec 1980. (p. 2.)

[12] S. Shinohara, A. Mochizuki, H. Yoshida, and M. Sumi, "Laser Doppler velocimeter using the self-mixing effect of a semiconductor laser diode," *Applied Optics*, vol. 25, no. 9, pp. 1417–19, may 1986. (p. 2.)

[13] G. Beheim and K. Fritsch, "Range finding using frequency-modulated laser diode," *Applied Optics*, vol. 25, no. 9, p. 1439, may 1986. (pp. 2 and 17.)

[14] S. Donati, G. Giuliani, and S. Merlo, "Laser diode feedback interferometer for measurement of displacements without ambiguity," *IEEE J. Quantum Electron.*, vol. 31, no. 1, pp. 113–9, 1995. (p. 2.)

[15] P. Roos, M. Stephens, and C. Wieman, "Laser vibrometer based on optical-feedback-induced frequency modulation of a single-mode laser diode," *Applied Optics*, vol. 35, no. 34, pp. 6754–61, dec 1996. (pp. 2 and 76.)

[16] T. Bosch, C. Bès, L. Scalise, and G. Plantier, "Optical feedback interferometry," in *Encyclopedia of Sensors*. American Scientific Publishers, 2006, vol. 7, pp. 107 – 126. (pp. 2 and 17.)

[17] *Philips Laser Sensors - Technology White Paper*, Philips, 2005. (pp. 2 and 76.)

[18] T. Bosch, N. Servagent, and F. Boyer, "Vibrations measurement with a self-mixing type laser displacement sensor for modal analysis," in *Proc. IEEE-I2MTC*, 1996, pp. 648–653. (p. 2.)

[19] T. Bosch, N. Servagent, and R. Chellali, "A scanning range finder using the self-mixing effect inside a laser diode for 3-D vision," in *Proc. IEEE-I2MTC*, 1996, pp. 226–231. (p. 2.)

[20] G. Giuliani, S. Donati, M. Passerini, and T. Bosch, "Angle measurement by injection detection in a laser diode," *Optical Engineering*, vol. 40, no. 1, pp. 95–99, 2001. (p. 2.)

[21] V. Annovazzi-Lodi, S. Merlo, and M. Norgia, "Measurements on a micromachined silicon gyroscope by feedback interferometry," *IEEE/ASME Trans. Mechatronics*, vol. 6, no. 1, pp. 1–6, 2001. (p. 2.)

[22] T. M. Fathi and S. Donati, "Thickness measurement of transparent plates by a self-mixing interferometer," *Optics Letters*, vol. 35, no. 11, pp. 1844 – 1846, 2010. (p. 2.)

[23] S. Odermatt and B. Witzigmann, "A microscopic model for the static and dynamic lineshape of semiconductor lasers," *IEEE J. Quantum Electron.*, vol. 42, no. 6, pp. 538 – 551, 2006. (p. 2.)

[24] P. J. Caber, "Interferometric profiler for rough surfaces," *Applied Optics*, vol. 32, no. 19, pp. 3438–3441, Jul 1993. (p. 2.)

[25] G. Giuliani and M. Norgia, "Laser diode linewidth measurement by means of self-mixing interferometry," *IEEE Photon. Technol. Lett.*, vol. 12, pp. 1028–1030, 2000. (p. 2.)

[26] Y. Yanguang, G. Giuliani, and S. Donati, "Measurement of the linewidth enhancement factor of semiconductor lasers based on the optical feedback self-mixing effect," *IEEE Photon. Technol. Lett.*, vol. 16, pp. 990–992, 2004. (pp. 2 and 36.)

[27] A. Courteville, T. Gharbi, and J. Cornu, "Noncontact MMG sensor based on the optical feedback effect in a laser diode," *Journal of Biomedical Optics*, vol. 3, pp. 281–285, 1998. (p. 2.)

[28] C. Zakian and M. Dickinson, "Laser Doppler imaging through tissues phantoms by using self-mixing interferometry with a laser diode," *Optics Letters*, vol. 32, no. 19, pp. 2798–2800, Oct 2007. (p. 2.)

[29] I. Milesi, M. Norgia, P. P. Pompilio, C. Svelto, and R. L. Dellaca, "Measurement of local chest wall displacement by a custom self-mixing laser interferometer," *IEEE Trans. Instrum. Meas.*, vol. 60, no. 8, pp. 2894–2901, aug. 2011. (p. 2.)

[30] S. Donati and G. Martini, "Self-mixing interferometry: A universal yardstick for optical measurements," in *Proc. IEEE-WIO*, jun 2011, pp. 1–3. (p. 3.)

[31] L. Yah Leng, J. R. Tucker, and A. D. Rakic, "Distance measurement using the change in junction voltage across a laser diode due to the self-mixing effect," in *Proc. SPIE*, vol. 6038, 2006, pp. 73–77. (p. 4.)

[32] J. Perchoux and T. Bosch, "Multimode VCSELs for self-mixing velocity measurements," in *Proc. IEEE-Sensors*, 2007, pp. 419–422. (p. 4.)

[33] J. Perchoux, L. Campagnolo, L. Yah Leng, and A. Rakic, "Lens-free self-mixing sensor for velocity and vibrations measurements," in *Proc. IEEE-COMMAD*, 2010, pp. 43–44. (p. 4.)

[34] K. Petermann, *Laser diode modulation and noise*. Kluwer Academin Publishers, 1991. (pp. 5, 7 and 11.)

[35] W. M. Wang, W. J. Boyle, K. T. Grattan, and A. W. Palmer, "Self-mixing interference in a diode laser: experimental observations and theoretical analysis," *Applied Optics*, vol. 32, no. 9, pp. 1551–1558, 1993. (p. 6.)

[36] C. Henry, "Theory of the linewidth of semiconductor lasers," *IEEE J. Quantum Electron.*, vol. 18, pp. 259–264, 1982. (p. 7.)

[37] G. Acket, D. Lenstra, A. Den Boef, and B. Verbeek, "The influence of feedback intensity on longitudinal mode properties and optical noise in index-guided semiconductor lasers," *IEEE J. Quantum Electron.*, vol. 20, no. 10, pp. 1163–1169, 1984. (p. 8.)

[38] L. Golderg, H. F. Taylor, A. Dandridge, J. F. Weller, and R. O. Miles, "Spectral characteristics of semiconductor lasers with optical feedback," *IEEE J. Quantum Electron.*, vol. QE-18, pp. 555 – 564, 1982. (p. 8.)

[39] G. Mourat, "Etude de diodes laser pour des applications métrologique de la rétro-injection optique," Ph.D. dissertation, Institut National Polytechnique de Toulouse, 1999. (p. 9.)

[40] R. W. Tkach and A. R. Chraplyvy, "Regimes of feedback effects in 1.5 pm distributed feedback lasers," *Journal of Lightwave Technology*, vol. LT-4, pp. 1655 – 1661, 1986. (p. 9.)

[41] J. El-Assad, T. Bosch, and G. Plantier, "Laser diode under strong feedback for mechatronics applications," in *Proc. IEEE-Sensors*, 2007, pp. 387–390. (p. 10.)

[42] S. Donati and M. T. Fathi, "Transition from short-to-long cavity and from self-mixing to chaos in a delayed optical feedback laser," *IEEE J. Quantum Electron.*, vol. 48, no. 10, pp. 1352–1359, Oct. 2012. (p. 10.)

[43] N. Schunk and K. Petermann, "Numerical analysis of the feedback regimes for a single-mode semiconductor laser with external feedback," *IEEE J. Quantum Electron.*, vol. 24, pp. 1242 – 1247, 1988. (p. 10.)

[44] S. Donati and H. Ray-Hua, "The diagram of feedback regimes revisited," *Selected Topics in Quantum Electronics, IEEE Journal of*, vol. 19, p. 1500309, 2013. (p. 10.)

[45] W. M. Wang, K. T. Grattan, A. W. Palmer, and W. J. Boyle, "Self-mixing interference inside a single-mode diode laser for optical sensing applications," *Journal of Lightwave Technology*, vol. 12, no. 9, pp. 1577–1587, 1994. (pp. 11 and 12.)

[46] N. Servagent, "Etude et conception de capteurs optoélectroniques auto-alignés de distances et déplacements pour le contrôle non destructif," Ph.D. dissertation, Institut National Polytechnique de Toulouse, 1997. (p. 11.)

[47] S. Ottonelli, F. De Lucia, M. di Vietro, M. Dabbicco, G. Scamarcio, and F. P. Mezzapesa, "A compact three degrees-of-freedom motion sensor based on the laser-self-mixing effect," *IEEE Photon. Technol. Lett.*, vol. 20, no. 16, pp. 1360–1362, Aug. 2008. (p. 14.)

[48] J. H. Churnside, "Signal-to-noise in a backscatter-modulated Doppler velocimeter," *Applied Optics*, vol. 23, pp. 2097–2101, 1984. (p. 14.)

[49] C. Bès, "Conception d'un système laser de mesures de déplacements par interférométrie à rétro-injection optique dans le cas de feedbacks faible et modéré," Ph.D. dissertation, Institut National Polytechnique de Toulouse, 2006. (pp. 14, 18, 19, 30 and 37.)

[50] J. Perchoux, H. E. Dougan, F. Bony, and A. D. Rakic, "Photodiode-free Doppler velocimeter based on self-mixing effect in commercial vcsel," in *Proc. IEEE-Sensors*. Ieee, 2008, pp. 290–293. (pp. 14 and 15.)

[51] G. Giuliani, M. Norgia, S. Donati, and T. Bosch, "Laser diode self-mixing technique for sensing applications," *Journal of Optics A: Pure and Applied Optics*, vol. 4, pp. 283–294, 2002. (pp. 17 and 22.)

[52] P. de Groot, G. Gallatin, and S. Macomber, "Ranging and velocimetry signal generation in a backscatter-modulated laser diode," *Applied Optics*, vol. 27, no. 21, pp. 4475–4480, Nov 1988. (p. 17.)

[53] G. Mourat, N. Servagent, and T. Bosch, "Optical feedback effects on the spectral linewidth of semiconductor laser sensors using self-mixing interference," *IEEE J. Quantum Electron.*, vol. 34, no. 9, pp. 1717–1721, 1998. (p. 17.)

[54] M. Norgia, A. Magnani, and A. Pesatori, "High resolution self-mixing laser rangefinder," *The Review of scientific instruments*, vol. 83, no. 4, pp. 45 113–45 113–6, Apr. 2012. (p. 17.)

[55] G. Plantier, C. Bes, and T. Bosch, "Behavioral model of a self-mixing laser diode sensor," *IEEE J. Quantum Electron.*, vol. 41, no. 9, pp. 1157–1167, sep. 2005. (pp. 18 and 20.)

[56] J. El-Assad, "Analysis of self-mixing moderate and strong feedback regimes for mechatronics applications," Ph.D. dissertation, Institut National Polytechnique de Toulouse, 2008. (p. 20.)

[57] U. Zabit, "Optimisation of a self-mixing laser displacement sensor," Ph.D. dissertation, Institut National Polytechnique de Toulouse, 2010. (pp. 20, 30, 31, 34, 37, 38, 44 and 83.)

[58] A. Luna-Arriaga, F. Bony, and T. Bosch, "Progress on self-mixing sensors for in-situ displacement measurement," in *Proc. IEEE-ECMSM*, 2013, pp. 1 – 5. (p. 23.)

[59] M. Norgia, S. Donati, and D. D'Alessandro, "A displacement-measuring instrument utilizing self-mixing interferometry," *IEEE Trans. Instrum. Meas.*, vol. 52, no. 6, pp. 1765 – 1770, dec. 2003. (pp. 23 and 123.)

[60] G. Giuliani, S. Bozzi-Pietra, and S. Donati, "Self-mixing laser diode vibrometer," *Measurement Science and Technology*, vol. 14, pp. 24 – 32, 2003. (p. 24.)

[61] A. Magnani, A. Pesatori, and M. Norgia, "Self-mixing vibrometer with real-time digital signal elaboration," *Applied Optics*, vol. 51, no. 21, pp. 5318 – 5325, 2012. (pp. 25 and 33.)

[62] U. Zabit, O. D. Bernal, A. Chamorro-Coloma, and T. Bosch, "Real-time accelerometer coupled self-mixing laser displacement sensor for embedded applications," in *Proc. IEEE-Sensors*, 2012, pp. 1–4. (p. 26.)

[63] A. Valavanis, P. Dean, L. Yah Leng, R. Alhathlool, M. Nikolic, R. Kliese, S. Khanna, D. Indjin, S. Wilson, A. Rakic, E. Linfield, and G. Davies, "Self-mixing interferometry with terahertz quantum cascade lasers," *IEEE Sensors J.*, vol. 13, no. 1, pp. 37–43, 2013. (p. 30.)

[64] L. Campagnolo, M. Nikolic, J. Perchoux, L. Yah Leng, K. Bertling, K. Loubiere, L. Prat, A. D. Rakic, and T. Bosch, "Flow profile measurement in microchannel using the optical feedback interferometry sensing technique," *Microfluidics and Nanofluidics*, vol. 14, pp. 1613–4982, Jul. 2012. (p. 30.)

[65] U. Zabit, T. Bosch, and F. Bony, "Adaptive transition detection algorithm for a self-mixing displacement sensor," *IEEE Sensors J.*, vol. 9, no. 12, pp. 1879 – 1886, 2009. (pp. 31, 75, 80, 85, 100 and 142.)

[66] U. Zabit, T. Bosch, F. Bony, and A. Rakic, "A self-mixing displacement sensor with fringe-loss compensation for harmonic vibrations," *IEEE Photon. Technol. Lett.*, vol. 22, no. 6, pp. 410–412, 2010. (pp. 31, 34, 40, 44 and 51.)

[67] A. Luna-Arriaga, F. Bony, and T. Bosch, "Digital to analog conversion methodology applied to self-mixing displacement signals," in *Proc. AIP-AIVELA*, vol. 1457, 2012, pp. 125 – 131. (p. 32.)

[68] N. Servagent, T. Bosch, and M. Lescure, "Design of a phase-shifting optical feedback interferometer using an electro-optic modulator," *Selected Topics in Quantum Electronics, IEEE Journal of*, vol. 6, pp. 798–802, 2000. (p. 32.)

[69] D. Guo and M. Wang, "Self-mixing interferometry based on sinusoidal phase modulation and integrating-bucket method," *Optics Communications*, vol. 283, pp. 2186–2192, 2010. (p. 32.)

[70] D. Guo, "Quadrature demodulation technique for self-mixing interferometry displacement sensor," *Optics Communications*, vol. 284, no. 24, pp. 5766–5769, dec. 2011. (p. 32.)

[71] N. Takahashi, S. Kakuma, and R. Ohba, "Active heterodyne interferometric displacement measurement using optical feedback effects of laser diodes," *Optical Engineering*, vol. 35, pp. 802–807, 1996. (p. 32.)

[72] X. Cheng and S. Zhang, "Multiple selfmixing effect in VCSELs with asymmetric external cavity," *Optics Communications*, vol. 260, pp. 50–56, 2006. (p. 32.)

[73] M. Ruiz-Llanta and H. Lamela, "Self-mixing technique for vibration measurements in a laser diode with multiple modes created by optical feedback," *Applied Optics*, vol. 48, pp. 2915–2923, 2009. (p. 33.)

[74] R. Kliese, L. Yah Leng, K. Bertling, A. Ashrif, A. Bakar, T. Bosch, and A. D. Rakic, "Self-mixing displacement sensing using the junction voltage variation in a GaN laser," in *Proc. IEEE-COMMAD*, 2008. (p. 33.)

[75] M. Norgia and A. Pesatori, "New low cost analog self-mixing vibrometer," in *Proc. IEEE Sensors*, 2010. (p. 33.)

[76] A. Pesatori and M. Norgia, "Fully analog self-mixing laser vibrometer," in *Proc. IEEE-I2MTC*, 2011, pp. 1–4. (p. 33.)

[77] S. Merlo and S. Donati, "Reconstruction of displacement waveforms with a single-channel laser-diode feedback interferometer," *IEEE J. Quantum Electron.*, vol. 33, pp. 527–531, 1997. (p. 34.)

[78] C. Bès, V. Belloeil, G. Plantier, Y. Gourinat, and T. Bosch, "A self-mixing laser sensor design with an extended Kalman filter for optimal online structural analysis and damping evaluation," *IEEE/ASME Trans. Mechatronics*, vol. 12, no. 3, pp. 387 – 394, jun. 2007. (p. 34.)

[79] N. Servagent, F. Gouaux, and T. Bosch, "Measurements of displacement using the self-mixing interference in a laser diode," *Journal of Optics*, vol. 29, pp. 168–173, 1998. (p. 34.)

[80] U. Zabit, O. D. Bernal, and T. Bosch, "Self-mixing sensor for real-time measurement of harmonic and arbitrary displacements," in *Proc. IEEE-I2MTC*, 2012. (p. 34.)

[81] G. Plantier, C. Bes, T. Bosch, and F. Bony, "Auto adaptive signal processing of a laser diode self-mixing displacement sensor," in *Proc. IEEE-I2MTC*, 2005, pp. 1013–1017. (p. 34.)

[82] C. Bès, G. Plantier, and T. Bosch, "Displacement measurements using a self-mixing laser diode under moderate feedback," *IEEE Trans. Instrum. Meas.*, vol. 55, no. 4, pp. 1101–1105, 2006. (p. 34.)

[83] K. Petermann, "External optical feedback phenomena in semiconductor lasers," *Selected Topics in Quantum Electronics, IEEE Journal of*, vol. 1, no. 2, pp. 480–489, 1995. (p. 36.)

[84] G. H. M. Van Tartwijk and D. Lenstra, "Semiconductor lasers with optical injection and feedback," *Quantum Semiclass. Opt.*, vol. 7, pp. 87–143, 1995. (p. 38.)

[85] R. Oshana, *DSP software development techniques for embedded and real-time systems*. Newnes, 2006. (p. 43.)

[86] U. Zabit, F. Bony, and T. Bosch, *Optimization of the Nelder-Mead simplex method for its implementation in a self-mixing laser displacement sensor*. Springer, 2008, vol. 20, ch. IX, pp. 381–400. (p. 44.)

[87] U. Zabit, T. Bosch, and F. Bony, "A fast derivative-less optimization of the feedback coupling coefficient for a self-mixing laser displacement sensor," in *Proc. IEEE-NEWCAS-TAISA*, 2009. (p. 44.)

[88] J. G. Proakis and D. G. Manolakis, *Digital Signal Processing - Principles, Algorithms and Applications*. Pearson Prentice Hall, 2007. (p. 54.)

[89] A. Oppenheim and R. Schafer, *Discrete-time signal processing*. Prentice-Hall, 1989. (p. 55.)

[90] S. Maymon and A. Oppenheim, "Sinc interpolation of nonuniform samples," *IEEE Trans. Signal Process.*, vol. 59, pp. 4745 –4758, 2011. (p. 56.)

[91] A. Kaw and E. E. Kalu, *Numerical methods with applications*, http://www.autarkaw.com, Ed., 2011. (p. 57.)

[92] *P-753 LISA Linear Actuator and Stage [Brochure]*, Physik Instrumente, 2008. (p. 64.)

[93] A. Luna-Arriaga, F. Bony, and T. Bosch, "Real time displacement sensor based on self-mixing interferometry," in *Proc. IEEE-I2MTC*, 2012, pp. 1370 – 1374. (p. 65.)

[94] *TMS320C6414T, TMS320C6415T, TMS320C6416T Fixed - Point Digital Signal Processors*, Texas Instruments Std. (p. 67.)

[95] *TLV320AIC23 Stereo Audio Codec, 8-to 96 kHz, with Integrated Headphone Amplifier, Data Manual*, Texas Instruments Std. (p. 67.)

[96] S. Donati, M. Norgia, and G. Giuliani, "Self-mixing differential vibrometer based on electronic channel subtraction," *Applied Optics*, vol. 45, pp. 7264–7268, 2006. (p. 76.)

[97] M. Norgia, A. Pesatori, M. Tanelli, and M. Lovera, "Frequency compensation for a self-mixing interferometer," *IEEE Trans. Instrum. Meas.*, vol. 59, pp. 1368–1374, 2010. (p. 76.)

[98] U. Zabit, R. Atashkhooei, T. Bosch, S. Royo, F. Bony, and A. D. Rakic, "Adaptive self-mixing vibrometer based on a liquid lens," *Optics Letters*, vol. 14, no. 8, pp. 1278 – 1280, 2010. (p. 76.)

[99] B. Berge and J. Peseux, "Variable focal lens controlled by an external voltage: an application of electrowetting," *Eur. Phys. J. E.*, vol. 3, no. 2, pp. 159–163, 2000. (p. 76.)

[100] C. Bès, T. Bosch, G. Plantier, and F. Bony, "Characterisation of a self-mixing displacement sensor under moderate feedback," *Optical Engineering*, vol. 45, no. 8, pp. 84 402–1–84 402–6, 2006. (p. 77.)

[101] A. Doncescu, C. Bès, and T. Bosch, "Displacement estimation with an optical interferometer using an evolutionary algorithm," in *Proc. IEEE-Sensors*, 2007. (p. 77.)

[102] M. Norgia and C. Svelto, "Novel measurement method for signal recovery in optical vibrometer," *IEEE Trans. Instrum. Meas.*, vol. 57, no. 8, pp. 1703–1707, 2008. (p. 77.)

[103] L. Scalise, Y. Yu, G. Giuliani, G. Plantier, and T. Bosch, "Self-mixing laser diode velocimetry: application to vibration and velocity measurement," *IEEE Trans. Instrum. Meas.*, vol. 53, pp. 223–232, 2004. (p. 77.)

[104] A. Magnani, M. Norgia, and A. Pesatori, "Optical displacement sensor based on novel self-mixing reconstruction method," in *Proc. IEEE-Sensors*, 2010, pp. 517–520. (p. 79.)

[105] A. Magnani, A. Pesatori, and M. Norgia, "Novel displacement reconstruction method for vibration measurements," in *Proc. IEEE-I2MTC*, 2011, pp. 1–4. (pp. 79, 117 and 137.)

[106] S. Donati, "Speckle-pattern intensity and phase second order conditional statistics," *J. Opt. Soc. Amer.*, vol. 69, pp. 1690–1694, 1979. (p. 84.)

[107] F. Gouaux, "Optimization d'un capteur optoélectronique de distance et de déplacement pour le controle non destructif," Ph.D. dissertation, Institut National Polytechnique de Toulouse, 1999. (p. 84.)

[108] S. Ottonelli, M. Dabbicco, F. De Lucia, and G. Scamarcio, "Simultaneous measurement of linear and transverse displacements by laser self-mixing," *Applied Optics*, vol. 48, pp. 1784–1789, 2009. (p. 84.)

[109] R. Atashkhooei, S. Royo, and F. Azcona, "Dealing with speckle effects in self-mixing interferometry measurements," *IEEE Sensors J.*, vol. 13, pp. 1641–1647, 2013. (pp. 84, 85 and 123.)

[110] U. Zabit, O. D. Bernal, and T. Bosch, "Self-mixing laser sensor for large ddisplacement: Signal recovery in the presence of speckle," *IEEE Sensors J.*, vol. 13, pp. 824–831, 2013. (p. 85.)

[111] X. Zhang, J. Xi, Y. Yu, and J. F. Chicharo, "The Fourier spectrum analysis of optical feedback self-mixing signal under weak and moderate feedback," in *Proc. IEEE-DELTA*, 2008, pp. 491–495. (p. 92.)

[112] D. W. Kammler, *A first course in Fourier analysis*. Cambridge University Press, 2007. (p. 92.)

[113] R. Teysseyre, F. Bony, J. Perchoux, and T. Bosch, "Laser dynamics in sawtooth-like self-mixing signals," *Optics Letters*, vol. 37, pp. 3771–3773, 2012. (p. 96.)

[114] B. Boashash, "Estimating and interpreting the instantaneous frequency of a signal - part 1: Fundamentals," *Proceedings - IEEE*, vol. 80, pp. 520–538, 1992. (p. 99.)

[115] B. Picinbono, "On instantaneous amplitud and phase of signals," *IEEE Trans. Signal Process.*, vol. 45, pp. 552–560, 1997. (p. 99.)

[116] N. E. Huang, Z. Wu, S. R. Long, K. C. Arnold, X. Chen, and K. Blank, "On instantaneous frequency," *Advances in adaptive data analysis*, vol. 1, pp. 177–229, 2009. (p. 99.)

[117] S. L. Hahn, "The history of applications of analytic signals in electrical and radio engineering," in *Proc. IEEE EUROCON*, 2007. (p. 99.)

[118] R. N. Bracewell, *The Fourier transform and its applications*. McGraw-Hill, 1978. (p. 100.)

[119] Y. Fan, Y. Yu, J. Xi, and J. F. Chicharo, "Improving the measurement performance for a self-mixing interferometry-based displacement sensing system," *Applied Optics*, vol. 50, pp. 5064–5072, 2011. (pp. 100, 129 and 146.)

[120] J. Smith, U. W. Rathe, and C. P. Burger, "Lasers with optical feedback as displacement sensors," *Optical Engineering*, vol. 34, pp. 2802–10, 1995. (p. 109.)

[121] G. Liu, S. Zhang, Y. Li, and J. Zhu, "Optical feedback characteristics in a dial-frequency laser during laser cavity tuning," *Chinese Physics*, vol. 14, pp. 1984–06, 2005. (p. 109.)

[122] S. L. Marple, "Computing the discrete-time analytic signal via FFT," *IEEE Transactions on Signal Processing*, vol. 47, pp. 2600–2603, 1999. (p. 109.)

[123] L. Campagnolo, C. Tanasoiu, and J. Perchoux, "Discrimination du sens de deplacement par modulation d'une diode laser soumise à une réinjection optique," in *Mesures et Techniques Optiques pour l'Industrie Toulouse-Labège*, 2010. (p. 117.)

[124] Y. Yu, J. Xi, and J. F. Chicharo, "Measuring the feedback parameter of a semiconductor laser with external optical feedback," *Optics Express*, vol. 19, pp. 9582–9593, 2011. (p. 146.)

[125] A. Magnani and M. Norgia, "Spectral analysis for velocity measurement through self-mixing interferometry," *IEEE Journal of Quantum Electronics*, vol. 49, pp. 765–9, 2013. (p. 147.)

[126] A. Magnani, A. Pesatori, and M. Norgia, "Real-time self-mixing interferometer for long distances," *IEEE Trans. Instrum. Meas.*, vol. PP, p. 1, 2014. (p. 147.)

[127] L. Yah Leng, M. Nikolic, K. Bertling, R. Kliese, and A. D. Rakic, "Self-mixing imaging sensor using a monolithic VCSEL array with parallel readout," *Optics Express*, vol. 17, no. 7, pp. 5517–5525, 2009. (p. 148.)

[128] D. Markovic and R. W. Brodersen, *DSP Architecture Design Essentials*, A. P. Chandrakasan, Ed. Springer, 2012. (p. 148.)

Glossary

α	The linewidth enhancement factor or Henry factor
α_p	Coefficient for the losses due to absorption by free carriers
C	Feedback coupling coefficient
c	Speed of light
d	The width of the laser cavity
ε	The excess fringe of the self-mixing signal
e	The elementary charge
ϵ	Mismatch coefficient between the reflected and the lasing modes
F_{D}	Doppler frequency corresponding to the self-mixing signal frequency
g_{linear}	Linear threshold gain of the laser active region
g_{th_0}	Threshold gain of the active region in the absence of feedback
g_{th_F}	Threshold gain of the active region in the presence of feedback
J	The current density
λ_{F}	The laser emission wavelength with feedback
λ_0,λ	The laser emission wavelength without feedback
ℓ	Length of the laser diode cavity
ℓ_{ext}	Length of the external cavity
$L_{c\mathrm{min}}$	The minimum coherence length of a laser subject to feedback
μ_{e_0}	Effective refractive index of the active region without feedback
μ_{e_F}	Effective refractive index of the active region with feedback
$\mu_{\mathrm{e}'} - j\mu_{\mathrm{e}''}$	Effective refractive index in its complex form
$\overline{\mu_{\mathrm{e}_0}}$	Effective group index of the diode in the absence of target
m	Parameter representing the modulation of the laser diode
ν_0	Laser diode emission frequency in the absence of target
ν_F	Laser diode emission frequency in the presence of target
N	The number of Self-mixing fringes
n	Density of electrons
$n_F, n_{\mathrm{th}_{\mathrm{F}}}$	Density of electrons for the laser under feedback and at the threshold
n_0, n_{th_0}	Density of electrons for the stand-alone laser and at the threshold
n_{null}	Density of electrons corresponding to a null gain
P_0	The laser optical power without feedback
P_F	The laser optical power with feedback
$P`(t)$	The normalized laser optical power with feedback

q	longitudinal mode for the laser emission without back-reflections
r_1', r_2	Reflection coefficients for the electric field at the interfaces
r_3	Reflection coefficient for the electric field at the target
r_{eq}	Reflection coefficient for the electric field for equivalent cavity
N_0	Density of photons for the stand-alone laser
N_F	Density of photons for the laser under feedback
τ_{ext}	Time of flight of the laser beam in the external cavity
τ_ℓ	Time of flight of the laser beam in the laser cavity
τ_n	The electron average lifetime
V_F	Velocity of the target
Φ_0	Phase of the laser emission without feedback
Φ_{F}	Phase of the laser emission with feedback
Φ_{eq}	Inverse of the phase of the equivalent cavity reflection coefficient
x_{F}	Phase of the laser emission with feedback, in wavelength
x_0	Phase of the laser emission without feedback, in wavelength
θ	The angle of the rotating surface with the laser propagation direction
υ_g	The group velocity
ζ	Coupling effect parameter between the target and the laser cavity

List of Publications

International Conferences

- A. Luna-Arriaga, F. Bony, and T. Bosch, "Digital to analog conversion methodology applied to self-mixing displacement signals," in *Proc. AIP-AIVELA*, vol. 1457, 2012, pp. 125 – 131.
- A. Luna-Arriaga, F. Bony, and T. Bosch, "Real time displacement sensor based on self-mixing interferometry," in *Proc. IEEE-I2MTC*, 2012, pp. 1370 – 1374.
- A. Luna-Arriaga, F. Bony, and T. Bosch, "Progress on self-mixing sensors for in-situ displacement measurement," in *Proc. IEEE-ECMSM*, 2013, pp. 1 – 5.

National Conferences

- A. Luna-Arriaga, "Vers la conception d'un capteur embarqué pour la mesure du déplacement par interférométrie à rétro-injection laser", Journée école doctorale GEET, Toulouse, 2013.
- A. Luna-Arriaga, "Partitionnement matériel-logiciel d'un capteur de déplacement à rétro-injection optique pour la conception d'un SoC", Simposium CONACYT Fellows in Europe, Paris, 2011.

Patent

- A. Luna-Arriaga, T. Bosch, and F. Bony, "Dispositif optique de mesure d'un paramètre physique et procédé associé", Dépôt: FR.8/07/2013.

Prize

- A. Luna-Arriaga, "Concours linuxembedded 2012", Prix du Jury, Open Wide Ingénierie, Paris, France, le 28/11/2012.

Analysis & implementation of algorithms for embedded self-mixing displacement sensors design.

Abstract: The interaction between an emitted laser beam and a small portion of backscattered light from a pointed target that re-enters the laser's cavity, is at the origin of optical feedback phenomenon or self-mixing. Exploiting these unconventional interferometric fringes for non-contact sensors is attractive due to its minimal optical part-count and self-aligned nature. In this thesis we approach its development as a cost-effective embedded implementation for displacement measurement. To this end we explored signal processing methods for fringe detection and target's movement reconstruction, avoiding the usage of external components. We first identified some incompatibilities in prior algorithms from our research center, and then proposed further solutions. Based on interpolation theory, a simplified but proved real-time algorithm resulted for displacement reconstruction. Relying on analytical signal elaboration, an improved approach for phase calculation allowed us to provide a fringe detection algorithm robust to amplitude variations, disregarding the feedback regime and thus, allowing a seemly usage over an increased variety of applications.

Keywords: Self-mixing, Optical feedback interferometry, Displacement measurement, Laser diode sensor, Embedded system, Digital signal processing

---

Analyse et implémentation d'algorithmes pour la conception de capteurs de déplacement embarqués, utilisant la rétro-injection optique

Résumé: L'interaction entre un faisceau laser émis avec une partie de la lumière réfléchi depuis une cible qui rentre dans la cavité active du laser, est à l'origine du phénomène de rétro-injection optique ou self-mixing. L'utilisation de ces franges interférométriques non conventionnelles, semble attractive du au faible nombre des composant optiques et son caractère auto-aligné. Dans cette thèse nous approchons leur développement en tant qu'implémentation embarqué rentable pour la mesure du déplacement. A cette fin, nous avons exploré des méthodes du traitement du signal pour la détection des franges et la reconstruction du mouvement de la cible, en évitant l'usage de composant externes. Premièrement, nous avons identifié quelques incompatibilités dans des algorithmes précédentes établis dans notre centre de recherche, puis nous avons avancé des solutions. Fondé sur la théorie d'interpolation, an algorithme simplifié mais démontré convenable en temps-réel à été proposé pour la reconstruction du déplacement. En s'appuyant sur l'élaboration d'un signal analytique, il à été proposé une version amélioré pour le calcul de phase. Celle-ci nous à permit de fournir un algorithme pour la détection de franges, robuste aux variations d'amplitude, sans tenir compte du régime de rétro-injection, impliquant une convenable utilisation pour une variété d'applications.

Mot Clés: Interférométrie à rétro-injection optique, Mesure de déplacement, Capteur diode laser, Système embarqué, Traitement numérique du signal